ADVANCED ELECTRODE MATERIALS FOR LITHIUM- AND POTASSIUM-BASED ENERGY STORAGE DEVICES

A thesis presented for the award of the degree of

Doctor of Philosophy

from

University of Technology Sydney

By

Shuoqing Zhao, B. Eng., M. Sc.

September, 2021

CERTIFICATE OF ORIGINAL AUTHORSHIP

I, Shuoqing Zhao, declare that this thesis, is submitted in fulfilment of the requirements for the award of Doctor of Philosophy, in the Faculty of Science at the University of Technology Sydney.

This thesis is wholly my own work unless otherwise reference or acknowledgement. In addition, I certify that all information sources and literature used are indicated in the thesis.

This document has not been submitted for qualifications at any other academic institution.

This research is supported by the Australian Government Research Training Program.

Shuoqing Zhao

Production Note:
Signature removed prior to publication.

Sydney, Australia

September 2021

ACKNOWLEDGEMENTS

It has been four years since I was enrolled as a Ph.D. candidate in University of Technology Sydney (UTS) for the autumn of 2017. Due to the impact of COVID-19, up until now, I am still stranded in China and cannot return to Australia to get together with my friends. It is a really difficult and painful period, during which I have suffered from depression and the tragic loss. However, I should also embrace to this special experience and really appreciate the valuable help from my family members, friends and UTS.

Firstly, I express sincere thanks to my supervisor, Professor Guoxiu Wang, for his encouragement, invaluable suggestions and selfless assistance throughout my Ph.D. study at UTS.

Secondly, many thanks to my co-supervisor Dr. Bing Sun and Dr. Jane Yao for their kind help and support, which smoothly assisted my work in laboratory as well as my daily life in Sydney.

I would like to acknowledge my colleagues at UTS, Dr. Hao Liu, Dr. Dawei Su, Dr. Jinqiang Zhang, Dr. Yufei Zhao, Dr. Dong Zhou, Dr. Pan Xiong, Dr. Liubing Dong, Dr. Huajun Tian, Dr. Xin Guo, Dr. Weizhai Bao, Dr. Tuhin Sahu, Dr. Kang Yan, Dr. Xingxing Yu, Dr. Yi Chen, Dr. Xiaochun Gao, Mr. Fan Zhang, Mr. Tianyi Wang, Miss Ziqi Guo, Miss Pauline Jaumaux, Mr. Javad Safaei, Miss Yuhan Xie. Their kind collaboration and assistance were helpful.

Also, I want to thank my friends, Mr. Feng Liu, Mr. Tiexin Li and Dr. Jianjia Zhang, we shared a lot of happy memories in Sydney.

In addition, I appreciate the administrative and technical support from Miss Elizabeth Gurung Tamang, Dr. Ronald Shimmon, Dr. Linda Xiao, Miss Katie McBean, Mr. Geoff McCredie and Mr. Herbert Yuan, Mr. Iurii Bodachivskyi.

The financial support from Australian Rail Manufacturing Cooperative Research Centre (RMCRC) and UTS (International Research Scholarship) helped me completing my Ph.D. study, which is highly acknowledged.

Last but not the least, I would like to thank my family members for their wholly warm support throughout my life.

STATEMENT OF FORMAT

This is the statement indicating that seven published works are included in this doctoral thesis. Three review papers are referred to 1.2, 1.3, 1.4, 1.5 and 1.7 in the introduction. Four original published works are referred to chapter 3, chapter 4, chapter 5 and chapter 6. The related publications in this thesis are listed as follows:

1. Title: **Reaction Mechanisms of Layered Lithium-Rich Cathode Materials for High-Energy Lithium-Ion Batteries**. Authors: **Shuoqing Zhao**, Kang Yan, Jinqiang Zhang, Bing Sun and Guoxiu Wang. Journal: *Angew. Chem. Int. Ed.*, 2020, 202000262. DOI: 10.1002/anie.202000262. This work is referred to **1.2**, **1.3** and **1.4** in the introduction.

2. Title: **Towards High-energy-density Lithium-ion Batteries: Strategies for Developing High-capacity Lithium-rich Cathode Materials**. Authors: **Shuoqing Zhao**, Ziqi Guo, Kang Yan, Shuwei Wan, Fengrong He, Bing Sun and Guoxiu Wang. Journal: *Energy Stor. Mater.*, 2021, 34, 716-734. DOI: 10.1016/j.ensm.2020.11.008. This work is referred to **1.5** in the introduction.

3. Title: **The Rise of Prussian Blue Analogs: Challenges and Opportunities for High-Performance Cathode Materials in Potassium-Ion Batteries**. Authors: **Shuoqing Zhao**, Ziqi Guo, Kang Yan, Xin Guo, Shuwei Wan, Fengrong He, Bing Sun and Guoxiu Wang. Journal: *Small Structures*, 2020, 2000054. DOI: 10.1002/sstr.202000054. This work is referred to **1.7** in the introduction.

4. Title: **Aegis of Lithium-Rich Cathode Materials via Heterostructured $LiAlF_4$ Coating for High-Performance Lithium-Ion Batteries**. Authors: **Shuoqing Zhao**, Bing Sun, Kang Yan, Jinqiang Zhang, Chengyin Wang and Guoxiu Wang. Journal: *ACS Appl. Mater. Interfaces*, 2018, 10 (39), 33260-33268. DOI: 10.1021/acsami.8b11471. This work is referred to **Chapter 3**.

5. Title: **Construction of Hierarchical $K_{1.39}Mn_3O_6$ Spheres via AlF_3 Coating for High-Performance Potassium-Ion Batteries**. Authors: **Shuoqing Zhao**, Kang Yan, Paul Munroe, Bing Sun and Guoxiu Wang. Journal: *Adv. Energy Mater.*, 2019, 9 (10), 1803757. DOI: 10.1002/aenm.201803757. This work is referred to **Chapter 4**.

6. Title: **$K_2Ti_2O_5$@C Microspheres with Enhanced K^+ Intercalation Pseudocapacitance Ensuring Fast Potassium Storage and Long-Term Cycling Stability**. Authors: **Shuoqing Zhao**, Liubing Dong, Bing Sun, Kang Yan, Jinqiang Zhang, Shuwei Wan, Fengrong He, Paul Munroe, Peter H. L. Notten and Guoxiu Wang. Journal: *Small*, 2020, 16 (4), 1803757. DOI: 1906131. This work is referred to **Chapter 5**.

7. Title: **Phosphorus and Oxygen Dual-doped Porous Carbon Spheres with Enhanced Reaction Kinetics as Anode Materials for High-performance Potassium-ion Hybrid Capacitors**. Authors: **Shuoqing Zhao**, Kang Yan, Jiayu Liang, Qinghong Yuan, Jinqiang Zhang, Bing Sun, Paul Munroe and Guoxiu Wang. Journal: *Adv. Funct. Mater.*, 2021, 2102060. DOI: 10.1002/adfm.202102060. This work is referred to **Chapter 6**.

RESEARCH PUBLICATIONS

1. **Zhao, S.**; Yan, K.; Zhang, J.; Sun, B.*; Wang, G.*, Reaction Mechanisms of Layered Lithium-Rich Cathode Materials for High-Energy Lithium-Ion Batteries. *Angewandte Chemie International Edition* **2021**, 60 (5), 2208-2220.
2. **Zhao, S.**; Yan, K.; Liang, J.; Yuan, Q.; Zhang, J.; Sun, B.*; Munroe, P.; Wang, G.*, Phosphorus and Oxygen Dual-doped Porous Carbon Spheres with Enhanced Reaction Kinetics as Anode Materials for High-performance Potassium-ion Hybrid Capacitors. *Advanced Functional Materials* **2021**, 2102060, DOI: 10.1002/adfm.202102060.
3. **Zhao, S.**; Guo, Z.; Yan, K.; Wan, S.; He, F.; Sun, B.*; Wang, G.*, Towards high-energy-density lithium-ion batteries: Strategies for developing high-capacity lithium-rich cathode materials. *Energy Storage Materials* **2021**, 34, 716-734.
4. **Zhao, S.**; Guo, Z.; Yang, J.; Wang, C.; Sun, B.*; Wang, G.*, Nanoengineering of Advanced Carbon Materials for Sodium-Ion Batteries. *Small* **2021**, 2007431.
5. **Zhao, S.**; Guo, Z.; Yan, K.; Guo, X.; Wan, S.; He, F.; Sun, B.*; Wang, G.*, The Rise of Prussian Blue Analogs: Challenges and Opportunities for High-Performance Cathode Materials in Potassium-Ion Batteries. *Small Structures* **2021**, 2 (1), 2000054.
6. **Zhao, S.**; Dong, L.; Sun, B.*; Yan, K.; Zhang, J.; Wan, S.; He, F.; Munroe, P.; Notten, P. H. L.; Wang, G.*, $K_2Ti_2O_5$@C Microspheres with Enhanced K^+ Intercalation Pseudocapacitance Ensuring Fast Potassium Storage and Long-Term Cycling Stability. *Small* **2020**, 16 (4), 1906131.
7. **Zhao, S.**; Yan, K.; Munroe, P.; Sun, B.*; Wang, G.*, Construction of Hierarchical $K_{1.39}Mn_3O_6$ Spheres via AlF_3 Coating for High-Performance Potassium-Ion Batteries. *Advanced Energy Materials* **2019**, 9 (10), 1803757.
8. **Zhao, S.**; Sun, B.*; Yan, K.; Zhang, J.; Wang, C.; Wang, G.*, Aegis of Lithium-Rich Cathode Materials via Heterostructured $LiAlF_4$ Coating for High-Performance Lithium-Ion Batteries. *ACS Applied Materials & Interfaces* **2018**, 10 (39), 33260-33268.
9. Yan, K.; **Zhao, S.**; Zhang, J.; Safaei, J.; Yu, X.; Wang, T.; Wang, S.; Sun, B.*; Wang, G.*, Dendrite-Free Sodium Metal Batteries Enabled by the Release of Contact Strain on Flexible and Sodiophilic Matrix. *Nano Letters* **2020**, 20 (8), 6112-6119.
10. Guo, Z.; **Zhao, S.**; Li, T.; Su, D.*; Guo, S.; Wang, G.*, Recent Advances in Rechargeable Magnesium-Based Batteries for High-Efficiency Energy Storage. *Advanced Energy Materials* **2020**, 10 (21), 1903591.
11. Yan, K.; Wang, J.; **Zhao, S.**; Zhou, D.; Sun, B.*; Cui, Y.*; Wang, G.*, Temperature-Dependent Nucleation and Growth of Dendrite-Free Lithium Metal Anodes. *Angewandte Chemie International Edition* **2019**, 58 (33), 11364-11368.
12. Tian, H.; Wang, T.; Zhang, F.; **Zhao, S.**; Wan, S.; He, F.; Wang, G.*, Tunable porous carbon spheres for high-performance rechargeable batteries. *Journal of Materials Chemistry A* **2018**, 6 (27), 12816-12841.

TABLE OF CONTENTS

LIST OF FIGURES

LIST OF TABLES

ABSTRACT

With the growing demand for high-energy-density lithium-ion batteries, layered lithium-rich cathode materials with high specific capacity and low cost have been widely regarded as one of the most attractive candidates for next-generation lithium-ion batteries. However, issues such as voltage decay, capacity loss and sluggish reaction kinetics have hindered their further commercialization for decades. Herein, we propose a heterostructured $LiAlF_4$ coating strategy to overcome those obstacles. The as-developed lithium-rich cathode material shows a high reversible capacity and ultralong cycling stability. The enhanced performances can be attributed to the introduction of the lithium-ion-conductive nanolayer and the generation of nonbonding O^{n-} species in the active material lattice, which enable rapid and effective lithium ions transport and diffusion.

Considering the increasing cost and uneven distribution of lithium resources, potassium-ion batteries are attracting great interest for emerging large-scale energy storage, owing to their advantages such as low cost and high operational voltage. Herein, the synthesis of hierarchical $K_{1.39}Mn_3O_6$ microspheres as cathode materials for potassium-ion batteries is reported. Additionally, an effective AlF_3 surface coating strategy is applied to further improve the electrochemical performance of $K_{1.39}Mn_3O_6$ microspheres. The as-synthesized AlF_3 coated $K_{1.39}Mn_3O_6$ microspheres show a high reversible capacity, excellent rate capability, and cycling stability. *Ex situ* X-ray diffraction measurements reveal that the irreversible structure evolution can be significantly mitigated via surface modification.

As for anode materials, it is reported on carbon-coated $K_2Ti_2O_5$ microspheres (S-KTO@C) synthesized through a facile spray drying method. Taking advantages of both the porous microstructure and carbon coating, S-KTO@C shows excellent rate capability and cycling stability as an anode material for PIBs. As a proof of concept, a potassium-ion hybrid capacitor shows a high energy density, high power density, and excellent capacity retention.

Phosphorus/oxygen dual-doped porous carbon spheres, which possess expanded interlayer distances, abundant redox active sites and oxygen-rich defects, were also prepared in this thesis. The as-developed anode material shows superior electrochemical performances. *In situ* Raman spectroscopy and density functional theory calculations further confirm that the formation of P-C and P-O/P-OH bonds not only improves structural stability, but also contributes to a rapid surface-controlled potassium adsorption process. A potassium-ion hybrid capacitor was assembled by a dual-doped porous carbon sphere anode and an activated carbon cathode, which holds great promise as next-generation energy storage devices.

INTRODUCTION

The strong market incentives and pressing consumption of fossil fuels call for high safety, high-energy and eco-friendly energy storage systems. Renewable energy storage technology using lithium-ion batteries (LIBs) as power sources pushes rapid development of LIBs, owing to their remarkable advantages such as high energy density, low self-discharge rate and negligible memory effects. Although the large-scale application of LIBs continues to proliferate, the main impediment for such a growth is the unsatisfactory energy density and lifetime of next-generation LIBs that are powering most electric vehicles (EVs) in the market. As cathode materials primarily determine the Li^+ storage capability and the overall energy density of LIBs, the fast expansion of LIBs markets prompts the exploration for higher-energy and lower-cost cathodes. However, traditional intercalation transition metal oxide cathodes currently face severe challenges like the low specific capacity (< 250 mAh g^{-1}) and energy density (< 300 Wh kg^{-1}), which cannot meet the requirement of the EV market to achieve long-distance drive (> 300 miles) for larger and all-electric vehicles with low cost and fast charging rates.

Although LIBs have been developed for stationary energy storage since their first successful commercialization in 1991, lithium resources are costly and deficient in the earth's crust. Hence, due to the flourish of EVs and other electronic devices markets, the growing demand from modern society poses a potential threat on supply availability of lithium. Given the limited and uneven distribution of lithium resources, there is an urgent need to find suitable alternatives with low cost and high safety to fulfil the ever-increasing market demand. Potassium-ion

batteries (PIBs) are one type of rechargeable alkali-ion batteries that are capable of inheriting the working mechanism and advantages of LIBs. The natural abundance and nontoxicity of potassium could have a reduced environmental impact on large-scale production. Furthermore, the low standard redox potential of K/K^+ (−2.94 V v*s.* standard hydrogen electrode, SHE) leads to a high-output voltage and high energy density for PIBs. These features make PIBs one of the most attractive candidates for grid-scale energy storage.

Therefore, in this doctoral work, I investigated the synthesis of high-performance electrode materials for LIBs and PIBs. The research tasks are mainly focusing on surface modification and the nanostructure design of electrode materials. Meanwhile, I adopted the *in situ* characterization techniques to deeply understand the fundamental reaction mechanism and structural evolution of as-prepared electrode materials. In more detail, this doctoral work introduces the surface coating strategy as well as porous nanostructure to boost the electrochemical performance of both LIBs and PIBs. The contents are briefly outlined as follows:

※ **Chapter 1** demonstrates the background information and the working principle of LIBs and PIBs. Recent advance of electrode materials in lithium- and potassium-based energy storage devices were introduced.

※ **Chapter 2** provides the methodology and research facilities, including the material preparation process, material characterization, electrochemical measurements and data analysis.

※ **Chapter 3** introduces a heterostructured $LiAlF_4$ coating strategy to improve the electrochemical performance of layered lithium-rich cathode materials. Comparing with those of pristine and AlF_3-coated layered lithium-rich cathode materials, the enhanced performances can be attributed to the introduction of a lithium-ion-conductive nanolayer and the generation of nonbonding O^{n-} species. This work provides a new strategy to develop high-performance lithium-rich cathode materials for high-energy-density LIBs.

※ In **Chapter 4**, an effective AlF_3 surface coating strategy is applied to further improve the electrochemical performance of $K_{1.39}Mn_3O_6$ cathode materials. Galvanostatic intermittent titration technique and *ex situ* X-ray diffraction measurements reveal that the irreversible structure evolution can be significantly mitigated via surface modification. This work sheds light on rational design of high-performance cathode materials for potassium-ion batteries.

※ **Chapter 5** presents the fabrication of carbon-coated $K_2Ti_2O_5$ microspheres through a facile spray drying method. The intimate integration of carbon coating through chemical vapor deposition technology significantly enhances the K^+ intercalation pseudocapacitive behavior. As a proof of concept, a potassium-ion hybrid capacitor was constructed. The assembled device shows a high energy density, high power density, and excellent capacity retention. This work can pave the way for the development of high-performance potassium-based energy storage devices.

※ **Chapter 6** shows the synthesis of phosphorus/oxygen dual-doped porous carbon spheres, which possess expanded interlayer distances, abundant redox active sites and oxygen-rich

defects. The as-developed battery-type anode material shows high discharge capacity, outstanding rate capability, and ultralong cycling stability. *In situ* Raman spectroscopy and density functional theory calculations further confirm that the formation of P-C and P-O/P-OH bonds not only improves structural stability, but also contributes to a rapid surface-controlled potassium adsorption process. As a proof of concept, a potassium-ion hybrid capacitor was assembled by a dual-doped porous carbon sphere anode and an activated carbon cathode. It shows superior electrochemical performances, which opens a new avenue for innovative potassium-based energy storage technology.

※ **Chapter 7** summarizes the key conclusions in this thesis and provides outlooks and perspectives for the future research.

CHAPTER 1 LITERATURE REVIEW

1.1 Lithium-ion batteries

With the rapid development of our modern society, the massive consumption of fossil fuels causes severe climate change and global warming.[1-2] Electrification of road transport can effectively alleviate carbon dioxide emissions. Electric vehicles (EVs) using lithium-ion batteries (LIBs) as power sources are being produced with rapidly increased scale annually[3-5]. A typical LIB comprises a cathode, an anode, a separator and the corresponding electrolyte. Such kind of "rock chair" battery enables the reversible insertion and extraction of lithium ions (Li^+) in electrode materials during the operation of LIBs.[4, 6] Although the worldwide commercial market for LIBs continues to proliferate, the challenge is the development of LIBs with a significantly extended life span and much-increased energy density. The Li^+ storage capability and operation voltage of electrode materials determine the energy density of LIBs, which makes the electrode materials to play crucial roles in the entire battery system.[7-9] In 1980, Goodenough and co-workers[10] accurately predicted the high potential of transition metal oxides and reported layered $LiCoO_2$ as a suitable cathode material for LIBs. After SONY Corp. commercialized LIBs with $LiCoO_2$ as cathode materials and graphite as anode materials in 1991, research interests in discovering new electrode materials with higher energy densities have been accelerated. After almost 30 years of development, graphite anode materials still dominate the market today, whereas a series of cathode materials, including $LiMn_2O_4$[11], $LiFePO_4$[12] and $LiNi_{0.8}Co_{0.1}Mn_{0.1}O_2$[13], were intensively investigated and applied in large-scale LIBs to replace

$LiCoO_2$.[14] However, the development of the above-mentioned cathode materials has encountered a bottleneck for electric vehicles because of the low specific capacity (< 250 mAh g^{-1}) and energy density, which cannot meet the requirement of the automotive market to achieve long-distance drive (> 300 miles) and low cost.[15-16]

1.2 Lithium-rich cathode materials

The emergence of LLRM cathode materials (e.g., $xLi_2MnO_3•(1-x)LiMO_2$, M = transition metal (TM)) opens up a new possibility for designing high-energy-density LIBs.[17-20] **Figure 1.1** compares electrochemical performances and physical characteristics of LLRM cathode materials, commercial $LiFePO_4$ cathode materials, and $LiNi_{0.8}Co_{0.1}Mn_{0.1}O_2$ (NCM 811) cathode materials.[21-32] LLRM cathode materials have high specific energy, low cost, and good thermal stability. However, some inherent shortcomings inhibit their practical applications. These include a low initial Coulombic efficiency (CE), poor rate capability, serious voltage decay and significant capacity loss upon cycling. Due to the structural complexity and the intricate reaction mechanisms, the development of high-performance LLRM cathode materials has been impeded in the past two decades. Whereas, the recent strong demand from the automotive industry for high-energy-density rechargeable batteries propels the rejuvenation of LLRM cathode materials.

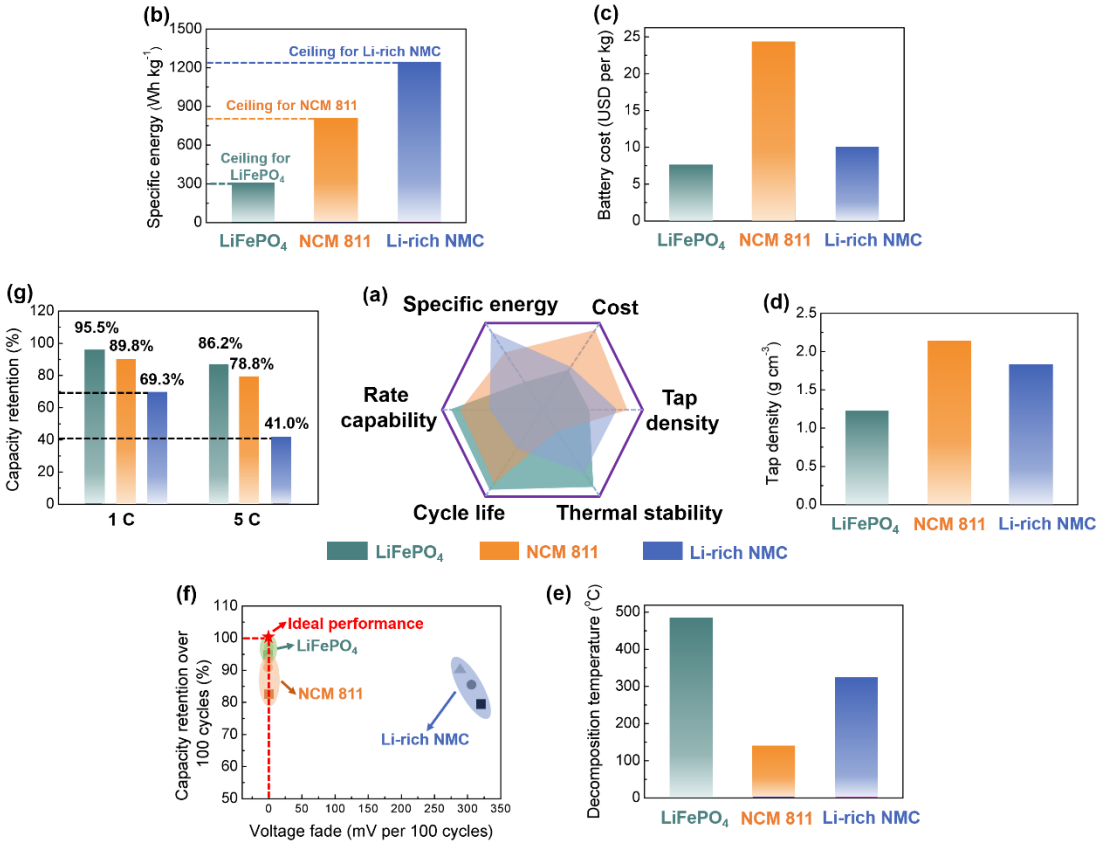

Figure 1.2 Benchmarking LLRM cathode materials ($0.5Li_2MnO_3$•$0.5LiNi_{0.8}Mn_{0.1}Co_{0.1}O_2$, Li-rich NMC) against $LiFePO_4$ and classical layered oxide cathode materials ($LiNi_{0.8}Co_{0.1}Mn_{0.1}O_2$, NCM 811). (a) Radar plot compares $LiFePO_4$, NCM 811 and Li-rich NMC according to six critical criterions that are crucial for practical applications.[21-22] (b) Specific energy according to the weight of cathode materials (coupling with graphite anodes). (c) Average cost, (d) tap density and (e) thermal stability of three electrode materials. The data in (e) are determined by thermogravimetric analysis (TGA). (f) Cycling stability and (g) rate capability of three electrode materials based on previous publication.[23-32]

The evolution of various reaction mechanisms from both cationic and anionic aspects improves our understanding of LLRM cathode materials (**Figure 1.2**).[33-51] Moreover, the rapid

development of cutting-edge characterization technologies provides powerful tools to unravel the structural change of LLRM cathode materials in LIBs. Although previous researchers have already revisited the development of LLRM cathode materials in detail, few of them focus on the reaction mechanisms behind the performance degradation.[20, 52-56] Therefore, we present here a comprehensive review on the reaction mechanisms of LLRM cathode materials. We aim to elucidate the rapid development in exploring high-performance LLRM cathode materials and thus provide inspiration for future research on next-generation high-energy-density LIBs.

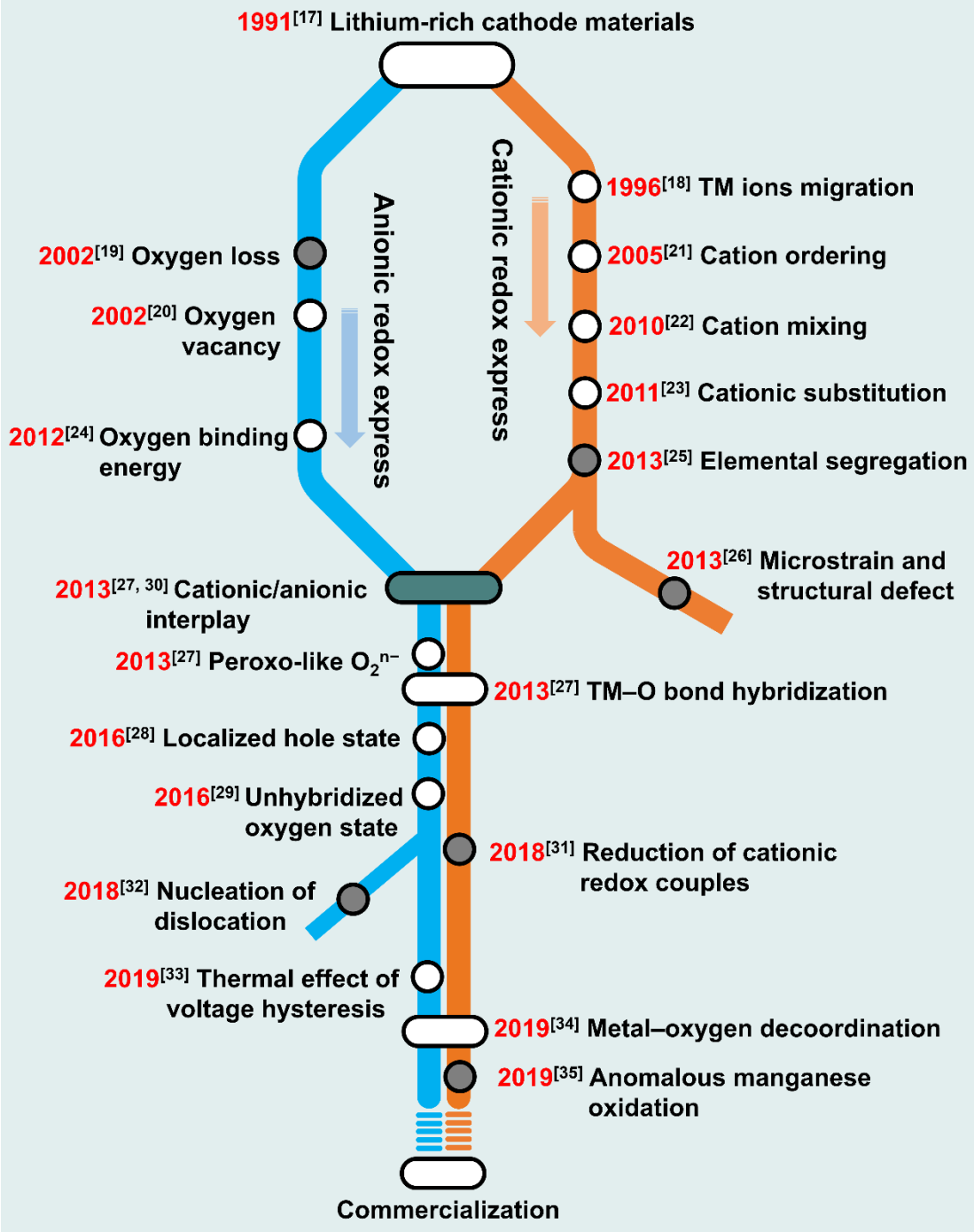

Figure 1.3 Key steps for the development of the reaction mechanisms of LLRM cathode materials.[33-51]

1.3 Structure and chemical composition of LLRM cathode materials

The concept of $xLi_2MnO_3•(1-x)LiMO_2$ (M=transition metal) was first proposed by Rossouw *et al*. in 1991[33], where the single $LiMO_2$ phase can be adjusted with different transition metal contents (M = Ni, Mn, Co, Cr, Fe, Mg, Al, Y, etc.). The diversity of $xLi_2MnO_3•(1-x)LiMO_2$ components ensures various electrochemical features, including specific capacity, rate capability, and cycling stability.[57-59] **Figure 1.3**a and 1.3b exhibit the crystal structure of the representative $LiMO_2$ (rhombohedral phase, space group: $R\ \bar{3}m$) and Li_2MnO_3 (monoclinic phase, space group: $C2/m$). Specifically, the Li_2MnO_3 structure can be rewritten as $Li[Li_{1/3}Mn_{2/3}]O_2$, where Mn in rhombohedral $LiMO_2$ is partially substituted by Li atoms. As an extreme case of $LiMO_2$, monoclinic Li_2MnO_3 consists of alternating $Li_{1/3}Mn_{2/3}$ and Li layers, respectively.[37, 57, 60-64] Furthermore, as shown in Figure 1.3c and 1.3d, the close-packed monoclinic (001) and trigonal (003) layers in Li_2MnO_3 and $LiMO_2$ show the same interlayer spacing (~4.7 Å). Hence Li_2MnO_3 can be integrated with $LiMO_2$ at the atomic level due to the compatibility of the close-packed layer.[65-66] The similarity of these two phases indicates that their crystal structures should be indexed to the α-$NaFeO_2$-type rock-salt phase.[17] However, the structural complexity of the $xLi_2MnO_3•(1-x)LiMO_2$ system gives rise to an ongoing debate on its structural composition.[65, 67-68]

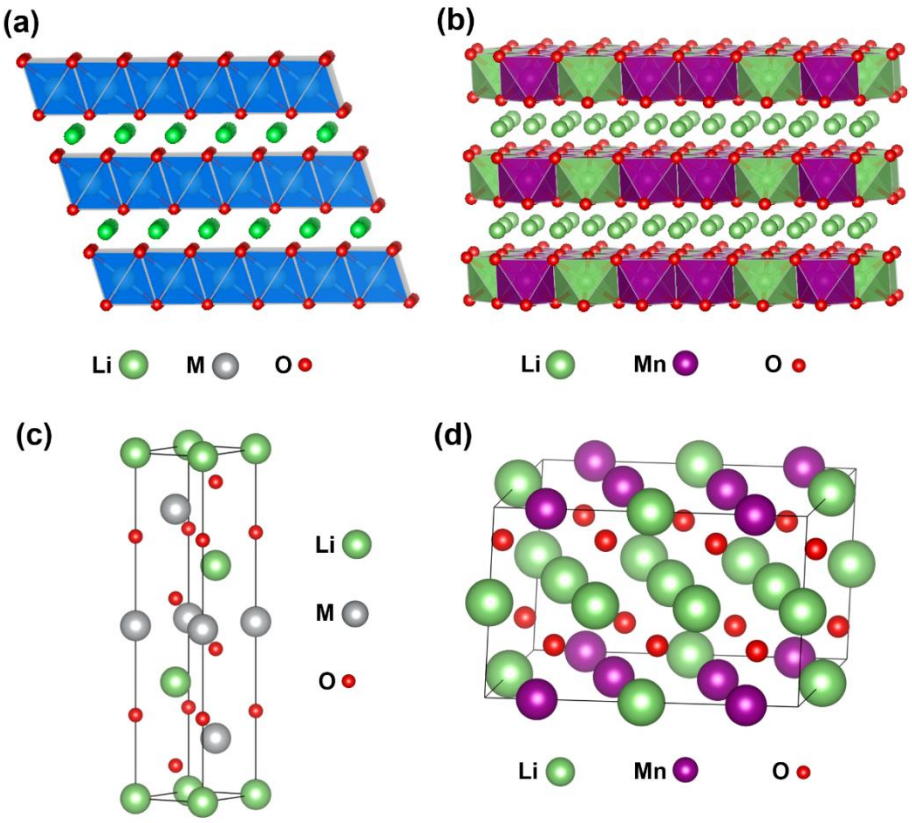

Figure 1.4 Crystal structure models of (a) rhombohedral $LiMO_2$ and (b) monoclinic Li_2MnO_3 seen from the [100] crystallographic direction. Unit cell and atomic arrangement of (c) trigonal $LiMO_2$ and (d) monoclinic Li_2MnO_3.

1.4. Reaction mechanisms of LLRM cathode materials

Recently, various reaction mechanisms were proposed and extensively discussed, aiming to handle the current issues to the sophisticated LLRM cathode material. However, most of them cannot rationally explain all electrochemical behaviors. Herein, we highlight several proposed reaction mechanisms in terms of cationic and anionic aspects.

1.4.1 Prevailing reaction mechanisms

The prevailing theory of the multistep reaction mechanism relies on the three-dimensional compositional phase diagram.[17, 54] For a typical LLRM cathode material ($(1-x)LiMO_2 \bullet xLi_2MnO_3$), Li-ion is continuously extracted from the $LiMO_2$ phase under 4.4 V during the first charge process (**Figure 1.4**a and 1.4b, from point 1 to point 2). Subsequently, a unique and distinguishable voltage plateau appears as shown in Figure 1.4a, which stands for the release of oxygen and the extraction of Li-ions from the Li_2MnO_3 phase induced by complicated chemical reactions and structure evolutions (from point 2 to point 3 in Figure 1.4b).[54, 69] The following discharge process indicates that the reinsertion of Li-ion is associated with the reduction of TM species (from point 3 to point 4). The reversible insertion/extraction of Li-ion in the subsequent cycle shows less voltage hysteresis along with the absence of the voltage plateau at 4.5 V (Figure 1.4c and 1.4d, from point 3 to point 4). However, this prevailing theory cannot well interpret all drawbacks of LLRM cathode materials, especially the severe capacity loss and voltage decay during electrochemical cycling.[70-71] Therefore, we highlight several recently proposed reaction mechanisms in terms of anionic and cationic aspects.

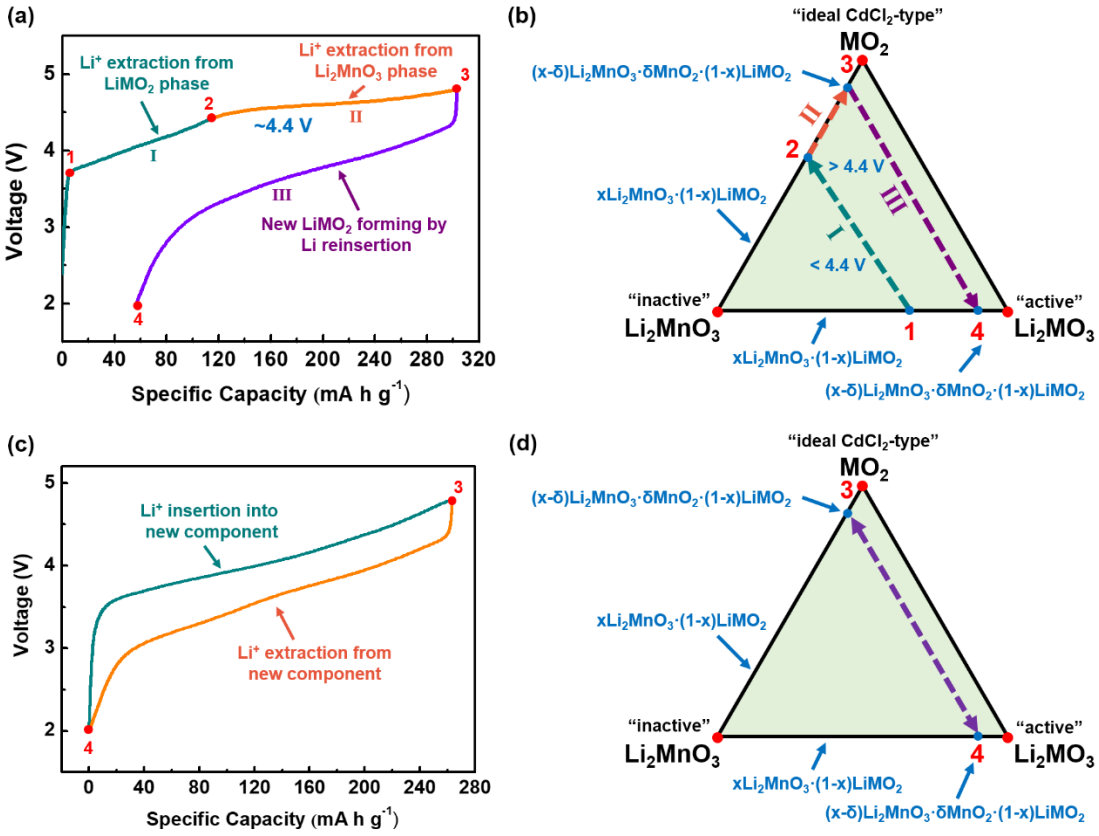

Figure 1.5 Charge–discharge curves and corresponding reaction pathways of layered $xLi_2MnO_3•(1-x)LiMO_2$, based on a compositional phase diagram. (a) Charge/discharge curves and (b) reaction pathways in the first cycle. (c) Charge-discharge curves and (d) reaction pathways in the second cycle.

1.4.2 Anionic redox reaction mechanism

1.4.2.1 Oxygen loss

The concept of "oxygen loss" was first proposed by Lu *et al*. in 2002.[35] Due to the incomplete oxidation state of Ni (< +4), the $Li/Li[Ni_xLi_{(1/3-2x/3)}Mn_{(2/3-x/3)}]O_2$ cathode material shows a reversible intercalation process at the beginning of the first charge. However, a long voltage

plateau is observed after the charge voltage increased to around 4.5 V, where Ni has already reached its maximal contribution to the charge capacity. Through the *in situ* X-ray Diffraction (XRD) investigation, the authors inferred the simultaneous release of both Li and oxygen from the material, especially at the high charge voltage of 4.8 V, corresponding to the irreversible capacity loss in the initial charge stage. Bruce and co-workers[69, 72-74] also confirmed that the removal of Li_2O from the $Li/Li[Ni_xLi_{(1/3-2x/3)}Mn_{(2/3-x/3)}]O_2$ surface accompanied by the creation of vacancies in the bulk material. To provide direct evidence, Armstrong[69] and Manita[75] *et al*. conducted *in situ* differential electrochemical mass spectrometry (DEMS) and detected the oxygen evolution phenomenon from LLRM cathode materials during the initial charge process.

The extensive extraction of oxygen and Li-ion at the high charge voltage plateau (*ca.* 4.4 – 4.6 V) results in the lattice breakdown and irreversible layered-to-spinel phase transformation.[76] Gu *et al*.[77] demonstrated both $LiMO_2$ $R\bar{3}m$ and Li_2MO_3 $C2/m$ phases of the layered $Li_{1.2}Ni_{0.2}Mn_{0.6}O_2$ gradually transferred to the spinel structure after 300 charge/discharge cycles. As shown in **Figure 1.5**a, the pristine $LiMO_2$ $R\bar{3}m$ phase exhibits a layered structure with open Li-ion fast-diffusion channels. The transition from the $LiMO_2$ $R\bar{3}m$ phase to the spinel phase occurs from the surface to the bulk upon cycling, due to the gradual migration of TM ions to Li sites and the movement of Li-ion into the tetrahedral sites. This phenomenon leads to the formation of mosaic structured spinel grains without breaking down the lattice of the parent particles (Figure 5c). However, the irreversible phase transformation destroys the layered structure and blocks the Li-ion fast-diffusion channels, which is one of the major factors leading to the sluggish reaction kinetics of LLRM cathode materials. As for the transition of the Li_2MO_3

C2/m phase to the spinel phase, it involves the removal of both Li-ion and oxygen from the lattice, which generates large strain and leads to breakdown of the lattice of the parent particles. Figure 5b shows the typical HAADF-STEM image as well as atomic structural models of the pristine *C2/m* Li_2MO_3 phase in $Li_{1.2}Ni_{0.2}Mn_{0.6}O_2$ cathode materials. Apparently, the material possesses different variants within the single particle. After 60 cycles of charge/discharge, some nanometer-scale spinel domains were observed and dispersed randomly in the bulk particle (Figure 5c). The nucleation and growth of small spinel domains inevitably leads to lattice distortion/amorphization and the formation of cracks and nanopores within cycled materials. Hu *et al*.[47] further confirmed the formation of large pores generated by oxygen loss upon cycling. The increase in porosity produces more cracks, which leads to capacity loss and voltage decay.[78-79] Although reasons for the oxygen evolution have been intensively studied and discussed, the lack of sufficient evidence to unravel the origination of oxygen loss and underlying mechanisms requires further investigation.

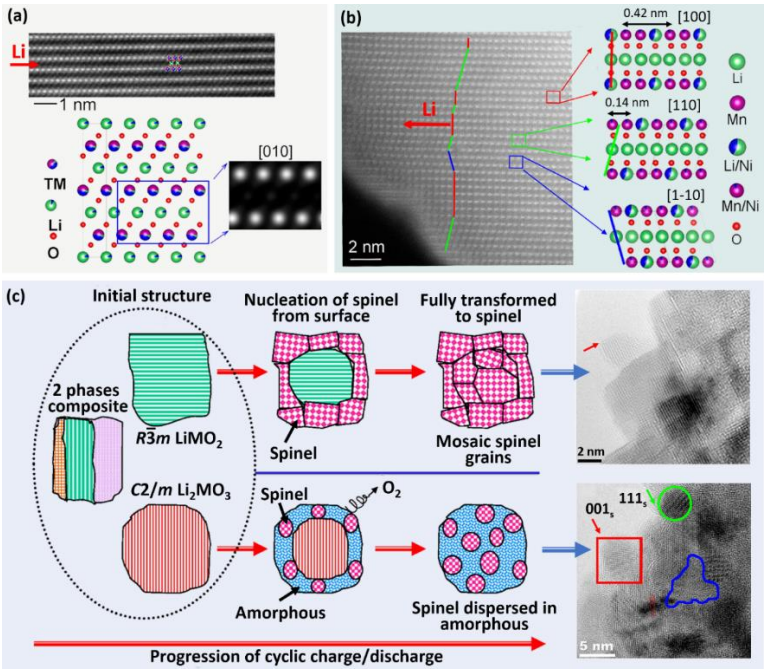

Figure 1.6 (a) The atomic resolution image and the structural model of the *R* $\bar{3}$*m* phase along the [010] projection. (b) The Z-contrast image of the *C2/m* phase. [100], [110], [1-10] zone projection is labelled with different color lines in the image. (c) Schematic diagrams of the different formation mechanism of spinel grains in *R* $\bar{3}$*m* $LiMO_2$ and *C2/m* Li_2MO_3 upon cycling. The nucleation of spinel crystal domains has been confirmed in different crystal orientation.[77]

1.4.2.2 Interplay between cationic/anionic redox activity

According to the conventional (1-x)$LiMO_2$•xLi_2MnO_3 system, Mn^{4+} is stable in the Li_2MnO_3 phase and, therefore, is unlikely to participate in the redox activity during the charge and discharge process. However, only a capacity of less than 160 mAh g^{-1} can be achieved considering the extreme case that all TM species in the $LiMO_2$ phase are fully oxidized to their

highest valence states (+2 → +4). Previous studies from Tarascon's group confirmed the existence of the oxygen-based anionic redox activity in Li-rich materials, such as Li_2IrO_3[80] and Li_2RuO_3[43]. Therefore, recently, several research groups reached a consensus that both TM cations and oxygen-based anions can reversibly participate in redox reactions during the charge and discharge process of LLRM cathode materials. The bulk oxygen species are responsible for the reversible anionic redox reaction.[81] Sathiya *et al*.[43] detected the presence of peroxo-like O_2^{n-} (or the "non-bonding" oxygen state) dimers using neutron powder diffraction during cycling. The combination of both cationic and anionic redox reactions is mainly attributed to the TM(d) – O(sp) antibonding effect and antisite–vacancy defects, which is different from the hybridized TM–O bond formed in conventional layered $LiMO_2$ phase. The O 2p configuration in the band structure of LLRM cathode materials is different from that in the classical layered $LiMO_2$ phase, where all three 2p doublets participate in M-O bond formation in layered $LiMO_2$. By contrast, in the structure of LLRM cathode materials, one of the O 2p orbitals is weakly bonded due to small overlap with Li 2s orbitals.[21] Therefore, it offers the removal of extra electrons without causing phase transformation. Li *et al*.[82] further visualized the formation and extinction of the peroxo O-O bond via *in situ* Raman spectroscopy. In addition, Luo *et al*.[44] demonstrated that the extraction of additional Li-ion is compensated by localized electron holes on the oxygen species coordinated by Li^+/Mn^{4+}.

The concept of "non-bonding" oxygen species is strongly supported by the investigation from Assat *et al*.[21, 46] The reversible oxygen-based redox activity plays a dominant role in the charge stage at the high voltage. As shown in **Figure 1.6**a, oxidized O^{n-} ($n<2$) appears above

4.46 V and declines gradually before it reaches the end of discharge (2.0 V), accounting for at least 109 mAh g^{-1}. Further cycling reveals the regrowth and vanishment of the oxidized lattice oxygen, indicating the sustained and reversible anionic redox reactivity. In addition, galvanostatic intermittent titration technique (GITT) demonstrates that cationic redox is kinetically faster than anionic redox. Therefore, the presence of an enormous amount of the anionic activity explains the sluggish kinetics and voltage decay issues of LLRM cathode materials. The advantages of the layered structure are summarized in Figure 1.6b. Unlike the classical $LiMO_2$ system where additional electrons are generated from the stabilized TM–O bond, the layered Li_2MO_3 crystal structure in LLRM cathode materials makes it possible to extract extra electrons from the non-bonding oxygen state without causing structural failure. Therefore, the interplay between cationic/anionic redox provides more specific insights into the reaction mechanism behind the high specific capacities of LLRM cathode materials.

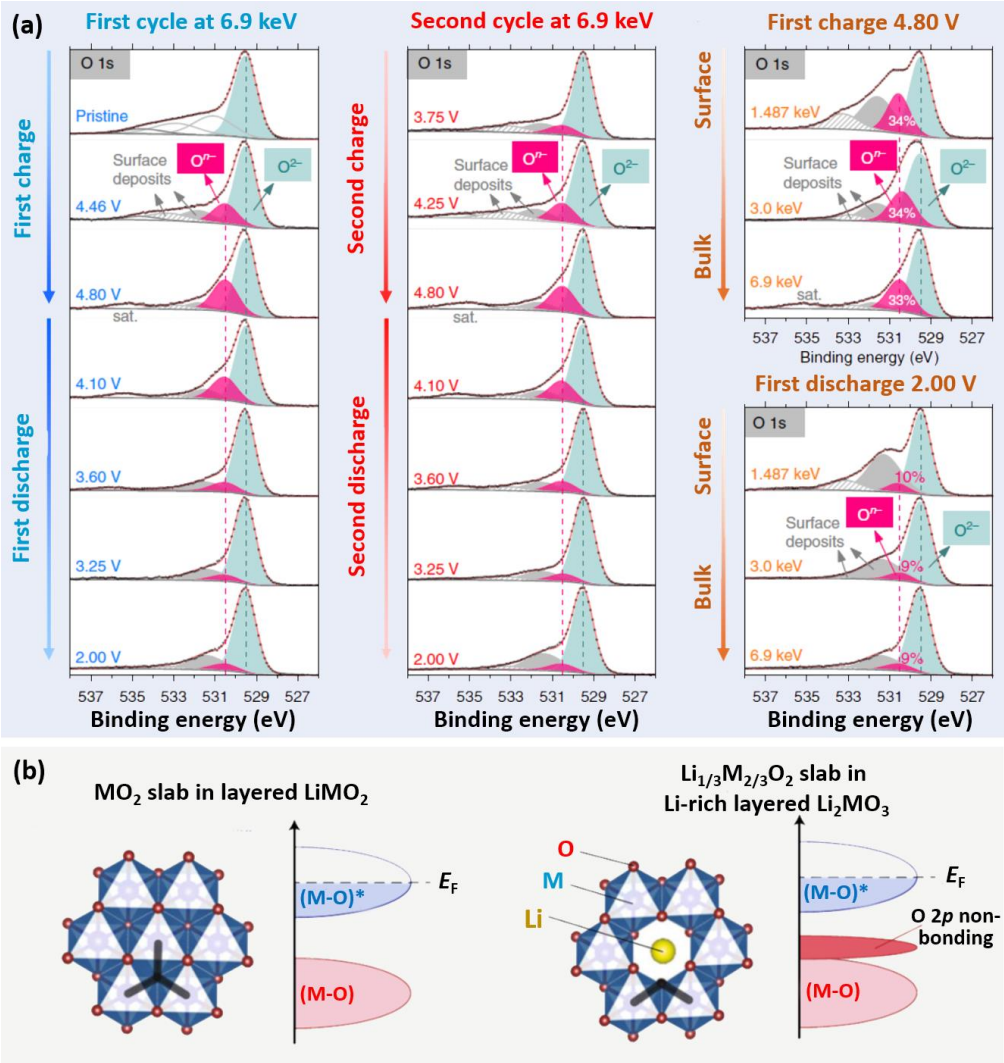

Figure 1.7 (a) Hard X-ray photoelectron spectroscopy (HAXPES) results of O1s photoelectron spectra during the first and second cycles.[46] (b) A comparison of $LiMO_2$ and Li_2MO_3 crystal structures and relevant band structures.[21]

1.4.3 Cationic redox reaction mechanisms

1.4.3.1 Cation reorganization and elemental segregation

The early established theories point out that the migration of TM cations during cycling causes reorganization and segregation of TM cations on the surface of LLRM cathode materials

(Figure 1.2).[83] It is a critical issue that causes severe degradation of the crystal structure and the electrochemical performance of LLRM cathode materials. Boulineau *et al*.[41] first illustrated distinct elemental segregation between Mn and Ni using HAADF-STEM equipped with electron energy-loss spectroscopy (EELS). As shown in **Figure 1.7**a, an extra defective spinel phase (around 2 to 3 nm thick) emerged on the surface of particles after the first cycle. In the first charge process, the intensive extraction of Li-ion accompanies the irreversible loss of O^{2-} from the surface. This reduces the stability of TM ions and induces those TM ions to migrate to the octahedral sites left by the removal of Li-ion in Li layers. As the diffusion pathway is perpendicular to the TM layer, this TM ion migration does not cause a chemical gradient. After 50 cycles, there is no obvious increase in the thickness of the spinel phase. However, the chemical gradient of Mn and Ni elements, which relates to the charge and discharge depths, is gradually established (Figure 1.7a). The migration of Mn from the surface to the bulk phase via the Li vacancies within the TM layer causes the chemical gradient and the densification of the cathode material. After Mn occupies the vacant Li sites of the TM layer, the LLRM cathode material evolves towards a non-overlithiated layered oxide, which is considered to be the origin of voltage decay rather than phase transformation from layered to spinel.

Recent investigations discovered the unusual appearance of elemental segregation in the pristine LLRM cathode material even before electrochemical cycling.[84-85] During the synthesis and processing of cathode materials, TM ions, such as Ni and Co ions, preferentially migrate and segregate at selective surface facets, terminating with a mix of cations and anions.[86] For instance, Gu *et al.*[84] discovered the existence of Ni segregation in the pristine $Li_{1.2}Ni_{0.2}Mn_{0.6}O_2$

material before cycling (Figure 1.7b). The X-ray energy dispersive spectroscopy (XEDS) mapping results in Figure 1.7c exhibit the distribution of Ni is extremely uneven in particles of LLRM cathode materials. It is rich in some surface areas and grain boundaries but deficient in the bulk phase of particles. As the Li-ion diffusion channels within the Ni-rich surface layer are approximately perpendicular to the fast Li-ion diffusion channels in the bulk phase (Figure 1.7b), this distinguishable Ni elemental segregation results in a high diffusion barrier and, consequently, slows down the transport rate of Li-ion.

As the continuing TM ion migration and Li-ion depletion on the surface of LLRM cathode materials during cycling, a surface reconstruction layer (SRL) has been observed and reported.[87-89] This SRL is regarded as a dynamic barrier for Li-ion diffusion, which gives rise to high voltage polarization and induces rapid capacity decay of LLRM cathode materials. Yan *et al.*[90] reported the SRL of $Li_{1.2}Ni_{0.2}Mn_{0.6}O_2$ materials went through a phase transition process in the sequences of $C2/m \rightarrow I41 \rightarrow$ spinel (Figure 1.7d). As illustrated in Figure 1.7e, the pristine material shows a $C2/m$ phase with the pristine Ni segregation (PNS) region on $(20\ \bar{2})$ planes. After long-term cycling, a thin SRL is formed on the particle except the PNS area owing to the TM ion migration. Furthermore, the outside SRL is Ni depleted and Mn-rich, while the inner SRL is Ni-rich. Given the complicated surface redox chemistry of LLRM cathode materials during long-term cycling, suppressing the TM ions migration and elemental segregation is crucial to maintain the structural stability of LLRM cathode materials.[89]

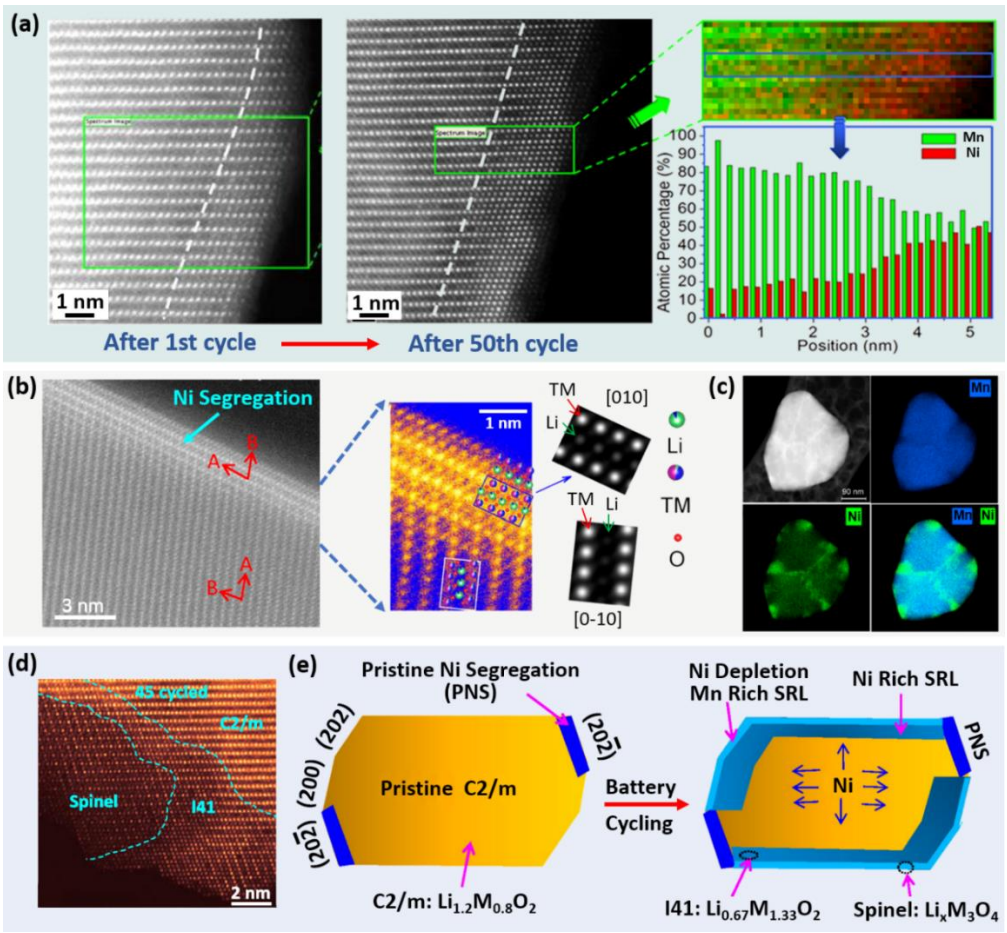

Figure 1.8 (a) HAADF-STEM images, chemical maps, and plots of Mn and Ni atomic concentration obtained from STEM-EELS results.[41] (b) Atomic resolution Z-contrast image of the surface region and (c) X-ray energy dispersive spectroscopy (XEDS) images of a $Li_{1.2}Ni_{0.2}Mn_{0.6}O_2$ nanoparticle.[84] (d) STEM-HAADF image of cycled $Li_{1.2}Ni_{0.2}Mn_{0.6}O_2$ with the spinel structure and the *I*41 structure in SRL. (e) Schematic illustration of the SRL evolution after cycling.[90]

1.4.3.2 Evolution of redox couples

Apart from elemental segregation on the surface, the gradual evolution of cationic redox

couples is another challenge causing the voltage decay and sluggish kinetics of LLRM cathode materials.[91] Hu *et al*.[47] conducted multi-length-scale X-ray spectroscopic and provided valuable insights into the origin of the voltage fading upon cycling using $Li_{1.2}Ni_{0.15}Co_{0.1}Mn_{0.55}O_2$ as the prototype cathode material. As shown in **Figure 1.8**a, the average valence state of each TM ion obtained from X-ray absorption spectra (XAS) analysis is continuously reduced upon cycling. Such a result is refined via a semi-quantitative analysis based on XAS data and concluded in Figure 1.8b. The contribution to total discharge capacity from oxygen redox couples (O^{2-}/O^{-}) and nickel redox couples (Ni^{2+}/Ni^{3+} and Ni^{3+}/Ni^{4+}) significantly diminished after 83 cycles, while the contribution from manganese redox couples (Mn^{3+}/Mn^{4+}) and cobalt redox couples (Co^{2+}/Co^{3+}) steadily increased after cycling. Although the decrease of the discharge capacity is compensated by the increased contribution from manganese and cobalt components. Such an evolution from nickel/oxygen to manganese/cobalt redox couples is responsible for the gradual voltage decay. In the band structure of insertion cathode materials, the Fermi level (E_F) is related to their electrochemical redox potential with holes above E_F and electrons below E_F form a redox couple.[92] It is well known that the open-circuit voltage (OCV) of Li-based batteries is determined by the relative Fermi level energy, which is basic requirement to move electrons from the cathode material to the Li metal anode. Originally, the Fermi level is positioned above the major Ni^{2+}/Ni^{3+} redox couple (Figure 1.8c). The loss of oxygen during cycling leads to the reduction of transition metals. The reduction of Ni implies the formation of SRL on particles of LLRM cathode materials, which reduces the capacity contribution from Ni-based redox couples. Meanwhile, the reduction of Mn and Co activates the Mn^{3+}/Mn^{4+} and Co^{2+}/Co^{3+} redox couples,

which increases the Fermi level and reduces the OCV and working voltage. Moreover, the reduction of TM elements also weakens the covalency nature between oxygen and transition metals. Consequently, less oxygen is involved in the subsequent redox reaction.

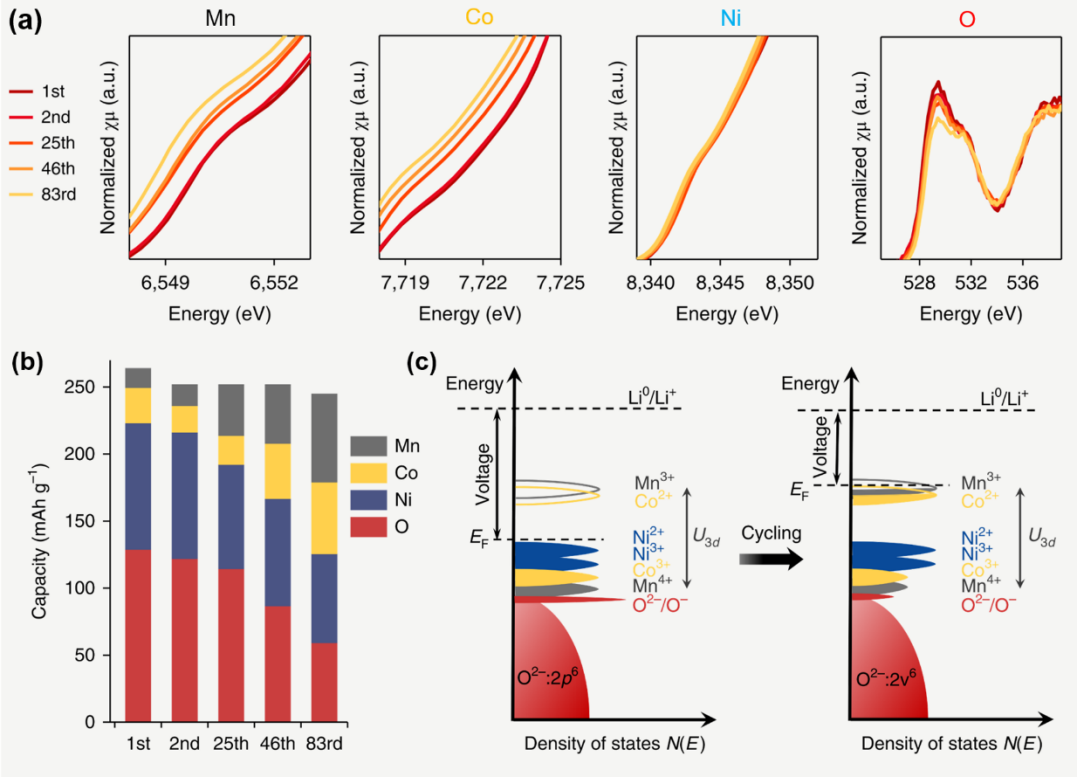

Figure 1.9 (a) K-edge XAS of various elements in $Li_{1.2}Ni_{0.15}Co_{0.1}Mn_{0.55}O_2$ recorded at the discharge stage after cycling. (b) The contribution to the discharge capacity from different redox couples at different cycles. (c) An illustration of the relationship between the Fermi level and electronic structure. The evolution of redox couples shifts the Fermi level higher upon the original state and lower the open-circuit voltage.[47]

1.4.3.3 Anomalous manganese oxidation

Although the O^{2-}/O^{-} redox reaction explained the high capacity contribution of LLRM cathode materials, the lack of direct evidence for the oxygen redox hypothesis stimulates the exploration of alternative reaction mechanisms for LLRM cathode materials and other 4d and 5d transition-metal oxides.[50, 80-81] Therefore, a new Mn^{4+}/Mn^{7+} reaction mechanism hypothesis emerges. The oxidation of Mn beyond +4 could involve in the migration of Mn ions between octahedral and tetrahedral sites, providing another possible mechanism to interpret this high specific capacity.[93] The possible formation mechanism of mixed Mn^{4+}/Mn^{7+} phases was proposed by Radin *et al.*[51] The oxidation of Mn^{4+} to Mn^{7+} experiences a series of phase transitions that containing Mn^{4+} compounds (MnO_2 and $Li_4Mn_5O_{12}$) and Mn^{7+} compounds (Mn_2O_7 and $LiMnO_4$). The mixed Mn^{4+}/Mn^{7+} phases, i.e. $Li_{1/2}MnO_3$, is theoretically possible from the Li_2MnO_3 phase because it only requires the single migration of Mn from octahedral sites to tetrahedral sites. In this case, Mn^{4+} tends to reside in octahedral coordination while Mn^{7+} prefers the tetrahedral site (**Figure 1.9**a). Therefore, as shown in Figure 1.9b and 1.9c, the hypothesized $Li_{1/2}MnO_3$ structure can be shaped if two-quarter Mn atoms migrate to tetrahedral sites in the nearby Li layers. The emerging of an irreversible plateau during the first charge could also be ascribed to the formation of such configuration. As the cycling proceeds, the absence of such a 4.5 V plateau in the subsequent discharge process is due to the presence of multiple tetrahedral-octahedral migration pathways. The continuous rearrangement of Mn ions could further trigger the voltage decay upon cycling. Furthermore, the authors combine the Mn^{4+}/Mn^{7+} oxidation hypothesis with the oxygen-based anionic redox reaction. The migration

of Mn ions from octahedral sites to tetrahedral sites might cause the generation of oxygen species, in which the Mn^{7+} is unlikely to be reduced and tends to return to octahedral sites (Figure 1.9d). This unusual manganese oxidation mechanism suggests the possibility of utilizing high valence transition metal oxides without inducing cation migration to design high-capacity cathode materials for LIBs.

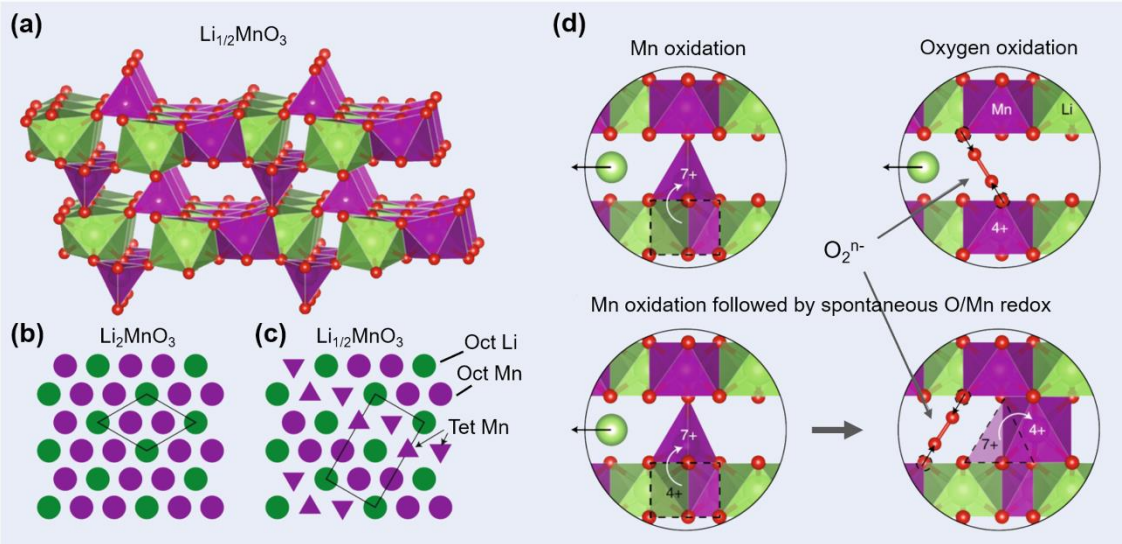

Figure 1.10 (a) The hypothesized $Li_{1/2}MnO_3$ crystal structure after activation, where red, green and purple representing O, Li and Mn, respectively. (b, c) Comparison of the hypothesized $Li_{1/2}MnO_3$ and Li_2MnO_3 structures. The circles and triangles stand for the octahedral (Oct) and tetrahedral (Tet) sites, respectively. (d) Alternative charge mechanisms in LLRM cathode materials. The Mn^{4+}/Mn^{7+} oxidation followed by the formation of trapped oxygen molecules or peroxide ions.[51]

1.5 Strategies for improving electrochemical properties of LRCMs

Despite the compelling features of LRCMs, currently developed cathode materials are far behind the requirement for next-generation LIBs with practical high-specific-capacity and long-service-life. The evolution of oxygen gas naturally leads to volume expansion when fabricating prototype lithium-ion pouch cells.[94-95] Furthermore, the side reaction is another issue considering the complexity of the redox reaction of LRCMs. Additionally, voltage decay is one of the toughest challenges. The energy density of LRCMs could decrease from 1000 to 500 W h kg^{-1} after 100 cycles due to the uncontrollable voltage decay, which could not be fully explained by capacity fade alone.[96-98] Moreover, the poor rate performance and deteriorated cycling stability make LRCMs more difficult for commercial production. Although the degradation of LRCMs is unpredictable, efforts to overcome obstacles for practical applications have never been stopped for years. Inspired by previous research achievements in intercalation-type cathode materials for LIBs, nowadays, we can tackle these challenges by employing various improvement strategies for LRCMs. These approaches, from the aspect of cathode materials to electrolyte, including surface modification and doping, composition optimization, structure engineering and electrolyte additives etc. (**Figure 1.10**).

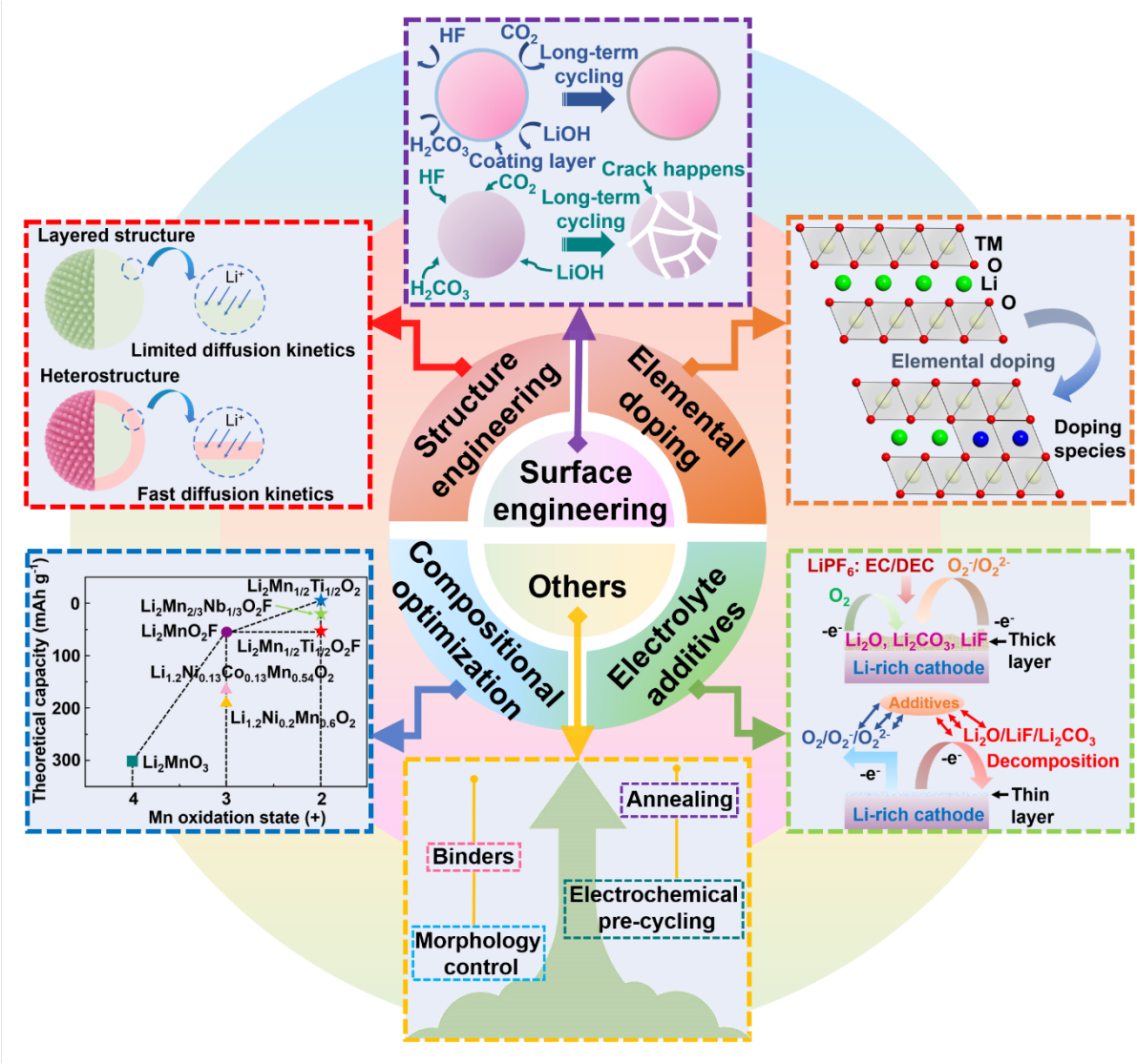

Figure 1.11 Strategies for improvement of layered LRCMs.

1.5.1 Surface engineering

1.5.1.1 Surface coating

Surface engineering involves surface coating or chemical and physical surface treatment on LRCMs. Surface coating has been regarded as one of the most promising and reliable methods to improve the electrochemical performance of LIB cathode materials.[99] Since Cho and co-

workers[100] first illustrated the contribution of the ZrO_2 coating layer on $LiCoO_2$ cathode materials, many investigations have been conducted in this area.[101-102] An ideal coating material should possess high ionic conductivity while maintain electrochemical inactivity during cycling. For LRCMs, surface coating is beneficial to suppress the lattice-constant change and undesired oxygen loss during cycling, thereby restricting the irreversible layered to spinel-like phase transformation and enhancing the structural stability as well. Moreover, a surface coating layer prevents the accumulation of by-products on the cathode surface that leads to rapid capacity degradation.[103] The previously reported coating strategies are summarized in **Table 1.1**. Zheng *et al*.[104] reported the use of the AlF_3 material as a coating layer on LRCMs. The AlF_3-coated LRCM shows negligible capacity loss after 100 cycles. Meanwhile, voltage decay and rapid capacity degradation have been significantly mitigated after cycling. The AlF_3 protective layer could minimize the occurrence of adverse side reactions between the electrolyte and electrode, restricting oxidation of the electrolyte and the generation of a thick cathode electrolyte interface (CEI). This outer shield layer can protect the cathode material against further corrosion and etching by corrosive species and reduce the generation of the oxygen-deficient surface. Moreover, the irreversible phase transformation has been suppressed to a certain extent and therefore maintains the structural integrity (**Figure 1.11**a). However, the layered to spinel-like structure evolution cannot be eliminated as indicated by the drop of the average operating voltage. The authors employed electron energy-loss spectroscopy line scan (EELS) to further demonstrated that the average Mn valence in the AlF_3-coated cathode material is higher than

that in the pristine one after cycling, which could alleviate the disproportionation of Mn^{3+} and increase the structural durability.

It is worth noting that a good lithium-ion-conductive coating layer contributes to the rapid Li^+ diffusion and reduces the electrode polarization upon cycling. As previously reported in the lithiated Al_2O_3 coating layer,[105] once the Al_2O_3 protective layer is lithiated by Li^+, a new phase $Li_\delta AlO_xF_y$ is formed to promote the Li^+ diffusion and transport in the surface layer. Zhao *et al*.[30] further investigated the effect of surface coating by employing the lithium-ion-conductive $LiAlF_4$ as the coating material. The coating of $LiAlF_4$ not only can ensure a high Li^+ diffusivity but also bring the increased proportion of non-bonding O^{n-} species in the LRMC, which contributes to the effective anionic redox reaction and fast lithium-ion transport. As a result, the $LiAlF_4$-coated cathode material shows a reversible capacity of 246 mAh g^{-1} at 0.1 C and excellent rate capability (133 mAh g^{-1} at 5 C). Meanwhile, the cycling stability has been boosted via $LiAlF_4$ surface coating, especially compared with the poor lithium-ion-conductive AlF_3-coated and uncoated LRCMs. Zheng *et al*.[106] demonstrated the heterostructured cathode material by constructing a spinel $Li_4Mn_5O_{12}$ coating layer onto LRCMs. According to the transmission electron microscopy (TEM) analysis, the surface of primary particles was coated by a uniform layer of spinel structure with a thickness of 14 nm. The $Li_4Mn_5O_{12}$ coating layer effectively inhibits the irreversible lattice oxygen loss from the pristine cathode material and thus results in high ICE. Meanwhile, the protective layer also avoids the nucleation of spinel-like domains on the surface and restricts the decomposition of carbonate solvents caused by reactive oxygen species. These advantages help to improve the structural stability of LRCMs.

Moreover, the external three-dimensional (3D) spinel framework facilitates the transportation of Li^+, which satisfies the requirement of rapid diffusion kinetics. As a consequence, the $Li_4Mn_5O_{12}$-coated cathode material shows a higher specific capacity of 276 mAh g^{-1} at 0.05 C, better rate performance (192 mAh g^{-1} at 1 C) and capacity retention of 83.1% after 300 cycles than that of the pristine one. All these findings suggest the feasibility of surface coating to improve the electrochemical properties of LRCMs. Nevertheless, synthesizing well-coated cathode materials is not easy to get right. For example, solid-state coating technology is productive and efficient for large-scale application, but the uniformity of its thickness is poor. Moreover, the wet-chemistry coating strategy is often limited by its multi-step reactions and may bring in residual water molecules during the preparation procedure.

Apart from single-component coating materials, multi-component coating materials have also paly significant roles in improving electrochemical performance of LRCMs. For example, Bian and co-workers proposed a spinel material, $Li_4Mn_5O_{12}$, associated with a Li_2O-$LiBO_2$−Li_3BO_3 glass layer as coating materials.[107] The Li_2O-$LiBO_2$−Li_3BO_3 glass surface layer not only serves as a good ionic conductor for Li^+ diffusion but also effectively suppresses side reactions occurring at the high working voltage. Meanwhile, the spine $Li_4Mn_5O_{12}$ can grow inward from the surface instead of conventional $LiMn_2O_4$ (Figure 1.11b). The phase transformation of $Li_4Mn_5O_{12}$ is kinetically slower than the $LiMn_2O_4$ transformation in LRCMs, which puts off voltage decay and results in remarkable capacity retention. As a result, the heterostructured cathode material exhibits a reversible specific capacity of 259 mAh g^{-1} at 0.2 C and improved cycling stability of 92.2% after 100 cycles. They also found that such a

"swallowed effect" exists in the $Li_4M_5O_{12}$@BiOF@LRCM heterostructure, showing a high discharge capacity (292 mAh g^{-1} at 0.2 C) and excellent capacity retention (92% after 100 cycles).[108] Moreover, Liu *et al*.[109] reported the role of NH_4F and Al_2O_3 surface co-coating on the electrochemical performance of LRCMs. The ICE of co-coated $Li_{1.2}Ni_{0.2}Mn_{0.6}O_2$ is improved from 82.7% to 87.5%, while the discharge capacity is enhanced from 253 to 287 mAh g^{-1} at 0.05 C. This phenomenon is owing to formation of the amorphous Al_2O_3 nanolayer, which prevents the cathode material from being attacked by by-products and reduces irreversible oxygen loss during electrochemical cycling (Figures 1.11c–e). Furthermore, the weak acid treatment of NH_4F during surface coating facilitates the partial reduction of surface Mn^{4+}. The generated nanoislands and pre-activated Mn^{3+} on the surface area ensure the reversibility of the oxygen-based anionic redox reaction and stabilize the Ni-redox pair.

Although the surface coating strategy has been proven to effectively improve the electrochemical property of LRCMs, there are still many technical challenges to obtain high-quality coating layers on LRCMs. Many coating techniques such as solid-state routes, wet-chemistry routes, and nanoengineering routes have been introduced in preparation of high-performance LRCMs, as shown in **Table 1.2**.[30, 78, 106, 110-112] For example, solid-state coating technology is productive and efficient for large-scale applications. However, the uniformity of the coating layer's thickness is poor. Moreover, the wet-chemistry coating strategy is often limited by its multi-step reactions and may lead to residual water molecules remained during the preparation procedure Although nanoengineering routes like chemical vapor deposition (CVD), molecular layer deposition (MLD) and atomic layer deposition (ALD) achieve

promising results such as the uniform coating layer and adjustable coating thickness, these cutting-edge techniques are often expensive and would be not suitable for large-scale production.

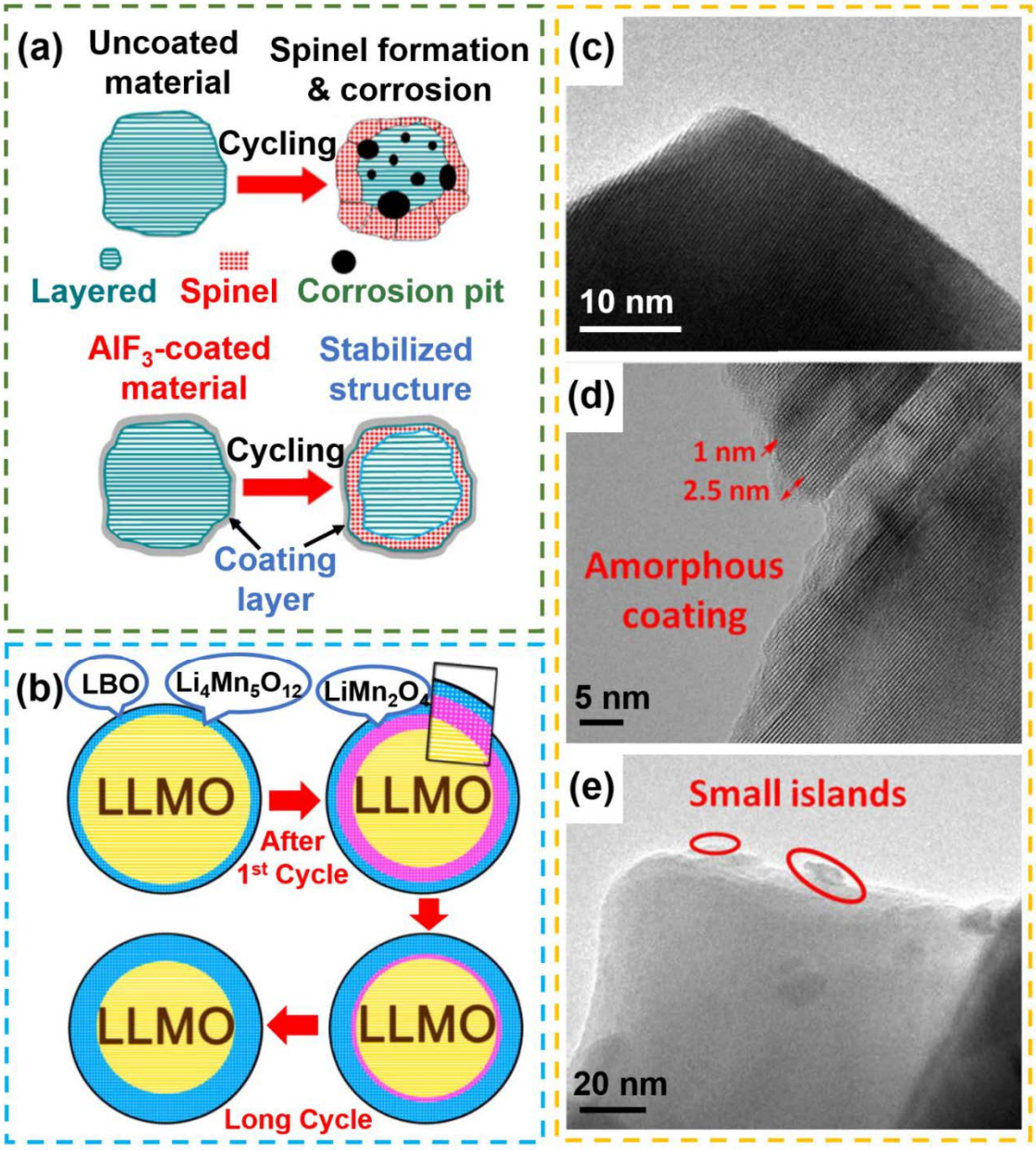

Figure 1.12 (a) Scheme of the AlF_3 coating strategy and its working mechanism during cycling.[104] (b) The phase transformation of heterostructured $Li_4M_5O_{12}$@LBO@LRCM during cycling.[107] (c–e) TEM images of NH_4F and Al_2O_3 co-coated LRCM.[109]

Table 1.1 Different types of surface coating strategies.

Type of surface coating	Coating materials	Initial Coulombic efficiency	Discharge capacity (mAh g^{-1} at 0.1 C)	Capacity retention	Ref.
Oxides	ZnO	~85%	267	90.2% (130 cycles, 0.5 C)	[113]
	Al_2O_3	51%	285.5	80% (20 cycles, 0.1 C)	[111]
	TiO_2	79.65%	287	78% (50 cycles, C/3)	[111]
	MnO_2	88%	299	93% (50 cycles, 0.5 C)	[114]
	MoO_3	99.6%	272.7	88.5% (50 cycles, 0.1 C)	[115]
	Mg_2TiO_4	84.6%	271	81% (700 cycles, 2 C)	[86]
	$AlPO_4$	85.2%	261.9	90.8% (40 cycles, 0.1 C)	[78]
	$FePO_4$	85.1%	271.7	95% (100 cycles, 0.5 C)	[116]
	$LiFePO_4$	-	282.8	98.1% (120 cycles, 0.1 C)	[112]
	$LiCoPO_4$	82.5 %	250	98% (40 cycles, 0.08 C)	[117]
	$LiAlO_2$	82.9 %	257.6	96.5% (50 cycles, 1C)	[118]
	$Li_4Mn_5O_{12}$	79 %	261	83.1% (300 cycles, 0.2 C)	[106]
Fluorides	AlF_3	90.8%	245.6	79.6% (100 cycles, 0.5 C)	[110]
	CaF_2	89.6 %	277.3	91.2% (80 cycles, 0.2 C)	[119]
	FeF_3	80 %	280	95% (100 cycles, 0.5 C)	[120]
	MgF_2	76 %	220	86% (50 cycles, 0.1 C)	[121]
	$LiAlF_4$	81.2 %	246	90.9% (3000 cycles, 5 C)	[30]
Carbon	Carbon	96.7 %	263	92% (100 cycles, 0.2 C)	[122]
	Carbon	92.2 %	334.5	~90% (50 cycles, 1 C)	[123]
	MWCNT	87 %	241.5	75.7% (50 cycles, 0.2 C)	[124]
	Graphene	74 %	290	90% (100 cycles, 0.5 C)	[29]
	Polyaniline	89 %	313.5	~100% at 0.1 C	[125]

Table 1.2 Comparison of different surface coating strategies in term of their advantages and disadvantages.

Methods	Advantages	Disadvantages
Solid-state routes (Ball-milling, mechanical mixing, *etc*.)	•Low cost •Suitable for scale-up production •Facile procedure	•Non-uniform coating on particles •Easy to collapse and polluted •Discontinuous coating layer •Improved mechanical stress
Wet-chemistry routes (Chemical coprecipitation, sol-gel, hydrothermal, *etc*.)	•Continues coating layer •Low cost •Improved structural stability	•Non-uniform coating on particles •Complicated preparation procedure •Non-adjustable coating thickness •Residual water molecules
Nanoengineering routes (ALD, MLD, CVD, *etc*.)	•Uniform coating on particles •Continues coating layer •Adjustable and precise coating thickness •Ultrathin coating layer	•Expensive •Complicated preparation process •Limited deposition source •Difficult for scale-up production

1.5.1.2 Surface treatment

In addition to surface coating, surface treatment has also been found to be effective in many reports.[126-128] This strategy is intended to make cathode materials to be more resistant to chemical corrosion and improve structural stability as well. $Na_2S_2O_8$ aqueous solution has been identified as an effective surfactant for the surface treatment of LRCMs.[129] After treated by 40 wt.% $Na_2S_2O_8$ solution, the modified cathode material shows a high initial discharge capacity (285 mAh g^{-1} at 0.1 C) and enhanced ICE (93.2%). X-ray photoelectron spectroscopy (XPS) results indicate that the lattice oxygen near the surface of particles is oxidized to form O_2^{2-} species with the extraction of Li^+ from the Li_2MO_3 region, rather than being oxidized to O_2 at the pristine particle surface. In most cases, the release of O_2 causes the formation of oxygen

vacancies and triggers the structural evolution from layered to defect-spinel phase on the surface. Therefore, this surface modification strategy is beneficial to increase the rate performance and cycling stability of LRCMs. Qiu *et al.*[130] reported the gas-solid interface reaction in enhancing the electrochemical property of LRCMs. The control of the cumulative oxygen activity and the interface reaction was achieved by creating the appropriate number of oxygen vacancies. **Figure 1.12**a and 1.12b show the reaction mechanism of the pristine and activated LRCMs before and after the first full charge process. Before cycling, the pre-activated cathode material contains numerous oxygen vacancies, which alleviate the partial pressure of oxygen release and prevents the oxygen evolution at the high working voltage (>4.5 V). Subsequently, owing to reduced adverse reactions occur at the interface, a thinner CEI layer is generated on the surface of the cathode material and, therefore, reducing the electrochemical resistance upon cycling. Furthermore, the increased number of oxygen vacancies enables intensive reversible oxygen-based anionic redox reactions, which ensures high Li^+ diffusivity within the bulk material, together with the minimal structural change. The modified cathode material delivers a high specific capacity of 301 mAh g^{-1} at 0.05 C without obvious capacity degradation after 100 cycles.

Erickson *et al.*[131] reported the influence of ammonia treatment on LRCMs. Based on their findings, Mn and Co are partially reduced as a result of NH_3 treatment. Additionally, the change of oxygen species was observed from the NH_3-treated cathode material, which indicates the generation of surface LiOH and peroxo-like species after 2 and 4 h ammonia treatment, respectively. The increased amount of peroxo-like species and gradual elimination of O_2^{2-} from

the particle surface of cathode materials give rise to the formation of an oxygen-deficient, spinel-like surface phase, which is expected to increase the specific capacity and mitigate voltage decay. Moreover, a urea-treated thermal treatment strategy is also effective in LRCMs.[132] As shown in Figure 1.12c, this surface treatment strategy introduces oxygen vacancies into the lattice and forms a protective surface layer containing C_3N_4 and $LiNO_3$. The presence of oxygen vacancies lowers the valence state of Mn to some extent and weakens TM-O bond strength as well. Meanwhile, a passivation surface layer prevents the cathode material from being attacked by harmful products. The urea-treated LRCM shows higher activation extent (270 mAh g^{-1} over 45 cycles) than the pristine one (255 mAh g^{-1} after 150 cycles). Meanwhile, the modified cathode material exhibits a good cycling performance (98.49%) and low voltage decay (15.66%) after 300 cycles. *In situ* synchrotron X-ray diffraction (XRD) measurement reveals that oxygen loss is greatly suppressed in the urea-treated LRCM, as the change of d-spacing is nearly zero at the high potential (>4.5 V). Chen et al.[133] investigated the surface oxygen group and highlighted the importance of surface chemistry on L_2MnO_3. They pointed out that the overoxidation and irreversible loss of surface oxygen is due to the undercoordinated configuration with cationic vacancies that gives rise to high energy orbital ($lO_{2p'}$) on the surface. To solve this problem, they employed a facile sulfur deposition strategy to induce the formation of polyanionic surface oxygen (SO_4^{2-}) rather than under-coordinated one and thereby stabilize the interfacial stability. The inducive effect of the S-O bond is stable enough to withstand the long-term cycling and shows highly conserved crystal structure. Zhu and co-workers reported an artificial surface prereconstruction for $Li_{1.2}Mn_{0.6}Ni_{0.2}O_2$ through a

MoO_3 leaching method, which forms a crystal-dense and anion-redox-free $LiMn_{1.5}Ni_{0.5}O_4$ layer that completely encloses $Li_{1.2}Mn_{0.6}Ni_{0.2}O_2$ particles.[134] The treated cathode material displays a stable discharge capacity of 253 mAh g^{-1} at 60 mA g^{-1} with improved capacity retention (~102%) and average discharge voltage (3.3 V) after 200 cycles. They found that the irreversible oxygen loss and structural collapse derived from global oxygen migration is mitigated in cycling, which suppresses Mn^{3+} dissolution and the electrolyte decomposition in the high working voltage. Moreover, coupled with a commercial graphite anode and lean electrolyte, the assembled pouch full-cell can deliver a high specific energy density of 280 Wh kg^{-1} and still maintain 66% of its discharge energy density after 125 cycles.

In summary, surface engineering provides an effective and practical approach to prevent cathode materials from chemical etching caused by harmful by-products, and thus enhances the structural stability of LRCMs. Meanwhile, the irreversible structure evolution has also been suppressed via surface modification. However, there are still some drawbacks that need to be improved further. The electrically insulating nature of many coating materials adds an inactive portion into the cathode material and thus lowers the energy density of LRCMs. Furthermore, the currently available surface coating techniques are unable to achieve a pure and homogeneous coating layer at a low cost. More importantly, surface engineering merely postpones the progress of cathode material degradation. As the cycling proceeds, the mechanical stress and irreversible structural transformation continue to build up and eventually degrade the electrochemical performance of LRCMs.

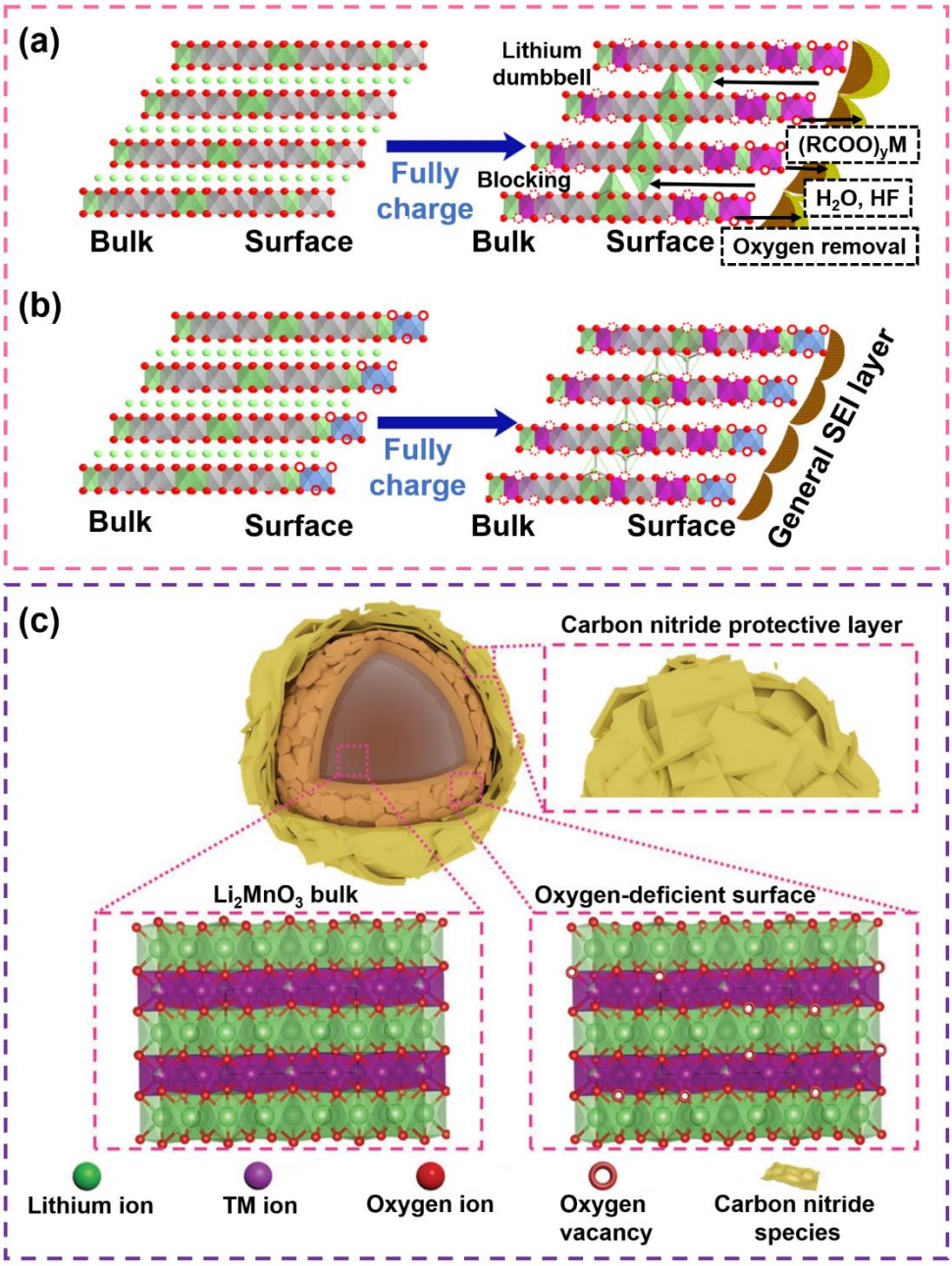

Figure 1.13 The interfacial reaction of (a) pristine and (b) GSR LRCMs before and after the fully first charge. The pre-activated surface layer helps to form a thin CEI layer on the particles' surface.[130] (c) Illustration of urea treatment on the Li_2MnO_3-like cathode material.[132]

1.5.2 Elemental doping

Heterogeneous ions doping in the crystal structure of cathode materials is a good method to improve the Li^+ diffusion kinetics and structural stability of the bulk phase. With the introduction of stabilizing dopants, the modified local environment can tolerate cationic disorder and structural change to a certain extent. Meanwhile, the doping ions can expand the interplanar spacing of LRCMs without damaging their original layered structure, thereby significantly enhancing the rate performance and reinforcing the structural integrity.[135]

1.5.2.1 Cationic doping strategy

Cation-doping has been widely employed to improve the electrochemical property of LRCMs. A series of metal cations such as Na^{+}[136], K^{+}[137], Mg^{2+}[138], Al^{3+}[139] and Cr^{3+}[140] have been employed in term of this strategy (**Table 1.3**). Wang *et al*.[135] introduced a facile Sn-doping approach in $Li_2MnO_3 \cdot LiMn_{0.5}Ni_{0.5}O_2$ cathode material. XRD results confirm that the Sn-doped structure has a relatively larger interplanar spacing of (003) planes compared with the pristine material. The expanded (003) spacing does not block the lithium diffusion path among different lithium layers and dramatically reduces the energy barrier for Li^+ diffusion and transport. Consequently, the Sn-doped cathode material delivers a much better rate performance and faster Li^+ diffusivity than the pristine material. The feasibility of Nb-doping in $Li_{1.2}Mn_{0.54}Ni_{0.13}Co_{0.13}O_2$ has also been studied.[141] As shown in the annular bright-field (ABF) image and the energy-dispersive X-ray (EDX) mapping results, the Nb-O bond located near the

surface region strongly constraints the O-TM(Li)-O slabs (**Figure 1.13**a). During charging and discharging, the surface oxygen species remains inactive while the lattice oxygen composition is oxidized, which is crucial for suppressing oxygen loss and improving structural stability of LRCMs. Furthermore, Soft X-ray adsorption structural (SXAS, Figure 1.13b) spectroscopy demonstrates that Mn^{4+} cations presented in the TM layer are stabilized and keep unchanged upon cycling, which prevents the unwanted layered-spinel transformation and ensures the structural stability (Figure 1.13c). Meanwhile, irreversible voltage decay and capacity loss are significantly suppressed through Nb-doping. He *et al.*[142] reported the Zr-doped $Li_{1.2}Mn_{0.54}Ni_{0.13}Co_{0.13}O_2$ as a cathode material for LIBs. The Zr-doped sample with a 3D hollow structure provides additional space for Li^+ transport and diffusion. Moreover, the crystal structure change of LRCMs is alleviated by Zr-doping. As indicated in Figure 1.13d, despite the generation of impurities after 100 cycles, the shift of diffraction peaks towards the lower position has been restricted. This tendency implies that the pristine cathode material is plagued with more severe capacity degradation than the doped sample. As a result, the Zr-doped $Li_{1.2}Mn_{0.54}Ni_{0.13}Co_{0.13}O_2$ cathode exhibits a reversible discharge capacity of 256 mAh g^{-1} at 12.5 mA g^{-1} and exceptional capacity retention of 95% after 100 cycles.

1.5.2.2 Polyanionic doping strategy

Apart from the frequently reported cation-doping method, polyanion-doping is also applied and discussed in many studies. Zhang *et al.*[143] illustrated the utilization of SiO_4^{4-} and SO_4^{2-}

polyanions as dopants in LRCMs. As expected, the polyanion-doped cathode materials show a lower degree of Li^+/Ni^{2+} cation mixing and voltage decay, compared with the pristine sample. This advantage is ascribed to the local defects caused by polyanion-doping, which can effectively block the notorious structural degradation and, therefore, maintain the high-energy-density of LRCMs. More importantly, the ICE and cycle stability are also improved owing to the effect of polyanion-doping. Moreover, tetrahedral PO_4^{3-} polyanions were also introduced into LRCMs.[144] The study shows that the optimal amount of PO_4^{3-} doping can minimize the local environment evolution and immobilize TM ions in the layered structure. Such a special synergistic effect between large PO_4^{3-} polyanions and O^{2-} anions reduces the possibility of Li^+/Ni^{2+} cation mixing during cycling. Although the migration of TM cations is more likely to trigger undesirable spinel domains within the primary layered phase, PO_4^{3-} doping can delay the subsequent phase transformation and has a positive effect on the electrochemical performance of LRCMs.

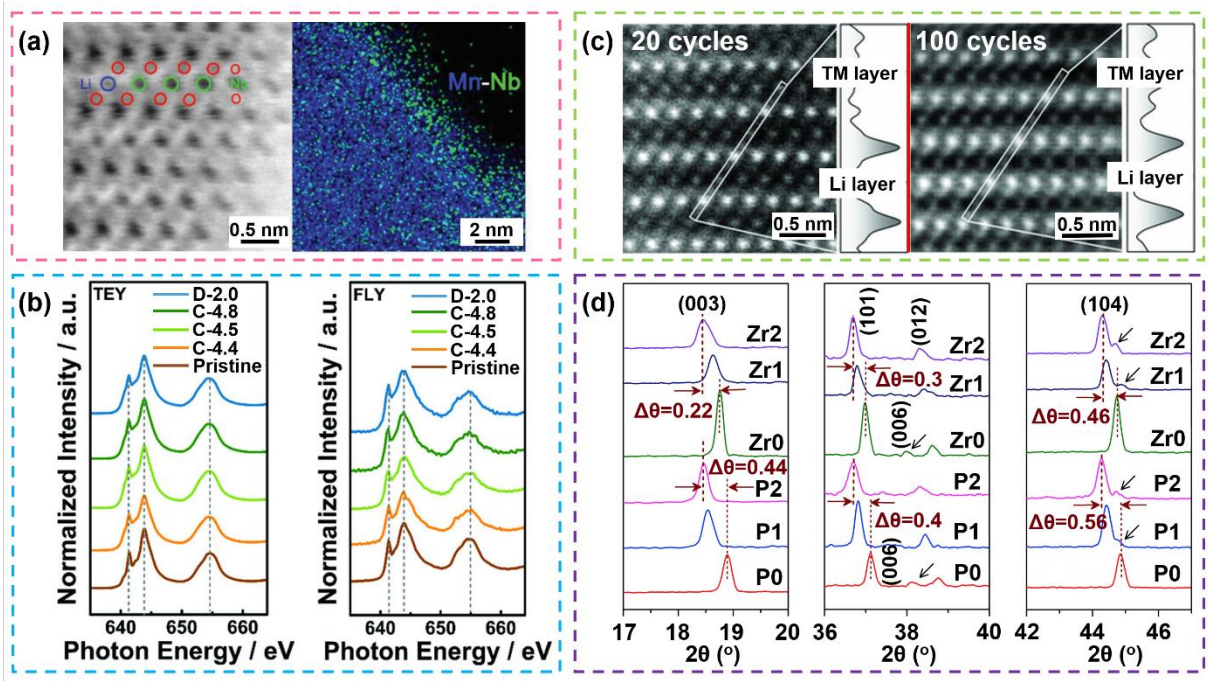

Figure 1.14 (a) The annular bright-field (ABF) image and the energy-dispersive X-ray (EDX) mapping of Nb-doped $Li_{1.2}Mn_{0.54}Ni_{0.13}Co_{0.13}O_2$. The images reflect the elemental distribution near the surface. (b) The Mn $L_{2,3}$ edge spectra of the Nb-doped cathode material in the TEY and FLY modes at different charge/discharge states upon the first cycle. (c) The high-angle annular dark-field (HAADF) images of Nb-doped LLCM near the subsurface area after 20 cycles (left) and 100 cycles (right).[141] (d) XRD patterns of uncoated and Zr-doped cathode materials after 0, 20 and 100 cycles.[142]

1.5.2.3 Cationic/anionic co-doping strategy

In contrast to the mono-doping strategy, the combination of cationic and anionic doping can take full advantage of heterogeneous ions doping and boost the electrochemical performance of LRCMs. Liu et al.[145] introduced the synergistic effect of Na and F co-doping to address poor

cycling stability and rate capability of $Li_{1.2}Ni_{0.2}Mn_{0.6}O_2$. As shown in **Figure 1.14**a, an appropriate amount of Na and F is located on Li and O sites, respectively, without destroying its original layered structure. In this case, Na-doping can restrict the irreversible layered to spinel-like phase transformation, while F-doping obviously enhances both electronic and ionic conductivity. Therefore, the as-prepared cathode material shows the excellent rate performance (167 mAh g^{-1} at 5 C) and superior cycle life (~100% after 100 cycles at 0.2 C). The effect of Cd and S co-doping on $Li_{1.2}Ni_{0.2}Mn_{0.6}O_2$ was also investigated by Chen and co-workers.[146] Figures 1.14b and 1.14c illustrate high-angle annular dark field-scanning transmission electron microscopy (HAADF-STEM) images of the pristine and co-doped cathode materials. Unlike the local environment of the pristine material, the significant contrast peaks in Figure 1.14c appear along both the H3 and H4 direction, which is an evidence of heavy atoms doping in Li and TM layers. The presence of Cd^{2+} and S^{2-} doping species leads to an expansion of the (003) interlayer spacing and acts as a "support pillar" to improve structural stability. Meanwhile, the lattice spacing remains nearly unchanged (from 4.83 to 4.81 nm) after 100 cycles, and the co-doped LRCM exhibits a much higher Li^+ diffusion coefficient (1.4×10^{-12} cm^2s^{-1}) than the pristine cathode material (4.88×10^{-13} cm^2s^{-1}) during charge and discharge. Liu et al.[147] reported a new type of $Li_{1.2}Ni_{0.13}Co_{0.13}Mn_{0.54}O_2$ through Na^+ and PO_4^{3-} co-doping. Such a co-doping strategy not only enlarges the interlayer spacing and alleviates the volume change in the charge and discharge processes, but also minimizes Li/Ni mixing within the layered structure and, therefore, improves the cycling stability. As a result, the co-doped cathode material shows an enhanced rate performance (106 mAh g^{-1} at 10 C), good capacity retention (94% at 10 C after

100 cycles) and negligible voltage decay. Although many progresses have been made towards the goal of an all-around performance boost through the elemental doping strategy, the effect of heterogeneous ions doping is hard to predict, and the role of doping ions should be further investigated. Similar to surface engineering, elemental doping cannot eliminate irreversible phase transformation.

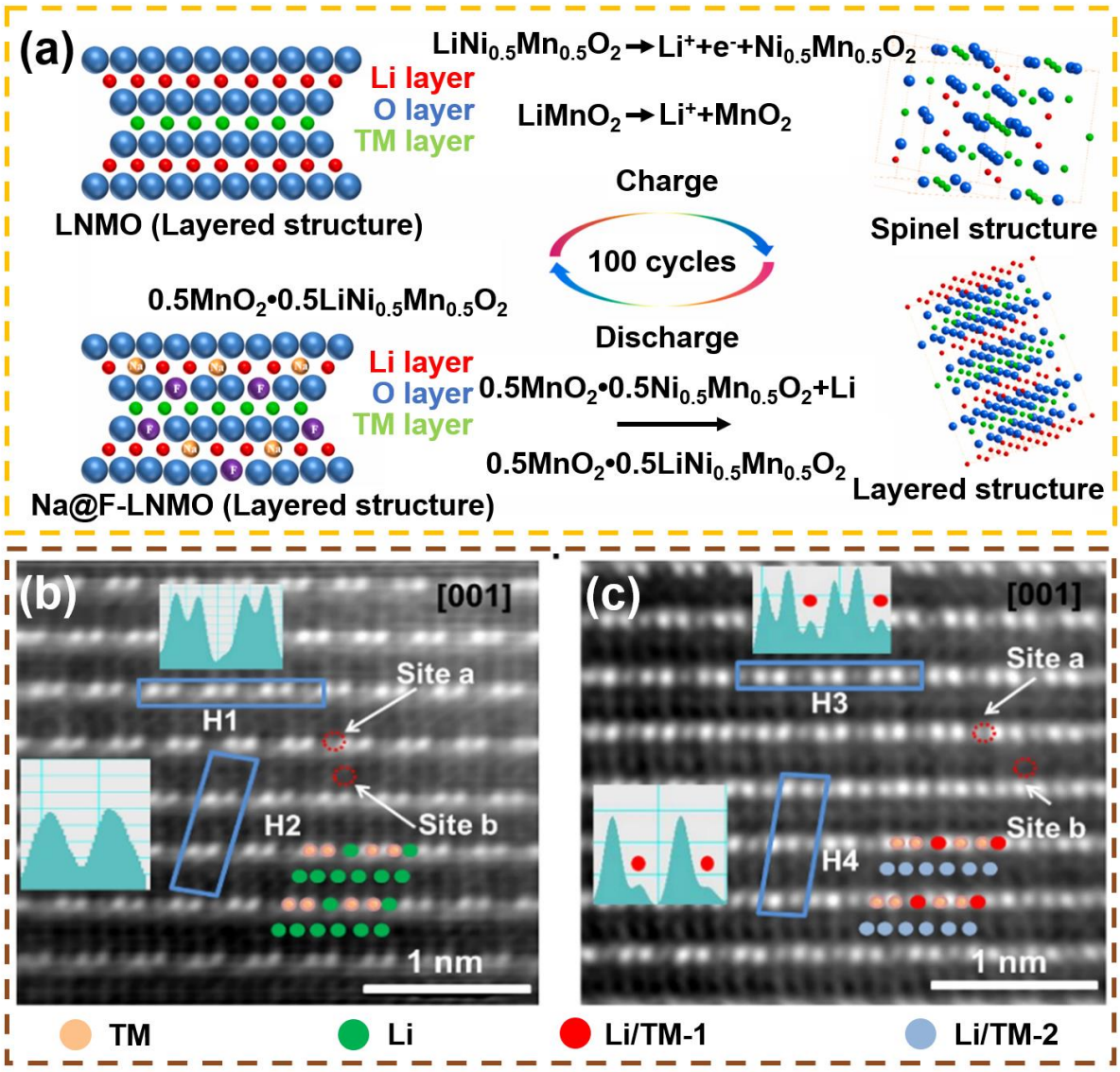

Figure 1.15 (a) Phase transformation of the pristine and co-doped LRCMs upon cycling.[145] HAADF-STEM images of the (b) pristine and (c) Cd and S-doped cathode materials.[146]

Table 1.3 Different types of elemental doping strategies.

Type of doping	Type of dopant	Initial Coulombic efficiency	Discharge capacity (mAh g^{-1} at 0.1 C)	Capacity retention	Ref.
Cationic doping	Na^{+}	87%	286	87.9% (100 cycles, 0.2 C)	[136]
	K^{+}	77%	315	85% (110 cycles, 0.08 C)	[137]
	K^{+}	87%	299	94% (100 cycles, 0.5 C)	[148]
	Mg^{2+}	87.9%	248.6	94.2% (200 cycles, 0.5 C)	[149]
	Al^{3+}	82.3%	280	96% (100 cycles, 0.1 C)	[139]
	Fe^{3+}	87.8%	230	90.4% (50 cycle, 0.1 C)	[150]
	Fe^{3+}	77.5%	232	70% (200 cycles, 1 C)	[151]
	Cr^{3+}	93.4%	~230	77.6% (133 cycles, 0.2 C)	[140]
	Y^{3+}	79%	281	95.6% (40 cycles, 1 C)	[152]
	La^{3+}	90.4%	286.4	93.2% (100 cycles, 1 C)	[153]
	Sn^{4+}	77%	232.2	86% (400 cycles, 0.12 C)	[154]
	Ti^{4+}	73%	~320	71% (300 cycles, 0.2 C)	[155]
	Zr^{4+}	70.9%	242	~95% (100 cycles, 0.1 C)	[142]
	Ru^{4+}	87.7%	276.4	92.5% (50 cycles, 2 C)	[156]
	Nb^{5+}	87%	320	94.5% (100 cycles, 0.1 C)	[141]
	Mo^{6+}	72.87%	245	91.8% (204 cycles, 0.1 C)	[157]
	W^{6+}	81%	284	~78% (100 cycles, 1 C)	[158]
Anionic doping	SiO_4^{2-}	83.5%	261.2	~83% (400 cycles, 0.12 C)	[143]
	SO_4^{2-}	83.2%	282.2	~80% (400 cycles, 0.12 C)	[143]
	PO_4^{3-}	84.2%	252.4	~95.6% (300 cycles, 0.1 C)	[144]
	BO_4^{5-}	94%	~240	85% (100 cycles, 0.24 C)	[159]
Cationic/ anionic Co-doping	Na^{+}/F^{-}	~68%	~260	~100% (100 cycles, 0.2 C)	[145]
	Cd^{2+}/S^{2-}	87.2%	268.5	84.4% (200 cycles, 1 C)	[146]
	Na^{+}/PO_4^{3-}	85.7%	255.7	93.8% (100 cycles, 1 C)	[147]
	Al^{3+}/F^{-}	81.1%	287	88.2% (150 cycles, 0.5 C)	[160]

1.5.4 Composition optimization

1.5.4.1 Synthesis process

According to the previous discussion in the elemental segregation section, a selective surface area with preferential segregation of cations has been discovered for LRCMs, which serves as

a dynamic barrier for Li^+ diffusion. The synthesis process shows a great influence on the distribution of TM ions. The impact of the synthesis route on $Li_{1.2}Ni_{0.2}Mn_{0.6}O_2$ was investigated by Zheng and co-workers.[161] They found that the electrochemical performances of LRCMs are affected by synthesis routes, including co-precipitation (CP), hydrothermal assisted (HA) and so-gel (SG) methods. X-ray energy dispersive spectroscopy (XEDS) mappings in **Figure 1.15**a illustrate that the cathode material synthesized via a HA method shows an improved homogeneous distribution of Ni within the material, thereby increasing Ni-Mn interaction and improving the structural stability. Scanning transmission electron microscope (STEM) characterization reveals that the HA method facilitates to generate a solid solution dominated by the Li_2MnO_3 type monoclinic C2/m phase (Figure 1.15b). This feature is different from other LRCMs, which consist of both trigonal $LiMO_2$ R-3m and monoclinic Li_2MnO_3 C2/m components. Meanwhile, it plays as a positive role in against oxygen loss and unexpected side reactions during cycling. Consequently, the HA cathode material exhibits the best rate performance (119 mAh g^{-1} at 5 C) and the lowest average voltage decay (0.15 V after 200 cycles) among three samples. In addition, the pH condition during the synthesis process has a significant influence on the electrochemical performance of LRMCs.[162] The relatively low pH value (< 7.5) normally results in a high residual Mn and Ni concentrations in precursors, which could lead to undesired chemical stoichiometry and distribution. However, when pH reaches a comparatively high value (> 8.5), it gives rise to a continuous increase of the residual Ni concentration and formation of nickel hydroxide, which is detrimental to the quality of LRCMs. A moderate pH range between 7.5 and 8.5 effectively minimizes the residual TM concentration

in solution and provides the optimized condition to synthesize LRCMs, thereby improving the electrochemical performance.

Furthermore, the synthesis process also determines the primary particle size of LRCMs. It is well known that the cathode material with smaller particle size shows higher ionic conductivity and shorter Li^+ diffusion pathway. Hence, optimizing the synthesis process is beneficial to control the primary particle size and, therefore, improve the electrochemical performance of LRCMs. Liu *et al.*[163] confirmed the primary particle size of LRCMs is correlated with calcination temperature. The particle size of materials changes to 80 nm, 200 nm, and 500 nm at the elevated temperature (800 ºC, 900 ºC and 1000 ºC). The sample with the smallest particle size shows the highest discharge capacity (237 mAh g^{-1} at 0.1 C) and ICE (75.1%), which is ascribed to the small dynamic barrier for Li^+ intercalation owing to the size effect. Apart from the sintering temperature, other conditions such as the preparation method[164] and the lithiation process[165] also remarkably influence the primary particle size of LRCMs. In this regard, how to optimize the synthesis process with both the excellent electrochemical performance and the possibility for potential commercial applications should be given priority.

1.5.4.2 Cationic substitution

Substitution with high-valent cation in the cathode material is another useful way to improve the electrochemical performance of LRCMs. A key step of this substitution strategy is to reduce, for example, the Mn valence (Mn^{4+}) to a lower state by introducing high oxidation state cation

species (Nb^{5+} and Ti^{4+}) in the lithium-rich manganese-based cathode material.[22] Through this method, oxygen can only participate in the redox reaction when charging to above 4.7 V, as indicated by a distinguishable voltage plateau in the galvanostatic charge-discharge profile. By controlling the charge voltage to 5 V, the revisable capacity (>300 mAh g^{-1}) is higher than the theoretical capacity of the cationic Mn^{2+}/Mn^{4+} double redox reaction (270 mAh g^{-1}). The involvement of the Mn^{2+}/Mn^{4+} reaction minimizes the sluggish anionic redox activity and enables rapid Li^{+} diffusion. Meanwhile, reducing the contribution from the excessive oxygen-based anionic redox upon the charge-discharge process also considerably enhances the structural stability and rate capability. Liu and co-authors reported a new type of Ti^{4+}-substituted LRCM, $Li_{1.2}Ti_{0.26}Ni_{0.18}Mn_{0.18}Co_{0.18}O_2$, where Ti ions present in both Li and TM layers.[166] As we can see from Figure 1.15c, a native Li–Ti cation mixing structure with strong Ti-O bonding restricts migration of TM ions and, therefore, inhibits the irreversible structural transformation from layered to spinel. Moreover, both of Mn^{4+} and Ti^{4+} are electrochemically inert and keep stable during charging and discharging, which contributes to enhanced structural stability. The voltage decay of the Ti^{4+}-substituted LRCM is only 90 mV after 100 cycles, while the capacity loss is also inhibited to a large extent (3% after 182 cycles). Additionally, the presence of Li–Ti cation mixing also lowers oxidation potential and thereby ensures the reversibility of the oxygen-based redox activity.

Substituting Ru^{4+} for Mn^{4+} ions in the $Li_{1.2}Mn_{0.6}Ni_{0.2}O_2$ system has been discussed by Knight and co-workers.[167] As the percentage of Ru^{4+} is increased, the size of the primary particles grows accordingly, and monoclinic *P12/m* phase peaks obtained by XRD analysis appear in the

high Ru^{4+} content cathode material, implying the formation of Ru-Ru dimer. Although the presence of the active $Ru^{4+/5+}$ redox couple could improve the electrochemical performance of the Ru^{4+}-substituted LRCM, its plateau region declines in length with increasing the degree of Ru^{4+} substituting and the whole LRCM system behaves more like Li_2RuO_3. At the same time, the oxygen-loss voltage plateau also decreases and becomes more slope-like voltage curve, illustrating the irreversible anionic redox activity is suppressed. Until now, there are only few reports about the cationic substitution strategy on LRCMs. Cationic substitution may break up the structural consistency and change the crystal structure from order to partial disorder. Meanwhile, the effect requires further evaluation and analysis.

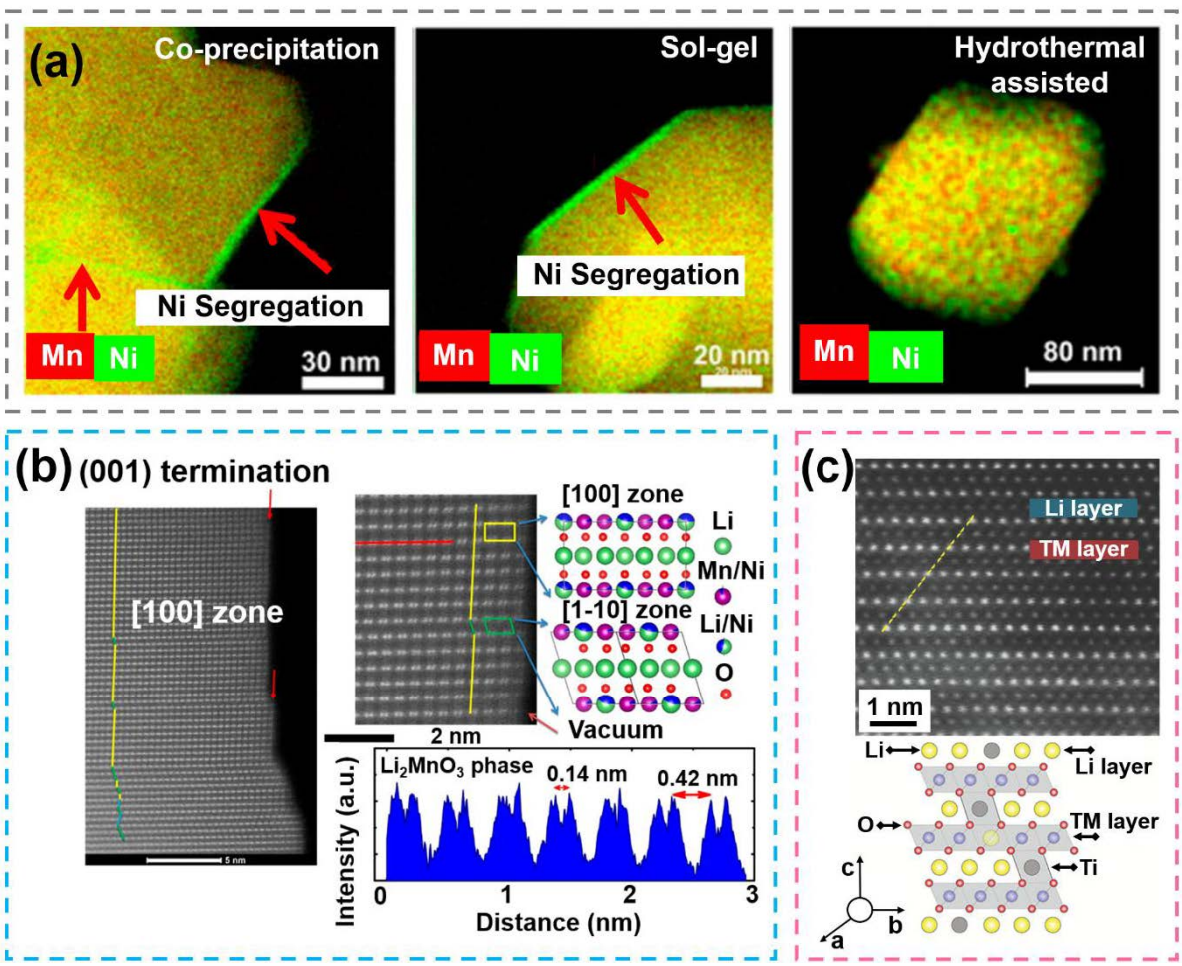

Figure 1.16 (a) X-ray energy dispersive spectroscopy (XEDS) mappings of cathode materials synthesized by different methods. (b) STEM images, atomic model and intensity plot of the HA cathode material.[161] (c) The HAADF image and the atomic model of Li-Ti mixed structure.[166]

1.5.4.3 Anionic ligands

Although the oxygen-based anionic redox activity gives rise to a high specific capacity of LRCMs as mentioned above, it also gives rise to significant voltage decay and sluggish reaction kinetic. Replacing the oxygen with more electronegative fluorine in LRCMs holds great promise because the working voltage and cycling stability are enhanced via substituting O^{2-} for

F^-. House *et al.*[168] demonstrated the partial substitution of O^{2-} with F^- in $Li_{1.9}Mn_{0.95}O_{2.05}F_{0.95}$. With the incorporation of the fluoride anion into the cathode material, anionic substitution increases the electronegativity of the as-prepared cathode material and reduces the valence of TM ions. The F^--substituted cathode material exhibits a high discharge capacity of 283 mAh g^{-1} derived from both the Mn^{3+}/Mn^{4+} and anionic redox reactions. Owing to the existence of the F^- anion in the cathode material, the lithiated oxyfluoride material suppresses the oxygen loss originated from the oxygen redox. *Ex situ* XRD reveals the reversible extraction and insertion of Li^+ without obvious structural change even after 100 cycles. Unlike the ordered layered Li_2MnO_3, the disordered $Li_{1.9}Mn_{0.95}O_{2.05}F_{0.95}$ structure with cation vacancies eliminates the cooperative Jahn-Teller distortion associated with Mn^{3+} in the ordered structure and, therefore, resulting in improved long-term cycling stability.

Another approach is to substitute less electronegative sulfur for oxygen, which can initiate the reversible anionic redox reaction. Saha *et al.*[169] introduced a new lithium-rich layered sulfide, $Li_{1.13}Ti_{0.57}Fe_{0.3}S_2$, which takes advantage of both cationic and anionic redox reactions and accounts for a high discharge capacity about 245 mAh g^{-1} with an average voltage of 2.5 V. *In situ* XRD shows that the sulfide cathode first undergoes a solid-solution reaction and then a biphasic process at the end of the initial charge. While the discharge process is a little different from its charge counterpart, as indicated by an additional solid solution process before full discharge. Hence, the charge and discharge paths are not symmetric at the beginning. However, the cathode material remains its long-range layered crystal structure throughout cycling (**Figure 1.16**a). $Li_{1.13}Ti_{0.57}Fe_{0.3}S_2$ shows negligible initial capacity loss and minimized voltage decay

(35 mV) compared with the $Li_{1.2}Ni_{0.13}Mn_{0.54}Co_{0.13}O_2$ cathode materials, which could be assigned to the efficient and highly reversible sulfur-based anionic redox. The irreversibility associated with oxygen loss in oxides is unlikely to occur in sulfides because of the presence of less electronegative sulfur. In addition, the absence of the large irreversible anionic redox also rules out the possibility of TM migration in the cathode material, therefore restricting the unwanted layered to spinel-like phase transformation. Galvanostatic intermittent titration technique (GITT) further reveals a much smaller voltage hysteresis (30 mV) than $Li_{1.2}Ni_{0.13}Mn_{0.54}Co_{0.13}O_2$ (300 mV), indicating the rapid reaction kinetics. However, it should be noticed that these attractive features come at the expense of the high energy density (600 Wh kg^{-1} for sulfides compared with 1000 Wh kg^{-1} for oxides), and some of the reaction mechanisms are still unclear. More efforts and attentions should be pursued in this research direction.

1.5.4.4 Lithium deficiency engineering

A deep delithiation state always comes along with irreversible loss of oxygen species within LRCMs. Therefore, the lithium content can determine the electrochemical performance of LRCMs to a large extent. Recently, lithium-deficient layered LRCMs have shown excellent electrochemical performances.[170] Lithium vacancies in lithium-deficient layered LRCMs cause *in situ* nickel doping and spine phase coating on the surface, which not only restricts the oxygen loss via forming strong Ni−O bonds but also improves the structural stability. Owing to the suppressed oxygen activity and reduced energy barrier for Li^+ diffusion, the lithium-deficient

layered LRCMs delivers much higher ICE (83.9%) and better rate capability (132.9 mAh g^{-1} at 10 C) than the pristine layered LRCMs. Furthermore, the lithium-deficient layered LRCMs also maintains its high specific capacity (93.1%) and energy density (84.5%) after 500 cycles at 1 C, confirming the improved cycling and voltage stability. *In situ* XRD measurement demonstrates that the lithium-deficient layered LRCMs shows smaller shift of diffraction peaks than the pristine layered LRCMs during the first three cycles, implying the slight change in lattice parameters upon cycling.

Zhu *et al.*[171] proposed the concept of lithium-gradient from 'lithium-richness' to 'lithium-poorness' in LRCMs. As shown in Figure 1.16b, creating a lithium-poor region on the surface of the particle ($X(r_{surface}) = X_{poor} \leq 0$) reduces the TM oxidation state in the surface region, which promotes the cationic redox activity and in turn limits the oxygen-based redox activity. In addition, the lithium-rich area in the bulk of the particle ($X(r_{core}) = X_{rich} > 0$) ensures the reversible and abundant anionic redox reaction regarding the lattice oxygen species. The lithium-gradient cathode material exhibits very high ICE (90.8%) and discharge capacity (293.1 mAh g^{-1} at 0.1 C). Moreover, both of $Mn^{3+/4+}$ and oxygen redox peaks in cyclic voltammetry (CV) curves maintain unchanged after 50 cycles, further demonstrating excellent structural integrity. The design of such a lithium-poor surface can eliminate oxygen release and gaseous escape into the electrolyte according to the DEMS test results, improving the cycle life and safety under the long-term working condition. In addition, the lithium-rich core is capable of trapping axial Li–O_{2p}–Li configurations and achieving a high specific capacity. Consequently, both capacity loss and voltage decay are effectively suppressed.

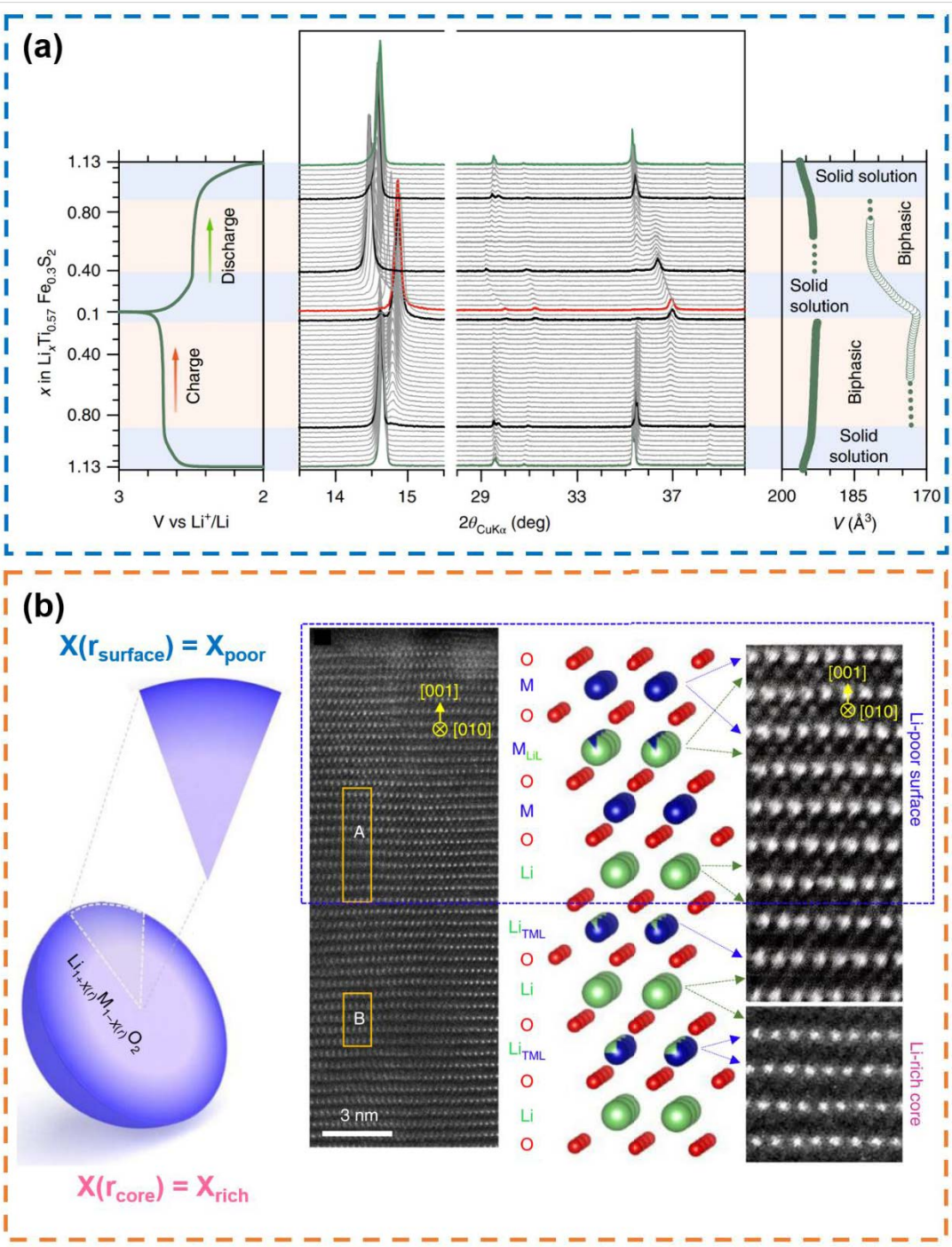

Figure 1.17 (a) *In situ* XRD patterns and the corresponding charge-discharge profile of the $Li_{1.13}Ti_{0.57}Fe_{0.3}S_2$ cathode during the first cycle.[169] (b) Schematic and STEM-HAADF lattice images of the Li-gradient region from the lithium-rich (lithium substitution in M layer) bulk to the lithium-poor (M substitution in lithium layer) surface.[171]

1.5.5 Structure engineering

Rational adjusting the structural composition with 3D open framework is expected to effectively improve the electrochemical performance of LRCMs. Unlike the afore-mentioned surface engineering and elemental doping methods, such structural optimization strategies include both the bulk phase and the surface of cathode materials. In light of this, Wu *et al*.[172] emphasized the importance of the spinel structure with a 3D Li^+ diffusion path on the electrochemical property of LRCMs. Owing to the high voltage and Li^+ ionic conductivity of the lithium-rich spinel phase, the spinel/layered heterostructure cathode material exhibits excellent rate capability and remarkable cycling stability. The microstructure of the heterostructure cathode material was further investigated using high-resolution transmission electron microscopy (HRTEM). By contrast to the single-layered structure, the heterostructure presents a clear and distinct interface near the edge (**Figure 1.17**a and 1.17b). Figure 1.17c reveals that the outer shell is indexed to the cubic-spinel structure, while the inner core maintains its original layered structure. The structural compatibility of the spinel/layered heterostructure takes advantage of both the merits of the layered structure and the 3D diffusion channel of the nano spinel layer (Figure 1.17d), thereby yielding a discharge capacity above 270 mAh g^{-1} with excellent cycling stability.

A high percentage of exposed (010) facets could significantly contribute to overcoming the Li^+ transport barrier for LRCMs.[173] As shown in Figure 1.17e and 1.17f, the cathode material

displays the typical hexagonal nanobricks under TEM characterization. Two sets of the lattice distance with an angle of 120 degree correspond to the (010) exposed facet (Figure 1.17g and 1.17h). These (010) planes are parallel to the c axis, which have large diffusion channels along the [001] direction and provide facile pathways for the migration and exchange of Li^+ during charge and discharge process. Therefore, the obtained cathode material has good capacity retention (93.5% at 10 C) and superior rate capability (130 mAh g^{-1} at 15 C) as well.

Liu *et al*.[174] synthesized a 3D cube-maze-like LRCM. As shown in Figure 1.17i, this cube-maze-like microstructure is composed of two-dimensional (2D) nanosheets with high surface area, rapid Li^+ diffusion channels, enhanced structural stability, and many exposed (010) crystal facets. Such a unique 3D self-assembled architecture shows a high discharge capacity of 285.3 mAh g^{-1} at 0.1 C and the remarkable rate performance (133.4 mAh g^{-1} at 20 C). When cycling at a very high current density (20 C), the cathode material exhibits minimized capacity loss of 25% even after 1000 cycles. Coupling with the graphite anode material, the lithium-rich full cell shows a reversible specific capacity (275.2 mAh g^{-1} at 0.1 C) and superior cycling stability (84.8% after 100 cycles). All these findings demonstrate that the structure optimization strategy is beneficial to the development and practical application of LRCMs.

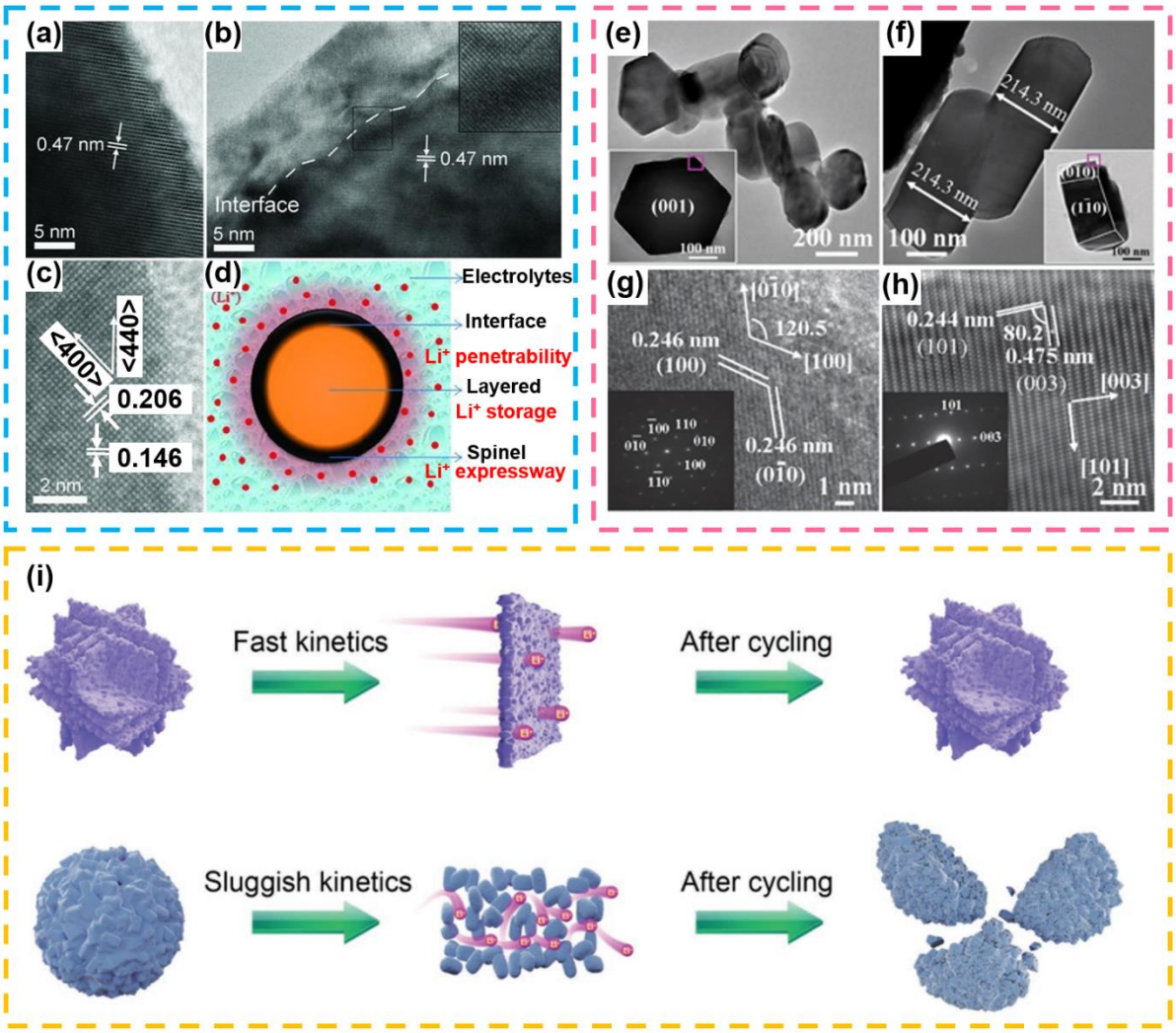

Figure 1.18 (a-c) HRTEM images of the pristine and spinel/layered heterostructured cathode materials. (d) Schematic diagram of the spinel/layered heterostructure.[172] (c) TEM images of LRCM nanobricks from the (e, g) frontal view and (f, h) lateral view, respectively.[173] (e) The difference of lithium diffusion kinetics in 3D cube-maze-like and microsphere-like LRCMs.[174]

1.5.6 Electrolyte additives

The formation of a stable and conductive passivation layer on the surface of cathode materials by adding additives into the electrolyte has been proved as a promising strategy to resolve tough problems such as voltage decay and structural instability. Indeed, the high cut-off voltage (>4.6 V) usually causes drastic decomposition of carbonate-based electrolytes, which deteriorates the electrochemical performance of LRCMs. A stable passivation can layer prevent direct contact between electrode materials and electrolytes, which efficiently inhibits the decomposition of electrolyte at the high working voltage and thus ensures structural integrity. Therefore, using electrolyte additives is expected to enable carbonate-based electrolytes thermodynamically stable under the high voltage operating condition. Based on this point, Abouimrane *et al.*[175] studied the role of 3-hexylthiophene (3HT) as an additive in the electrolyte of 1.2 M $LiPF_6$ in ethylene carbonate/ethyl methylcarbonate (EC/EMC = 3/7). The cell with 5 wt% 3HT in the electrolyte exhibits distinguishable redox peaks in the CV measurement, which is ascribed to the generation of poly (3HT) on the surface of the LRCM. Furthermore, the lithium-ion cell with 0.1 wt% 3HT in the electrolyte shows the best cyclability and the highest CE among other cells with different 3HT contents in the electrolytes at both room temperature and 55 ^{o}C. The addition of 3HT in the electrolyte reduces the interfacial resistance and assists the formation of a protective layer against corrosive acid species such as HF and H_2CO_3.

Zhu and co-workers[176] investigated the contribution of $LiF_2BC_2O_4$ (LiDFOB) as the electrolyte additive on the electrochemical performance of $Li_{1.2}Ni_{0.15}Mn_{0.55}Co_{0.1}O_2$. Specifically, the LiDFOB additive endows a passivation surface layer on the cathode material,

which restricts the dissolution of TM species accompanied by drastic electrolyte decomposition. This buffer effect remarkably decreases the cell impedance, and the irreversible capacity loss is reduced from 73% to 35% after 200 cycles (**Figure 1.18**a and 1.18b). Tan *et al*.[177] reported tri(hexafluoro-iso-propyl)phosphate ($(C_3HF_6O)_3PO$ or HFiP) as an electrolyte additive to increase the cycling stability of $Li_{1.2}Ni_{0.16}Mn_{0.56}Co_{0.08}O_2$ cathode materials. Their study reveals that HFiP preferentially decomposes on the electrode surface at a relatively low voltage. The HFiP additive promotes the formation of a stable CEI layer on the cathode material, which results in the decrease of polarization. Thus, more Li_2MnO_3 phase participates in the activation process and delivers higher discharge capacity (250 mAh g^{-1} at 18 mA g^{-1}) than the electrolyte without additives. Moreover, the rate performance (124.7 mAh g^{-1} at 5 C) of the $Li_{1.2}Ni_{0.16}Mn_{0.56}Co_{0.08}O_2$ cathode has been boosted with the HFiP additive in the electrolyte.

Furthermore, selected electrolyte additives can trap active oxygen species and minimize the negative impact of oxygen loss from the crystal lattice. Zheng *et al*.[178] introduced tris(pentafluorophenyl)borane ($(C_6F_5)_3B$, TPFPB) as an electrolyte additive for the $Li_{1.2}Ni_{0.2}Mn_{0.6}O_2$ cathode material. The highly active oxygen species (O_2^-/O_2^{2-}) released from the Li_2MnO_3 component are detrimental to the stability of the crystal structure and induce the decomposition of the electrolyte (Figure 1.18c). Under such a circumstance, TPFPB is expected to capture these oxygen species and avoid their further reaction with the electrolyte. In addition, other parasitic products are also soluble in TPFPB. Therefore, the interfacial stability is enhanced. Benefit from these advantages, carbonate-based electrolytes with 0.2 M TPFPB can

significantly contribute to the improvement of discharge capacity and cycling stability of LRCMs (Figure 1.18d).

The presence of electrolyte additives can enhance the cycling performance of LRCMs and stabilize the electrode/electrolyte interface, as shown in **Table 1.4**. However, most of the electrolyte additives are expensive and generally not suitable for large-scale commercialization. In addition, some electrolyte additives are highly corrosive to current collectors. These problems need to be further addressed for practical application.

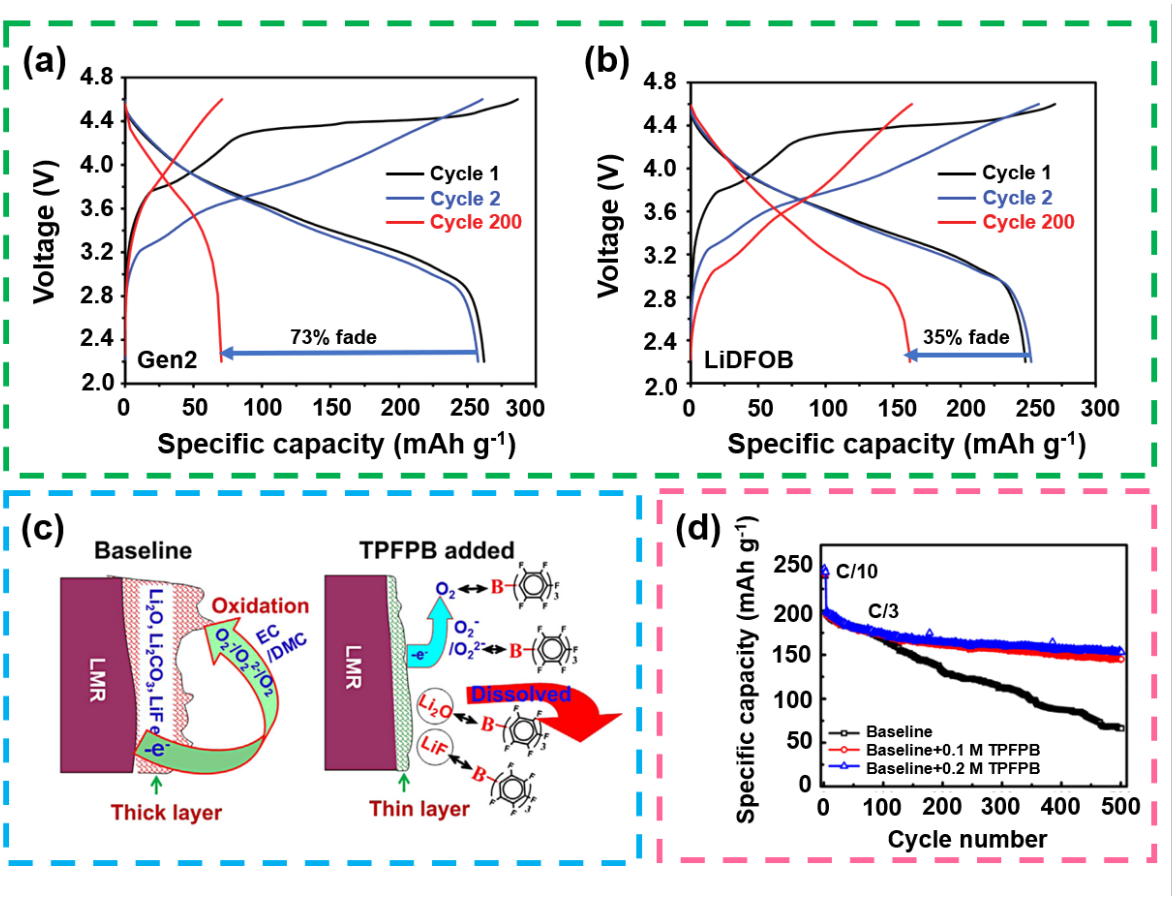

Figure 1.19 Galvanostatic charge-discharge curves for cells containing (a) Gen 2 electrolyte and (b) Gen 2 electrolyte with 2wt% LiDFOB additive.[176] (c) Scheme of the functioning mechanism of TPFPB. The addition of TPFPB in electrolyte significantly reduces formation of a thick passivation layer. (d) long-term cycling performances of LRCMs with and without TPFPB.[178]

Table 1.4 Different types of electrolyte additives species.

Type of electrolyte additives	Initial Coulombic efficiency	Discharge capacity (mAh g^{-1})	Capacity retention	Ref.
Trimethyl phosphite (TMP)	92.2%	~270 (0.1 C)	81.3% (100 cycles, 0.5 C)	[179]
Triphenyl phosphite (TPPi)	-	204.3 (0.5 C)	90.8% (100 cycles, 0.5 C)	[180]
Tri(hexafluoro-iso-propyl)phosphate (HFiP)	78.9%	250 (0.07 C)	72.3% (130 cycles, 0.72 C)	[177]
Trimethylsilyl (trimethylsiloxy) acetate (bi-TMSA)	70.2%	237.56 (0.1 C)	80.1% (374 cycles, 1 C)	[181]
Tris(2,2,2-trifluoroethyl) phosphite (TTFP)	81.4%	280 (0.2 C)	82.1% (110 cycles, 0.2 C)	[182]
Tris(trimethylsilyl)borate (TMSB)	80.3%	213 (0.5 C)	73.6% (220 cycles, 0.5 C)	[183]
Tris(pentafluorophenyl)borane (TPFPB)	~79.5%	245 (0.1 C)	76.8% (500 cycles, C/3)	[178]
Tris(trimethylsilyl)phosphate (TMSP)	76.2%	225 (0.08 C)	91.1% (50 cycles, 0.08 C)	[184]
3-hexylthiophene (3HT)	~85%	~280 (0.1 C)	90% (70 cycles, 0.1 C)	[175]
$LiF_2BC_2O_4$ (LiDFOB)	~91.2%	251 (0.06 C)	65% (200 cycles, 0.06 C)	[176]
Lithium bis(oxalato)borate (LiBOB)	88.4%	284 (0.1 C)	98.1% (120 cycles, 0.5 C)	[185]
Lithium difluoro(bisoxalato)phosphate (LiDFBP)	~82.5%	~246 (0.1 C)	90% (100 cycles, 0.5 C)	[186]
Ethylene glycol bis (propionitrile) ether (EGBE)	-	203.5 (0.1 C)	89% (150 cycles, 0.5 C)	[187]
Methyl diphenylphosphinite (MDP)	88.5%	230 (0.1 C)	93.9% (80 cycles, 0.1 C)	[188]
Phenyl vinyl sulfone (PVS)	74%	~260 (0.1 C)	80% (240 cycles, 0.5 C)	[189]
Fluoroethylene carbonate (FEC)	70%	~280 (0.1 C)	92.5% (100 cycles, 0.5 C)	[190]

1.5.7 Other strategies

Apart from the afore-mentioned improvement strategies, there are still other approaches to overcome the current and forthcoming challenges of LRCMs. Binders are very important and determine the overall electrochemical performance of LRCMs in LIBs. Yang *et al.*[191] chose polyacrylic acid (PAA) as a binder for LRCMs. Unlike the commonly used polyvinylidene difluoride (PVDF) binder, PAA can form a tight and uniform protection film based on its carboxyl groups and, therefore, prevent the cathode material from being attacked by corrosive products from side reactions. Meanwhile, it also introduces H^+ into the crystal lattice via H^+/Li^+ exchange to suppress TM ions migration. Benefiting from this surface/interface modification method, the dissolution of TM species, especially for Ni, is greatly restricted compared with the traditional PVDF binder (1.65% for PAA and 5.93% for PVDF, respectively). Moreover, the presence of carboxylate groups in PAA inclines to bond with both the cathode material and the current collector, thereby enhancing the structural integrity and stability, exhibiting good retention rate of 88% over 500 cycles. Liu *et al.*[192] prepared a binder-free heterostructured spinel/layered LRMC through the electrospinning technique. The obtained one-dimensional (1D) nanofibers consist of many uniform LRCM nanoparticles, which ensures high Li^+ diffusivity and good structural stability. The synthesized cathode material was directly used as an electrode for LIBs without any additives, showing very high ICE (≈100%), excellent rate performance (150 mAh g^{-1} at 5 C), and outstanding cycling stability (> 80% after 70 cycles). Moreover, *in situ* XRD and Raman investigations demonstrate that the introduction of the spinel phase in the primary layered structure can effectively utilize oxygen vacancies without causing

obvious structure evolution. Meanwhile, the spinel structure on the surface promotes the diffusion and transport of Li^+. The absence of conductive agents and binders also lowers the charge transfer resistance and reduces the weight of electrodes.

Annealing is also an effective and facile method to overcome disadvantages such as voltage decay and structural defects for LRCMs. Singer and co-workers[193] demonstrated voltage decay that occurs in LRCMs could be recovered by high-temperature calcination. The superstructure in LRCMs gradually disappears upon cycling, further triggering the phase transformation and the severe voltage decay. Nonetheless, the high-temperature heat treatment allows for the recovery of the superstructure and the oxygen stacking sequence, which facilitates to restore the voltage decay. Electrochemical pre-cycling treatment, which is different from traditional methods, is also promising to improve the electrochemical performance of LRCMs.[194] Generally, LRCMs experience significant capacity loss when cycling at high voltage (> 4.6 V). However, this problem can be greatly mitigated if the cell is pre-cycled at the relatively low voltage (4 ~ 4.5 V) for several times. Moreover, such effects could be further improved if the cell is treated with a stepwise pre-cycling strategy, i.e., cycles at the various potential windows for several times.

1.6 Potassium-ion batteries

Although the intensive research of LIBs has attracted people's interest and attention in recent years, the limited and uneven distribution of lithium resources leads to a high cost and make

them less promising for grid-scale energy storage.[195-199] This economic concern has driven the industrial community to explore other alternatives to LIBs. Recently, potassium-ion batteries (PIBs) emerge as a potential candidate for next-generation rechargeable alkaline batteries.[200-202] Potassium shares similar chemical properties as lithium while shows other distinct advantages such as their abundant resources in the crust and low standard redox potential (−2.94 V for K/K^+ *vs* standard hydrogen electrode, SHE, compared to −3.04 V for Li/Li^+ *vs* SHE).[203-204] The representative "rocking-chair" working mechanism in LIBs perfectly fits in the potassium-based energy storage system, which renders PIBs a good alternative to LIBs. Moreover, K^+ has a smaller Stokes radius and the higher ionic conductivity than Li^+ owing to its weaker Lewis acidity and smaller desolvation energy.[205-206] Another advantage is using low-cost Al foils rather than Cu foils as current collectors and thereby lowers costs for mass production. Despite the appealing potential of PIBs, the intercalation of large-sized K^+ into electrode materials is kinetically unfavorable and causes severe volume expansion, resulting in their relatively low capacity, unsatisfactory rate capability and poor cycling performance.

1.7 Electrode materials for potassium-ion batteries

Considering the much higher mass-to-charge ratio of K^+ (39.1) than Na^+ (23) and Li^+ (6.94), the bulk K^+ normaly results in larger volume expansion and sluggish reaction kinetics during charge and discharge.[200, 207] This phenomenon requires stable crystal structures and large diffusion channels for K^+ migration, which put much pressure on the development of suitable electrode materials.

1.7.1 Cathode materials for potassium-ion batteries

Generally, PIBs cathode materials can be classified into three types: layered transition metal oxides,[208-211] Prussian blue analogs (PBAs),[212-214] polyanionic compounds[215-217] and organic materials. (**Figure 1.19**a-c).[218-220]

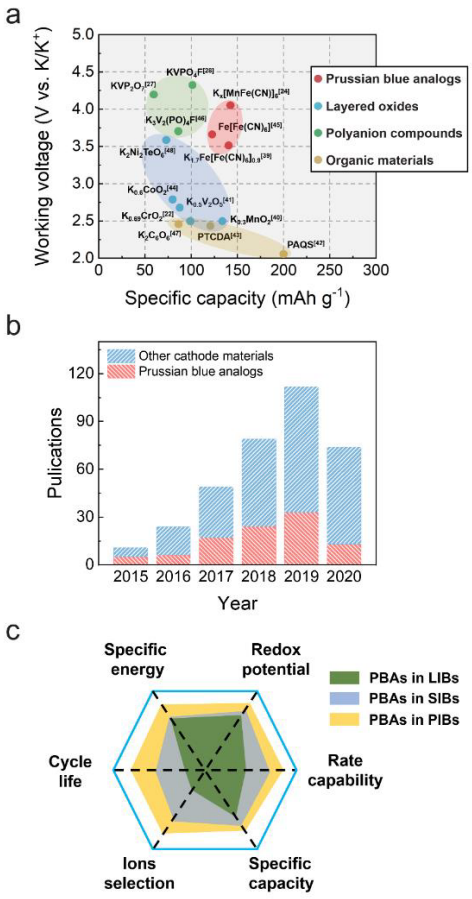

Figure 1.20 (a) Specific capacity versus working voltage of different cathode materials for non-aqueous PIBs.[210, 212, 215-216, 221-230] (PTCDA: perylenetetracarboxylic dianhydride. PAQS: poly(anthraquinonyl sulfide)). All of the data is based upon the mass of the cathode material only. (b) The number of publications on cathode materials for PIBs according to Web of Science database (June 22, 2020). (c) Radar plot comparing electrochemical performances of PBAs in LIBs, SIBs and PIBs according to six key characteristics.

1.7.1.1 Prussian blue analogs cathode materials

The general formula for potassium-based PBAs can be defined as $K_xM^{III}[M'^{II}(CN)_6]_{1-y}\square_y \cdot zH_2O$ ($0 \leq x \leq 2$, $0 \leq y \leq 1$), wherein M and M' stand for TM ions, □ designates $M'(CN)_6$ vacancies, and H_2O represents the interstitial/coordination water. As shown in **Figure 1.20**a and 1.20b, if trivalent M^{III} is fully reduced to divalent M^{II} after the intercalation of K^+, the resulted compound with maximal potassium content ($K_2M^{II}[M'^{II}(CN)_6]\cdot nH_2O$) is called Prussian white (PW). On the other hand, a K-poor and even K-free compound ($M^{III}[M'^{III}(CN)_6]\cdot nH_2O$) generated after the extraction of K^+ is described as Berlin green (BG).[231-232] Due to the influence of the crystal field, M and M' in PBAs exhibit different spin states as a result of 3d orbitals splitting (Figure 1.20c). The N-coordinated site presents a weaker crystal filed than the C-coordinated site. Therefore, the splitting of the M 3d orbitals is much less than that in M' 3d, which gives rise to a low-spin (LS) M' state accompanied by a high-spin (HS) M state. For the case of $K_2Fe^{2+}[Fe^{2+}(CN)_6]$, in the ideal condition (x=2, y=z=0), the oxidation of TM firstly starts from the decline of spin-up orbitals (Fe^{LS}), and is then followed by a change in the Fe^{HS} electronic structure. This process is symmetric and entirely reversible upon potassiation (Figure 1.20b). The redox reactions of Fe^{HS} and Fe^{LS} determine the reversible capacity and the working voltage of PBA cathode materials.

The difference of Berlin green, Prussian blue and Prussian white is mainly reflected by the molar ratio of K/TM. Particularly, K^+ content (x) and water species (z) affect the stability and

symmetry of the crystal structure. Three influence factors that need to be taken into account, including Pauli repulsion, d–π orbital overlap and Coulomb attraction. Among them, the first two are responsible for the volume shrinkage, while the latter decreases the lattice volume. The introduction of K^+ brings about an enhancement in Coulomb attraction, while a high water content increases the Pauli repulsion. When potassiation (*x* increasing) or dehydration (*z* decreasing) occurs, the Coulomb attraction grows stronger and becomes more significant than the other two indicators, which eventually results in a twisted structure. In contrast, depotassiation (*x* decreasing) or hydration (*z* increasing) promotes Pauli repulsion and leads to a regular structure.[233] Therefore, similar to the reports on Na-poor counterparts, K-poor PBAs usually present cubic structures. However, unlike the previous findings of Na-rich PBAs with rhombohedral structures[234], most of K-rich PBAs display typical monoclinic structures regardless of crystal water content. This result can be interpreted by the large ionic radius of K^+ that enhances the Pauli repulsion and suppresses lattice shrinkage.[235-236]

The crystal parameters of *x*, *y* and *z* are adjustable and highly dependent on the ratio of K/TM and synthesis conditions. Normally, a high ratio of K (large *x*) and a low percentage of $Fe(CN)_6$ vacancies (small *y*) result in a low degree of crystal water content. For example, a typical Berlin green, $Fe_4[Fe(CN)_6]_3 \cdot nH_2O$, presents a double-perovskite stacking with a cubic face-centered structure. As indicated by the stoichiometries (Fe^{3+} : $Fe(CN)_6^{4-}$ = 4:3), there are at least a quarter of $Fe(CN)_6$ vacancies within the structure according to charge conservation.[237] It should be noted that these vacancies are very difficult to be fully activated and thereby cause low electrochemical performances, respectively. Figure 1.20d illustrates the potential occupation

sites of K^+ in the cubic structure can be designated with Wyckoff notations as 8c (body-center), 24d (face-center), 32f (displaced from 8c sites toward N-coordinated corner), 32f' (displaced from 8c sites toward C-coordinated corner) and 48g (displaced between 8c and 24d). Density functional theory (DFT) calculations reveal that K^+ preferentially occupies the body-centered 8c site with large interstitial voids, whereas occupation of the face-centered 24d site is energetically favorable for Na^+.[207, 231, 237]

PBAs-based cathode materials have some unparalleled advantages when used in PIBs: (1) Prussian blue cathode materials have much higher ion-selection priority for potassium than sodium and lithium in the non-aqueous system (K > Na ≫ Li). Goodenough's group has confirmed that K^+ has a stronger preference than Na^+ to access the PBAs framework, enabling low lattice strain and rapid ion-diffusion kinetics.[212, 238-239] Meanwhile, in the aqueous system, Prussian blue cathode materials also show a strong tendency for accommodating K^+ in the same order of K > Na ≫ Li, and the crystal water in PBAs could facilitate the transport of K^+ while stabilizing the 3D open structure.[240] (2) Prussian blue cathode materials demonstrate high reversibility and cycle life, following the order of K > Na ≫ Li. Due to the mismatch between the Prussian blue crystal lattice and Li^+, the reversible Li^+ de/intercalation and cycling stability are deteriorated.[241-242] However, this phenomenon is different for Na^+ and K^+. The better compatibility between K^+ and Prussian blue crystal structure contributes to the exceptional cycle lifespan as cathode materials for PIBs.[205, 243] (3) Good mutual compatibility between Prussian blue and K^+ leads to a lower Gibbs free energy and, therefore, a higher redox potential as a result.[207] Taking MnFe-based PBAs as an example, KMnFe-PBA, NaMnFe-PBA and

LiMnFe-PBA show average discharge voltages of 3.7, 3.4 and 3.5 V in K, Na and Li half cells, corresponding to specific energy densities of 521, 476, and 479 W h kg^{-1}, respectively.[206] These attractive advantages make PBAs promising cathode materials for high-energy-density and long-working-life PIBs.

Meanwhile, there are many challenges to use PBAs as cathode materials for PIBs. Firstly, most PBAs have a large amount of interstitial water, which is almost inevitable during their wet-chemistry synthesis process. The high working voltage for PIBs normally causes irreversible decomposition of carbonate-based electrolytes, which can further react with interstitial water and lead to drastic side reactions and other safety issues. On the other hand, some critical structural parameters, such as the lattice integrity and symmetry, are highly dependent on the portion of interstitial water and of great significance to the structural stability.[207, 243-244] Secondly, due to the fast reaction kinetics of chemical coprecipitation routes, the nucleation and growth of PBAs crystal grains happen immediately and produce low-crystallinity and small grains containing numerous coordinated water and $Fe(CN)_6$ vacancies. The presence of certain levels of interstitial/coordinated water, as well as vacancies, shows adverse impacts on their electrochemical performance.[231, 245] Moreover, PBAs suffer from low bulk density and poor electrical conductivity, which further degrades their power density.[221, 243]

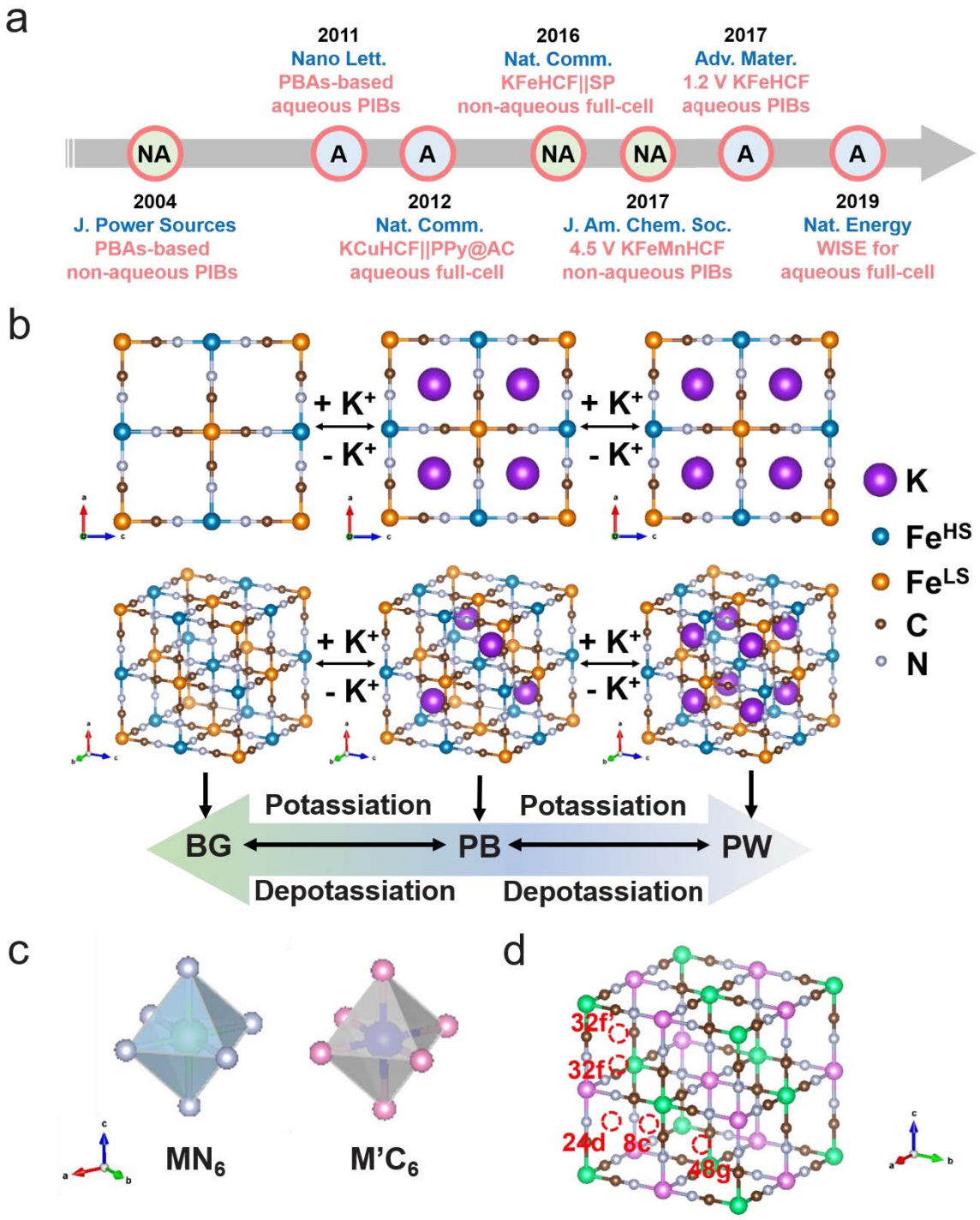

Figure 1.21 (a) The recent research process of PBA cathode materials in PIBs. (b) Schematic illustration of structural transformation among BG, PB and PW. (c) Spin states of N-coordinated (left) and C-coordinated (right) TMs in PBAs. (d) Crystal structure of a defect and water-free $Fe_4[Fe(CN)_6]_3$ model and possible intercalation sites for K^+.

1.7.1.2 Layered oxides cathode materials

Layered K_xMO_2 (M = 3d transition metals, $0 \leq x \leq 1$) oxides have been extensively studied as cathode materials for PIBs.[200, 246] Generally, α-$NaFeO_2$ is one of the most representative layered structures proposed in the research field of cathode materials. This material demonstrates a layered rock-salt type structure with an $R\ \bar{3}m$ space group (SG) built from MO_2 slabs containing alkali metals and edge-sharing MO_6 octahedra.[206] Theoretically, K^+ has two major coordination environments in the layered K_xMO_2, which can be described as edge-shared octahedral "O" sites and face shared prismatic "P" sites, respectively. In the "O"-type structure, MO_2 slabs with cubic close-packed (ccp) oxygen are stacked along the c-axis, while alkali-metal ions occupy the octahedral sites between TM layers. The "O" stands for the octahedral sites where K^+ are located and the number "2" or "3" indicates the MO_2 slabs stack sequence in the hexagonal unit cell.[211] (For example, O3-type crystal structure comprises three MO_2 slabs as the AB-CA-BC stacking order in the each hexagonal unit cell). In the "P"-type layered structure, K^+ is located at the prismatic sites between the MO_2 slabs with the oxygen packing such as AB-BA (P2-type) and AB-BC-CA (P3-type), respectively.[206]

Chromium (Cr) is the only 3d transition metal that crystallizes into the O3-type structure with K. In a potassium-based half-cell, O3-type layered $KCrO_2$ shows a discharge capacity of 90 mAh g^{-1} with various and complex phase transitions (O3−O′3−P′3−P3−P′3−P3−O3) within the potential range of 4.0−1.5 V when K^+ is inserted and extracted (**Figure 1.21**a).[247] These intricated structural evolutions can be ascribed to the strong K^+–K^+ repulsion. The K^+–K^+ interaction stabilizes the K^+/vacancy ordering in the interslabs upon K^+ deintercalation and

thereby results in stepwise voltage profiles as observed in Figure 1.21b, which leads to sluggish reaction kinetics and poor cycling stability.[210]

"P"-type layered K_xMnO_2 and K_xCoO_2 ($0 \leq x \leq 1$) are two of most frequently reported layered cathode materials for PIBs.[208, 248-249] Specially, nonstoichiometric K_xMnO_2 and K_xCoO_2 oxides are more easily to crystallize into P3- and P2-type phases, and the K content x directly affects the structural type of final products. Most of them deliver a high specific capacity from 70 to 110 mAh g^{-1} at the given potential range ($1.5 \leq x \leq 4.2$ V). However, they are suffering from the severe structure change during potassiation and depotassiation. One of the solutions is to synthesize binary, ternary, and quaternary transition oxides cathode materials where fewer and reversible voltage steps are expected to be realized.[211, 250]

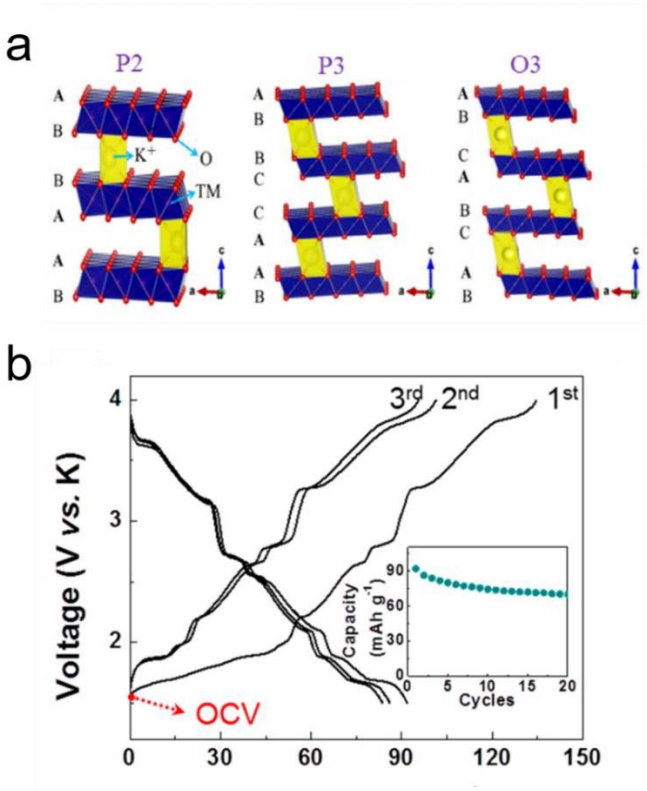

Figure 1.22 (a) Schematic illustrations of layered oxides crystal structures of P2- P3- and O3-, K_xMO_2.[246] (b) Galvanostatic charge and discharge profiles of $KCrO_2$ in a potassium half-cell.[247]

1.7.1.3 Polyanionic compounds cathode materials

As discussed above, layered oxides cathode materials exhibit low working voltage (< 3.5 V) and complex structure transitions when cycling. The relative low energy density and poor lifespan switch people's attention to other cathode materials with 3D open frameworks and fast diffusion channels for K^+.[202, 206] Apart from aforementioned PBAs cathode materials, polyanionic compounds stand out as one of the potential candidates to meet the demand for high-energy-density cathode materials. This class of cathode materials comprises TMO_x and $(XO_4)^{n-}$ (X = P, Si, S and Mo) polyhedra. Due to the presence of the polyanionic group, the highly covalent X−O bond decreases the covalency of the TM−O bond. Such an inductive effect enhances the redox potential of TM and, therefore, increases the working voltage.[215, 217] Owing to the rapid ionic diffusion and the inductive effect, polyanionic compounds have been extensively studied as cathode materials for PIBs. Vanadium-based fluorophosphates, such as $K_3V_2(PO_4)_2F_3$ and $KVPO_4F$, are one of the representatives among them. Lin et al.[217] synthesized the orthorhombic $K_3V_2(PO_4)_2F_3$ through the electrochemical exchange from $Na_3V_2(PO_4)_2F_3$ and studied its electrochemical performances. Such a polyanionic compound displays a specific capacity ~100 mAh g^{-1} with reversible phase transformations (**Figure 1.22**) and a high working potential of 3.7 V *vs.* K/K^+. Furthermore, it also shows excellent capacity retention (95%) after 180 cycles. The synthesis of $KVPO_4F$ as a cathode material for PIBs was proposed by Kim et al.[216] According to their report, the prepared $KVPO_4F$ exhibits a high discharge capacity of 105 mAh g^{-1} with a high average voltage (~4.33 V).

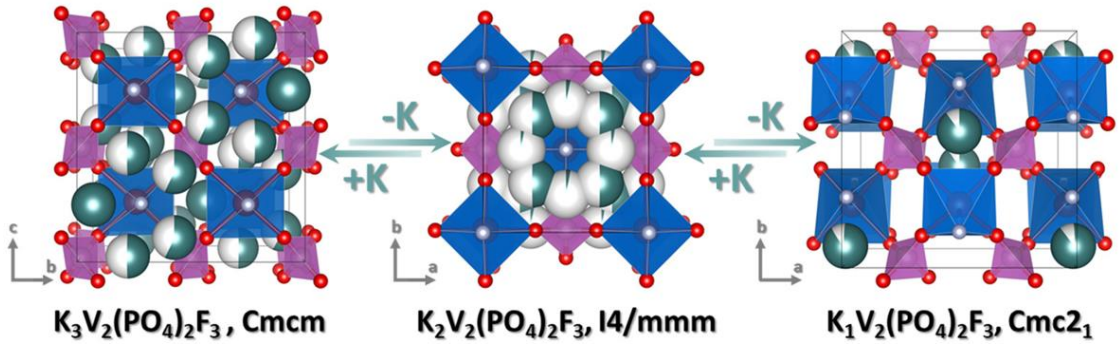

Figure 1.23 Phase transformations of $K_3V_2(PO_4)_2F_3$ during K^+ intercalation and deintercalation.[217]

1.7.1.4 Organic cathode materials

Owing to advantages such as environmental friendliness, low cost, high electrochemical activity and recyclability, a large amount of organic materials, including conducting polymers, small organic molecules and nonconjugated polymers, have been explored as cathode electrodes for PIBs.[218-220] The most frequently reported inorganic cathode materials usually require the high-temperature calcination process or high energy ball milling. However, these tedious preparation processes are unnecessary for organic materials and thereby lowering the production cost and reducing the carbon dioxide emission.[206] Furthermore, many organic cathode materials have large voids and active sites, which are favorable for storage and transport of the large radius K^+.[202] Poly(anthraquinonyl sulfide) (PAQS) holds great promise as the cathode material for PIBs.[224] It undergoes a reversible redox reaction with two obvious voltage plateaus at 2.1 and 1.5 V in the charge and discharge profiles, corresponding to the

redox reaction of two carbonyl groups of the quinone moieties (**Figure 1.23**a and 1.23b). PAQS shows a very high ICE that close to 90% and good capacity retention of 75% after 50 cycles in the potassium half-cell. However, it also manifests poor rate capability at the high current density, which is originated from sluggish reaction kinetics in the crystal structure. Another type of the organic cathode material, perylene-3,4,9,10-tetracarboxylic dianhydride (PTCDA), has also been studied among researchers.[219] Interestingly, PTCDA can store up to eleven K^+ at the fully discharged state (Figure 1.23c, 0.01 V *vs.* K/K^+), which implies the possibility as a high specific capacity cathode material for PIBs. However, like most of organic cathode materials, PTCDA experiences severe capacity fade caused by low electronic conductivity and dissolution in the electrolyte. In addition, its relatively low redox potential (2-2.5 V) reduces the overall energy density of the full cell.

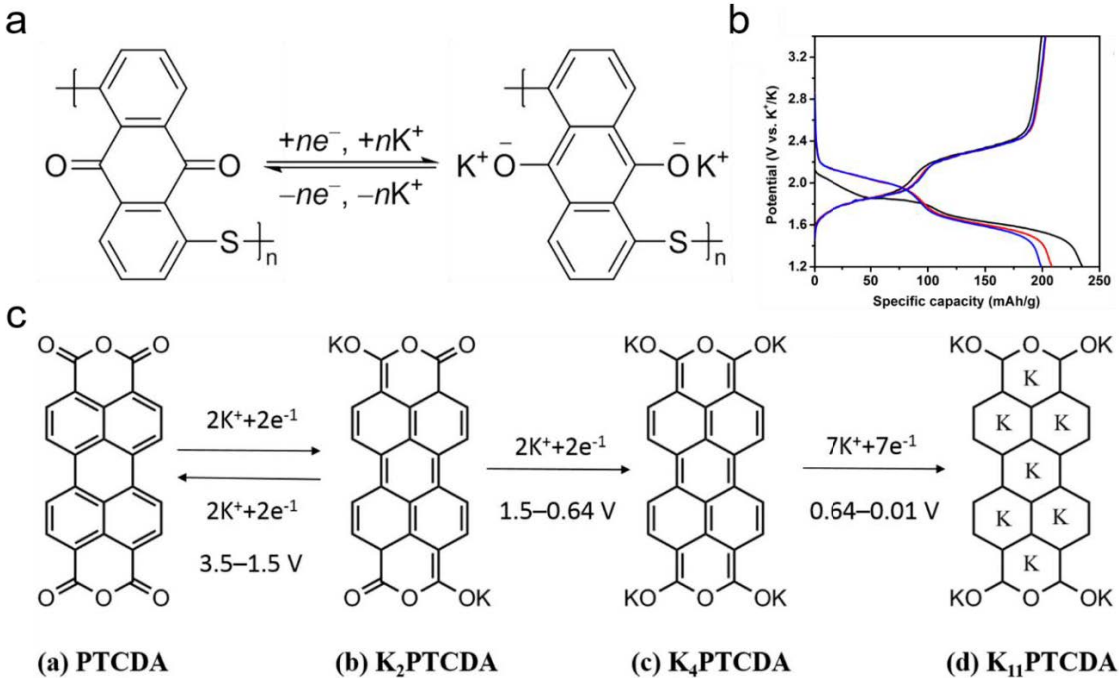

Figure 1.24 (a) Illustration of potassium storage mechanism in poly(anthraquinonyl sulfide) (PAQS). (b) Charge and discharge profiles of PAQS for initial three cycles.[224] (c) Illustration of potassium storage mechanism in perylene-3,4,9,10-tetracarboxylic dianhydride (PTCDA).[219]

1.7.2 Anode materials for potassium-ion batteries

1.7.2.1 Carbon anode materials

Carbon materials are one of the most promising anodes for PIBs owing to their low cost and superior long-term cycling stability.[251-253] For example, graphite, which is the most successful anode materials in commercial LIBs, shows a discharge specific capacity of 279 mAh g^{-1} through reversibly forming "stage X (1-3)" potassium graphite intercalation compounds (GICs, **Figure 1.24**).[254-256] The graphite anode material has a large interlayer distance of 3.35 Å, small surface area (20 m^2 g^{-1}) and large crystalline domains. Hence, they are expected to achieve high

ICE and good structural stability. However, the intercalation and deintercalation of K^+ within graphite anodes would inevitably cause drastic volume expansion about 61% and lead to structural collapse. Moreover, the sluggish diffusion kinetics is responsible for unsatisfactory rate capability of graphite materials in the potassium half-cell. Hard carbons with small domains of sp^2 carbon layers and a large interlayer distance (~3.6 Å) have also been investigated as anodes for PIBs.[206, 253, 257] Most of hard carbon materials possess a wide range of micro/macropores with abundant defects and active sites, which promotes the efficient surface-controlled capacitive process to achieve rapid potassium storage but relatively low ICE.[258-259] For example, Chen et al.[260] prepared porous hard carbon microspheres and studied their electrochemical performances. The microspheres deliver a reversible potassiation capacity of 230 mAh g^{-1} at 50 mA g^{-1} and a high potassiation capacity of 158 mAh g^{-1} at 1 A g^{-1}. In addition, owing to highly structural flexibility and large lattice spacing, soft carbons also demonstrate attractive electrochemical properties when using as anode materials for PIBs. Increasing the crystallization degree contributes to more discharge capacity below 1 V, which is a critical factor to ensure high energy density and avoids the risk of potassium metal dendrites compared to the low potassiation voltage of graphite anodes (~0.1 V). Liu and co-workers also confirmed the feasibility of soft carbons as high-performance anode materials in the potassium half-cell, but the cycling stability of soft carbons is still needed to be improved.[261]

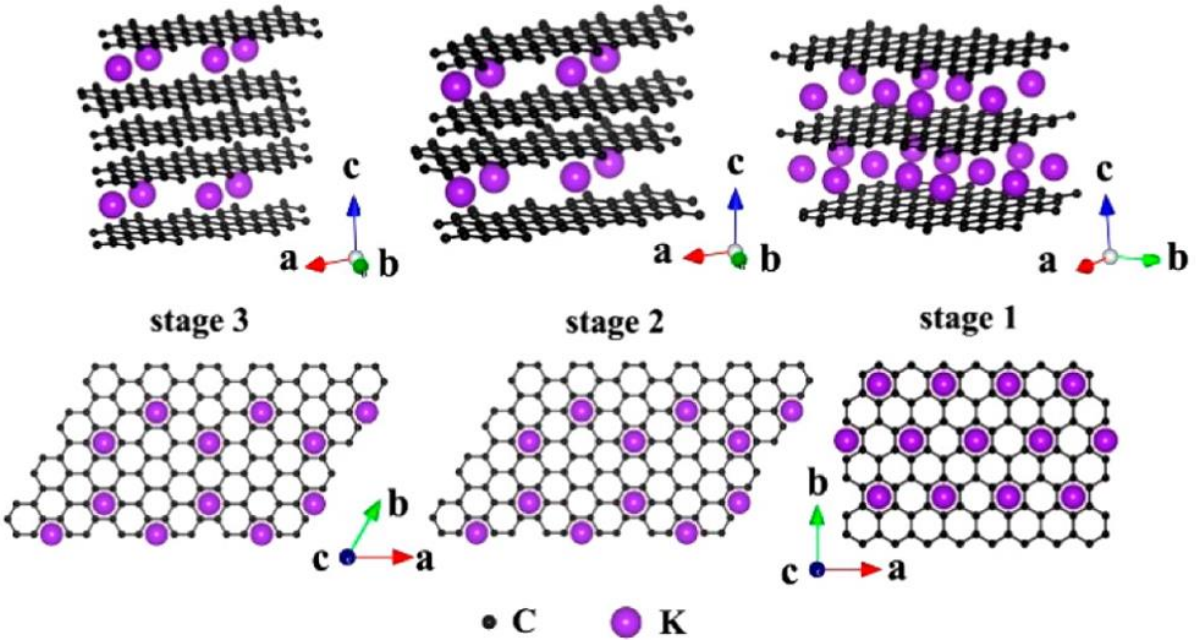

Figure 1.25 Structure diagrams of different potassium graphite intercalation compounds (stage 3-1).[255]

1.7.2.2 Transition metal oxides/sulfides/selenides

Transition metal chalcogenides (TMCs) are most commonly reported anode materials in lithium/sodium/potassium-ion batteries.[207, 262-264] This class of materials can reversibly participate in conversion reactions ($TM_aC_b + (b \cdot n)K \leftrightarrow aTM + bK_nC$). Sultana et al.[265] firstly introduced a mixed transition metal oxide of Co_3O_4–Fe_2O_3-C and studied its electrochemical performances in the potassium half-cell. The Co_3O_4–Fe_2O_3-C anode demonstrates a high initial discharge capacity about 400 mAh g^{-1} but gradually fades to ~220 mAh after 50 cycles, indicating the dramatic and irreversible structure change during charge and discharge. Liu et al.[266] reported the phase transition of Sb_2S_3 for PIBs during charge and

discharge. As shown in **Figure 1.25**, *in situ* synchrotron XRD points out that the Sb_2S_3 anode experiences conversion reactions from $K_xSb_2S_3$ to K_3Sb and K_2S_3, which results in a discharge capacity about 500 mAh g^{-1} and excellent capacity retention of 76% at a high current density (500 mA g^{-1}). Ge et al.[262] synthesized the carbon coated $MoSe_2$ as an anode material for PIBs. It follows the similar steps as Sb_2S_3 ($K_xMoSe_2 \rightarrow K_5Sb_3 + Mo$) and thereby demonstrates a high potassiation capacity of 260 mAh g^{-1} after 300 cycles. These complicated intermediate reactions that occur in TMCs contribute to the high specific capacity while cause the loss of active materials during cycling.

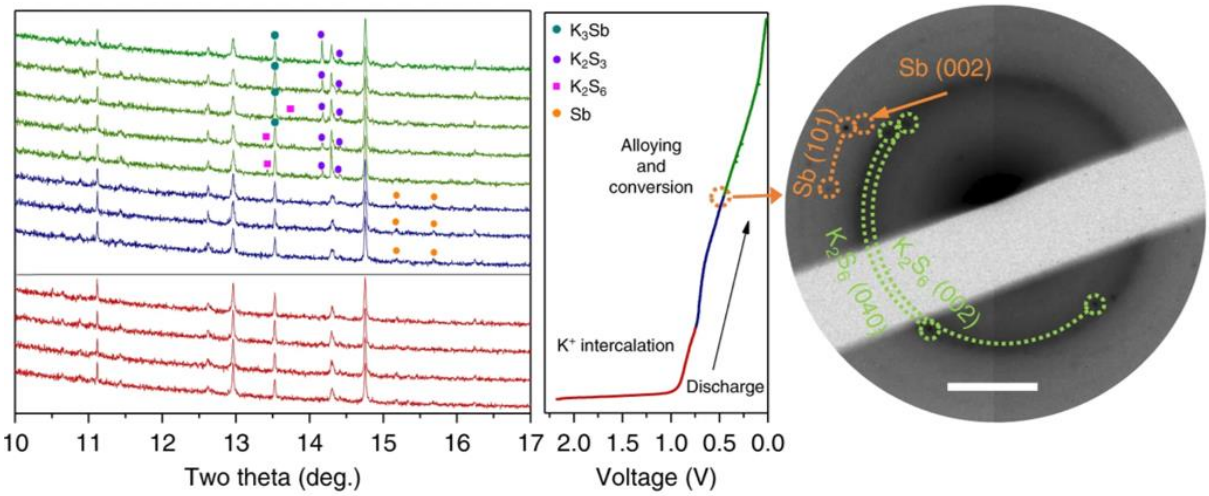

Figure 1.26 *In situ* synchrotron XRD results and *ex situ* SAED patterns of Sb_2S_3 at different charge and discharge states.[266]

1.7.2.3 Alloying anode materials

Alloying materials show the extremely high theoretical specific capacity and low redox potential as anodes in LIBs, SIBs and PIBs (**Figure 1.26**a).[202, 207] However, the quest for ideal

anode materials has always been a game of compromise. This type of anode materials suffers from serious volume change and poor electronic conductivity during the charge and discharge process. Thus, the reversible K^+ intercalation/deintercalation into/from anodes leads to large diffusion barrier and deteriorated cycling stability.[267] For example, metallic antimony (Sb) has a high theoretical capacity of 660 mAh g^{-1} with three-electron alloy compounds of K_3Sb (Figure 1.26b). However, the huge volume expansion caused by potassium alloying reactions has become a tough question for Sb anodes in PIBs.[268] Bismuth (Bi) is another potential anode material owing to the high electrochemical stability of K_3Bi and displays a reversible capacity of 400 mAh g^{-1} with a low voltage plateau. Through forming binary alloying materials with Sb, the optimal Bi-Sb alloying buffers the volume change to a large extent and exhibits outstanding potassium storage capability and long cycle life.[269-270] Phosphorus (P), such as red P and black P, is one of the most promising alloying anode materials because of its ultrahigh theoretical discharge capacity of 2500 mAh g^{-1} among the current available alloying anode materials for PIBs.[271] Unfortunately, like most alloying anode materials, the dramatic volume expansion and sluggish reaction kinetics of phosphorus pose a threat to its further applications.[272]

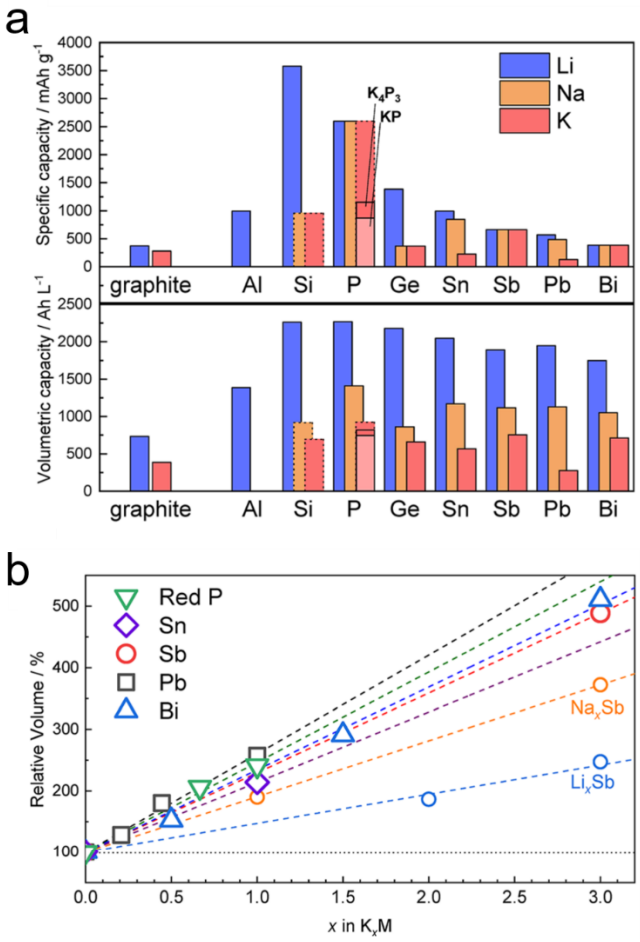

Figure 1.27 (a) Theoretical specific and volumetric capacities of various anode materials for LIBs, SIBs and PIBs. (b) Volume expansion upon alloying reactions with different alkaline metals (Li, Na and K) as a function of x.[206]

CHAPTER 2 EXPERIMENT AND METHODOLOGY

2.1 Overview

The preparation methods, material characterization and electrochemical measurements are systematically summarized in **Figure 2.1**. Four parts, including the synthetic strategy, material characterization, electrochemical tests and data analysis, construct the basic framework in each experimental section of this thesis. Some in-depth investigations associated with theoretical calculation are also employed to fully understand the reaction mechanism behind experimental findings.

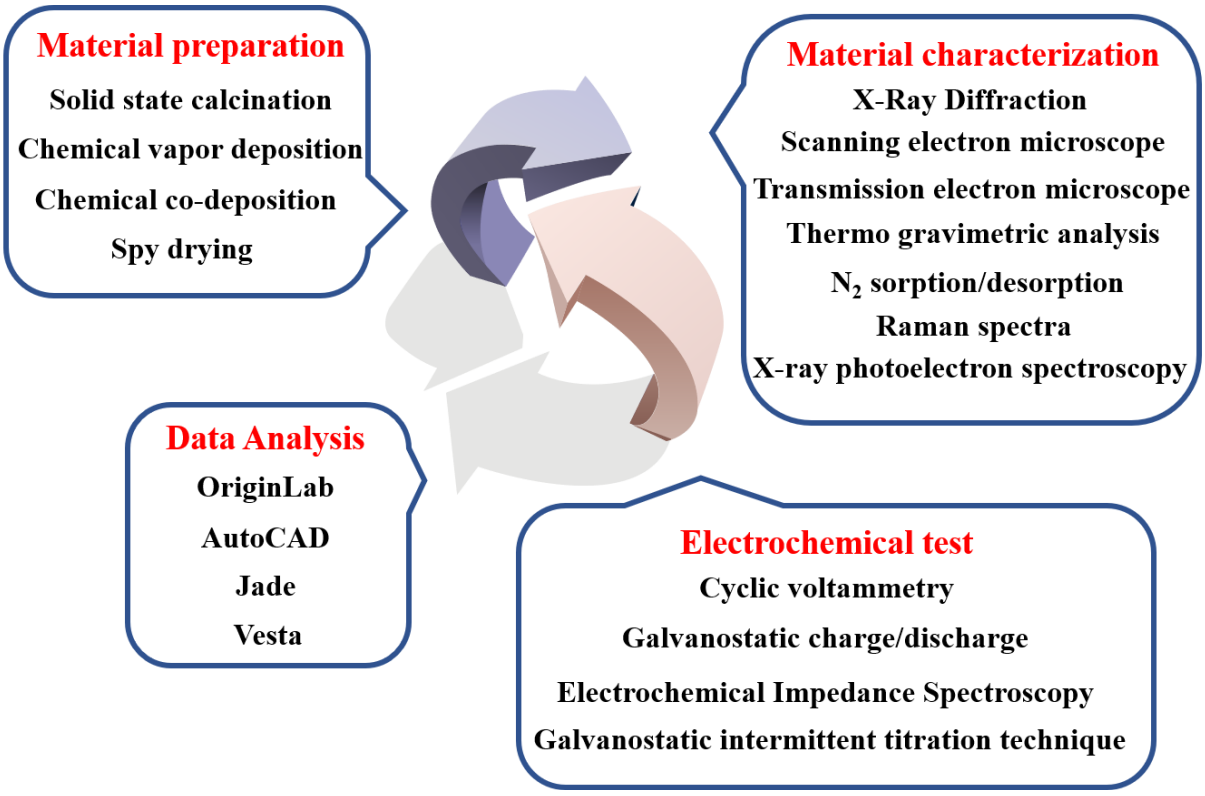

Figure 2.1 The framework of the experiment and methodology.

2.2 Chemical reagents

Chemical	Formula	Purity	Supplier
Carbon black	C	99%	SCI Materials Hub
Ethanol	C_2H_5OH	99.8%	Sigma-Aldrich
Poly(vinylidene fluoride) (PVDF)	$(CH_2CF_2)_n$	-	Sigma-Aldrich
Nickel sulfate hexahydrate	$NiSO_4•6H_2O$	99%	Sigma-Aldrich
Manganese sulfate monohydrate	$MnSO_4•H_2O$	99%	Sigma-Aldrich
Sodium bicarbonate	$NaHCO_3$	99%	Sigma-Aldrich
lithium carbonate	Li_2CO_3	99%	Sigma-Aldrich
Lithium hexafluorophosphate	$LiPF_6$	98%	Sigma-Aldrich
Aluminum nitrate	$Al(NO_3)_3$	99%	Sigma-Aldrich
Ammonium fluoride	NH_4F	99%	Sigma-Aldrich
lithium nitrate	$LiNO_3$	99%	Sigma-Aldrich
Ethylene carbonate	$(CH_2O)_2CO$	98%	Sigma-Aldrich
Diethyl carbonate	$OC(OCH_2CH_3)_2$	98%	Sigma-Aldrich
Potassium hexafluorophosphate	KPF_6	98%	Sigma-Aldrich
Potassium bis(fluorosulfonyl)imide	KFSI	98%	DoDoChem
Anatase titanium dioxide	TiO_2	99%	Sigma-Aldrich

Potassium carbonate	K_2CO_3	99%	Sigma-Aldrich
Glucose	$C_6H_{12}O_6$	99%	Sigma-Aldrich
Hypophosphite monohydrate	$NaH_2PO_2•H_2O$	99%	Sigma-Aldrich
Hydrochloric Acid	HCl	36%	Sigma-Aldrich
Activated carbon	C	99%	Sigma-Aldrich
Copper foil	Cu	99%	MTI Kejing Co.
Lithium metal	Li	99.9%	Hohsen Co.
Potassium metal	K	99.9%	Sigma-Aldrich

2.3 Preparation methods

2.3.1 Solid state calcination

The high temperature solid state calcination reaction is a representative strategy to synthesize electrode materials, which simply mixes various raw materials in solid state and followed by calcination under different atmosphere (air or inert condition). The as-obtained materials show high crystallinity and extremely low water content. For the practical implementation of this process, some parameters, for example, the ratio of reactants, humidity, heating rate and time, paly crucial roles in determining the physicochemical property of as-prepared materials. In this thesis, cathode materials ($Li_{1.2}Ni_{0.2}Mn_{0.6}O_2$ and $K_{1.39}Mn_3O_6$) were synthesized through the solid-state calcination method.

2.3.2 Chemical co-deposition

The chemical co-deposition reaction provides opportunities to synthesize various materials in the liquid condition. Owing to the rapid diffusion rate of TM ions in solvents, such a liquid phase reaction is beneficial to prepare high-quality materials with the wide range of chemical compositions. Therefore, the chemical co-deposition method is suitable for designing electrode materials with good quality uniformity and high efficiency. In this thesis, the chemical co-deposition method was employed to synthesize precursors such as $Ni_{0.25}Mn_{0.75}CO_3$ and $MnCO_3$ for lithium-ion and potassium-ion batteries.

2.3.3 Chemical vapor deposition

Chemical vapor deposition (CVD) is a unique vacuum deposition method to fabricate high quality materials, especially to produce thin films on substrate surfaces. In a typical CVD experiment, volatile precursors would react or decompose on the substrate surface to endow the uniform and desired deposit. In this thesis, a very thin and uniform carbon layer was grown on the surface of electrode materials through CVD treatment.

2.3.4 Spray drying

Spray drying is a traditional way to produce solid powders from a slurry via rapidly drying with the hot air or N_2 (if the product is oxygen-sensitive) gas. Electrode materials with a consistent particle size distribution is a reason for spray drying in some industrial activities. Spray dryers often employ a spray nozzle to disperse the slurry into a controlled drop size spray. According to the requirement of the fabrication process, secondary particles range from 10 to 500 μm can be obtained through the appropriate choice. With the help of hot gas drying medium, the fine powders are generated from the first stage drying and then recycle in continuous flow at the bottom of the chamber. In this thesis, $K_2Ti_2O_5$ microspheres were synthesized through a spray drying process.

2.4 Material characterization

2.4.1 Scanning electron microscopy

Scanning electron microscopy (SEM) reveals the microstructure and morphology of samples via scanning the surface with the electron beam. The electron beam firstly interacts with the material, generating various signals including secondary electrons, backscattered and reflected electrons. Hence, the morphology can be obtained by collecting these signals to produce images. In this thesis, a Zeiss Supra 55VP field emission scanning electron microscopy (FESEM) coupled with Oxford energy dispersive spectroscopy (EDX) was chosen to study the microstructure information of samples. The aperture is 10-30 mm associated with the accelerating voltage range from 5 to 20 kV.

2.4.2 Transmission electron microscope

Transmission electron microscopy (TEM) is an advanced technique in which an electron beam is transmitted through a specimen to form images. In comparison to SEM, TEM can produce high resolution images (even at atomic scale) that contain morphology information owing to smaller de Broglie wavelength of electrons. Furthermore, TEM measurements consist of many operating modes such as conventional imaging, cryogenic TEM imaging (Cryo-TEM), scanning TEM imaging (STEM) and high-angle annular dark-field scanning transmission electron microscope (HAADF-STEM) imaging. Furthermore, selected area electron diffraction (SAED) device auxiliary equipment is used to analyze the crystal structure of samples. In this

thesis, a transmission electron microscopy (field emission CM200, Fei) equipped with an energy-dispersive X-ray spectrometer was employed.

2.4.3 X-ray diffraction

X-ray powder diffraction (XRD) is a widely used technique to primarily identify crystallographic information of unknown materials based upon unit cell dimensions. In addition, X-rays are particularly used to obtain the diffraction pattern because their interplanar spacing d is nearly the same order of magnitude as wavelength λ in the crystal. The crystal structure of samples can be further determined by Bragg's law:

$$n\lambda=2d\sin\theta$$

wherein λ is the wavelength of the X-rays beam, d represents the spacing between planes. θ stands for the incident angle, and n is any integer. In this thesis, XRD measurements were carried out using a Bruker D8 Discover X-ray diffractometer with Cu Kα radiation (λ = 1.5418 Å). As for the *in situ* XRD test, a Swagelok cell associated with a Be window (positive part) was used for real-time analysis.

2.4.4 Raman spectroscopy

Raman Spectroscopy is a non-destructive chemical spectroscopic analysis technique which provides useful information about phase, molecular interactions and chemical structures. Such a chemical analysis is based on the inelastic scattering of photons, which are also known as Raman scattering. A source of the high intensity laser light (from the visible to near the ultraviolet range is used) is used. The laser light interacts with phonons, molecular vibrations

or other excitations in the system, leading to the energy of the laser photons being moved up or down. The change in energy provides information about the vibrational modes in the system. In this thesis, Raman spectra was performed on a Renishaw inVia Raman spectrometer system (Gloucestershire, UK) in conjunction with a 17 mW Renishaw He-Ne laser source at 633 nm. In addition, the transparent cell used for *in situ* Raman was fabricated via a glass slide based two-electrode configuration.

2.4.5 Thermogravimetric analysis

Thermogravimetric analysis (TGA) is often used for thermal analysis in which the total mass variation of a sample is calculated over time as the temperature goes up. This method gives valuable information about thermal decomposition, phase transitions and solid-gas reactions. The temperature is normally increased at a fixed rate to induce a thermal reaction. This thermal reaction may occur under vacuum, ambient air or inert gas (N_2). In this thesis, the carbon content of $K_2Ti_2O_5$@C microspheres was determined by a thermogravimetric analyzer (2960 SDT system) with a heating rate of 10 °C min^{-1} in air atmosphere.

2.4.6 X-ray photoelectron spectroscopy

X-ray photoelectron spectroscopy (XPS), which belongs to the family of photoemission spectroscopies, is the most widely used surface-sensitive quantitative technique which provides quantitative information of the chemical state and composition from the surface of materials. The average depth for an XPS analysis is approximately 5 nm in terms of the surface condition. It not only reveals what elements are present in materials, but also what other elements they are

bonded to. Therefore, XPS measurements show quantification of different elements within the local environment. In this thesis, X-ray photoelectron spectroscopy (XPS) was conducted on an ESCALAB250Xi (Thermo Scientific, UK) associated with mono-chromated Al K alpha (energy: 1486.68 eV).

2.4.7 N_2 adsorption/desorption

N_2 adsorption/desorption (Brunauer-Emmett-Teller, BET) reflects physical characteristics such as specific surface area, pore volume and pore size distribution. On the basis of nitrogen adsorption/desorption isotherms at 77 K, data from the low-pressure part to high-pressure range is collected. Due to the adsorbed nitrogen gas is a function of the relative pressure P/P_0, pores including micropores, mesopores and macropores can be easily identified from adsorption/desorption isotherms. In this thesis, The Brunauer-Emmett-Teller surface area analysis was performed based on a Micromeritics 3Flex analyzer.

2.5 Electrochemical measurements

2.5.1 Electrode preparation

The electrodes were prepared by mixing active materials, carbon black and polyvinylidene difluoride (PVDF) with a weight ratio of 8:1:1 in N-Methyl-2-pyrrolidone (NMP). Subsequently, the formed slurry was directly coated onto current collectors (Al foils for cathodes and Cu foils for anodes.) and dried at 100 °C under vacuum overnight. 2032-type coin cells (CR2032) were assembled in an Ar-filled glove box. For lithium-ion batteries, lithium

metal foils were used as both counter and reference electrodes. Celgard 2400^{TM} membranes were used as separators. The electrolyte was 1M $LiPF_6$ dissolved in a mixture of diethyl carbonate (DEC), ethylene carbonate (EC) and dimethyl carbonate (DMC, 1:1:1 in volume). As for potassium-ion batteries, potassium metal foils were used as both counter and reference electrodes. Glass microfiber filters (Whatman, Grade GF/D) were used as separators. Meanwhile, 0.8 M potassium hexafluorophosphate (KPF_6) and 1 M potassium bis(fluoroslufonyl)imide (KFSI) in EC and DEC with a volume ratio of 1:1 were electrolytes.

2.5.2 Cyclic voltammetry

Cyclic voltammetry (CV) is a potentiodynamic electrochemical technique which records the applied current within the pre-set potential window. A typical CV measurement is carried out in an electrochemical cell fitted with three electrodes: working electrode, counter electrode and reference electrode. The working electrode's potential firstly starts from an open-circuit voltage (OCV) and then is ramped linearly versus time. After the set potential is reached, the potential runs the opposite direction to go back to its initial sate. This process may repeat as multiple cycles as needed. In this thesis, cyclic voltammetry was used to investigate the electrochemical behavior of electrode materials under different conditions (electrolytes and scan rates).

2.5.3 Galvanostatic charge/discharge

Galvanostatic charge/discharge (GCD) is a typical technique which measures the voltage change versus time within a fixed potential window. A constant charge/discharge current is applied on the working electrode. When charging, an external electrical power enables alkaline

metal ions (Li^+ or K^+) to migrate from the cathode to the anode, which is known as intercalation or conversion. During discharge, alkaline metal ions (Li^+ or K^+) carry the constant current from the anode to the cathode through the separator and electrolyte. In this thesis, galvanostatic charge/discharge measurements were performed on a computer-controlled Neware battery testing system to study electrochemical properties such as rate capability and cycle life of electrode materials.

2.5.4 Electrochemical impedance spectroscopy

Electrochemical impedance spectroscopy (EIS) is a highly sensitive technique to record the electrochemical impedance of a battery system in reliance on AC potential frequencies. The potentiostat in the impedance spectra can be adjusted over a wide frequency range from 0.001 Hz to 100,000 Hz. A typical Nyquist plot of a rechargeable battery mainly consists of three parts: (1) an ohmic resistance R_Ω (the intercept on the real axis) at the high frequency. (2) Charge transfer resistance Rct (the diameter of the semi-circle) in the middle range. (3) Diffusion related WARBURG impedance (the slope of the straight line) at the low frequency. In this thesis, Electrochemical impedance spectroscopy measurements were characterized to discuss the interfacial reaction and the kinetic process of electrodes.

2.5.5 Galvanostatic intermittent titration technique

Galvanostatic intermittent titration technique (GITT) is an electrochemical process to study both thermodynamics and kinetics parameters of a battery system. Galvanostatic intermittent titration technique adopts time-domain voltage data resulting from a low pulse current with a

long-lasting rest period. Taking the positive current pulse as an example, the cell potential rapidly rises to a value proportional to the IR drop. Subsequently, due to the galvanostatic charge pulse, the potential gradually increases in order to remain a constant concentration gradient. When the charge current is interrupted upon the relaxation period, the electrode is more likely to become homogeneous diffusion and, therefore, the potential slowly declines until the electrode is in an equilibrium stage. Afterwards, the pulse current is applied again, followed by the same current interruption process until the cell is fully charged. In this thesis, galvanostatic intermittent titration technique was used to investigate reaction kinetics and the interfacial resistance of electrode materials.

2.6 Density functional theory calculation

Density functional theory (DFT) calculation is a very popular and versatile computational calculation method in solid-state physics, materials science and chemistry to study the electronic structure of different material systems through specific atoms and molecules. With the help of this theory, many physicochemical properties can be accurately predicted by using functional models. In the case of DFT, these are functionals of the spatially dependent electron density. In this thesis, density functional theory (DFT) calculation was employed to investigate the adsorption energy and the diffusion barrier of K^+ in different theoretical models. All calculations were performed using Perdew-Burke-Ernzerhof (PBE) generalized gradient exchange approximation correlational functional and the projected augmented wave (PAW) pseudopotentials as implemented Vienna ab initio Package (VASP).

CHAPTER 3 AEGIS OF LITHIUM-RICH CATHODE MATERIALS VIA HETEROSTRUCTURED $LiAlF_4$ COATING FOR HIGH-PERFORMANCE LITHIUM-ION BATTERIES

3.1 Introduction

The ubiquitous use of fossil fuels has caused serious environmental and economic issues such as global warming and energy crisis.[273-274] In order to widely adopt renewable energy resources, lithium-ion batteries (LIBs) have been intensively developed as the most promising and reliable candidates for renewable energy storage devices.[195, 275-276] Driven by the stringent requirement for high energy density energy storage devices for electric vehicles, significant progresses have been achieved for high performance LIBs in the past few decades. However, there are still many shortcomings when compared with other types of high energy density power sources such as commercial fuel cells.[277-279] In particular, the specific capacities of LIBs are mainly restricted by their cathode materials. For instance, the specific capacities of well-developed commercial cathode materials vary from 140 mAh g^{-1} (layered $LiCoO_2$[280]) to 190 mAh g^{-1} ($LiNi_{0.8}Co_{0.1}Mn_{0.1}O_2$[281]), which lags far behind their anode counterparts (~330 mAh g^{-1} for graphite).[282-283] Recently, layered lithium-rich oxides (e.g. $xLi_2MnO_3 \cdot (1-x)\ LiMO_2$, M=Transition metal) have been regarded as one of the most promising cathode materials for next generation high-energy density LIBs due to their super high theoretical specific capacity of over 350 mAh g^{-1} and relatively high discharge voltage.[284-285] However, the rate capability and cycling stability of lithium-rich cathode materials are poor due to their low electronic

conductivity and the irreversible phase transformation from layered structure to spinel structure induced by the migration of transition metal (TM) ions during charge and discharge process.[286] Meanwhile, the reaction kinetics of lithium-rich materials is not only limited by traditional cationic redox reaction mechanisms, but also by anodic redox processes.[287] Although the reversible anodic oxygen redox reaction boosts output capacity, it simultaneously promotes more metal ions to reside in the Li^+ insertion sites which has been observed to lead to unavoidable voltage decay.[288-289] Moreover, the high operating voltage is more likely to generate byproducts such as HF at the surfaces of cathode materials, which raises safety concerns.[290] Therefore, how to overcome these drawbacks without hindering the existing merits of lithium-rich cathode materials remains a big challenge.

Considering surface side reactions and poor Li^+ diffusion kinetics, surface modification has been demonstrated to be an effective and convenient approach to remarkably enhance the electrochemical performance of lithium-rich cathode materials.[291] Many coating materials, including Al_2O_3,[292] AlF_3,[293] $AlPO_4$,[294] Li_3PO_4,[295] $LiFePO_4$[296] and $Li_4M_5O_{12}$[297-298] have been incorporated into lithium-rich bulk materials without hampering their inherent advantages. Among them, AlF_3 shows potential to suppress the decomposition of electrolytes at high voltage to stabilize the electrode/electrolyte interfaces, which could significantly extend the cycle life of LIBs. However, it still suffers from poor Li^+ conductivity, which restricts the high-rate performance of LIBs. Recently, Xie et al. firstly reported the use of a unique $LiAlF_4$ thin film fabricated by atomic layer deposition (ALD) as a protective layer on commercial $LiNi_{0.8}Mn_{0.1}Co_{0.1}O_2$ cathode materials.[299] The thermodynamically stable and high lithium-ion

conductive $LiAlF_4$ coating layer significantly improved the electrochemical performance of $LiNi_{0.8}Mn_{0.1}Co_{0.1}O_2$ cathode materials. Nerveless, it remains a tough challenge to apply this concept on large scale to state-of-the-art lithium-rich cathode materials.

In this paper, we describe our successful fabrication of a lithium-ion conductive $LiAlF_4$ nano-layer coated onto $Li_{1.2}Ni_{0.2}Mn_{0.6}O_2$ (LNMO) via an intricate yet facile co-precipitation method followed by post-calcination treatment. In the first step, the preparation of pristine LNMO samples was optimized. Thereafter, both AlF_3 and $LiAlF_4$ coated LNMO cathode materials show significantly increased discharge specific capacities as well as rate capabilities. Furthermore, as a lithium-ion conductor, $LiAlF_4$ proved to be most beneficial to facilitate Li^+ transport and achieved faster redox kinetics compared with AlF_3. Our findings suggest that surface modification strategy is an essential way to improve the electrochemical performances of lithium-rich cathode materials in general.

3.2 Experimental section

3.2.1 Synthesis of $Li_{1.2}Ni_{0.2}Mn_{0.6}O_2$ (LNMO) microspheres

Experimental details for the synthesis of LNMO microspheres are as follows: 3.942 g of nickel sulfate hexahydrate ($NiSO_4{\cdot}6H_2O$) and 7.605 g of manganese sulfate monohydrate ($MnSO_4{\cdot}H_2O$) were dissolved in 300 mL deionized water and stirred for 30 min. Subsequently, 25.203 g sodium bicarbonate (NH_4HCO_3) was added into the mixed aqueous solution and stirred for another 30 min. Then, the obtained precipitation was washed with deionized water

and ethanol several times and dried at room temperature overnight. Finally, the powder was mixed with 0.28 g lithium carbonate (Li_2CO_3, 3% excess of lithium) followed by calcination at different temperature for 10 h to obtain the final products.

3.2.2. Synthesis of AlF_3 and $LiAlF_4$-Coated $Li_{1.2}Ni_{0.2}Mn_{0.6}O_2$ (LNMO) microspheres

To prepare the $LiAlF_4$ coated LNMO microspheres, a certain amount of aluminum nitrate ($Al(NO_3)_3$), ammonium fluoride (NH_4F) and lithium nitrate ($LiNO_3$) were dissolved in 20 ml of deionized water with a stoichiometric molar ratio of Li : Al : F to be 1:1:4 ($LiNO_3+4NH_4F+Al(NO_3)_3 \rightarrow LiAlF_4+4NH_4NO_3$). Then, 8.4 g LNMO were added in the solution under continues stirring at 80 ^oC for 6 h. After that, the mixture was dried at 70 ^oC in a vacuum oven overnight. Subsequently, the obtained powder was calcined at 400 ^oC for 6 h under Ar atmosphere to get $LiAlF_4$-coated LNMO (LNMO@$LiAlF_4$) with 1 wt % $LiAlF_4$. For comparison, AlF_3-coated LNMO (LNMO@AlF_3) was also synthesized under the same condition without lithium nitrate.

3.2.3. Materials characterization

The crystallographic structure of the as-synthesized materials was identified via a Bruker D8 Discovery X-ray diffractometer (Cu Kα radiation, collected from 5° to 80° 2-Theta). The morphology characterization and relevant elemental distribution analysis were conducted using field-emission scanning electron microscopy (Zeiss Supra 55VP) and transmission electron microscopy (JEOL JEM-2011). X-Ray photoelectron spectroscopy (Thermo Scientific, UK)

with mono-chromated Al K alpha (energy: 1486.68 eV) was carried out to confirm the chemical composition of as-prepared samples.

3.2.4. Electrochemical measurements

All the electrodes were prepared by mixing active materials, carbon black and PVDF binder (weight ratio of 8:1:1) onto aluminum foils as cathodes and lithium metal foils as anodes, respectively. 1M $LiPF_6$ was dissolved in a mixture of diethyl carbonate (DEC), ethylene carbonate (EC) and dimethyl carbonate (DMC) (1:1:1 in volume) as electrolyte. CR2032-type coin cells were employed to assemble half-cells in an Ar-filled glove box with considerably low moisture and oxygen concentrations (≤0.1 ppm), using a Celgard 2400^{TM} membrane as the separator. The tap density of the as-synthesized pristine LNMO obtained at 1000 °C is 1.58 g cm^{-3}. The mass loading of the active material for electrode preparation is ~ 1.6 mg cm^{-2}. For the electrochemical tests, galvanostatic charge and discharge (GCD) measurements were conducted in the voltage range of 2.0 - 4.8 V on a NEWARE^{TM} battery tester. Cyclic voltammogram (CV) tests were recorded by a Biologic VMP3 electrochemical workstation at a scan rate of 0.1 mV s^{-1} in the voltage range between 2.0 V and 4.8 V. Meanwhile, electrochemical impedance spectra (EIS) was acquired in the frequency range from 100 kHz to 10 mHz.

3.3 Results and discussion

The prerequisite for high performance lithium-rich cathodes is derived from the rational design of shape-controlled precursors. As shown in **Figure 3.1**, highly regular and homogeneous manganese-nickel carbonate microspheres (the cation ratio is Ni:Mn=1:3) are initially prepared by a facile precipitation method. Subsequently, the as-synthesized carbonate precursors are mixed with Li_2CO_3 followed by a calcination process to produce LNMOs at different temperature. Surface modification process of AlF_3 or $LiAlF_4$ coating was then conducted on LNMOs to further enhance the electrochemical performance of lithium-rich cathode materials.

The calcination temperature plays an important role in determining the electrochemical performances of lithium-rich cathode materials as noted in a previous report.[300] To identify the optimal calcination temperature for the synthesis of LNMO cathode materials, we tried a broad range of temperatures at 50 ºC intervals since we expected this would have measurable impacts on the morphology and electrochemical performances of the final products. **Figure 3.2** reveals the morphology of carbonate precursors with a diameter of 1.2~1.5 μm. Obviously, the surface of the as-prepared samples is quite smooth without obvious irregularities, and these uniform and regular carbonate samples are capable of preparing high-performance cathode materials afterwards. **Figure 3.3** illustrates the morphological evolution of LNMO materials at 800 °C, 850 °C and 900 °C denoted as LNMO-800, LNMO-850 and LNMO-900, respectively. The morphologies and diameters of LNMO microspheres remained unchanged except for the gradual aggregation and the growth of primary particles in the microspheres. With the

calcination temperatures increased to 950 °C, 1000 °C and 1050 °C (denoted as LNMO-950, LNMO-1000 and LNMO-1050, respectively), these primary particles of microspheres grown into rod-like structures, forming both open and compact flower-like microspheres (**Figure 3.4**). Although the variation of calcination temperature can obviously affect the morphologies of the as-prepared LNMO microspheres, XRD patterns were almost constant. The diffraction peaks, especially the distinct separation of (0 1 2)/(0 0 6) and (0 1 8)/(1 1 0) peaks, can be indexed to the layered α-$NaFeO_2$-type structure (**Figure 3.5**, JCPDS No. 04-020-5134).[301] Moreover, the sharp and well-defined diffractions demonstrate that these materials are highly crystalline. However, it should be noted that there are some weak peaks around $2\theta = 20\sim26^{o}$, which can be ascribed to rotation caused by cation ordering along the c-axis in the TM layer.[302]

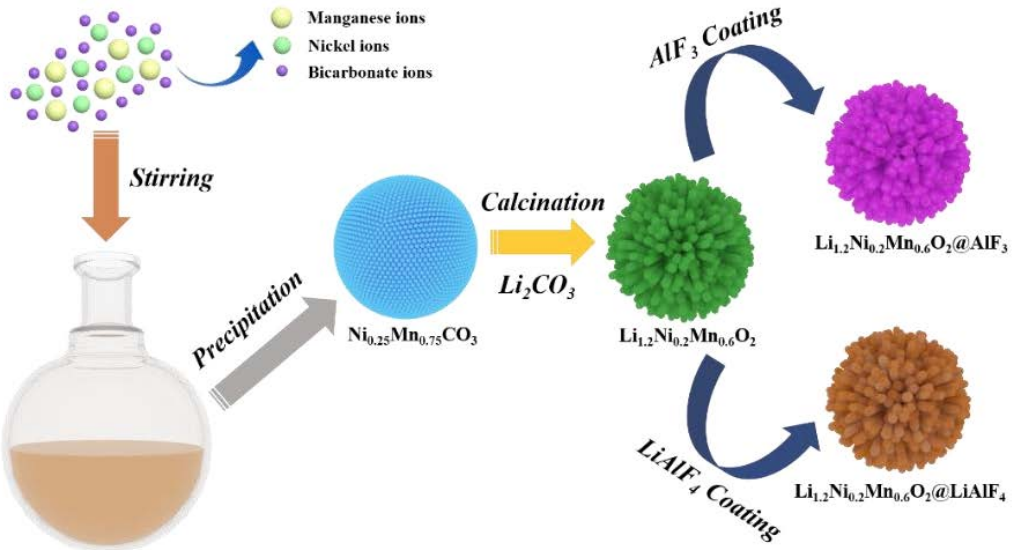

Figure 3.1 Schematic illustration of the synthesis process for pristine LNMO, LNMO@AlF_3 and LNMO@$LiAlF_4$.

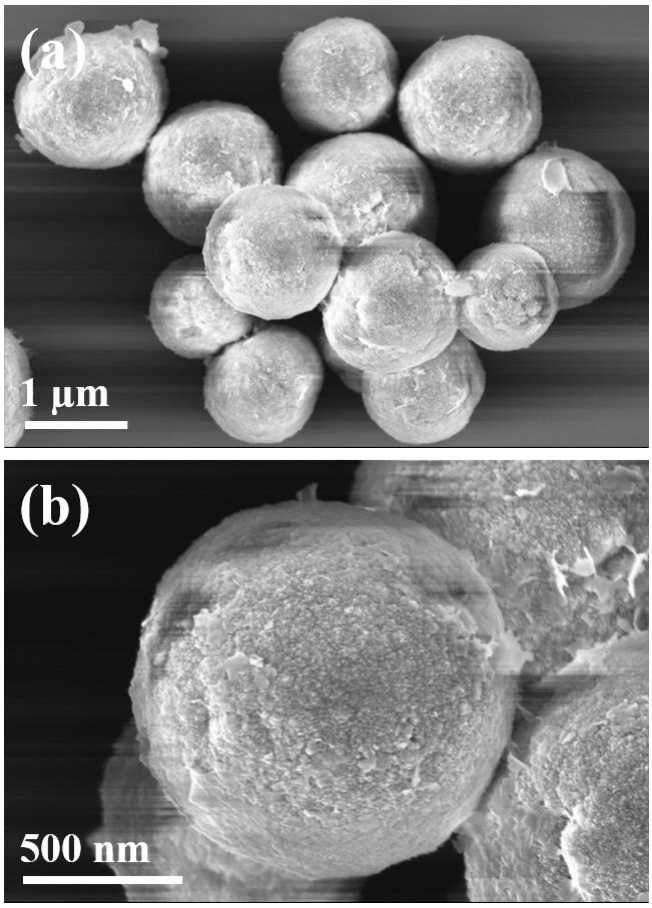

Figure 3.2 (a) Low-magnification and (b) high-magnification SEM images of nickel and manganese carbonate precursors.

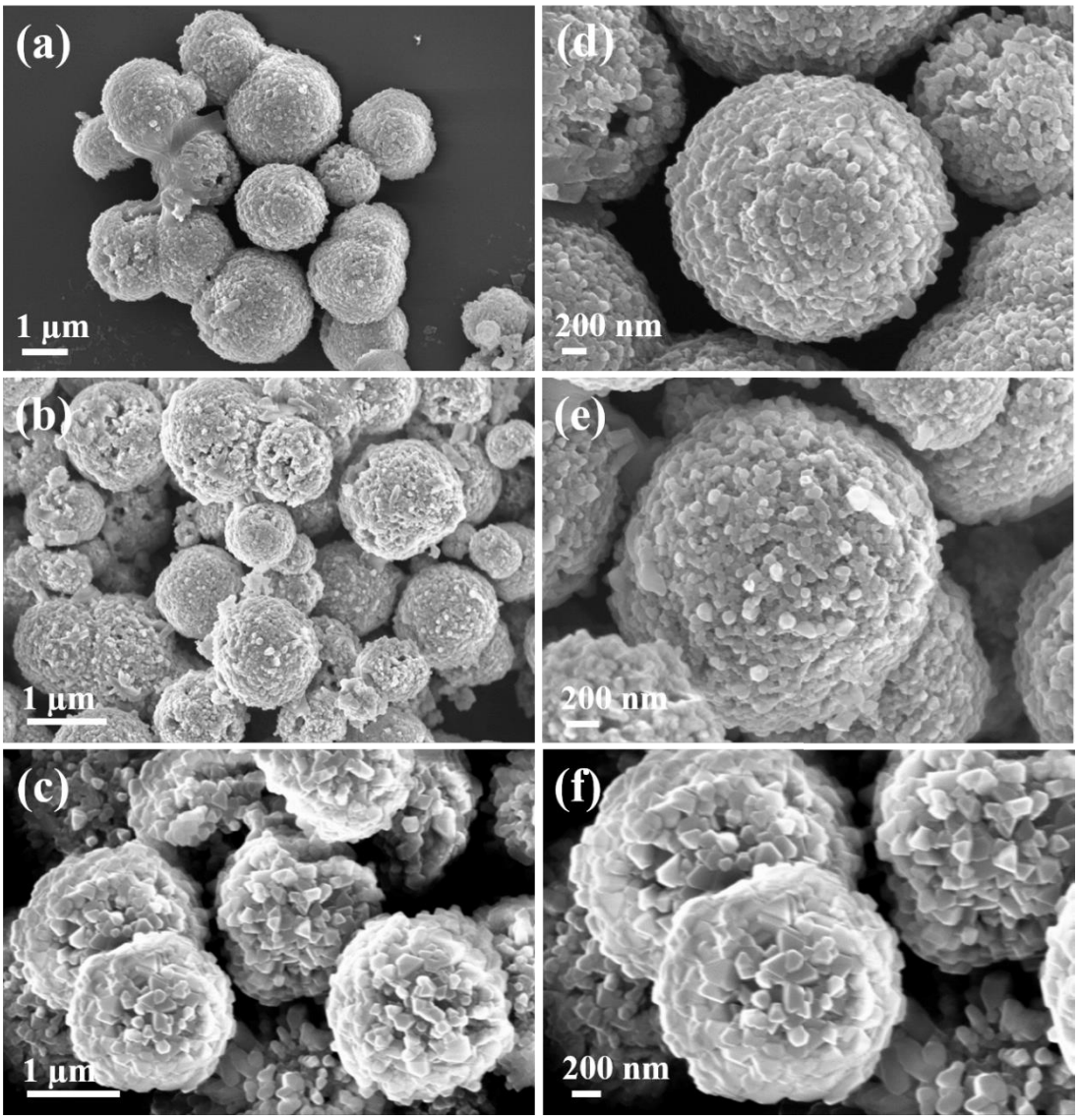

Figure 3.3 (a-c) Low-magnification and (d-f) high-magnification SEM images of LNMO obtained after calcinated at (a, d) 800 ºC, (b, e) 850 ºC and (c, f) 900 ºC.

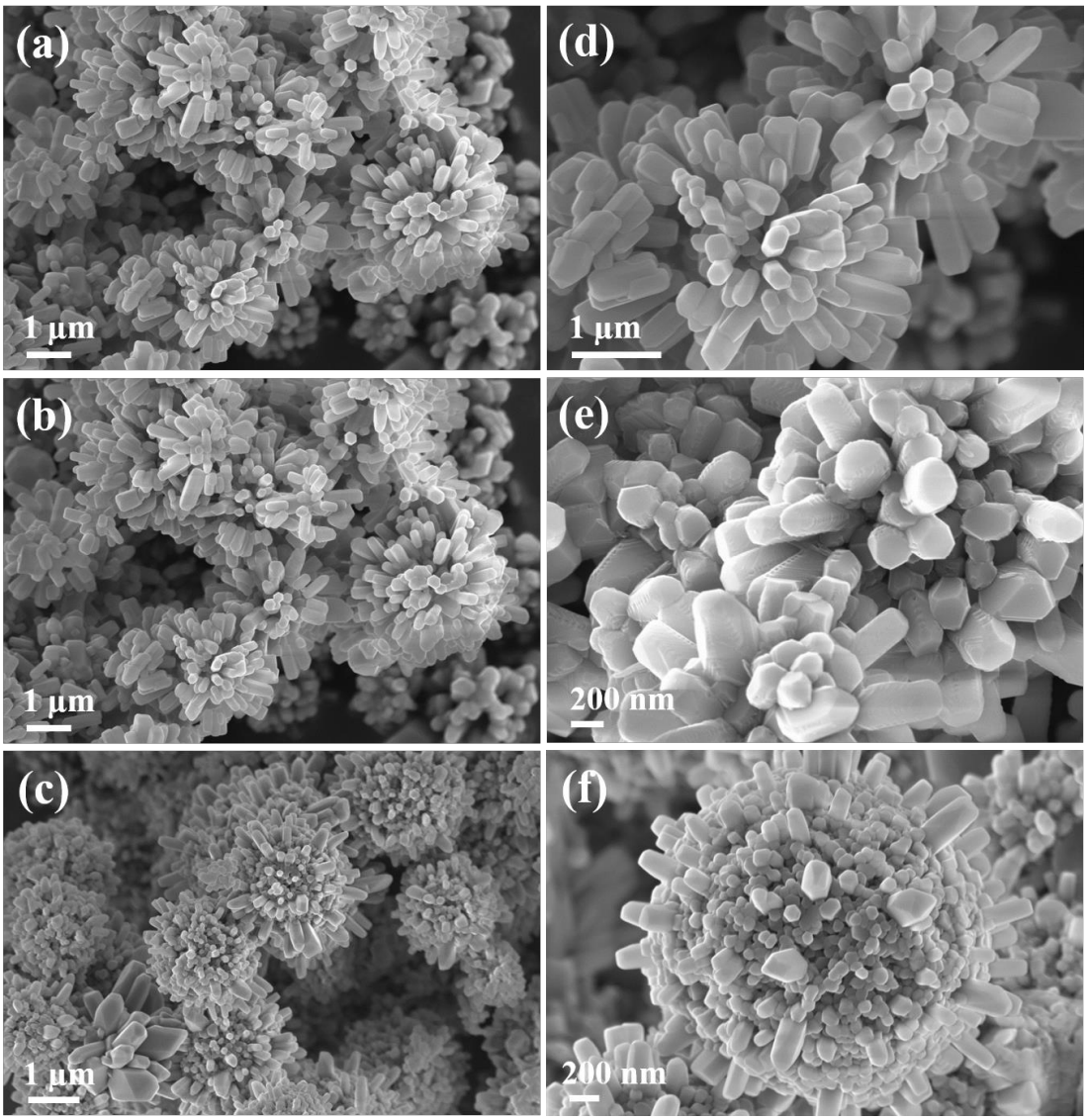

Figure 3.4 (a-c) Low-magnification and (d-f) high-magnification SEM images of LNMO obtained after calcinated at (a, d) 950 ºC, (b, e) 1000 ºC and (c, f) 1050 ºC.

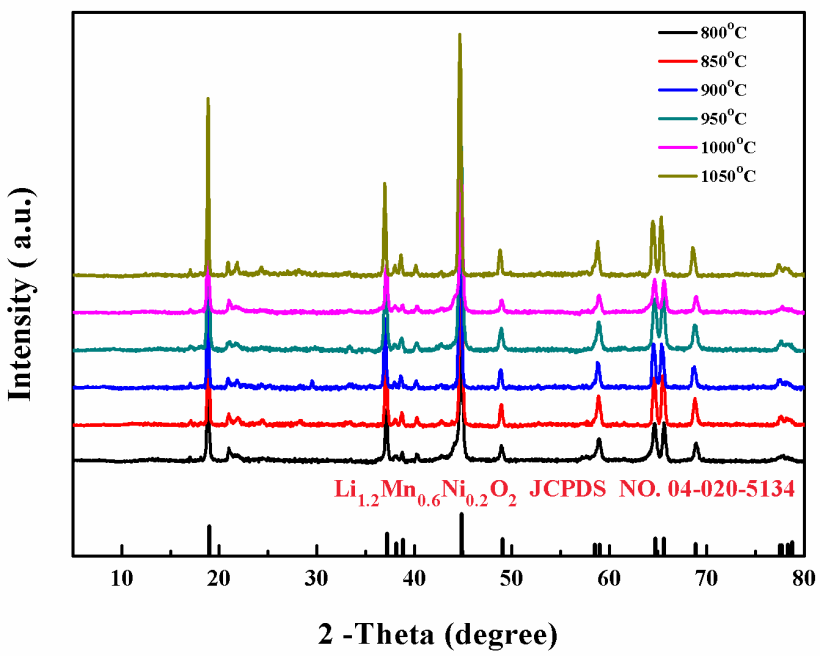

Figure 3.5 XRD patterns of LNMO obtained from different calcination temperatures.

Since the morphology of lithium-rich cathode materials can greatly influence their electrochemical performances, galvanostatic charge and discharge tests were conducted to investigate their electrochemical behaviors. **Figure 3.6**a demonstrates the capacity retention for the layered LNMO cycled with a charge/discharge rate of 0.1 C. As we can see from the picture, all samples experience temporary activation process followed by continuous capacity decay, and their electrochemical performances are improved with the calcination temperature elevation as well. The LNMO-1000 exhibits the highest specific capacity of 220 mAh g^{-1} and excellent cyclic stability after 100 cycles, corresponding to a capacity retention of 85 %. This improved electrochemical performance should be ascribed to the unique flower-like microstructure, which can increase the contact area between electrode and electrolyte and, therefore, facilitate the Li^+ diffusion. However, when the calcination temperature is further

increased to 1050 ºC, the cathode shows not only a fast capacity decay but also serious deteriorated cycling stability, which may be ascribed to the overgrowth of nano-particles on the surface of LMNO. Meanwhile, the rate performance of LNMO is concluded in Figure 3.6b. The characters of low electronic conductivity and polarization are confirmed by their poor rate retention capability. Although the LNMO-1000 shows the best retention rate and recovers substantially on returning to the original value at low rate, its rate performance retention (24% at 5 C) is still far behind practical applications. Therefore, we adopted LNMO microspheres obtained at 1000 ºC as the pristine material for further surface modification study.

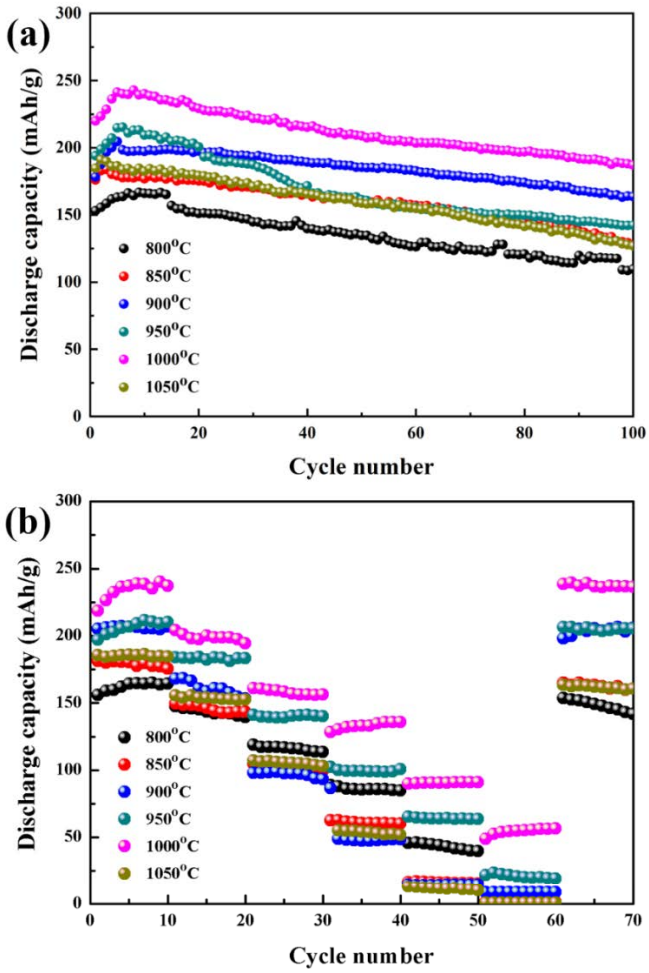

Figure 3.6 (a) Cycling performance at 0.1 C and (b) rate performance of LNMO obtained from different calcination temperatures.

To further enhance the electrochemical performances of LNMO cathode materials, a surface modification strategy was explored through AlF_3 and $LiAlF_4$ coating. **Figure 3.7**a shows the XRD diffraction patterns of pristine and surface-modified LNMO materials. No additional peaks are observed after surface modification, suggesting the AlF_3 and $LiAlF_4$ coating materials do not affect the bulk crystal structure of the pristine LNMO.[292] The SEM images of pristine LNMO samples in Figure 3.7b and e show clean and smooth surfaces. After modified by AlF_3 (Figure 3.7c and 3.7f) and $LiAlF_4$ (Figure 3.7d and 3.7g) nano-layers, the surface became much

rougher. HRTEM observation was performed to further investigate the morphology and structure in details. **Figure 3.8**a-c clearly indicates the formation of regular and stable protective layers with a thickness of about 5.2 nm on the surface of pristine materials (Figure 3.8b-c, highlighted in dotted red lines). Additionally, the lattice distance of 0.203 nm corresponds to the (1 0 4) plane of layered LNMO crystal structure. These results are consistent with the XRD and SEM findings. As a supplement, EDS mapping was employed to provide evidence of elemental distribution. It is obvious in Figure **3.9**a-f and Figure **3.10**a-f that all the selected elements (i.e., F, Mn, Ni, Al and O) are uniformly distributed in all the viewed regions. This confirms that both AlF_3 and $LiAlF_4$ have been homogeneously coated on the LNMO microspheres.

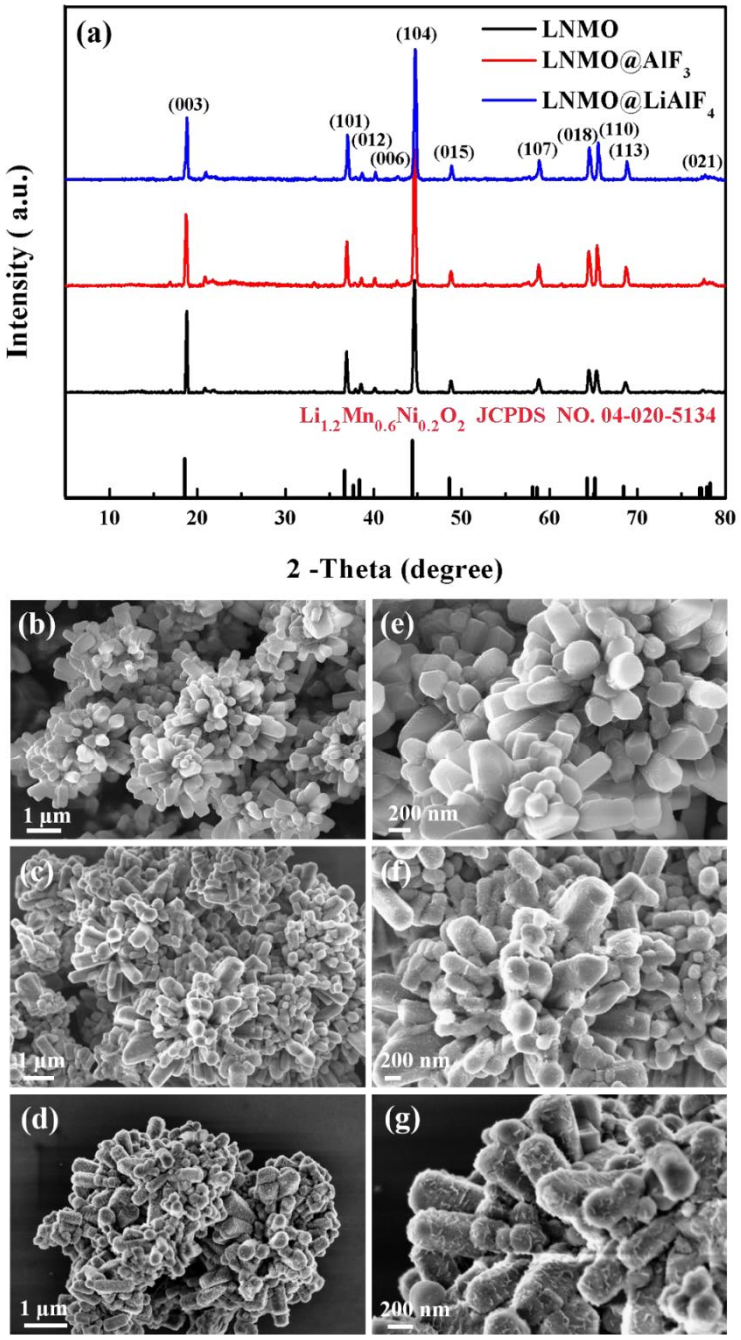

Figure 3.7 (a) XRD patterns of LNMO, LNMO@AlF_3 and LNMO@$LiAlF_4$. SEM images of (b, e) LNMO, (c, f) LNMO@AlF_3 and (d, g) LNMO@$LiAlF_4$ at different magnifications.

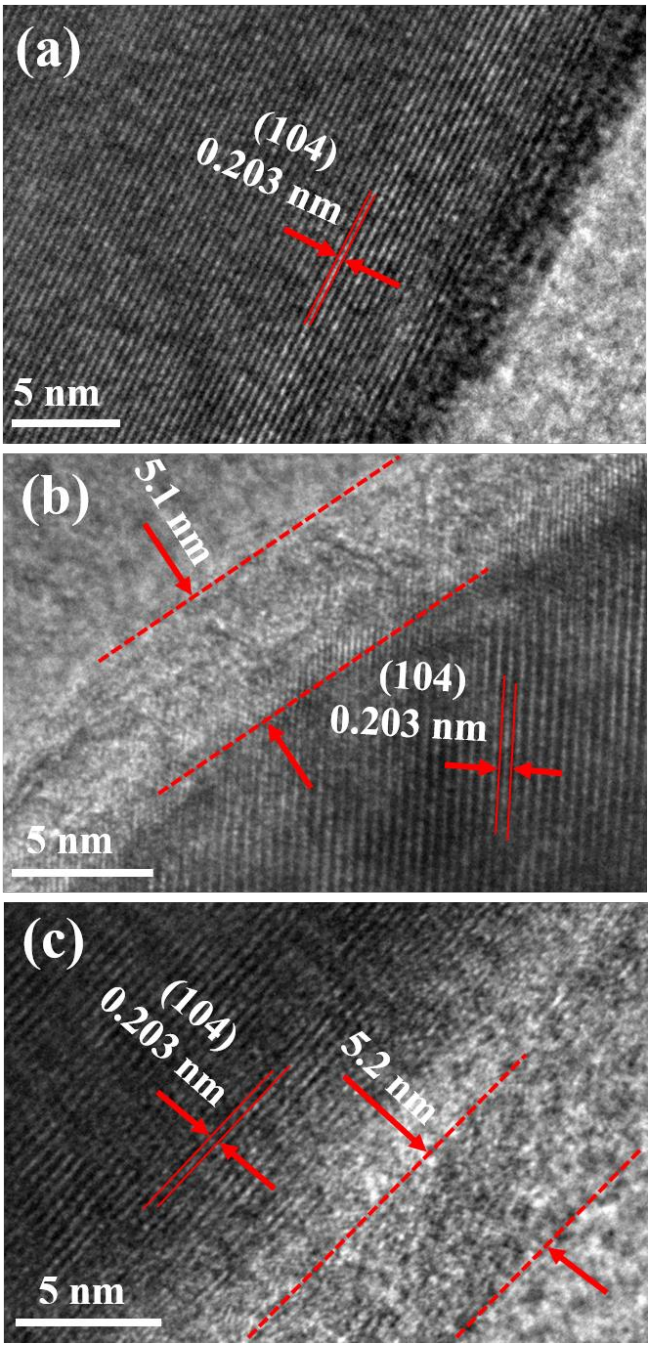

Figure 3.8 HRTEM images of the as-synthesized (a) LNMO, (b) LNMO@AlF_3 and (c) LNMO@$LiAlF_4$.

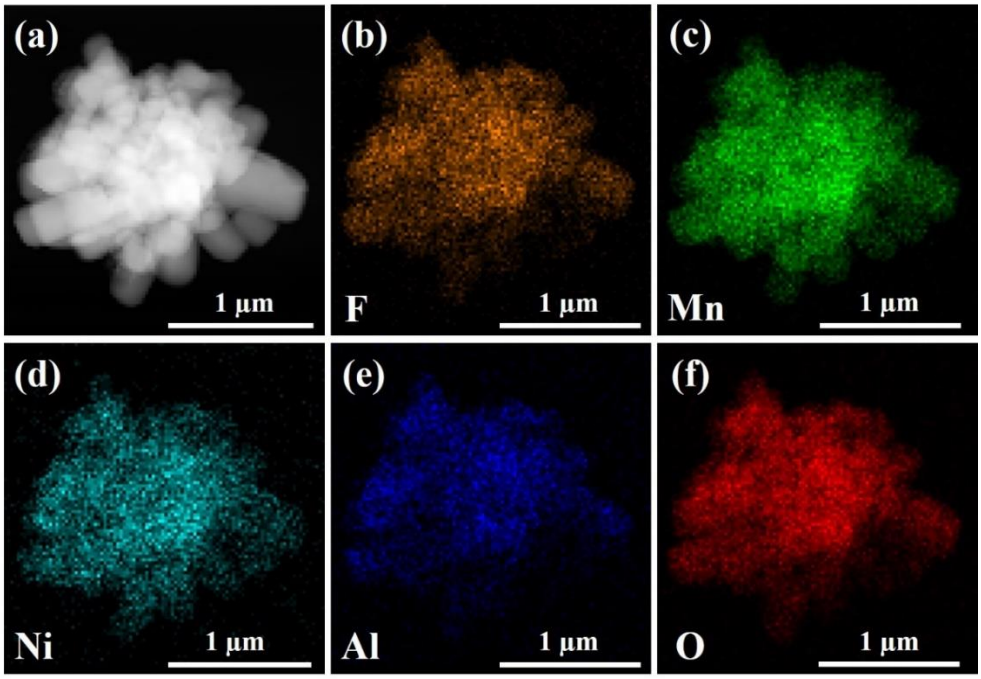

Figure 3.9 (a) TEM image of LNMO@AlF_3. (b-f) The corresponding EDS element mappings of LNMO@AlF_3. (b) F, (c) Mn, (d) Ni, (e) Al and (f) O.

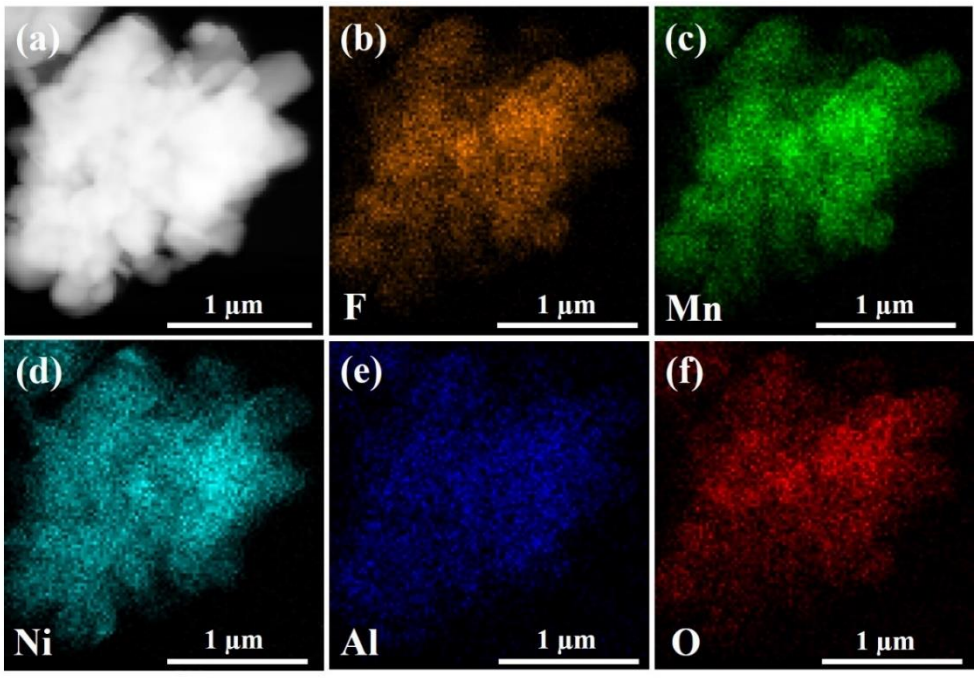

Figure 3.10 (a) TEM images of LNMO@$LiAlF_4$. (b-f) The corresponding EDS element mappings of LNMO@$LiAlF_4$. (b) F, (c) Mn, (d) Ni, (e) Al and (f) O.

To further determine the chemical composition and the oxidation states on the surface of the as-synthesized samples, XPS analysis was carried out. As shown in **Figure 3.11**a, the strong and distinct F and Al signals at 685.2 eV and 73.8 eV are detected in the XPS spectrum of the surface modified LNMO materials, which is in consistent with the EDS mapping results. There are two main peaks in the Ni XPS spectra: one is the Ni $2p_{1/2}$ spectral peak around 872.6 eV with a corresponding satellite peak at 880.3 eV. The other peak can be assigned to Ni $2p_{3/2}$ located at 856.9 eV and 855.4 eV with a small satellite peak at 867.7 eV. Figure 3.11b indicates the coexistence of Ni^{2+} and Ni^{3+} valence states in LNMO.[292, 303] Figure 3.11c presents two broad peaks at 654.2 eV and 542.5eV, which can be assigned to the Mn $2p_{3/2}$ and Mn $2p_{1/2}$ photoelectron peaks, respectively. This result reveals that manganese is in the highest valence state (+4) despite the presence of the fine structure with high binding energy. Many high-purity Mn^{4+} materials like MnO_2 and $LiMn_2O_3$ are well recognized to show similar subtle fine structure around the Mn $2p_{3/2}$ main peak.[285, 288] Although the bare and AlF_3-coated LNMOs show clear Li 1s peaks at 54.3 eV in **Figure 3.12**a, this value shifts to a higher binding energy position after coating with $LiAlF_4$. The introduction of more Li^+ could significantly increase electronegativity of the material surface, which was also reported by previous research.[299] Meanwhile, the main peaks of Al and F in the $LiAlF_4$-modified material experience the same shift to higher binding energies compared with the AlF_3-coated one, as expected (Figure 3.12b and Figure 3.12c). Concerning O, as illustrated in Figure 3.11d, the pristine LNMO shows a remarkable $O1s_I$ spectral peak about 529.3 eV but a weak $O1s_{III}$ peak at a higher binding energy of 533.3 eV, corresponding to the lattice O^{2-} and oxygen species deposited on the surface,

respectively. Furthermore, there is an $O1s_{II}$ peak in the middle range of 531.6 eV, which is in good agreement with the early reports on oxidized lattices O^{n-} ($n < 2$) in lithium-rich materials.[303-305] This oxygen species is closely related to the surface species and TM ions as well.[306] With the introduction of the AlF_3 protective layer, the intensities of $O1s_{II}$ and $O1s_{III}$ peaks have been greatly increased, while a slight decline of the lattice O^{2-} proportion is owing to the effect of surface modification. The peak intensity of lattice oxygen species (O^{n-}) increases when the coating material is replaced by $LiAlF_4$. Consequently, the $LiAlF_4$ surface coating is likely to generate more oxidized lattice O^{n-}, which is expected to achieve rapid and efficient anionic redox reactions during both charge and discharge processes.

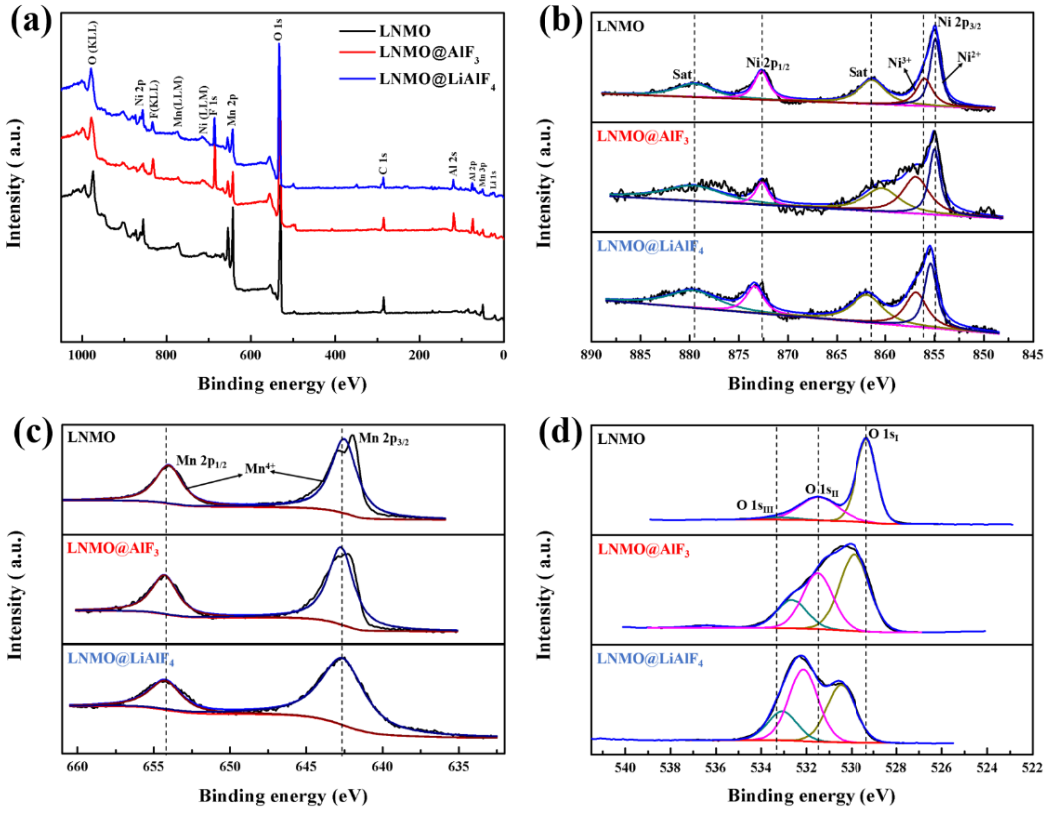

Figure 3.11 (a) XPS survey and (b-d) high-resolution spectra of (b) Ni2p, (c) Mn2p, and (d) O1s.

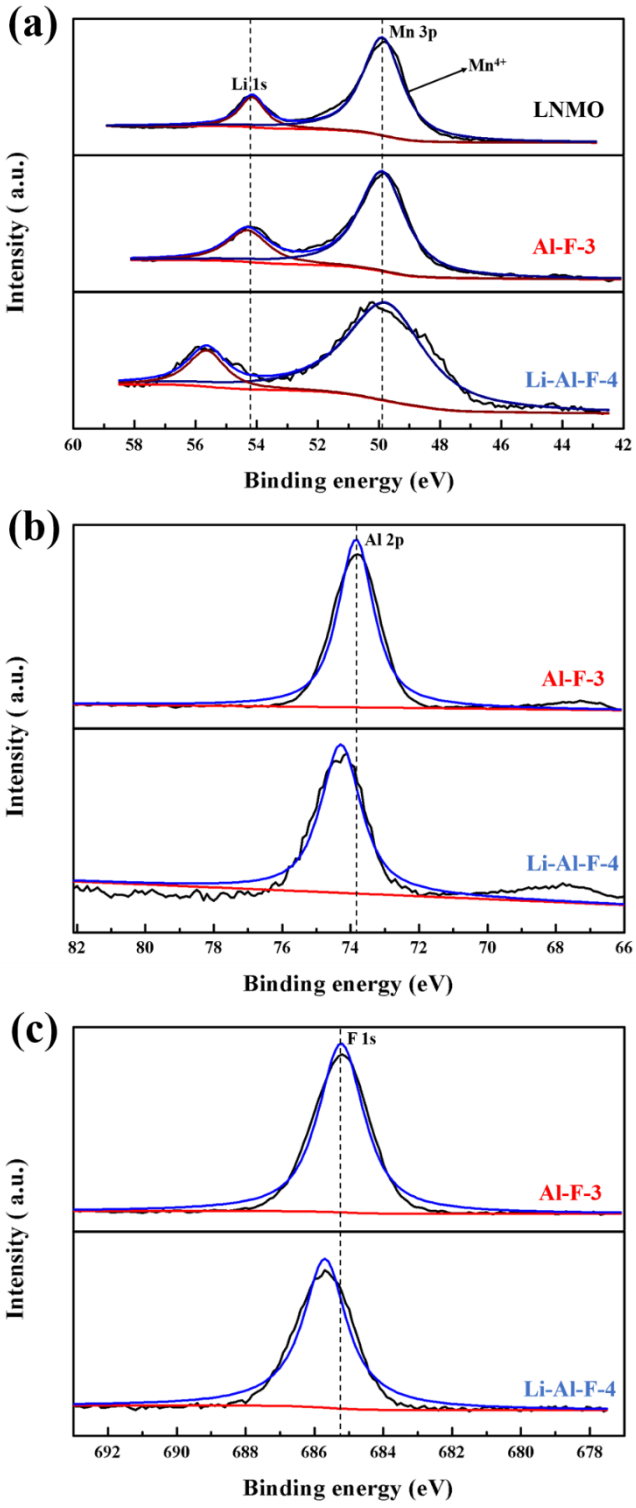

Figure 3.12 XPS spectra and fitting results of LNMO, LNMO@AlF_3 and LNMO@$LiAlF_4$: (a) Li1s, (b) Al2p and (c) F1s.

The electrochemical performances of pristine and surface-modified LNMO cathode materials were evaluated through galvanostatic charge/discharge measurements. **Figure 3.13**a-c show galvanostatic charge/discharge profiles of as-prepared cathodes at the current density of 35 mA g^{-1} (0.1 C) in a wide electrochemical window (2.0 V – 4.8 V). The Li_2MnO_3 phase usually undergoes an activation process in the initial few cycles, which is in agreement with previous work.[307] The corresponding initial Coulombic efficiencies are 71.3%, 75% and 81.2% for LNMO, LNMO@AlF_3 and LNMO@$LiAlF_4$ electrodes, respectively. The boost of initial charge/discharge efficiency by $LiAlF_4$ coating is mainly due to the presence of an appropriate amount of non-bonding O^{n-} species in the crystal lattice. Generally, most lithium-rich cathodes are suffering from poor initial Coulombic efficiency due to the irreversible lithium loss and the evolution of oxygen species ($O^{2-} \rightarrow O^{n-}$) during the first deintercalation. This transformation cannot be fully recovered in the first discharge, thereby maintains some oxidized oxygen when discharging to 2 V.[288-289] Consequently, a higher proportion of oxidized O^{n-} will undoubtedly lead to better initial charge–discharge efficiency since only a small part of O^{2-} in the lattice is able to participate in the redox reaction. This effectively preventing irreversible capacity loss during the first cycle. Furthermore, the lithium conductive $LiAlF_4$ layer also facilitates the transportation of lithium ions, forming a stable and conductive interface between electrolyte and electrode. On contrary, as a poor lithium-ion conductor, AlF_3 causes an increase of the overpotential, which could impede performance improvement.[299] Both aforementioned factors contribute to improve Coulombic efficiency in the first cycle. Moreover, voltage decay which often causes serious safety issues, has been effectively suppressed by employing the surface

protective layer. As demonstrated in Figure 3.13a, the uncoated LNMO cathode shows an irreversible structure transformation from the original layered phase to a spinel-like phase due to the migration of TM ions into the lithium vacancies after 100 cycles.[308] However, this tendency has been mitigated to a large extent in the surface modified LNMO, especially for LNMO@$LiAlF_4$, whose primary layered structure can be well preserved throughout cycling, as shown in Figure 3.13c. The first discharge capacity of LNMO@AlF_3 and LNMO@$LiAlF_4$ are 244 mAh g^{-1} and 246 mAh g^{-1}, respectively, which is much higher than that of the pristine LNMO microspheres. For LNMO electrode, we should note that the charge capacity of only 126 mAh g^{-1} can be achieved if all nickel ions are completely oxidized to Ni^{4+}, representing only 0.4 Li^+ extraction. However, after charging to 4.8 V, there is about 0.99 Li^+ totally extracted from the lattice structure, and only 0.7 Li^+ is reinserted into the lattice structure at the end of first discharge, indicating that more than half of the capacity is compensated by the anionic redox reaction because Mn^{4+} is electrochemically inactive during charge and discharge processes.[288, 304] Therefore, the high capacity is contributed by both cationic oxidation of transition metal ions and anionic redox derived from the layered lithium rich microstructure. Classical $xLiMO_2 \cdot (1-x)Li_2MnO_3$ ($M = Ni_xMn_{1-x}$, $0 < x < 1$) electrode materials can be described as $Li[Ni_xLi_{1/3-2x/3}Mn_{2/3-x/3}]O_2$, which has alternating $Ni_xLi_{1/3-2x/3}Mn_{2/3-x/3}$ and Li layers. When x = 0.2 in the lithium-rich materials, the mentioned average chemical composition, i.e., $0.5LiNi_{0.5}Mn_{0.5}O_2 \cdot 0.5Li_2MnO_3$, is obtained.[309] However, the activation of superstructure in the Li_2MnO_3 phase is more favorable to form oxygen-oxygen dimers compared with traditional

layered structure of $LiCoO_2$.[310] The capacity contribution starts with a rapid nickel oxidation reaction in the initial stage of charge as shown in **Equation 3.1**.

$$LiNi_{0.5}Mn_{0.5}O_2 \rightarrow Ni_{0.5}Mn_{0.5}O_2 + Li^+ + e^- \quad \textbf{Equation 3.1}$$

Subsequently, anionic oxidation becomes a dominant trend after the cathode has been charged to a higher potential, indicated as an obvious plateau at 4.5 V in Figure 3.13a.

$$Li_2MnO_3 \rightarrow Li_{2-x}MnO_{3-y} + xLi^+ + yO^{n-} + xe^- \quad \textbf{Equation 3.2}$$

Such a reversible oxygen-based reaction can be regenerated in the following cycle.[311] Based on **Equation 3.2**, we have also recorded the variation of lithium content as a function of corresponding charge/discharge profiles in Figure 3.13d and 3.13e to further study the fundamental reaction kinetics of LNMO cathodes. In contrast to the pristine LNMO cathode, more lithium ions can be removed and recovered from the AlF_3-coated sample in the initial stage. Although there is only 0.96 Li^+ released from the LNMO@$LiAlF_4$ during the first charge, the subsequent discharge demonstrates 0.78 Li^+ is able to reinsert into the structure, leading to high Coulombic efficiency. All the S-shaped hysteresis loops are stabilized from the second cycle onward and, noticeably, the $LiAlF_4$-modified electrode still has the smallest voltage hysteresis among all the electrodes. This further proves that a large percentage of non-bonding O^{n-} species and a lithium-ion conductive coating layer are both beneficial to fast kinetics compared with AlF_3 coated and non-coated lithium-rich cathode materials.

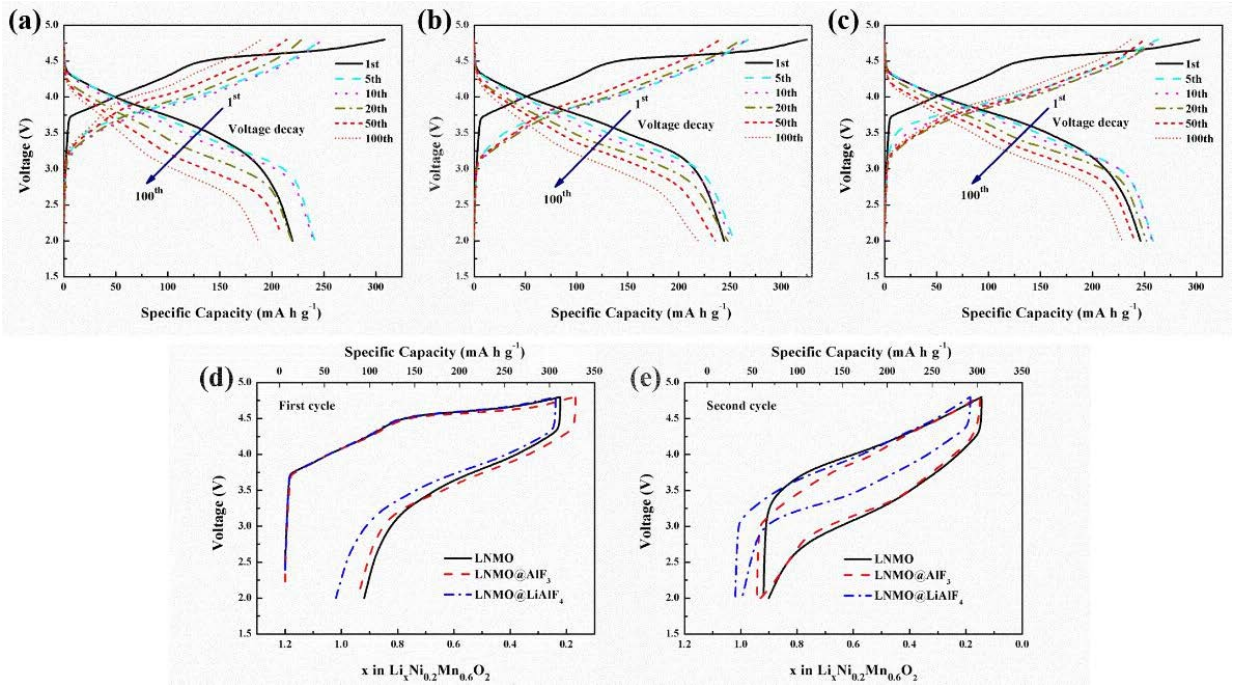

Figure 3.13 Galvanostatic charge/discharge voltage profiles of (a) LNMO, (b) LNMO@AlF_3 and (c) LNMO@$LiAlF_4$ at different cycles. Voltage profiles of LNMO, LNMO@AlF_3 and LNMO@$LiAlF_4$ as a function of Li content with corresponding charge/discharge curves for the (d) first and (e) second cycles.

Figure 3.14a illustrates the capacity retention after 100 cycles at 0.1 C. The capacity of bare LNMO cathodes declines to 187 mAh g^{-1} at the 100th cycle, showing a capacity decay of 14.9 %. However, the decay in capacity of surface-modified samples has been largely restricted after cycling (10.4% for LNMO@AlF_3 and 7.2% for LNMO@$LiAlF_4$, respectively). Fluoride-contained materials can effectively protect the LNMO from being attacked by byproducts such as HF, generated from the oxidization of electrolyte at high voltage.[293, 299] Furthermore, the coating layer can significantly suppress the irreversible structure transformation and improve the interfacial stability of LNMO. We have further analyzed the morphologies of the as-synthesized electrodes before and after 100 charge/discharge cycles. As shown in **Figure 3.15**a-

d, the surface of the LNMO electrode has been ruined due to the harsh operation conditions during cycling. However, the modified cathodes, especially LNMO@$LiAlF_4$, are able to maintain their original morphology without obvious deterioration after 100 cycles (**Figure 3.16**a-d and **Figure 3.17**a-d). This confirms that surface coating can efficiently prevent the LNMO electrode cracking or collapsing. Voltage decay is one of the most serious issue to develop high-performance lithium-rich cathode materials for practical application. In view of this, we concluded the average operating voltage profiles in **Figure 3.18**. Apparently, compared with the LNMO and LNMO@AlF_3, this shortcoming has been greatly mitigated after $LiAlF_4$ coating. Furthermore, the rate performances of the cathode materials are shown in Figure 3.14b. It is worth mentioning that lithium-rich cathodes normally show a poor rate performance and ineluctable capacity fading, which hampers their practical applications in the commercial market. However, the LNMO@$LiAlF_4$ demonstrates a superior capacity retention rate of 52.4% at 5 C (133 mAh g^{-1}), which is higher than LNMO@AlF_3 (40.8% at 5 C) and almost treble that of pristine LNMO (23.9% at 5 C). To evaluate voltage profiles at different current densities, we have shown the relevant charge/discharge curves in **Figure 3.19**a-c. As expected, the presence of lithium-ion conductive coating layers minimizes the voltage polarization at high current densities. In order to evaluate cyclability of the as-prepared electrodes, long-term cycling test was performed to evaluate the practical application of as-synthesized cathodes. There is no doubt that the LNMO@$LiAlF_4$ sample is stable enough to tolerate forceful operation conditions without suffering degradation, showing a minimal capacity loss of 6.4 % after 3000 cycles (Figure 3.14c, 14.4% for LNMO and 9.1% for LNMO@AlF_3, respectively). This result is better

than the previous reported ZnO,[312] $LiTi_2(PO4)_3$[313] and SnO_2[314] coated lithium-rich cathode materials. The coating of the lithium-ion conductive nanolayer reduces the risk of parasitic reactions and permit fast Li^+ diffusion as well. On the other hand, limiting oxygen loss helps to suppress the irreversible phase transformation and, consequently, the structure stability is enhanced, accordingly.[308] These conclusions are consistent with the electrochemical testing results.

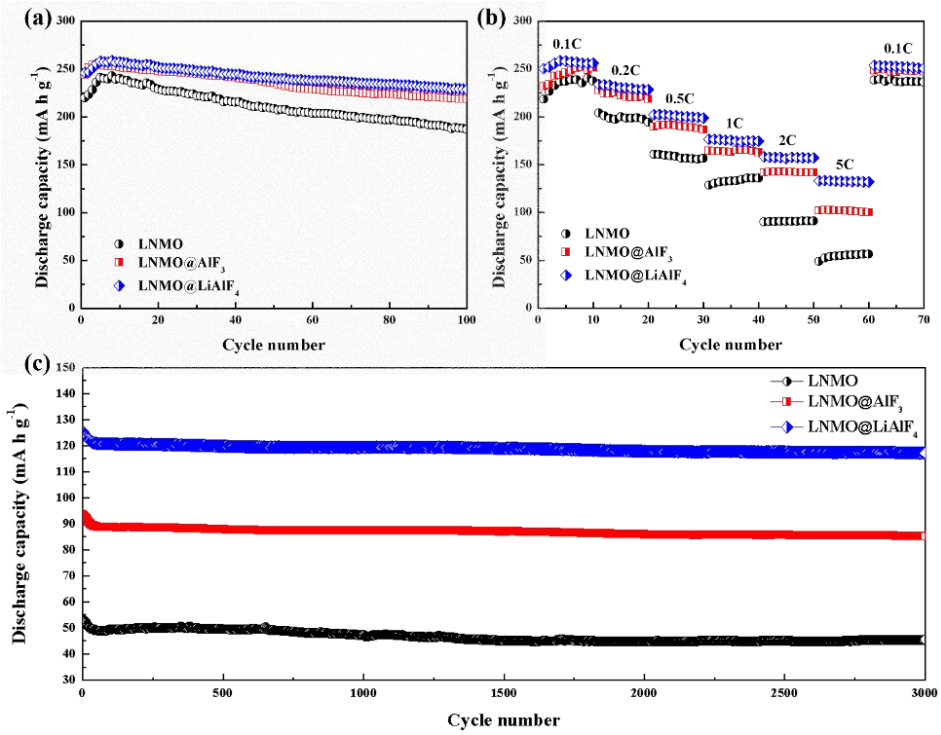

Figure 3.14 (a) Cycling performances of LNMO, LNMO@AlF_3 and LNMO@$LiAlF_4$ electrodes at 0.1 C in the voltage range of 2.0-4.8 V. (b) Rate performance of LNMO, LNMO@AlF_3 and LNMO@$LiAlF_4$ electrodes at various current densities from 0.1 C to 5 C. (c) The long-term stability test of LNMO, LNMO@AlF_3 and LNMO@$LiAlF_4$ electrodes at 5 C for 3000 cycles.

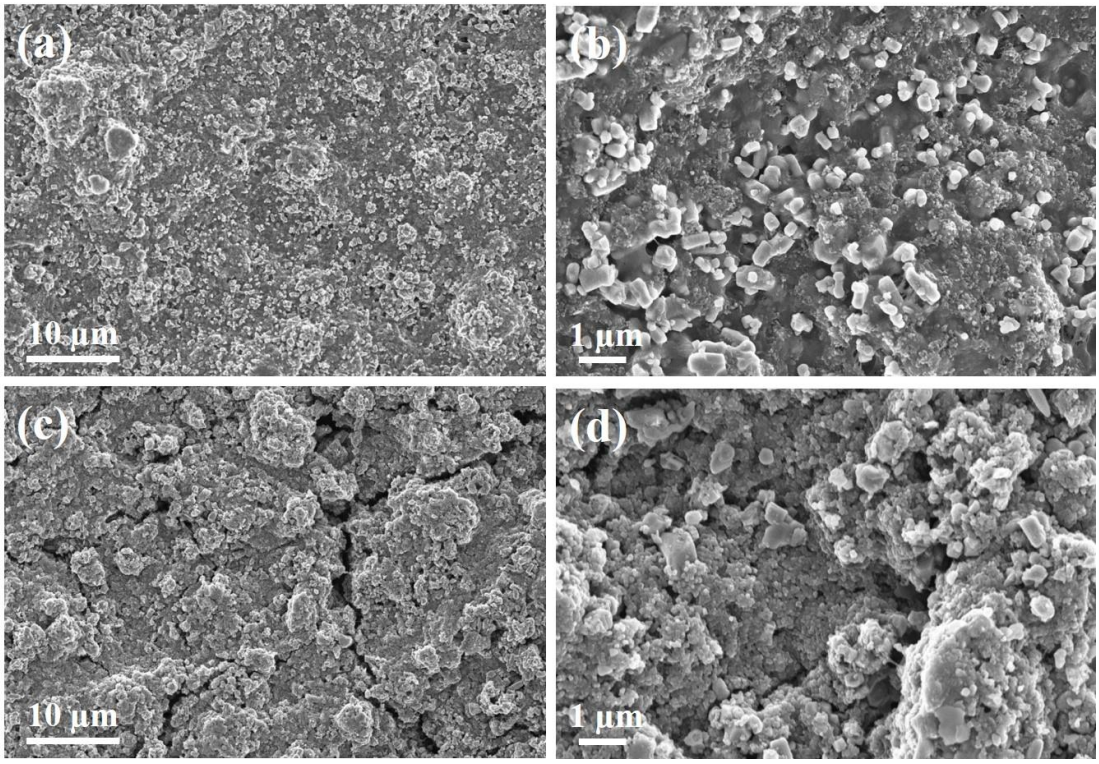

Figure 3.15 SEM images of LNMO electrodes (a, b) before and (c, d) after 100 cycles.

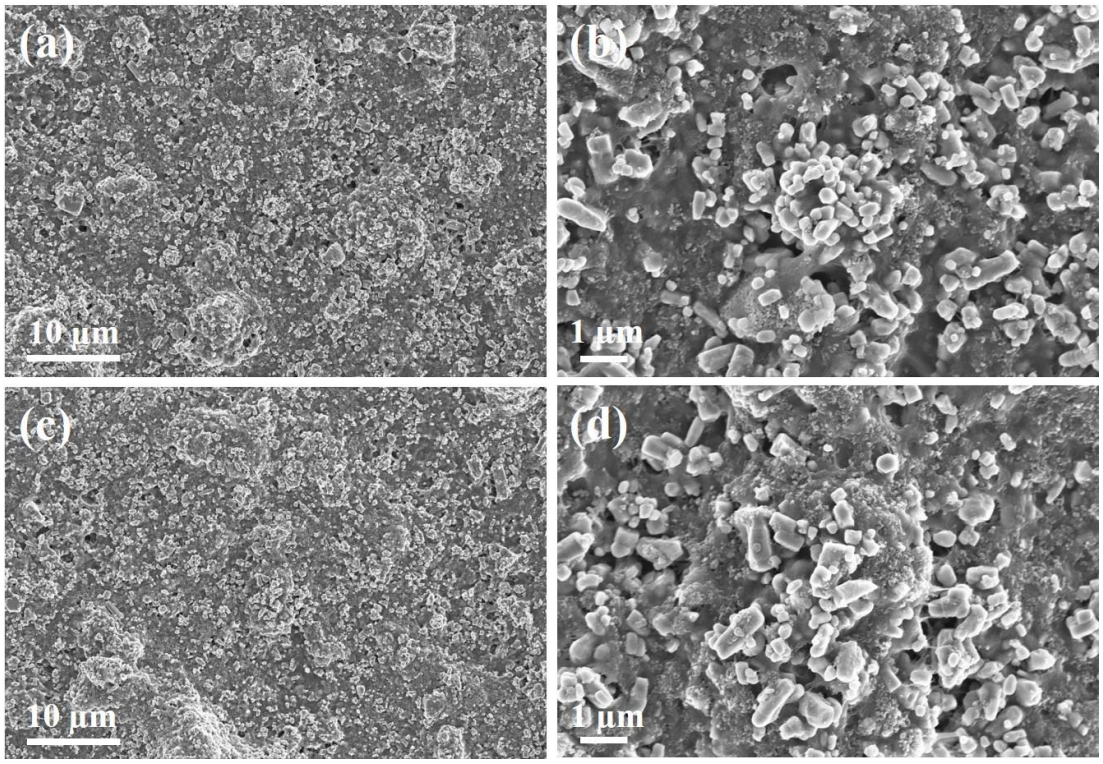

Figure 3.16 SEM images of LNMO@AlF_3 electrodes (a, b) before and (c, d) after 100 cycles.

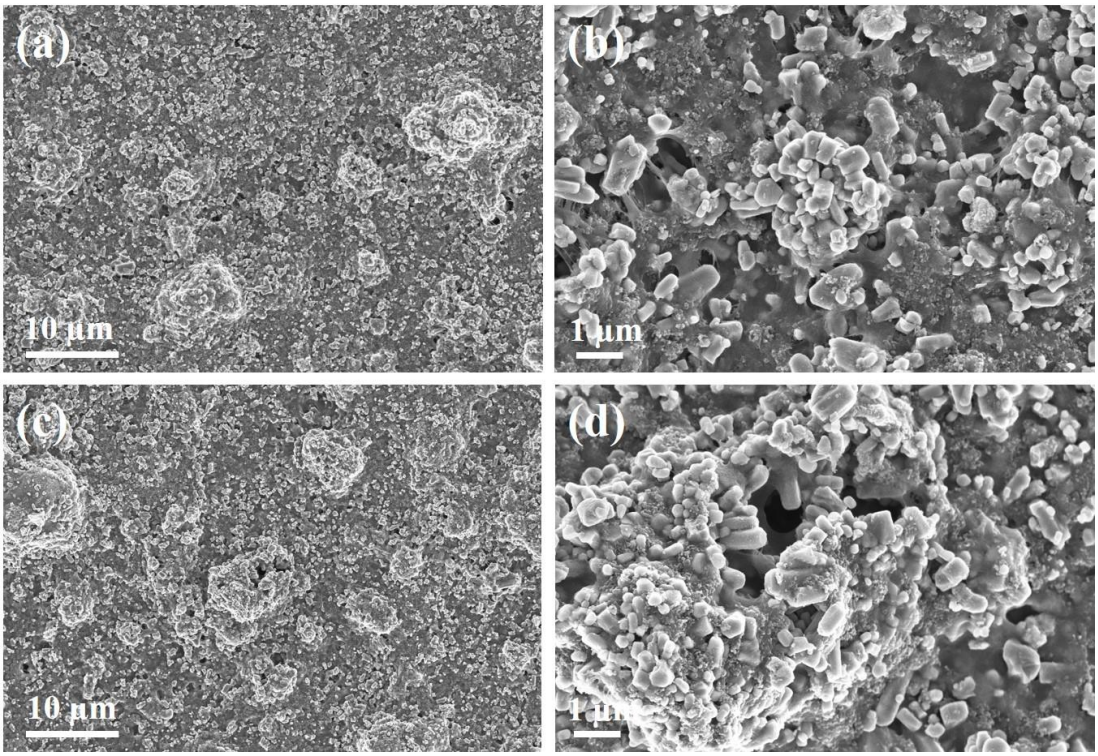

Figure 3.17 SEM images of LNMO@$LiAlF_4$ electrodes (a, b) before and (c, d) after 100 cycles.

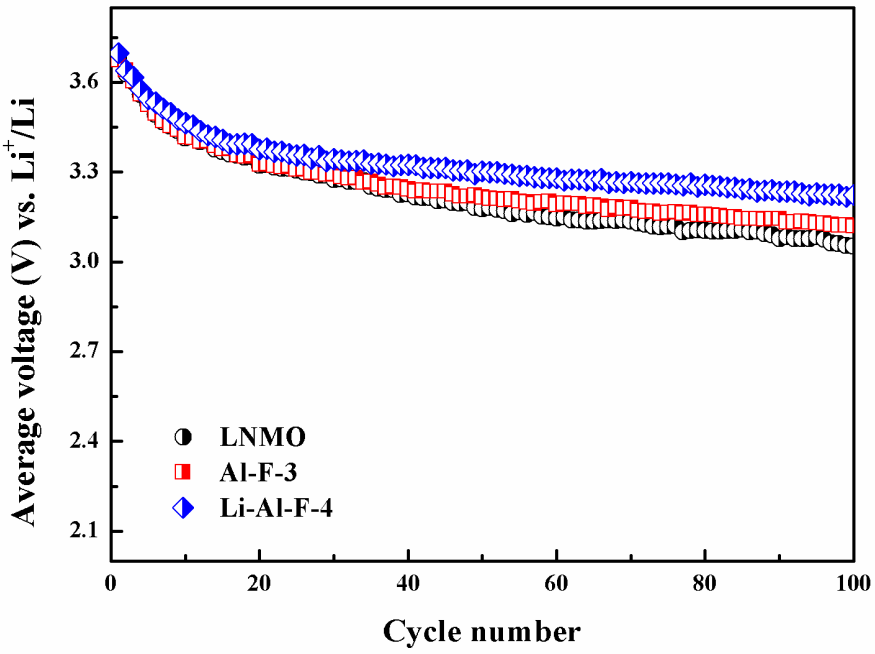

Figure 3.18 Average operating voltage vs. cycle number of LNMO, LNMO@AlF_3 and LNMO@$LiAlF_4$.

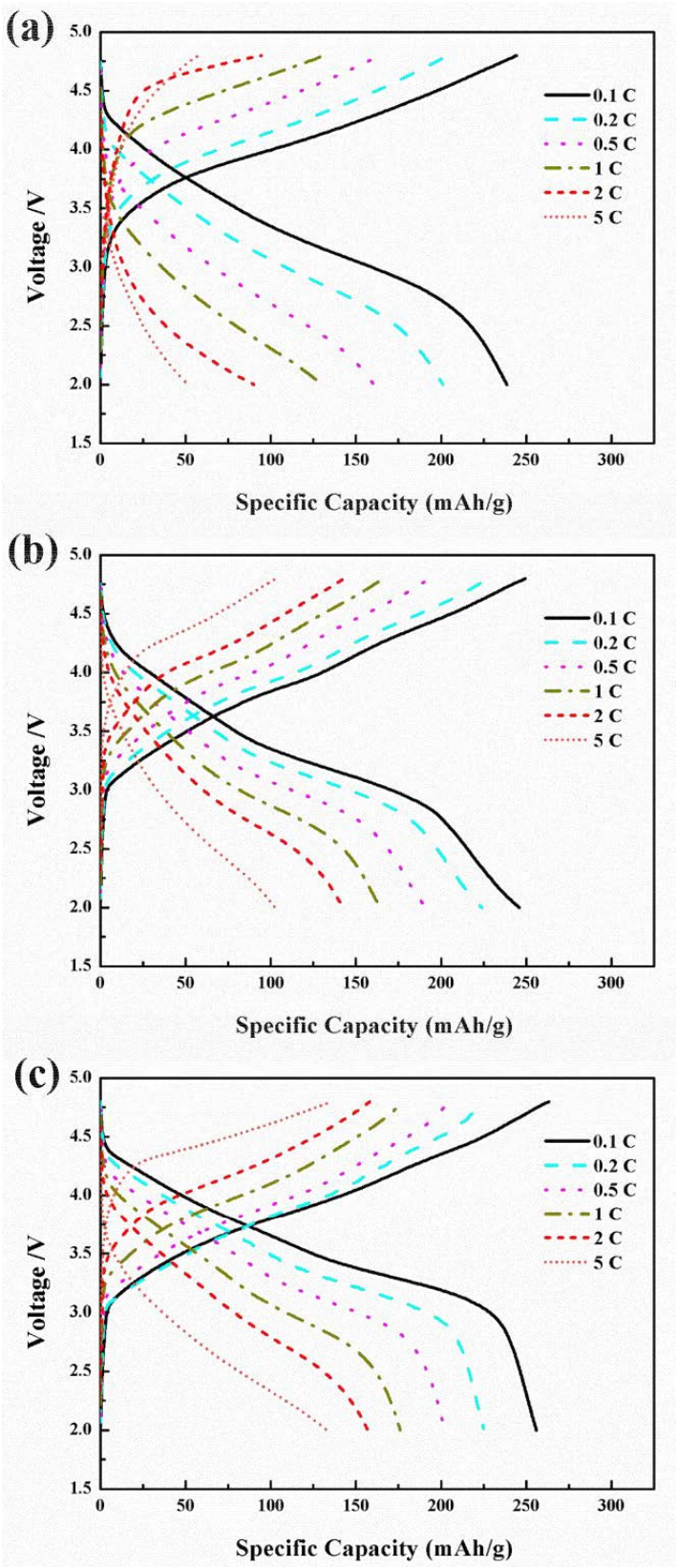

Figure 3.19 Voltage profiles of (a) LNMO, (b) LNMO@AlF_3 and (c) LNMO@$LiAlF_4$ at different current densities.

The advantages of $LiAlF_4$ surface coating were further elucidated via cyclic voltammograms (CV) tested with a scan rate of 0.1 mV s^{-1} (**Figure 3.20**a-c). There is a distinct anionic peak around 4.5 V in the first charge cycle, corresponding to the oxidation of oxygen species. The regular CV curves after the second cycle display two pairs of redox peaks at approximately 3.2 V / 3.9 V and 3.7 V / 4.4 V showing the cationic/anionic redox of nickel/oxygen, which is in good agreement with the voltage plateau exhibited in Figure 3.13a-c**.** It is obvious in Figure 3.20c that the voltage gap of LNMO@$LiAlF_4$ between cathodic and anionic peaks is smaller than the other two samples, implying improved reversibility.[315]

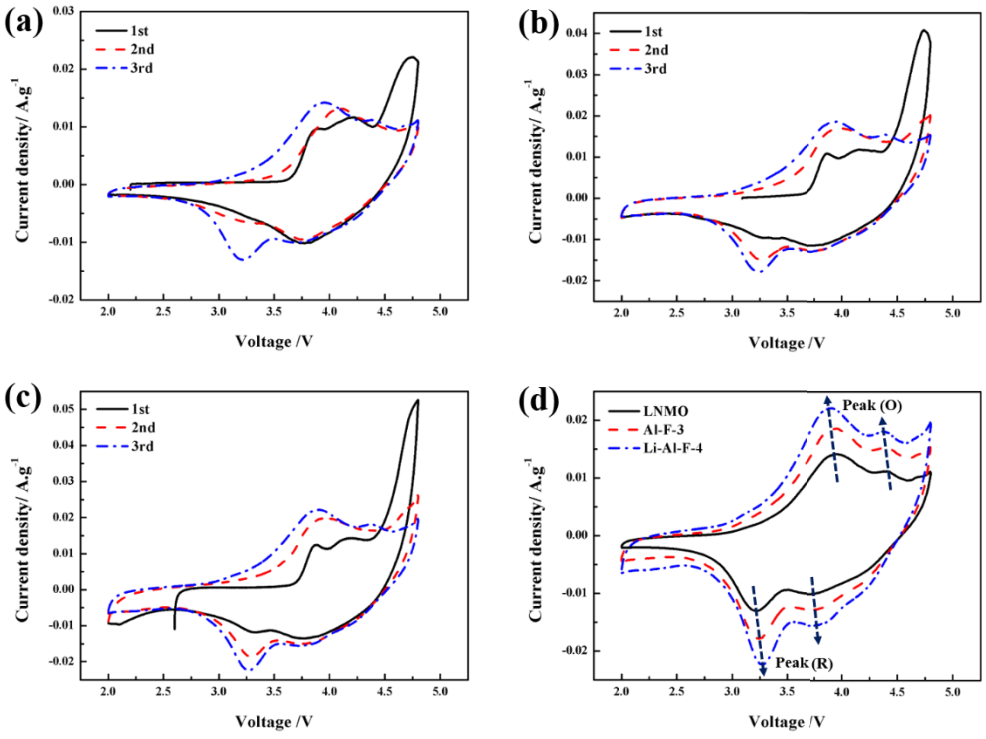

Figure 3.20 CV curves of (a) LNMO, (b) LNMO@AlF_3 and (c) LNMO@$LiAlF_4$ at the scan rate of 0.1 mV s^{-1}. (d) The corresponding CV curves at the 3rd cycle.

In order to fully explore the mechanism for the noticeable performance improvement of the surface-modified LMNOs, electrochemical impedance spectra (EIS) of the three cathodes were tested in the frequency range from 10 mHz to 100 kHz after the first charge and discharge (**Figure 3.21**a). All EIS spectra exhibit a semicircle in the high frequency area and a sloping line in the low frequency region, respectively. The intercept on the real axis represents internal resistance (Rs), while the numerical value of the diameter of semicircle gives an approximate indication of the charge transfer resistance (Rct) at the interface, and the straight line shows the ion diffusion in the bulk material. The relevant fitting results are listed in **Table 3.1**. The three cathode samples have almost the same internal resistance value in the fresh cells (**Figure 3.22**a), but the LNMO@$LiAlF_4$ shows the smallest Rct and W compared with the other two electrode materials. Moreover, these two parameters involved in the LNMO@$LiAlF_4$ cathode are nearly unchanging although we can observe a dramatic increase of transfer and diffusion resistances after the 1st cycle, suggesting the $LiAlF_4$ coating does not sacrifice the inherent advantages of LNMOs but effectively reduces the interfacial resistance, inhibits the secondary reactions between the cathode and electrolyte and enhances the lithium-ion conductivity of LNMOs. Accordingly, we can calculate the Li^+ diffusion coefficient D_{Li} after first cycle through the following equation:

$$D_{Li}=\frac{1}{2}\left(\frac{RT}{An^2F^2\sigma_w C}\right)^2 \qquad \textbf{Equation 3.3}$$

Wherein T is the absolute temperature, R is the gas constant, C indicates the molar concentration of lithium ions in the solid (0.0228 mol cm^{-3}), σ_w corresponds to the Warburg coefficient, which is depicted as the slope of the fitting lines in the Figure 3.21b. F and n

represents the Faraday constant and the number of electrons participating in the oxidation per mole, respectively. A is the working area of the prepared cathode. Based on the **Equation 3.3**, the diffusion coefficients D_{Li} are 3.36×10^{-17} cm^2 s^{-1} (LNMO), 5.61×10^{-16} cm^2 s^{-1} (LNMO@AlF_3) and 1.05×10^{-15} cm^2 s^{-1} (LNMO@$LiAlF_4$), respectively. Such a high D_{Li} achieved by LNMO@$LiAlF_4$ is able to minimize the kinetic barrier for Li^+ transportation and thereby enable efficient ions diffusion as a result.[316] We also note that the in-cell temperature is expected to play a crucial role in determining the kinetic processes of LNMOs. Taking this into consideration, a series of Nyquist plots were carefully recorded under different temperature conditions, as shown in Figure 3.22b-d. All the samples were increasingly activated by an increase in the EIS testing temperature. By comparing the various temperature dependent D_{Li} measurements summarized in **Table 3.2**, we can see that the LNMO@$LiAlF_4$ exhibits the best activation results among three electrode materials, which is consistent with the rapid reaction kinetics originating from non-bonding O^{n-} species.[303]

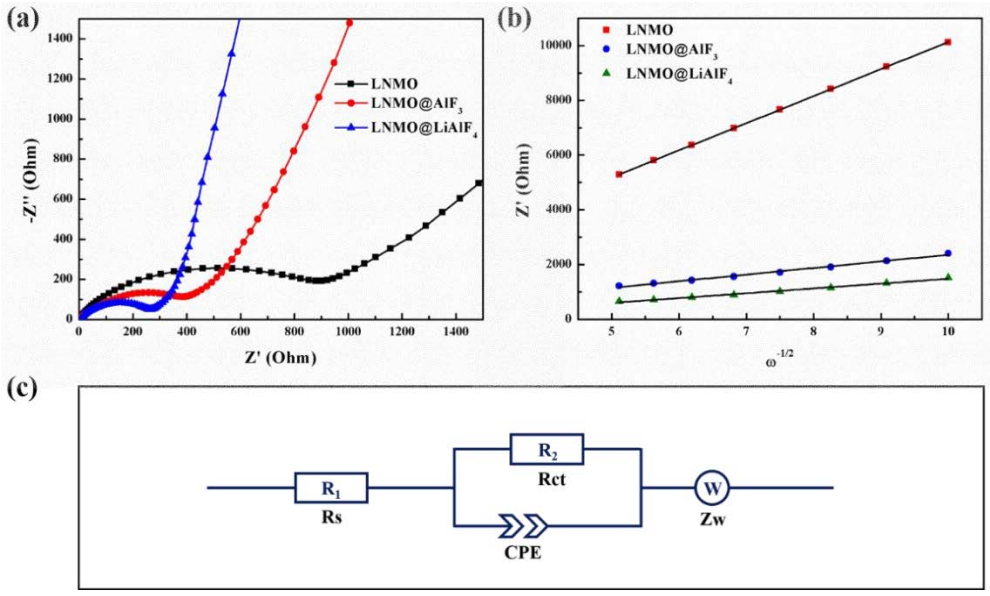

Figure 3.21 (a) Nyquist plots of the prepared electrodes from 100 kHz to 10 mHz after discharge to 2.0 V in the first cycle. The corresponding (b) linear fitting results of the Warburg impedance and (c) equivalent circuit.

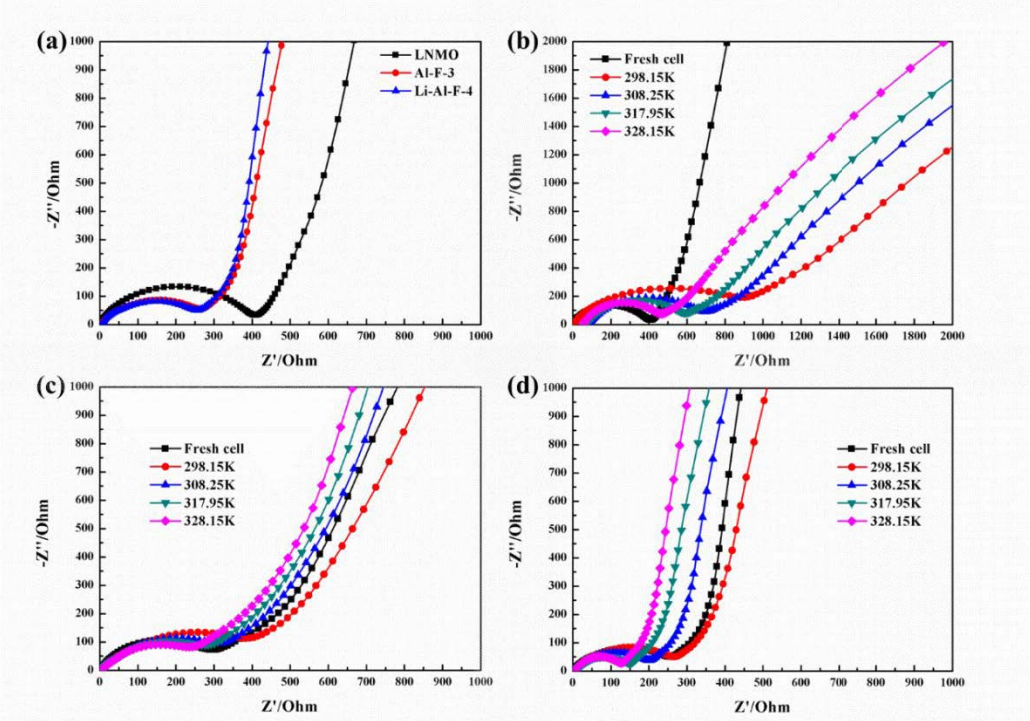

Figure 3.22 (a) Nyquist plots of fresh electrodes. (b-d) Nyquist plots of (b) LNMO, (c) LNMO@AlF_3 and (d) LNMO@$LiAlF_4$ electrodes at different measured temperatures.

Table 3.1 Electrochemical impedance spectra fitting values of three cathodes before and after the first cycle.

Fresh	Rs	Rct	Zw
LNMO	3.826	375	437.5
LNMO@AlF_3	5.656	204.1	364
LNMO@$LiAlF_4$	4.679	194.3	295.1

First cycle	Rs	Rct	Zw
LNMO	5.677	843.9	2488
LNMO@AlF_3	4.273	250.9	685.1
LNMO@$LiAlF_4$	6.231	205.1	378

Table 3.2 Diffusion coefficients D_{Li} of LNMO, LNMO@AlF_3 and LNMO@$LiAlF_4$ at different measured temperatures.

Temperature	$D_{f\text{-}LMNO}$	$D_{f\text{-}Al\text{-}F\text{-}3}$	$D_{f\text{-}Li\text{-}Al\text{-}F\text{-}4}$
298.15 K	3.36×10^{-17}	5.61×10^{-16}	1.05×10^{-15}
308.65 K	3.05×10^{-16}	7.12×10^{-16}	1.51×10^{-15}
318.25 K	4.49×10^{-16}	7.61×10^{-16}	2.29×10^{-15}
327.95 K	7.76×10^{-16}	8.15×10^{-16}	3.67×10^{-15}

3.4 Summary

In summary, we have developed a facile and effective $LiAlF_4$-coating strategy to improve the electrochemical performance of lithium-rich cathode materials. A $LiAlF_4$ nanolayer coating has been successfully incorporated onto bulk materials with a thickness of ~ 5.2 nm. Electrochemical tests illustrate that the LNMO@$LiAlF_4$ cathodes display an excellent rate capability and superior cycling stability compared with uncoated LNMO and non-ionic conductive LNMO@AlF_3. This is mainly because the introduction of a lithium conductive coating layer facilitates Li^+ diffusion and prevents the cathode being affected by unwanted side reactions. Meanwhile, the presence of a large portion of non-bonding O^{n-} species significantly improves the anionic redox kinetics and suppresses irreversible phase transformation. This study provides a new approach to address the existing drawbacks that hinder the practical applications of lithium rich cathode materials.

CHAPTER 4 CONSTRUCTION OF HIERARCHICAL $K_{1.39}Mn_3O_6$ SPHERES VIA AlF_3 COATING FOR HIGH-PERFORMANCE POTASSIUM-ION BATTERIES

4.1 Introduction

Rechargeable lithium-ion batteries (LIBs) have dominated the commercial market as power sources for portable electronic devices.[277, 317] Large-scale energy storage requires new generation rechargeable battery systems with low cost and environmental friendliness. Potassium, which shares some chemical similarity with lithium in the alkali metal group, is the 7th earth-abundant element and potassium-ion batteries (KIBs) are expected to follow similar operating principles to LIBs. It also has a relatively low standard redox potential (−2.94 V vs. K/K^+), and KIBs are expected to achieve high energy densities. Moreover, as the most popular commercial anode material, graphite shows a reversible specific capacity of 273 mAh g^{-1} in K/graphite half-cells with aprotic electrolytes, providing a practical approach for large-scale application.[318-319] Although potassium ions are larger (1.38 Å) than sodium ions (1.02 Å) and lithium ions (0.76 Å), the weak Lewis acidity and low desolvation energy of potassium ions contribute to their higher ionic conductivity as well as better diffusion kinetics than that of sodium ions and lithium ions.[320-321]

Until now, most studies on KIBs focused on anode materials including carbon-based materials,[318-319, 322-323] Prussian blue analogs,[324] transitional-metal dichalcogenides,[325] organic compounds,[219, 326] phosphorus-based alloy materials et al.[327] Meanwhile, the development of

cathode materials for KIBs is still in its infancy, which is urgently needed for the development of potassium-ion full batteries.[328] With tremendous success in LIBs, layered transition metal oxides (TMOs) are currently attracting considerable interest as cathode materials for KIBs owing to their high theoretical specific capacity, closed-packed structure and high volumetric energy density.[329-332] Vaalma et al, reported the electrochemical performances of the layered $K_{0.3}MnO_2$ material, which initially motivated the research on layered cathode materials for KIBs.[333] Later, Wang et al. reported the synthesis and application of earth abundant element-based $K_{0.7}Fe_{0.5}Mn_{0.5}O_2$ nanowires as high-performance cathode materials for KIBs, which deliver a high specific capacity (114 mAh g^{-1} at 100 mA g^{-1}) and excellent cycling stability (87% capacity retention after 450 cycles).[334] Very recently, several layered TMOs such as $K_{0.5}MnO_2$,[335] $K_{0.65}Fe_{0.5}Mn_{0.5}O_2$,[336] $K_{0.6}CoO_2$,[249, 337] and $K_{0.69}CrO_2$,[338] have been systematically investigated as cathode materials for KIBs. These pioneer studies undoubtedly paved the way for studying innovative layered TMO cathode materials for KIBs. Among all the layered TMOs candidates, potassium manganese oxides (KMOs) are highly attractive, owing to their low cost, earth abundance, environmentally friendliness and high operating voltage. Motivated by these outstanding features, it is promising to employ KMOs as cathode materials for KIBs.

Although many achievements have been made, significant structural change during potassium-ion insertion and the side reactions occurring on the surface of electrode materials are obstacles to their practical application.[330, 339] Considering the tremendous investigations devoted to rechargeable LIBs, appropriate strategies to enhance the electrochemical properties of LIBs are more likely to apply well in KIBs due to the chemical similarity of K to Li. Among

various techniques, surface modification has been recognized as one of the most effective and facile approaches to improving the electrochemical behaviors of layered TMO cathode materials for LIBs.[340] Numerous coating materials such as ZrO_2,[341] TiO_2,[342] $AlPO_4$,[343] AlF_3,[344] and $LiAlF_4$[345-346] have been introduced to improve electrochemical performances of layered TMO cathode materials for LIBs. Among them, AlF_3 coating can effectively prevent the cathode materials from being attacked by the byproducts generated from the oxidation of electrolyte at high voltage such as HF and CO_2, thereby stabilizing the interface between the electrode and electrolyte and preventing the formation of a thick cathode-electrolyte interphase (CEI) layer layer on the surface of cathode materials.[47, 293, 344, 347] Meanwhile, reducing the particle size is also a widely-recognized strategy to improve the alkali metal ion diffusion kinetics within the solid state lattice.[348] The characteristic time constant, τ, for alkali metal ion diffusion is given by $\tau = L^2/D$, where L is the diffusion length in the solid state and D is the diffusion constant. Reducing the particle size can significantly shorten the metal ion diffusion length within the solid state lattice, resulting in a much-enhanced high-rate performance.[349] Although the surface modification technique combined with a down-sizing strategy is efficient to enhance the electrochemical performance of cathode materials, it also significantly reduces the tap density of the cathode material. Since microspheres can easily form close-packed arrays, a three-dimensional micro/nano hierarchical sphere structure is considered as the ideal structure for high-energy density cathode materials.[350] Nanosized primary particles with surface coating can ensure high rate capability and excellent surface stability. Meanwhile, a micro-sized secondary sphere structure can maintain a high volumetric energy density.

Herein, we demonstrate the advantages of employing AlF_3 coated hierarchical $K_{1.39}Mn_3O_6$ microspheres (AlF_3@S-KMO) as a cathode material for KIBs. A precipitation approach combined with calcination was developed to synthesize $K_{1.39}Mn_3O_6$ microspheres (S-KMO) consisting of nanoparticles with a three-dimensional (3D) porous structure. The as-synthesized S-KMO has a relatively high tap density and shows excellent rate capability. Furthermore, the AlF_3 surface coating strategy has been proven to be a facile and effective way to further improve the electrochemical performances of S-KMO for KIBs. Electrochemical measurements confirm that surface modification is beneficial to boost the rate performance as well as cycling stability. The relevant structural evolution and reaction mechanisms were elucidated via *ex situ* XRD characterization. The hierarchical structure design combined with surface modification provides a new guideline for designing high-performance cathode materials for potassium-ion batteries.

4.2 Experimental section

4.2.1 Synthesis of AlF_3 coated $K_{1.39}Mn_3O_6$ (AlF_3@KMO) microspheres

To fabricate $K_{1.39}Mn_3O_6$ microspheres, Mn_2O_3 precursors were synthesized via a facile chemical precipitation method followed by calcination. Firstly, 1.69 g of manganese sulfate monohydrate ($MnSO_4•H_2O$, 99.9%, Sigma–Aldrich) and 0.84 g of sodium bicarbonate ($NaHCO_3$, 99.9%, Sigma–Aldrich) were dissolved in 100 mL distilled water, respectively. Then, the two solutions were mixed under stirring for 30 min. The resulting precipitations ($MnCO_3$)

were washed with deionized water and ethanol for several times and dried under vacuum at 80 ºC overnight. Then, the as-synthesized $MnCO_3$ microspheres were calcined at 600 ºC for 2 h in air to obtain the Mn_2O_3 microspheres. Subsequently, 115 mg of obtained Mn_2O_3 powders together with 97 mg potassium carbonate (K_2CO_3, 99.9%, Sigma–Aldrich) were dispersed into 10 ml deionized water under stirring for 30 min. After drying at 80 ºC under vacuum, the obtained mixture was annealed at 600 ºC for 2 h in air to obtain $K_{1.39}Mn_3O_6$ microspheres. For comparison, bulk $K_{1.39}Mn_3O_6$ (B-KMO) materials were prepared by simply mixing the commercial $MnCO_3$ and K_2CO_3 powders together followed by the same calcination process. For the synthesis of AlF_3@KMO, 4 mg of ammonium fluoride (NH_4F, 99.9%, Sigma–Aldrich) and 7.66 mg of aluminum nitrate ($Al(NO_3)_3$•$9H_2O$, 99.9%, Sigma–Aldrich) were dissolved in 20 ml of deionized water separately. Then, 172 mg $K_{1.39}Mn_3O_6$ powders were added in the aluminum nitrate aqueous solution, followed by slowly dripping the ammonium fluoride solution under constant stirring at 80 ºC for 5 h. The designed stoichiometric molar ratio of Al and F is 1:3, and the amount of AlF_3 coating material is 1 wt% in the final product. After the evaporation of water under vacuum at 80 ºC, the obtained powders were calcined at 400 ºC for 5 h in Ar.

4.2.2. Materials characterization

The morphological analyses were characterized by Field-emission scanning electron microscopy (FE-SEM, Zeiss Supra 55VP) and transmission electron microscopy (TEM, model field emission CM200, Fei) equipped with an energy-dispersive X-ray spectrometer. The

structure information of the as-prepared materials was recorded via a Bruker D8 Discovery X-ray diffractometer using Cu Kα radiation (5° ~ 80° 2-Theta, scanning step of 0.02° per second). X-Ray photoelectron spectroscopy was collected from an ESCALAB250Xi (Thermo Scientific, UK) associated with mono-chromated Al K alpha (energy: 1486.68 eV). Raman spectra were carried on a Renishaw inVia Raman spectrometer system (Gloucestershire, UK) equipped with a Leica DMLB microscope (Wetzlar, Germany) and a 17 mW Renishaw He-Ne laser source at 633 nm. Inductively coupled plasma optical emission spectroscopy (ICP-OES) measurements were performed on a Perkin Elmer OPTIMA 7300. To study the structural changes of as-synthesized electrode materials during cycling, coin cells were dissembled at various charge/discharge stages inside an Ar-filled glove box with water and oxygen levels less than 0.1 ppm. Then the working electrodes were washed with diethyl carbonate (DEC) for several times and dried under vacuum in the antechamber connected with the glove box. The cycled electrodes were directly conveyed to the *ex situ* XRD characterizations.

4.2.3. Electrochemical measurements

A slurry was prepared by mixing the as-synthesized cathode materials, carbon black and polyvinylidene difluoride (PVDF) with a weight ratio of 8:1:1 in N-Methyl-2-pyrrolidone (NMP). The electrodes were fabricated by casting the slurry onto aluminum foils and dried at 80 °C under vacuum overnight. Coin cells (CR2032) were assembled in an Ar-filled glove box with water and oxygen levels less than 0.1 ppm using the as-prepared electrodes as cathodes and potassium metal foils as anodes. Glass microfiber filters (Whatman, Grade GF/D) were

used as the separators. A solution of 0.8 M KPF_6 dissolved in a mixture of ethylene carbonate (EC) and diethyl carbonate (DEC) with a volume ratio of 1:1 was used as electrolyte. The calculated mass loading of the active materials in each electrode is ~ 1.5 mg cm^{-2}. For the electrochemical measurements, galvanostatic charge and discharge measurements were conducted on a computer-controlled NEWARE^{TM} battery tester. Cyclic voltammogram (CV) experiments were carried out on a Biologic VMP3 electrochemical workstation with a scan rate of 0.1 mV s^{-1} in the voltage range of 1.5 V ~ 4 V. In addition, electrochemical impedance spectra (EIS) were acquired in the frequency range from 100 kHz to 10 mHz at room temperature. For galvanostatic intermittent titration technique (GITT) measurements, all the tested cells were initially activated at a current density of 10 mA g^{-1} for 5 cycles before GITT tests. Subsequently, the electrodes were charged/discharged for 10 min at a pulse current of 10 mA g^{-1}, followed by a duration of 2 h relaxation to achieve potassium equilibrium potential.

4.3 Results and discussion

Layered AlF_3@S-KMO materials were synthesized via a typical precipitation method followed by several calcination steps in different atmospheres as shown in **Figure 4.1**a. The synthetic route includes the preparation of $MnCO_3$ microspheres followed by a calcination process to transform the carbonate precursors into oxides. **Figure 4.2** and **Figure 4.3** show the morphology and XRD pattern of the uniform $MnCO_3$ microspheres with a diameter about 1.5 μm. Subsequently, the precursors were converted into Mn_2O_3 (**Figure 4.4**) that still maintains

the microsphere morphology (**Figure 4.5** and **4.6**). After stoichiometrically mixing with K_2CO_3 and further calcining in air, porous spherical KMO was obtained as shown in Figure 4.1b, 4.1c and **Figure 4.7**. Obviously, S-KMO inherits the unique microstructure of the Mn_2O_3 microspheres despite a slight growth in the primary particle size. In addition, the high-resolution transmission electron microscope (HRTEM) image (Figure 4.1d) reveals a lattice spacing of S-KMO with a distance of 0.241 nm, corresponding to the (-112) crystal plane of the reported $K_{1.39}Mn_3O_6$ (monoclinic, C2/m).[351] The hierarchical porous microsphere structure can facilitate the impregnation of electrolyte inside the microspheres and shorten the transportation pathway of K^+ in the solid state lattice. Meanwhile, the closed packed microspheres can maintain a relatively high tap density compared with the bulk counterpart (1.12 g/cm^3 for S-KMO and 1.16 g/cm^3 for bulk materials, respectively). An additional surface coating strategy was applied on S-KMO to further improve its electrochemical performances. Figure 4.1e and 4.1f illustrate AlF_3@S-KMO materials maintain the hierarchical microsphere morphology after AlF_3 coating. The HRTEM image of AlF_3@S-KMO in Figure 4.1g demonstrates the formation of an amorphous AlF_3 coating layer with a thickness of 3.1 nm on the surface of the S-KMO material. Apart from that, the lattice distance of 0.241 nm is consistent with the (-112) plane observed in Figure 4.1d. The TEM-EDS element maps in Figure 4.1h confirms the homogeneous distribution of Al, F, K and Mn elements in the as-prepared AlF_3@S-KMO material. Bulk $K_{1.39}Mn_3O_6$ (B-KMO) was also prepared for comparison. **Figure 4.8** shows that the plate-like particles of B-KMO tend to agglomerate together, forming an aggregated rather than a hierarchical structure.

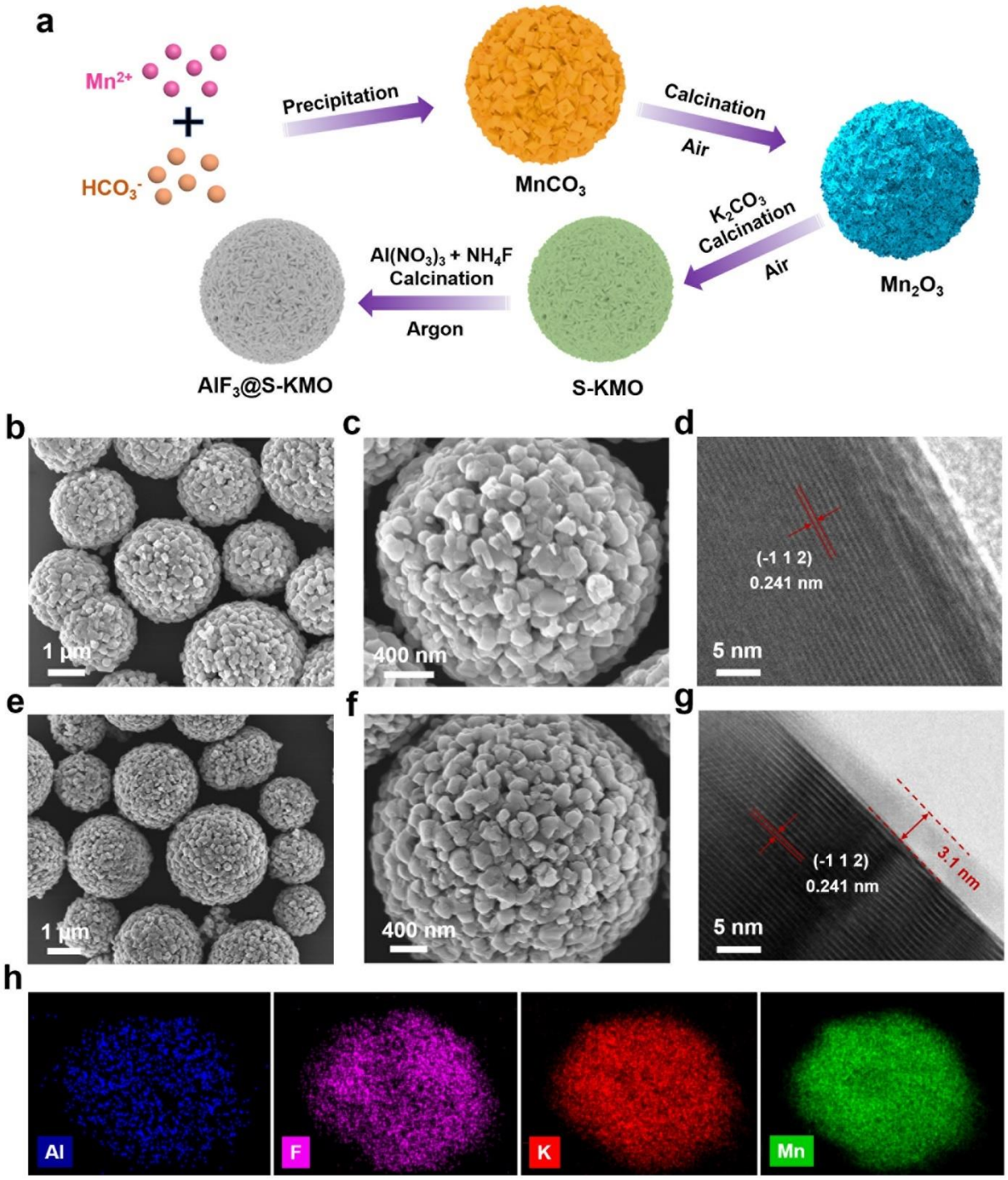

Figure 4.1 (a) Schematic illustration of the synthesis process of AlF_3@S-KMO. (b, c) SEM images and (d) HRTEM image of S-KMO. (e, f) SEM images and (g) HRTEM image of AlF_3@S-KMO. (h) TEM-EDS elemental maps for Al, F, K, and Mn in AlF_3@S-KMO.

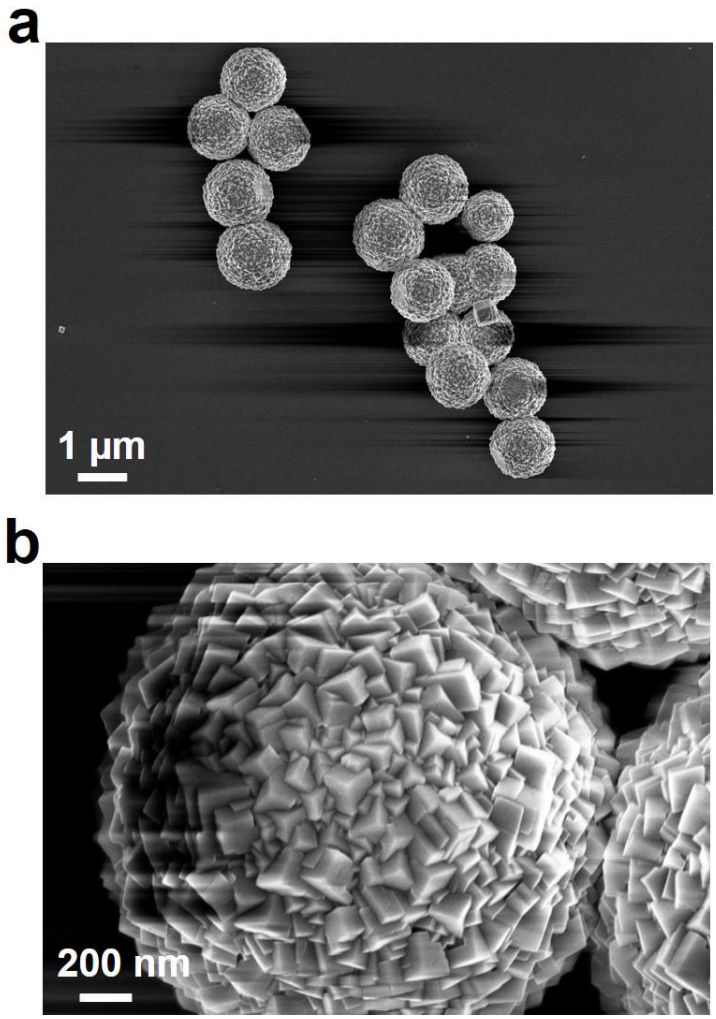

Figure 4.2 (a, b) SEM images of the $MnCO_3$ microspheres.

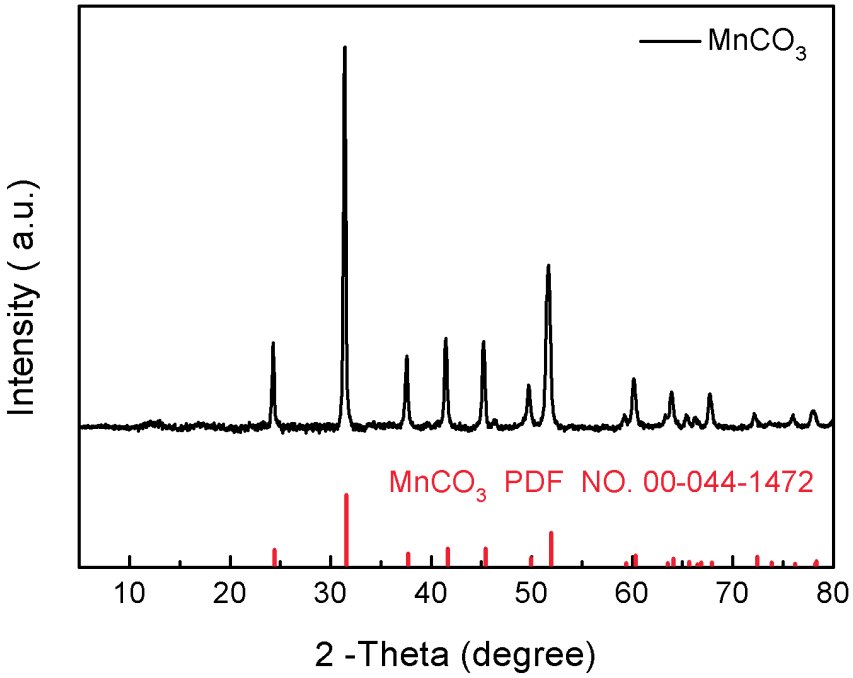

Figure 4.3 XRD pattern of the $MnCO_3$ microspheres.

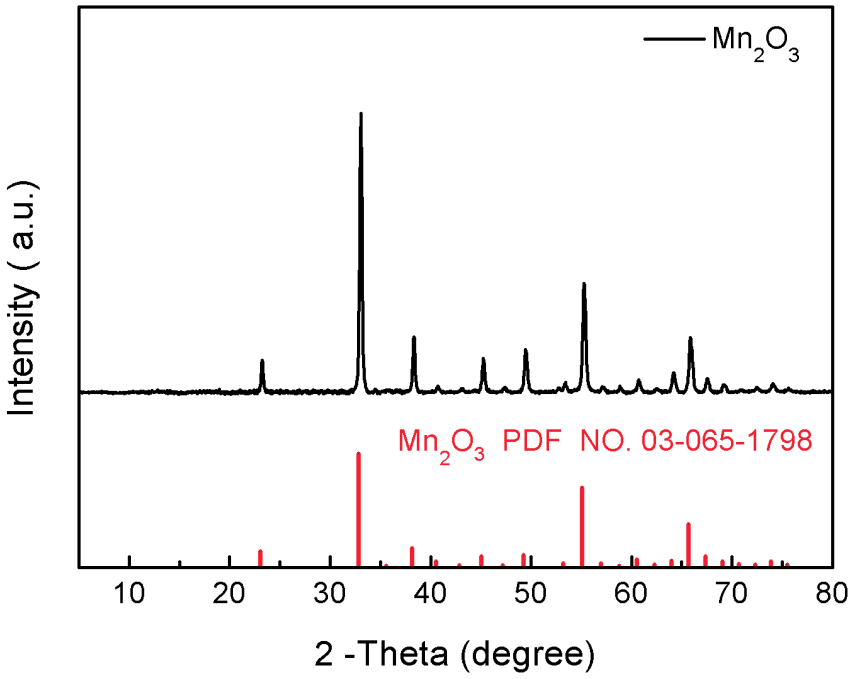

Figure 4.4 XRD pattern of the Mn_2O_3 microspheres.

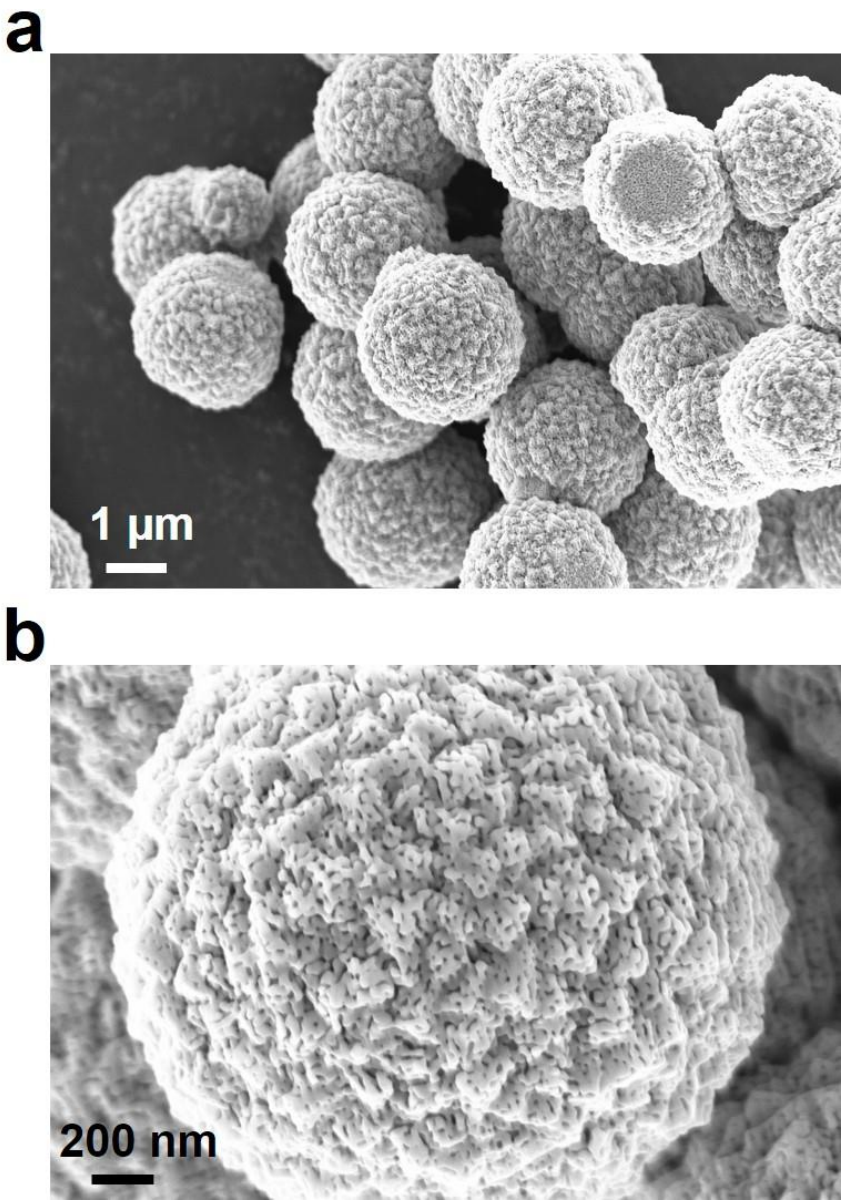

Figure 4.5 (a, b) SEM images of the Mn_2O_3 microspheres.

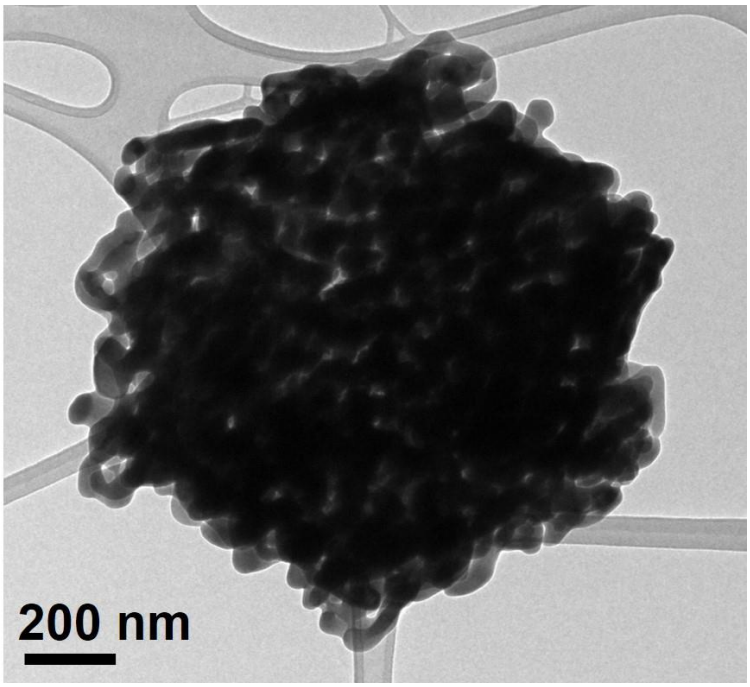

Figure 4.6 TEM image of the Mn_2O_3 microsphere.

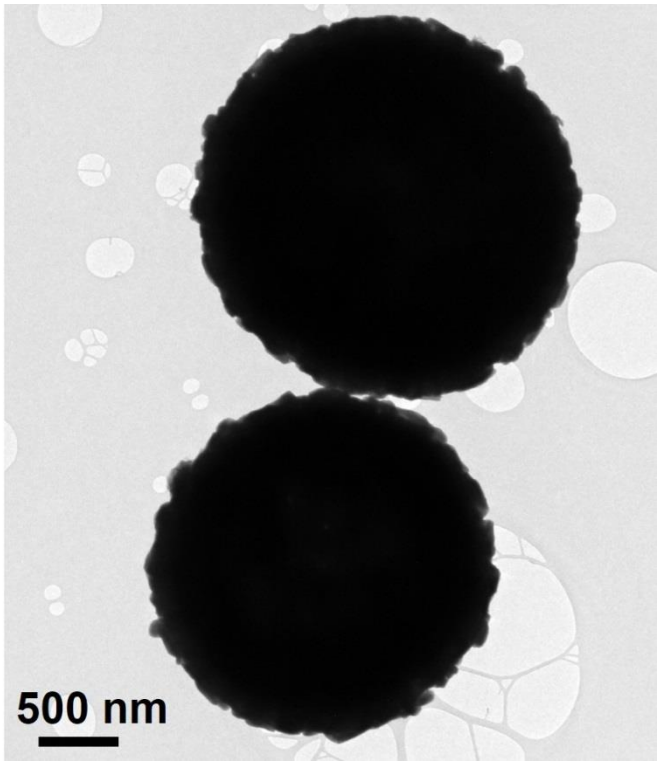

Figure 4.7 TEM image of S-KMO.

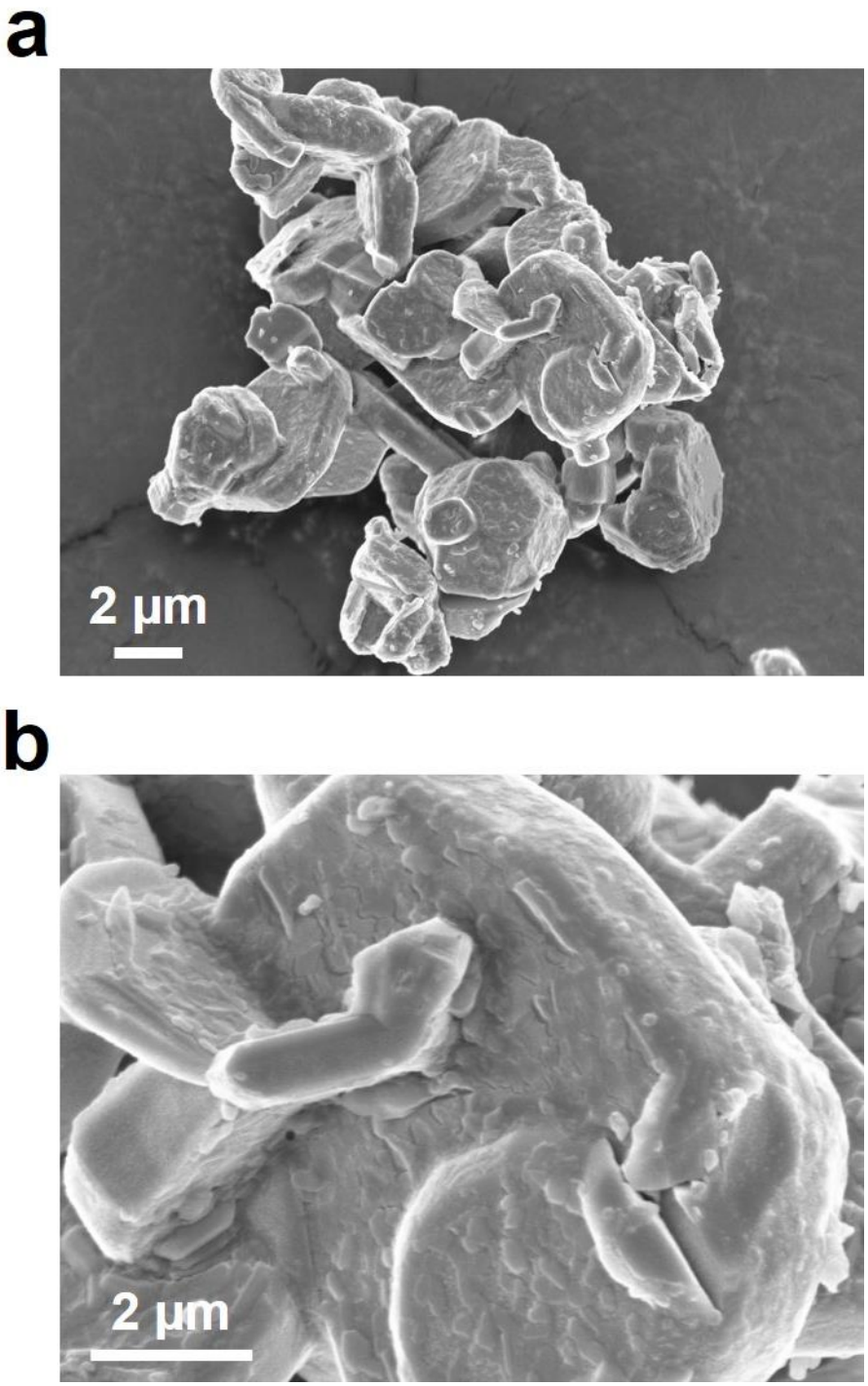

Figure 4.8 (a, b) SEM images of B-KMO.

The crystal structures of the as-synthesized materials were analyzed by X-ray diffraction (XRD). **Figure 4.9**a illustrates the XRD patterns of the as-synthesized KMO materials. All the characteristic peaks can be indexed to monoclinic $K_{1.39}Mn_3O_6$ (JCPDS No. 01-080-7317, a =

14.259 Å, b = 2.8438 Å, c = 9.526 Å) with the space group C2/m. No impurity is observed from the XRD results, indicating surface coating of AlF_3 on S-KMO does not affect the crystal structure of KMO microspheres. Furthermore, inductively coupled plasma optical emission spectroscopy (ICP-OES) analysis determines a K: Mn molar ratio of 0.472 in S-KMO, which is very close to the target value of 0.463, confirming the presence of the K-deficient phase. Raman spectra were obtained and analyzed, and the results are shown in Figure 4.9b. There are six bands located at 280, 402, 472, 509, 575 and 633 cm^{-1}. The higher bands range from 550 to 650 cm^{-1} and represent the symmetric vibration of the MnO_6 group with A_{1g} symmetry, while the lower ranges indicate the Mn-O stretching vibration with F_{2g} symmetry, suggesting the existence of Mn^{3+} and Mn^{4+} ions. All the findings are consistent with the previous reports on birnessite-type manganese oxides.[351-352] XPS analysis results and the corresponding fitting data of the as-synthesized materials are displayed in Figure 4.9c-i. Despite a series of shoulder peaks derived from adventitious carbon species, there are two pairs of XPS peaks in the K region (Figure 4.9d). One peak can be assigned to the $K2p_{3/2}$ spectral peak located at 292.7 eV with an additional satellite peak at 293.8 eV. The other peak reflects the $K2p_{3/2}$ peak at 295.7 eV associated with a weak satellite at 296.3 eV. As for the binding energy of Mn, Figure 4.9e shows two strong peaks at 642.5 and 653.9 eV related to the $Mn2p_{3/2}$ and $Mn2p_{1/2}$ spectra, implying the coexistence of Mn^{3+} and Mn^{4+} valences.[353-354] This conclusion is consistent with the Raman analysis. As regards to oxygen, we can identify four characteristic peaks of the O 1s spectrum in Figure 4.9f. It should be noted that there is a slight increase in the O 1sC peak intensity after AlF_3 coating, which is ascribed to the change in the proportion of oxygen species. Previous

reports have demonstrated that surface modification normally induced the growth of the oxidized lattice oxygen in lithium-rich materials.[346] The signals of F and Al are also detected from AlF_3@S-KMO (Figure 4.9g-i), confirming the existence of AlF_3 surface coating.

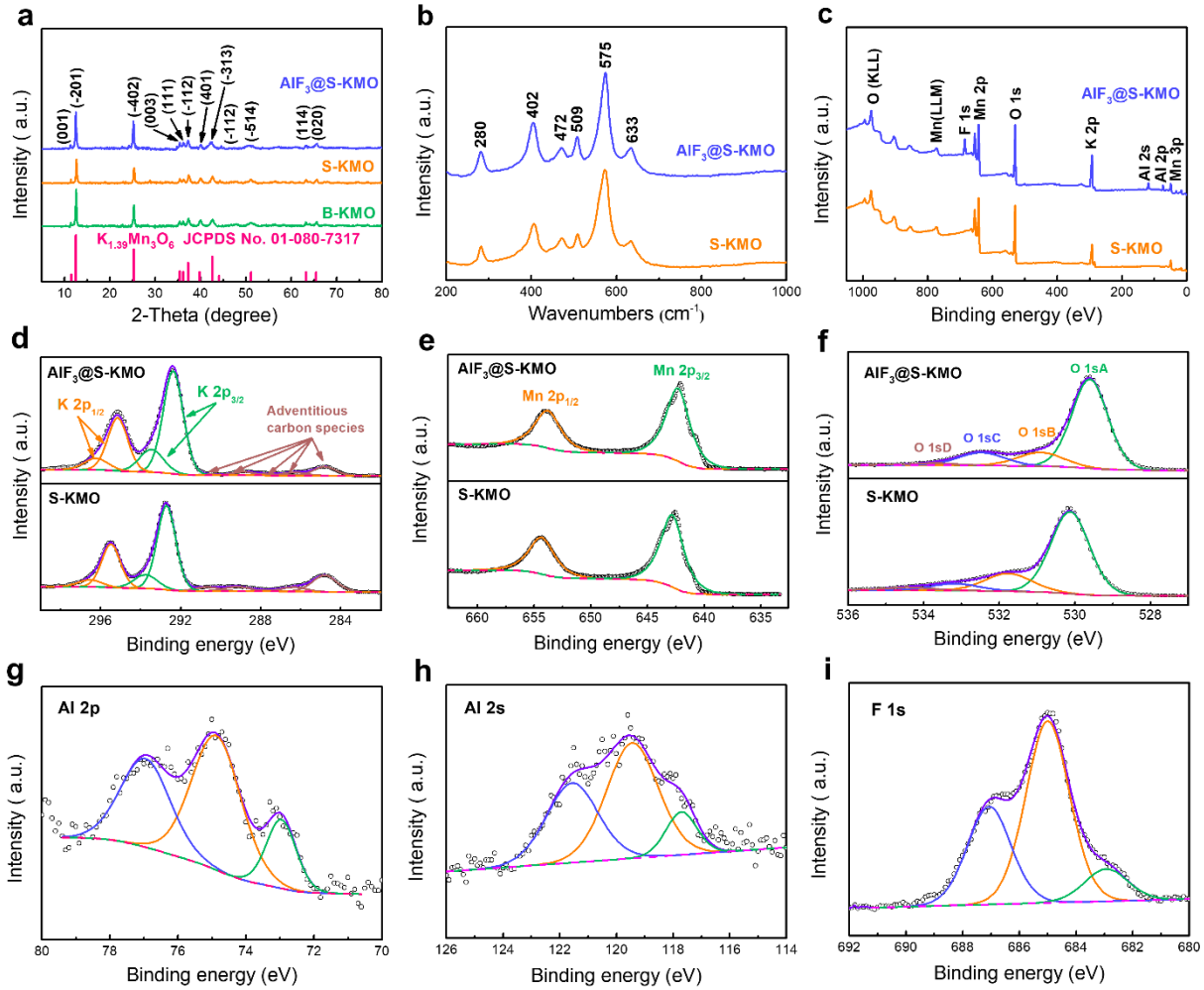

Figure 4.9 (a) XRD patterns of B-KMO, S-KMO and AlF_3@S-KMO. (b) Raman spectra of S-KMO and AlF_3@S-KMO. (c-f) XPS survey and high-resolution spectra of (d) K 2p, (e) Mn 2p and (f) O1s of S-KMO and AlF_3@S-KMO. (g-i) High-resolution XPS spectra of Al 2p, Al 2s and F 1s in AlF_3@S-KMO.

The electrochemical properties of as-synthesized materials were examined by cyclic voltammetry (CV) in the voltage range 1.5 – 4 V at a scan rate of 0.1 mV s^{-1}. In **Figure 4.10**a, there is a strong and distinct cathodic peak at 2.14 V during the first discharge process, which is less obvious in the following cycles. The evolution of such a cathodic peak in the initial discharge process reveals the excessive insertion of K^+ into the K-deficient phase. Moreover, during cycling, the intensities of the redox peaks in the high operating voltage range continuously increase, which is ascribed to the instability of the K-extracted phase and rapid decomposition of electrolyte. By contrast, in Figure 4.10b, the overlapped and well-kept CV curves of the AlF_3@S-KMO electrode suggest enhanced structural stability through AlF_3 coating. After the first scan, four pairs of redox peaks can be identified at 2.14/2.51 V, 2.53/2.95 V, 2.78/3.18 V and 3.5/3.83 V, indicating complex intermediate reactions occurring during the charge and discharge processes. Accordingly, **Figure 4.11** illustrates the CV curves of the B-KMO electrode. The intensities of the redox peaks are much smaller than the S-KMO electrode, indicating the low electrochemical activity of B-KMO materials.

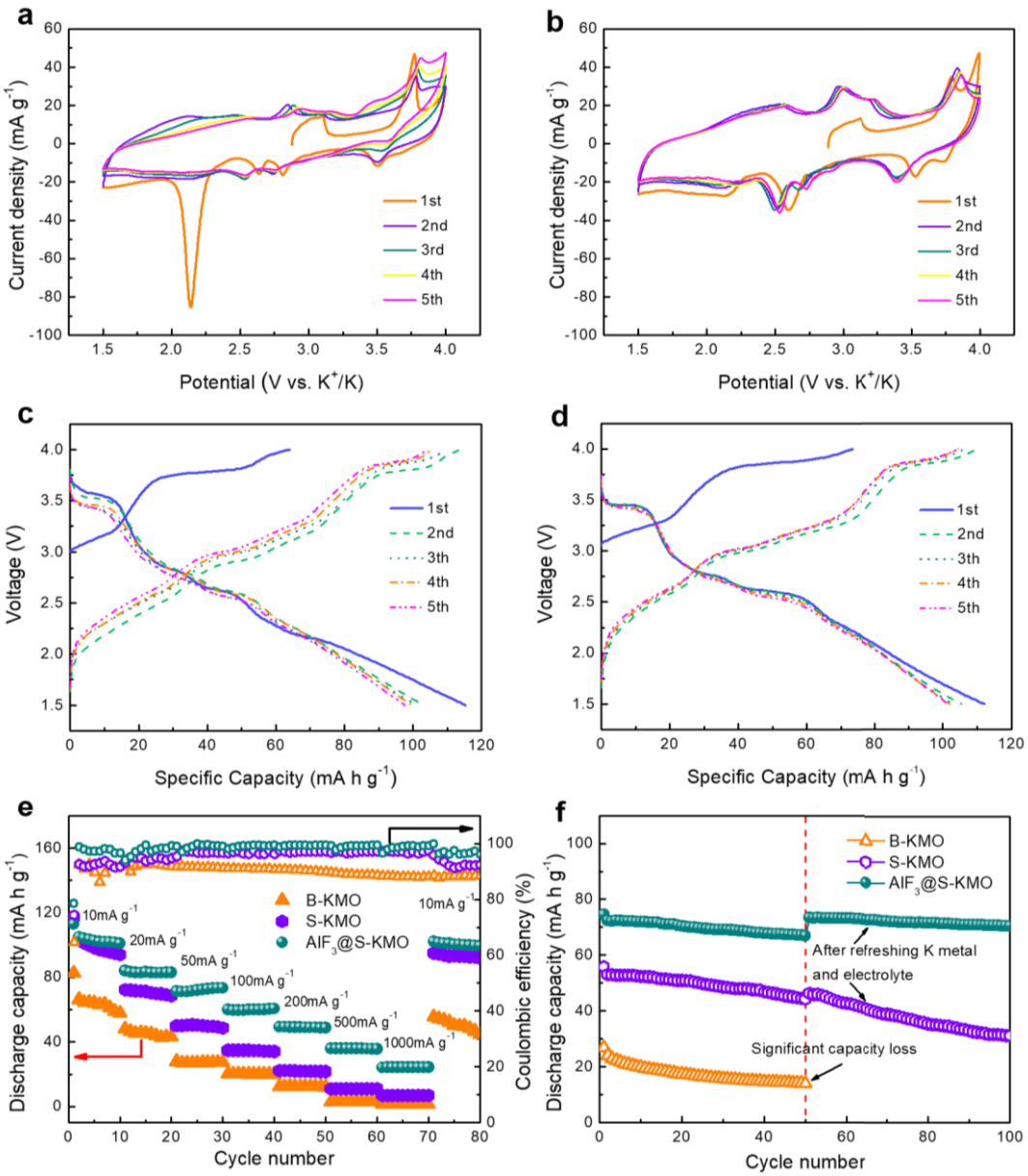

Figure 4.10 Cyclic voltammetry of cells with (a) S-KMO electrode and (b) AlF_3@S-KMO electrode between 1.5 and 4 V (vs. K^+/K) at a scan rate of 0.1 mV s^{-1}. Galvanostatic charge and discharge voltage profiles of cells with (c) S-KMO electrode and (d) AlF_3@S-KMO electrode under a current density of 10 mA g^{-1}. (e) Rate performances of cells with B-KMO, S-KMO and AlF_3@S-KMO electrodes at different current densities. (f) Cycling performance of cells with B-KMO, S-KMO and AlF_3@S-KMO electrodes at 50 mA g^{-1} before and after refreshing the potassium metal anodes and electrolyte.

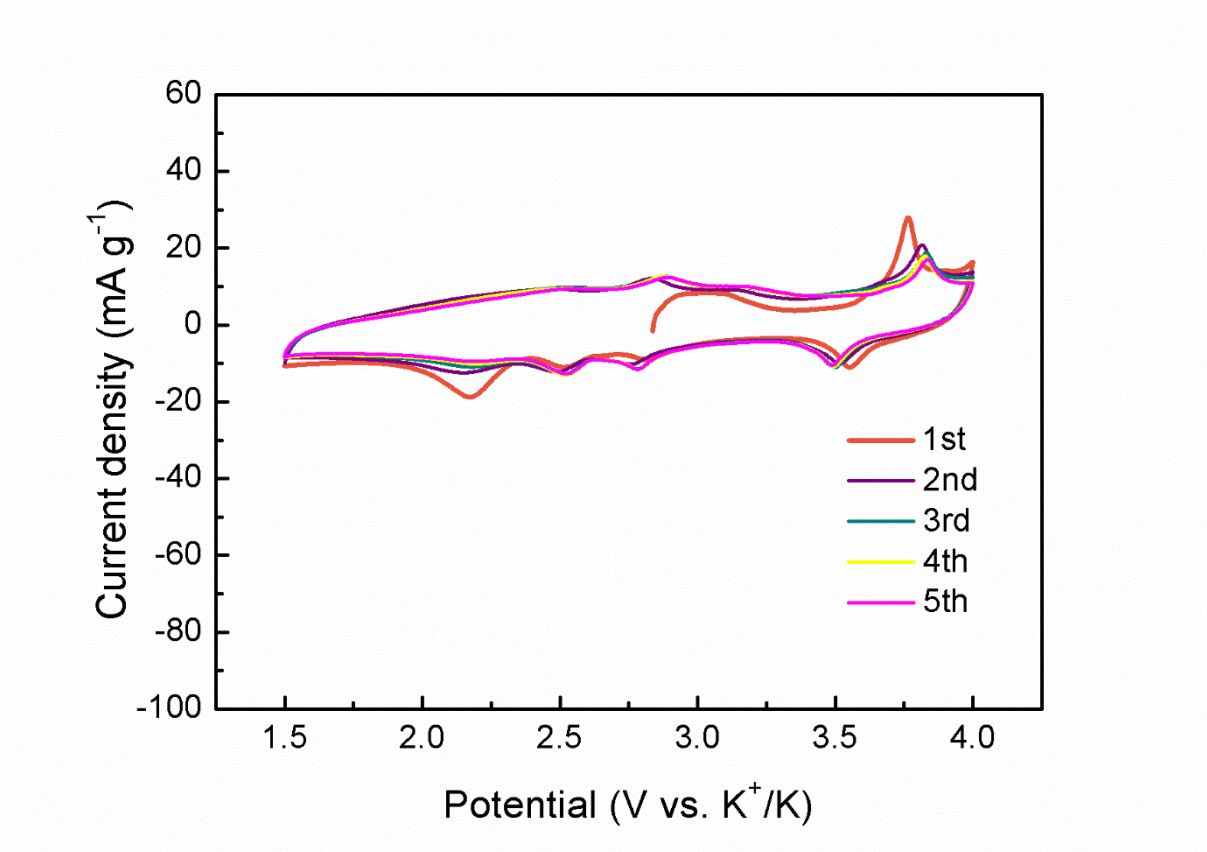

Figure 4.11 Cyclic voltammetry of B-KMO between 1.5 and 4 V vs. K^+/K at a scan rate of 0.1 mV s^{-1}.

To evaluate potassium storage capability of the as-synthesized materials, galvanostatic charge and discharge measurements were performed at a current density of 10 mA g^{-1}. Figure 4.10c and 4.10d show the voltage profiles of S-KMO and AlF_3@S-KMO electrodes. The sloped features of the voltage curves upon K^+ extraction and insertion match well with the redox peaks in the corresponding CV curves, suggesting the presence of multistep reactions. The first charge and discharge capacities of the S-KMO electrode are 64 mAh g^{-1} and 115 mAh g^{-1}, corresponding to the extraction of 0.75 K^+ and reinsertion of 1.35 K^+. The AlF_3@S-KMO electrode delivers capacities of 73 mAh g^{-1} and 112 mAh g^{-1} for the first charge and discharge

processes, representing the extraction of 0.86 K^+ and reinsertion of 1.32 K^+. It should be noted that the K-deficient phase is responsible for the lower initial charge capacity, which is consistent with the previous reports on $K_{0.5}MnO_2$ and $K_{0.5}V_2O_5$.[335, 355] Additionally, we can see a unique voltage slope in the first discharge of the S-KMO electrode at 2.14 V (Figure 4.10c) corresponding to the strong cationic peak in Figure 4.10a, while this feature is less obvious after the surface coating (Figure 4.10d). As the cycle proceeds, this voltage plateau almost disappears, which implies that the initial K^+ insertion process leads to a drastic and irreversible structural change in S-KMO materials, whereas this impact is less pronounced for AlF_3@S-KMO materials. For the B-KMO electrode, the most striking difference is the disappearance of the sloped characteristics of the voltage curves after the initial few cycles (**Figure 4.12**). This phenomenon reveals the low electrochemical activity of the bulk structure which hinders the diffusion of K^+ into the solid interior. Figure 4.10e compares the rate capability of as-prepared electrodes when cycling between 1.5 and 4.0 V. The AlF_3@S-KMO electrode shows much higher discharge capacities and Coulombic efficiencies (CEs) than that of B-KMO and S-KMO electrodes when the current density is increased from 10 mA g^{-1} to 1000 mA g^{-1}. Furthermore, the discharge capacities of the AlF_3@S-KMO electrode can be fully recovered when the current density is returned to 10 mA g^{-1}, indicating excellent electrochemical reversibility. These results manifest the poor and sluggish kinetics of K ions have been notably improved via surface modification.

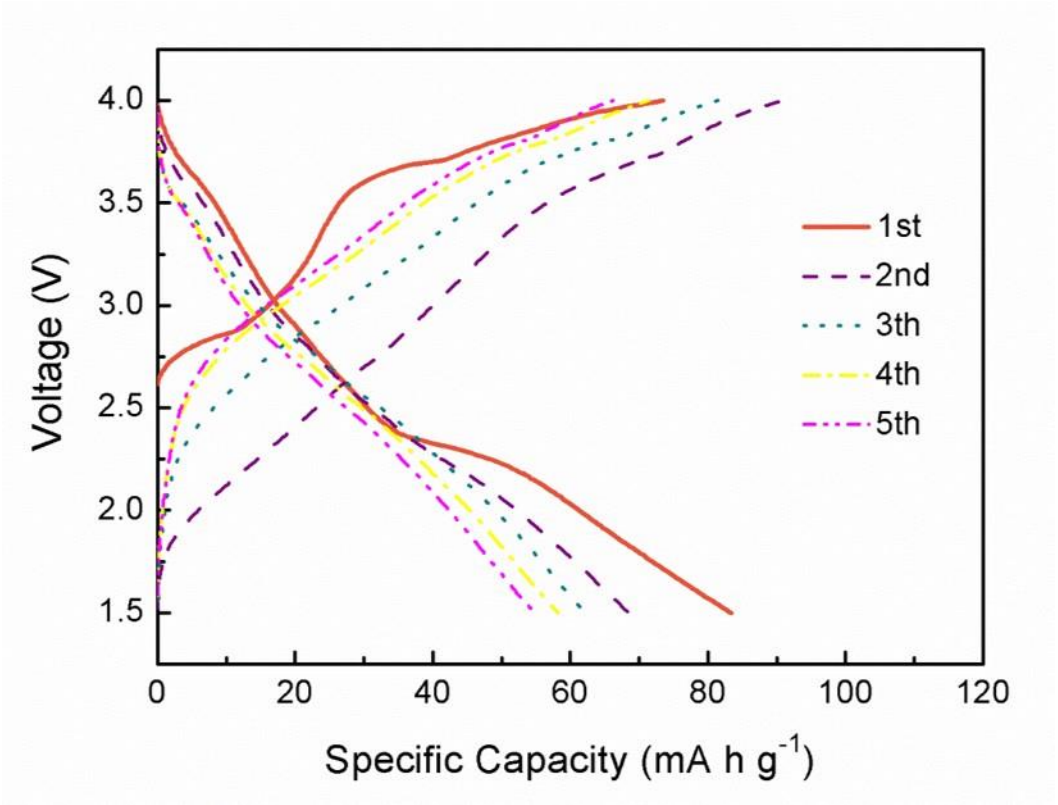

Figure 4.12 Galvanostatic charge/discharge voltage profiles of the B-KMO electrode at a current density of 10 mA g^{-1}.

As the cycle life is a very important criterion for practical application, all three types of electrodes were tested under a current density of 50 mA g^{-1} for 50 cycles. In Figure 4.10f, as expected, an AlF_3@S-KMO electrode exhibits better cycling stability than a S-KMO electrode or the B-KMO electrode after 50 cycles. However, they all suffer from a certain degree of capacity fading. According to previous reports, the major reasons for the significant capacity loss and structural change are from: i) the dramatic structural change during cycling, ii) the unremitting side reactions among cathodes, electrolytes and byproducts generated from electrolyte decomposition such as CO_2 and HF.[339] Based on this point, we observed the morphologies of the S-KMO and AlF_3@S-KMO electrodes before and after 50 cycles. The

SEM images in **Figure 4.13** illustrate the microsphere morphology of S-KMO was destroyed after 50 cycles. By contrast, the AlF_3@S-KMO electrodes maintained their primary microstructures after 50 cycles (**Figure 4.14**). Furthermore, the variation of the XRD patterns of the S-KMO and AlF_3@S-KMO electrodes were compared before and after different cycles as shown in **Figure 4.15**. Impurities observed through the presence of 2θ peaks between 30° and 40° are observed after the 10^{th} cycle for S-KMO electrodes, revealing the generation of by-products. In contrast, the AlF_3@S-KMO electrodes are able to maintain their primary XRD pattern even at the end of the 50^{th} cycle. To eliminate by-products from cycling, we refreshed the potassium metal anodes and electrolytes after 50 cycles. In this case, as shown in Figure 4.10f, the AlF_3@S-KMO electrode exhibits a high specific capacity of 73.44 mA g^{-1} and an excellent cycling stability after refreshing. At the same time, although part of the capacity is restored, the S-KMO electrode experiences much faster capacity degradation. Therefore, surface modification is an effective and facile method to minimize the influence of harmful reactions on cathodes and stabilize the electrode-electrolyte interface. The excellent rate capability and good cycling stability of AlF_3@S-KMO materials also showed better electrochemical performances than previous reported cathode materials for KIBs as shown in **Table 4.1**. Furthermore, such a benefit was also obtained at the elevated temperature. It is well known that the high working temperature normally accelerates side reactions in aprotic rechargeable batteries.[47, 335] As we can see from **Figure 4.16**, when testing the cells at 45 °C, the impact of high temperature on capacity loss for the AlF_3@S-KMO electrode is less significant than that in the S-KMO electrode. Three characteristic peaks located at 28.9°, 32.3°

and 36.1° after the 50th discharge are observed for the S-KMO electrode, which correspond to the Mn_3O_4 phase (PDF 00-024-0734). The appearance of additional peaks implies the partial dissolution of the cathode material during the harsh operating environment.

Table 4.1 The comparison of different layered TMOs for KIBs cathodes.

KIBs cathodes	Electrolyte	Specific capacity	Cycling life	Coulombic efficiency	Reference
P'2-$K_{0.3}MnO_2$	1.5 m KFSI in EC: DMC	70 mAh g^{-1} at 0.1 C	57% (685 cycles)	93%	[333]
P3-$K_{0.5}MnO_2$	0.7 m KPF_6 in EC: DEC	97 mAh g^{-1} at 10 mA g^{-1}	70% (50 cycles)	95%	[335]
$K_{0.7}Fe_{0.5}Mn_{0.5}O_2$	0.8 m KPF_6 in EC: DMC	114 mAh g^{-1} at 100 mA g^{-1}	87% (450 cycles)	98%	[334]
$K_{0.67}Ni_{0.17}Co_{0.17}Mn_{0.66}O_2$	0.8 m KPF_6 in EC: DEC	76.5 mAh g^{-1} at 20 mA g^{-1}	87% (100 cycles)	97.6%	[332]
P2-$K_{0.6}CoO_2$	0.7 m KPF_6 in EC: DEC	78 mAh g^{-1} at 2 mA g^{-1}	60% (120 cycles)	99%	[249]
P2-$K_{0.6}CoO_2$	0.9 m KPF_6 in EC: DEC	82 mAh g^{-1} at 10 mA g^{-1}	87% (300 cycles)	99%	[337]
P3-$K_{0.69}CrO_2$	0.5 m KPF_6 in EC: DEC	100 mAh g^{-1} at 0.1 C	65% (1000 cycles)	97%	[338]
$K_{0.5}V_2O_5$	1.5 m KFSI in EC: DEC	90 mAh g^{-1} at 10 mA g^{-1}	81% (250 cycles)	99%	[355]
$K_{1.39}Mn_3O_6$	0.8 m KPF_6 in EC: DEC	110 mAh g^{-1} at 10 mA g^{-1}	94.9% (100 cycles)	99%	This work

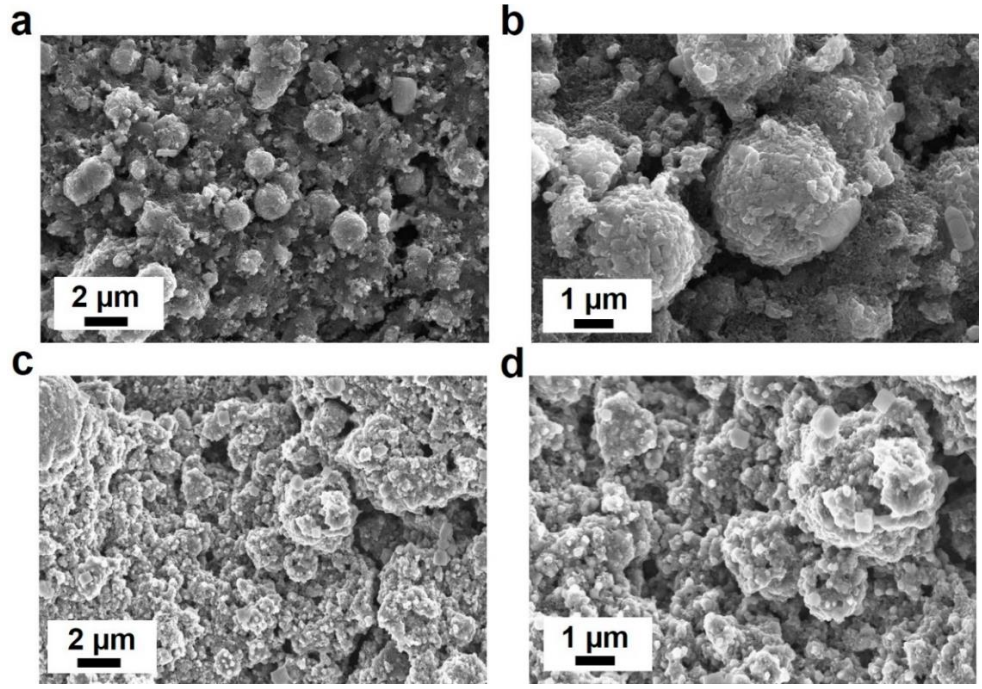

Figure 4.13 SEM images of S-KMO electrodes at different magnifications. (a, b) before and (c, d) after 50 cycles.

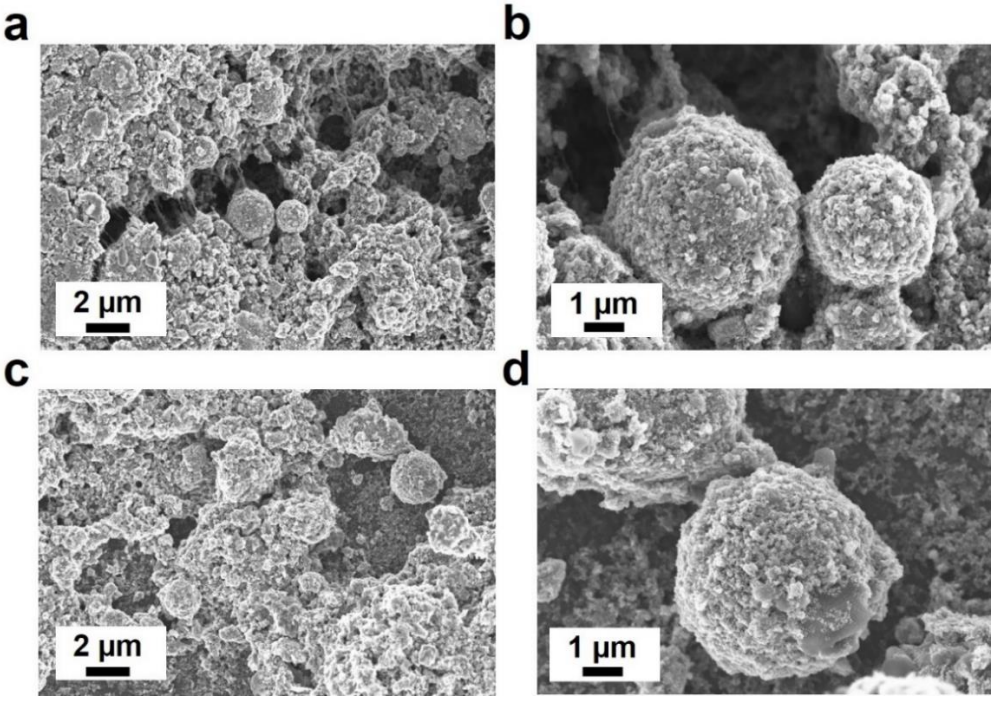

Figure 4.14 SEM images of AlF_3@ S-KMO electrodes at different magnifications. (a, b) before and (c, d) after 50 cycles.

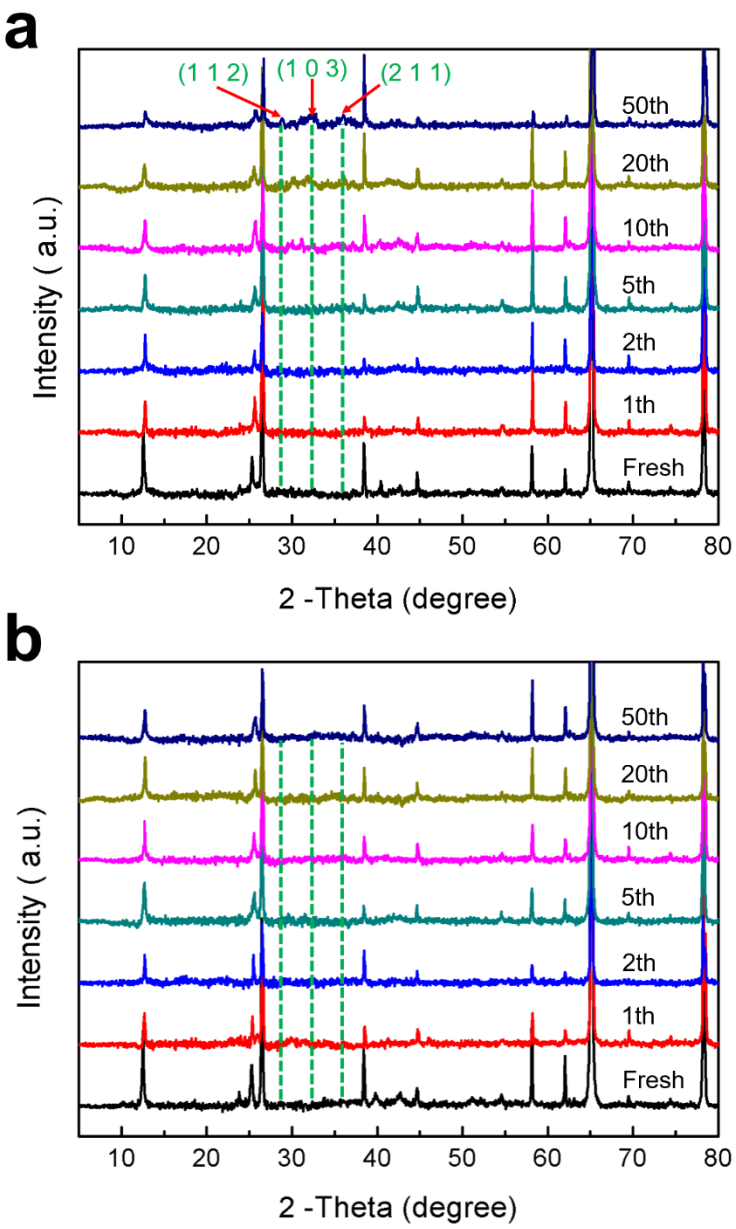

Figure 4.15 *Ex situ* XRD results of (a) S-KMO electrodes and (b) AlF_3@S-KMO electrodes before and after 1st, 2nd, 5th, 10th, 20th and 50th cycles. The cells were cycled at 50 mA g^{-1}.

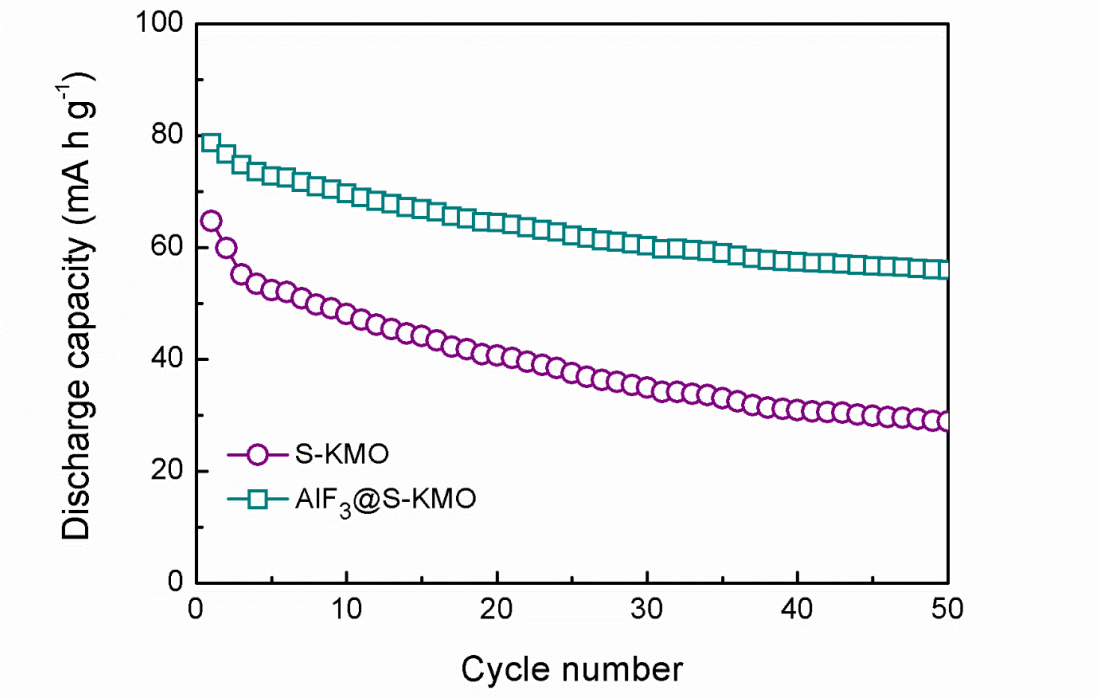

Figure 4.16 Cycling performances of S-KMO and AlF_3@S-KMO electrodes at 45 °C.

To determine whether the microstructure as well as the surface coating can affect the reaction kinetics of KMO cathode materials, galvanostatic intermittent titration technique (GITT) was employed to investigate the diffusion kinetics of K^+. **Figure 4.17**a, 4.17b and **Figure 4.18** clearly show the transient voltage responses versus specific capacity profiles after activation for 5 cycles. Obviously, the multiple sloped features of the voltage profiles are well maintained for S-KMO and AlF_3@S-KMO electrodes, whereas these features disappear in the B-KMO electrode. Meanwhile, the B-KMO electrode exhibits the largest overpotential among all the cells tested, especially noticeable at the very end of each charge or discharge process. The reaction resistances upon K^+ insertion and extraction were calculated and summarized in Figure 4.17c and 4.17d, respectively. At the beginning of the charging process, the reaction resistance of B-KMO electrode rises sharply to 92 Ω g, which is nearly triple the value obtained from the

S-KMO (36 Ω g) and AlF_3@S-KMO electrodes (28 Ω g). Despite the erratic fluctuation of resistances in B-KMO and S-KMO, the resistance values of AlF_3@S-KMO remain almost constant to the end of charge and discharge processes. To further determine the reaction kinetics of as-prepared cathodes, we evaluated the diffusion coefficient of K^+ (D_k) with respect to **Equation 1**.[356]

$$D_k = \frac{4}{\pi}\left(\frac{IV_m}{Z_A FS}\right)^2 \left[\frac{\left(\frac{dE}{d\delta}\right)}{\left(\frac{dE}{d\tau^{0.5}}\right)}\right]^2 \qquad \textbf{Equation 4.1}$$

Wherein, I, V_m, τ and Z_A are the applied current, molar volume of materials, duration of current pulse and the charge amount of K^+, respectively. F represents the Faraday constant, and S is the contact surface area between electrode and electrolyte. dE/dδ indicates the slope of the Coulometric titration profiles, and $dE/dt^{0.5}$ can be calculated from relation curves between voltage and response time. If the cell voltage is linearly proportional to $t^{0.5}$ (**Figure 4.19**), the diffusion coefficient D_k is obtained by simplifying the **Equation 4.2** according to the Fick's second law.[357]

$$D_k = \frac{4}{\pi\tau}\left(\frac{n_m V_m}{S}\right)^2 \left(\frac{\Delta E_s}{\Delta E_\tau}\right)^2 \qquad \textbf{Equation 4.2}$$

Wherein, ΔEs is the difference in equilibrium potential before and after the current pulse, ΔEτ is the variation of cell voltage caused by the impulse current. n_m represents the number of moles. The decrease of D_k in both B-KMO and S-KMO electrodes during the K^+ extraction and reinsertion is observed in Figure 4.17e and 4.17f. In contrast, the AlF_3@S-KMO electrode is able to maintain a considerable high diffusion coefficient. The calculated D_k of the AlF_3@S-KMO electrode is 0.84×10^{-13} cm^2 s^{-1} for charging at the end of the charge process and 1.1 ×

10^{-12} cm^2 s^{-1} for discharging at the end of the discharge process, respectively, which is much higher than that of the S-KMO electrode (0.36×10^{-13} cm^2 s^{-1} for charging and 0.77×10^{-13} cm^2 s^{-1} for discharging) and the B-KMO electrode (0.55×10^{-14} cm^2 s^{-1} for charging and 0.19×10^{-13} cm^2 s^{-1} for discharging). Therefore, the diffusion of K^+ into solid state AlF_3@S-KMO is kinetically more rapid compared with the cathode without surface modification. This is mainly because the complex side reactions on the surface of electrode materials have been minimized after surface coating with AlF_3.[47]

The electrochemical impedance spectra (EIS) of as-prepared electrodes were analyzed in the frequency range from 100 kHz to 0.01 Hz after the first and fifth cycles (**Figure 4.20**). The S-KMO electrode shows much lower charge transfer resistance (R_{ct}) than that of the B-KMO electrode, demonstrating the advantages of the hierarchical porous sphere structure. Reducing the primary nanoparticles of KMO materials can significantly enhance the K^+ transportation kinetics. However, both B-KMO and S-KMO electrodes show significantly increased R_{ct} at the fifth cycle. By contrast, although the R_{ct} of AlF_3@S-KMO electrode is similar to that of the S-KMO electrode after the first cycle, there is no obvious increase after the fifth cycle, indicating the good stability of the interface between the cathode materials and electrolyte. These results are consistent with the large reaction resistance found in the above GITT measurements, reflecting the large kinetic barrier caused by the unwanted side reactions on the surface of the cathode materials. Such a circumstance manifests the impact of adverse reactions occurring in the early stage has been effectively suppressed through AlF_3 coating.[358] Considering the

extremely poor electrochemical performance of the B-KMO electrode, we therefore chose S-KMO and AlF_3@S-KMO electrodes as research subjects in the following investigations.

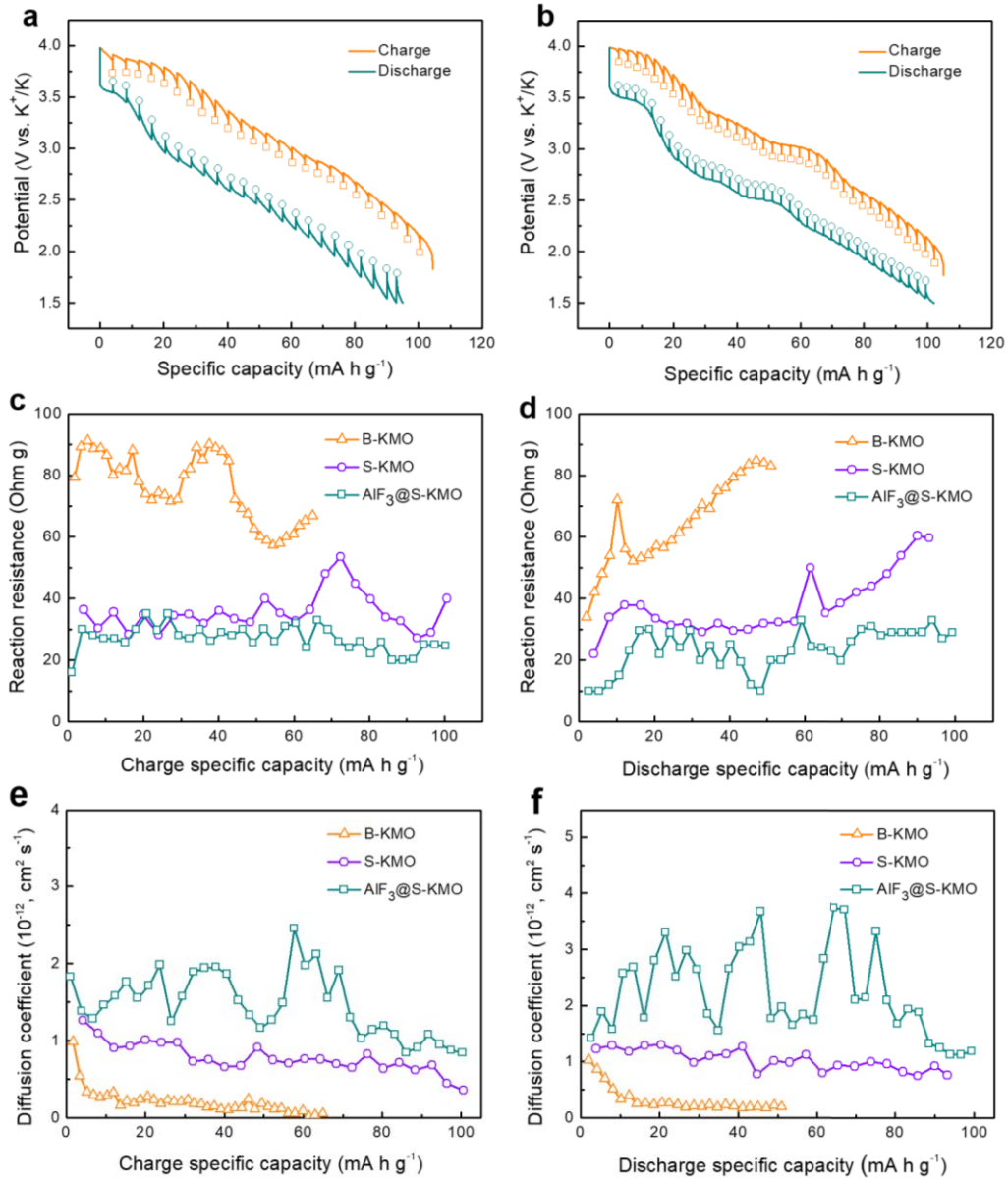

Figure 4.17 Galvanostatic intermittent titration technique (GITT) results for the (a) S-KMO electrode and (b) AlF_3@S-KMO electrode measured at a constant current density of 10 mA g^{-1}. (c) Charge reaction resistances and (d) discharge reaction resistances of B-KMO, S-KMO and AlF_3@S-KMO electrodes. The corresponding calculated diffusion coefficients of K^+ (e) insertion and (f) extraction *vs.* specific capacity.

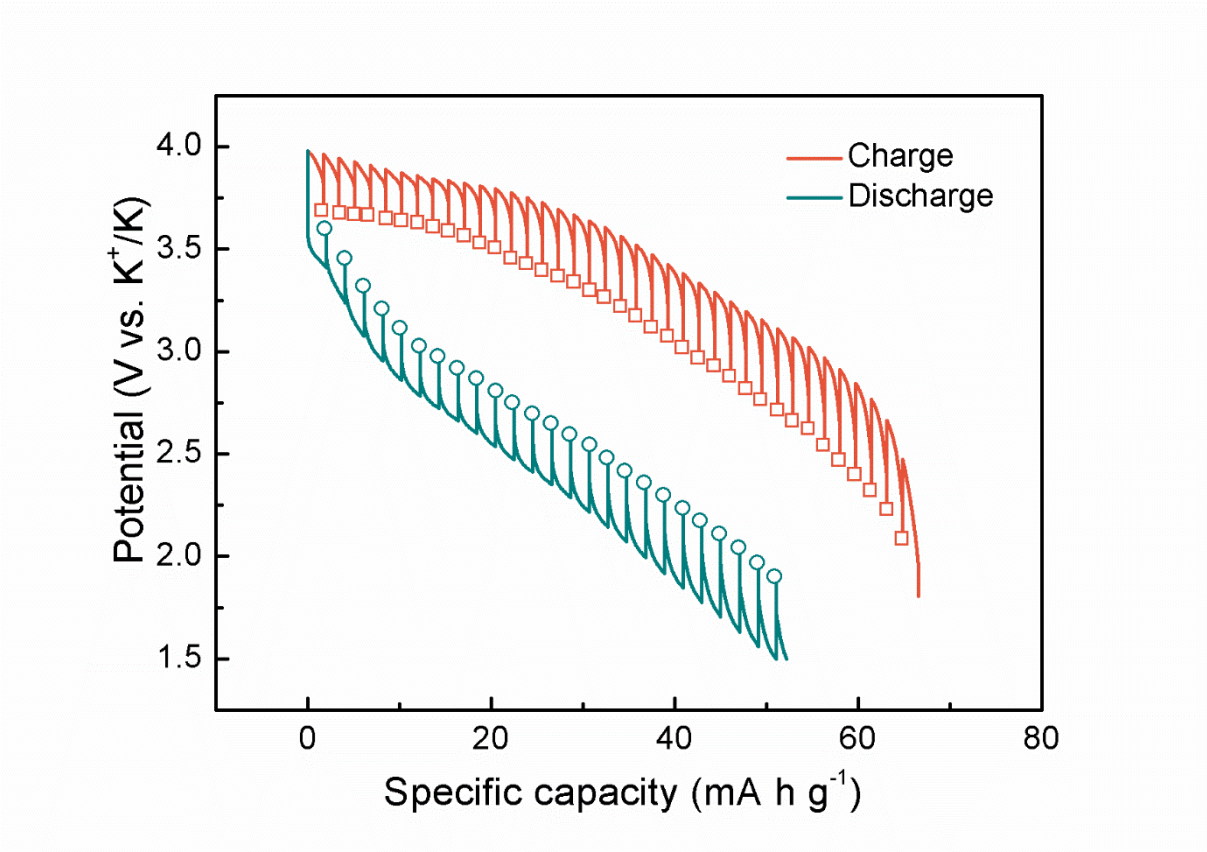

Figure 4.18 GITT profiles of the cell with B-KMO electrode at the current density of 10 mA g^{-1}.

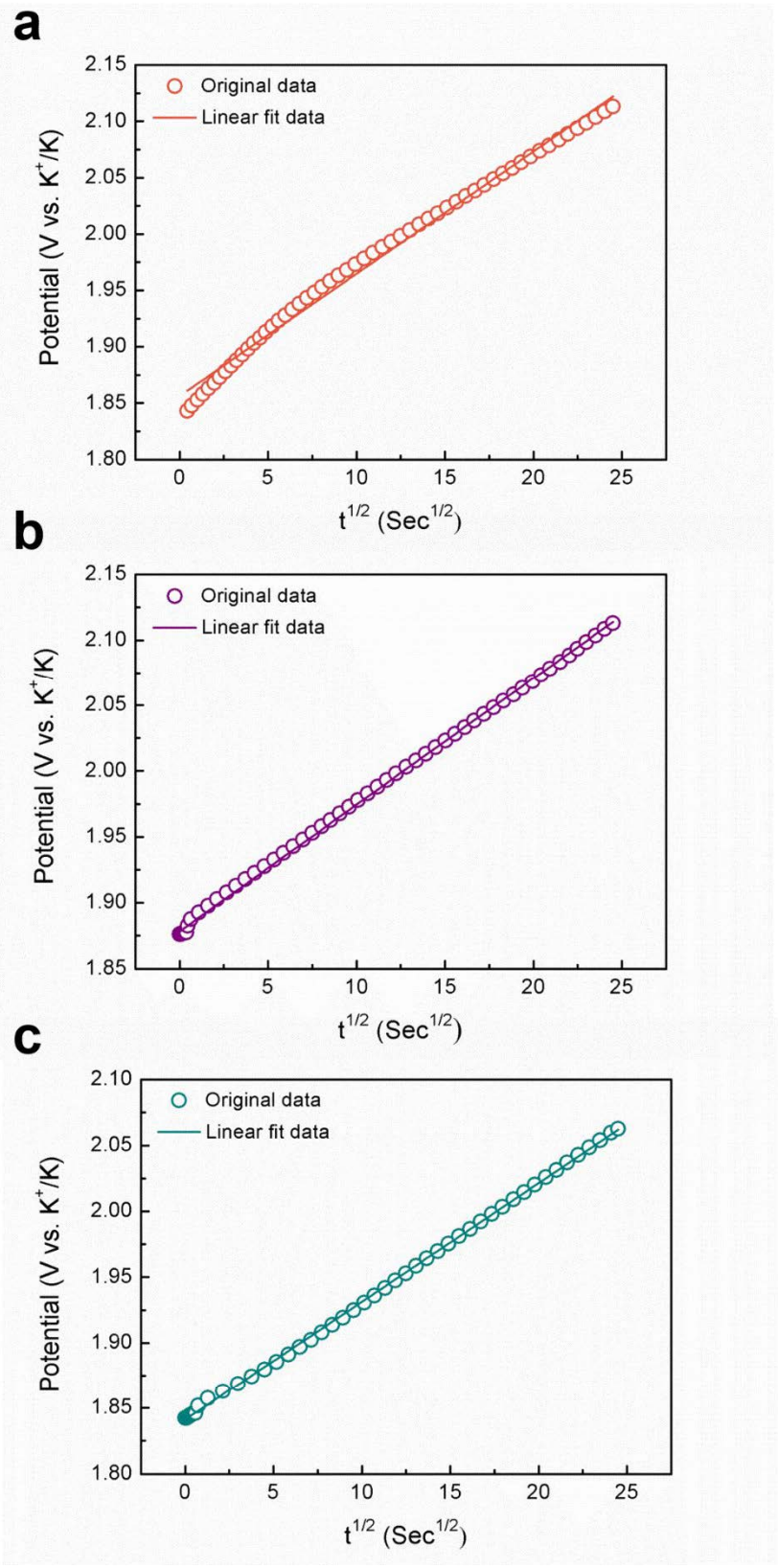

Figure 4.19 (a-c) Linear fitting results of the potential versus $\tau^{1/2}$ relationship.

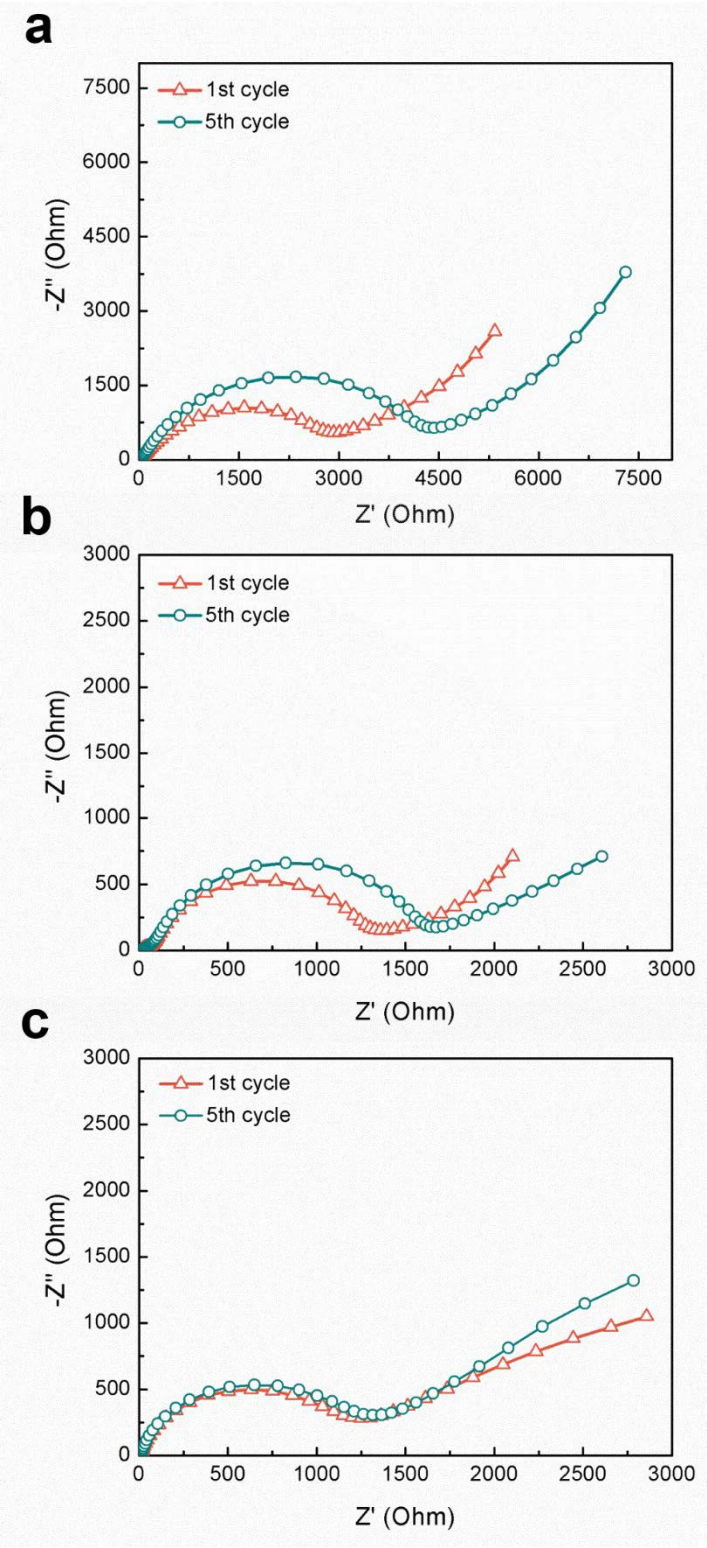

Figure 4.20 Electrochemical impedance spectra (EIS) of the cells with (a) B-KMO, (b) S-KMO and (c) AlF_3@S-KMO electrodes after the first and fifth cycles.

Ex situ XRD measurement was performed to further study the structure evolution and K-storage mechanisms of S-KMO and AlF_3@S-KMO electrodes. Before cycling, we can observe two characteristic peaks of (4 0 1) and (-3 1 3) located at 2θ = 39.9 and 42.7°, respectively (**Figure 4.21**). However, these two peaks disappear during the first charge process. This phenomenon is ascribed to an irreversible structural change during K^+ release in the initial charge stage. After the electrodes were fully charged to 4.0 V, the strong (-4 0 2) peaks disappear and the (-2 0 1) peaks become broad and weak. During the first discharge process, the intensities of (-4 0 2) and (-2 0 1) peaks recover and shift to higher angles without producing any observable new diffraction peaks. This trend could be originated from the decrease of repulsion power between the alternative oxygen atoms and the shrinkage of the MnO_2 slab distance after K^+ extraction.[335, 359] Additionally, an obvious shift towards a higher position is detected for the (-1 1 2) peak of S-KMO when discharging to 2.14 V (**Figure 4.22**a). This evolution is consistent with the strong cathodic peak of the CV curves in Figure 4.10a, indicating the irreversible structural change due to K^+ reinsertion. By contrast, there is no obvious change in the corresponding characteristic peak of AlF_3@S-KMO under the same situation (Figure 4.22b). Furthermore, at the end of the first discharge, both the (-4 0 2) and (-2 0 1) peaks shift to higher angles compared to their original positions, revealing the excessive insertion of K^+ (~1.55 mol). In the second charge and discharge process, both S-KMO and AlF_3@S-KMO electrodes exhibit slow shifts of (-4 0 2) and (-2 0 1) peaks toward lower angles and then gradually return to their previous positions, indicating the highly reversible K^+ extraction and insertion processes representing by the regular change of the interlayer distance.

Figure 4.23 compares the variation of the lattice spacing versus the corresponding 2θ degree at different charge and discharge stages. The changes of the lattice spacing of S-KMO are more significant than that in AlF_3@S-KMO, especially the huge increase of the crystal plane distance of (-1 1 2) peak at 2.14 V. This trend indicates that surface coating of a AlF_3 nanolayer on S-KMO effectively buffers the dramatic structure change upon K^+ extraction and insertion, which enhances the structural stability of layered KMO cathode materials.

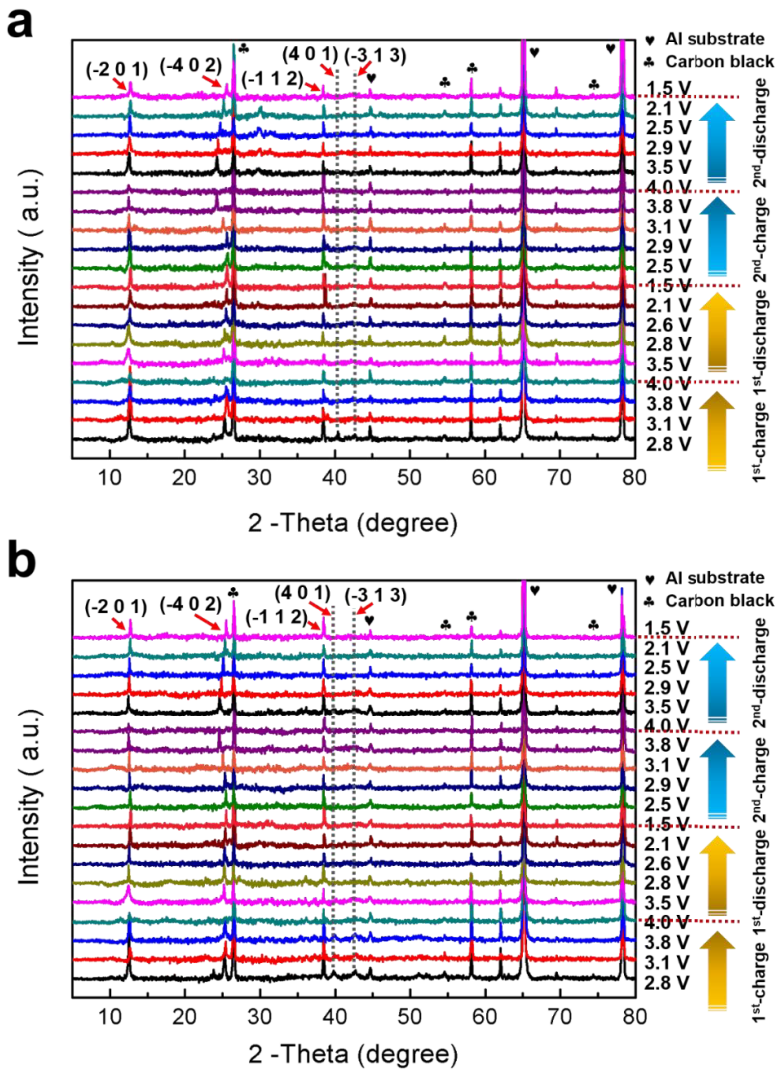

Figure 4.21 *Ex situ* XRD patterns of (a) S-KMO electrodes and (b) AlF_3@S-KMO electrodes at different charge and discharge stages in the first two cycles. The cells were cycled at 10 mA g^{-1}.

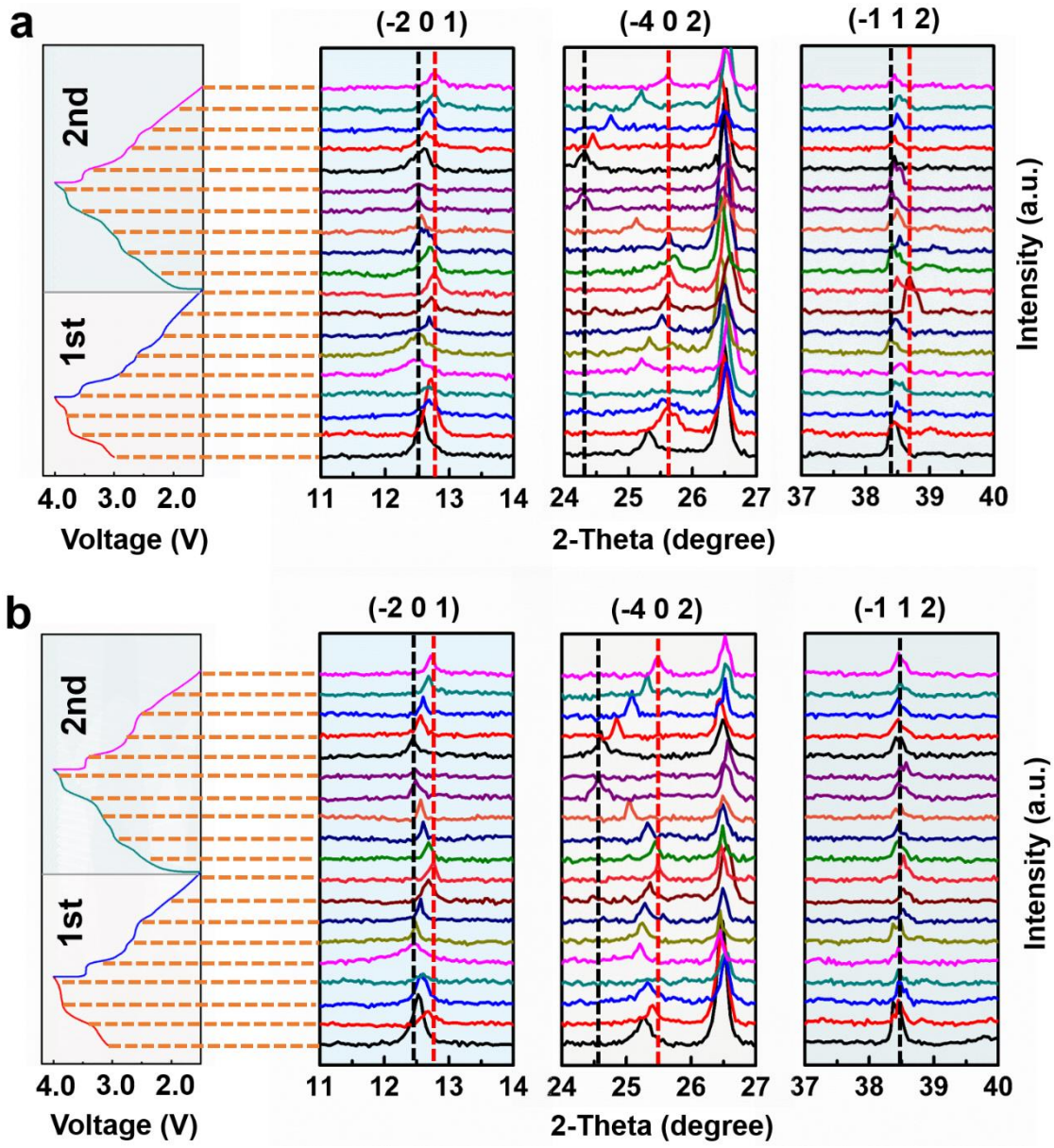

Figure 4.22 Enlarged images of *ex situ* XRD patterns of the a) S-KMO and b) AlF_3@S-KMO electrodes through the first two cycles at a current density of 10 mA g^{-1}.

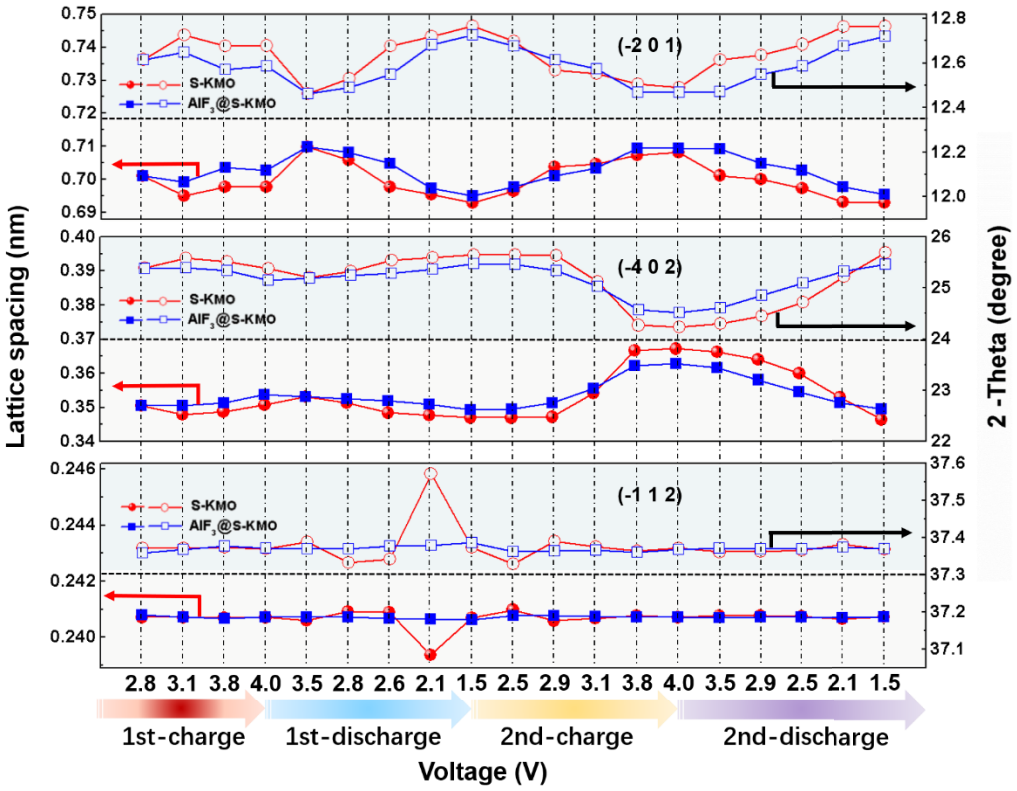

Figure 4.23 Relationship between the lattice spacing and the corresponding XRD diffraction peak position at various voltage states of S-KMO and AlF_3@S-KMO electrodes.

4.4 Summary

In summary, AlF_3-coated $K_{1.39}Mn_3O_6$ microspheres were successfully synthesized and investigated as cathode materials for potassium-ion batteries. The as-synthesized AlF_3-coated $K_{1.39}Mn_3O_6$ cathode materials show a highly reversible capacity of about 110 mAh g^{-1} at 10 mA g^{-1} in the voltage range of 1.5 – 4.0 V and excellent cycling stability over 100 cycles with a capacity retention of 94.9 %, which is much better than uncoated microspheres or the bulk counterpart. Systematic electrochemical measurements demonstrate that the diffusion kinetics of potassium-ion insertion and extraction during discharge and charge processes have been

significantly increased. The improved electrochemical performances could be ascribed to both the hierarchical sphere structure design and surface modification. Furthermore, *ex situ* XRD analysis demonstrates that the surface coating strategy effectively mitigates the dramatic structure change during potassium-ion insertion and extraction, which enhances the structure stability of layered $K_{1.39}Mn_3O_6$ cathode materials. This work not only provides a simple and reliable method to construct cathode materials but also explores new technology which offers huge potential for the development of high-performance potassium-ion batteries.

CHAPTER 5 $K_2Ti_2O_5$@C MICROSPHERES WITH ENHANCED K^+ INTERCALATION PSEUDOCAPACITANCE ENSURING FAST POTASSIUM STORAGE AND LONG-TERM CYCLING STABILITY

5.1 Introduction

Currently, lithium-ion batteries (LIBs) dominated the commercial market as the power source for modern consumer electronics, portable medical facilities and electric vehicles.[4, 360] Given the sparse geographic distribution of lithium resources, there is an urgent requirement to find suitable alternatives with low cost and high safety to satisfy the growing market demands.[361-363] Potassium-ion batteries (PIBs) are one type of rechargeable alkali-ion batteries that are capable of inheriting the working mechanism and advantages of LIBs. The natural abundance and non-toxicity of potassium could have a reduced environmental impact on large-scale production. Furthermore, the low standard redox potential of K/K^+ (−2.94 V vs. standard hydrogen electrode, SHE) leads to a high output voltage and high energy density for PIBs. These features make PIBs one of the most attractive candidates for grid-scale energy storage.[200, 255-256, 364]

Research on anode materials has accelerated the development of PIBs in the past decade. A series of anode materials such as carbonaceous materials,[26, 260, 365] transitional metal dichalcogenides,[262, 366] NASICON-structured compounds[367-368] and Prussian blue analogues[369]

have been developed and studied. However, the large volume expansion of PIB anode materials is the Achilles' heel of these anode materials.[272, 370] For example, graphite, which is the most successful anode material in commercial LIBs, manifests a dramatic volume expansion of about 61% during K-ion intercalation/extraction.[255-256] This phenomenon will, without doubt, lead to structural degradation and a poor cycling stability. In addition, most of PIB anode materials are also suffering from unsatisfactory rate performances due to poor electrical conductivity.[268, 364] Therefore, the quest for suitable anode materials with superior rate capability and long-lasting duration is a challenge for researchers worldwide. Amongst the candidates, Ti-based anode materials have aroused extensive interest, especially in LIBs[371] and sodium-ion batteries (SIBs)[372]. For example, $Li_4Ti_5O_{12}$ (LTO), one of the most attractive anode materials, shows a negligible volume change and excellent rate performance during cycling in LIBs.[373] As for PIBs, Ti-based intercalation compounds such as $K_2Ti_4O_9$[374] and $K_2Ti_6O_{13}$[375-376] are of great potential as anode materials, benefiting from their low costs and the large interlayer spacings to accommodate K^+. However, their relatively low specific capacity, poor cycling stability and unsatisfactory rate capability still cannot meet the requirements for practical applications.

It is well known that the sluggish diffusion kinetics of metal ions within the intercalation host and poor electron transfer between active particles restrict the rate performance of electrode materials.[23] Electrode materials with porous structures can significantly reduce the diffusion length of alkali metal ions within the solid-state lattice.[377] Normally, the diffusion kinetics is determined by $\tau = L^2/D$, where τ is the characteristic time constant, L represents the diffusion path in the solid-state, and D is the diffusion constant.[378] Herein, a shorter diffusion length can

lead to enhanced diffusion kinetics. Meanwhile, electrodes with spherical microparticles are expected to achieve a high volumetric capacity towards practical applications in the large-scale production.[379] To improve the electronic conductivity of electrode materials, coating the surface of materials with a thin layer of carbon or metallic material has proven to be an effective method.[377] Therefore, combining the surface modification strategy with rational structural design has emerged as an effective approach to improve the electrochemical performance of electrode materials. A series of carbon-coated electrode materials with microsphere morphology have been synthesized and exhibit high volumetric energy density and good rate capability in LIBs[380-383] and SIBs[384-385]. Undoubtedly, these improvement methods are attractive to be also employed in potassium-based energy storage devices.

Herein, we propose a spray drying method followed by chemical vapor deposition (CVD) treatment to prepare carbon-coated $K_2Ti_2O_5$ microspheres (S-KTO@C). The as-prepared S-KTO@C consists of carbon-coated nanorods and exhibits an open three-dimensional (3D) microstructure. When used as an anode material in PIBs, this S-KTO@C showed enhanced K-ion intercalation pseudocapacitive behavior, which is beneficial for both high rate capability and long-term cycling stability. Furthermore, a fabricated potassium-ion hybrid capacitor (PIHC) with the S-KTO@C (battery-type anode material) and of the activated carbon (AC, capacitor-type cathode material) also showed a high energy density, high power density, and excellent capacity retention.

5.2 Experimental section

5.2.1 Synthesis of $K_2Ti_2O_5$ microspheres (S-KTO)

Anatase titanium dioxide (TiO_2, Sigma–Aldrich, 32 g), potassium carbonate (K_2CO_3, Sigma–Aldrich, 30.4 g) and glucose ($C_6H_{12}O_6$, Sigma–Aldrich, 3.84 g) were mixed in 100 ml distilled water under continuous stirring for 5 h. The formed slurry was directly added into the spray dryer machine (BUCHI) by a peristaltic pump. In this case, K_2CO_3 and glucose serve as potassium source and binder, respectively. The S-KTO precursor was generated through a spray dry process with the inlet and outlet temperature controlled at 130 ºC and 90 ºC, respectively. Then, the obtained precursor was calcined at 700 ºC for 4 h in Ar to obtain S-KTO.

5.2.2 Synthesis of carbon-coated $K_2Ti_2O_5$@C microspheres (S-KTO@C)

S-KTO microspheres were placed in a CVD quartz tube furnace and preheated to 600 °C under 50 sccm Ar flow. Subsequently, acetylene (10 vol.% in Ar) was introduced with a flow rate of 50 sccm for 2 mins. After cooling to room temperature, the S-KTO@C microspheres were obtained and kept in the argon-filled glovebox.

5.2.3 Synthesis of bulk $K_2Ti_2O_5$ materials (B-KTO)

B-KTO materials were prepared by mixing commercial TiO_2 powders with K_2CO_3 in the same weight ratio and calcined at 700 ºC for 4 h under Ar.

5.2.4 Materials characterization

The morphology was investigated by field-emission scanning electron microscopy (FE-SEM, Zeiss Supra 55VP) and transmission electron microscopy (TEM, field emission CM200, Fei) in conjunction with an energy-dispersive X-ray spectrometer. The microstructure of the as-synthesized sample was characterized through a Bruker D8 Discovery X-ray diffractometer with Cu Kα radiation (2-Theta = 5° - 80°), and Raman spectra with a Renishaw inVia Raman spectrometer system (Gloucestershire, UK), using a Leica DMLB microscope (Wetzlar, Germany) and a 17 mW Renishaw He-Ne laser source at 633 nm. As for chemical composition, the carbon content was examined by a thermogravimetric analyzer (TGA, 2960 SDT system) with a heating rate of 10 °C min^{-1} in air atmosphere. X-ray photoelectron spectroscopy (XPS) was carried out on an ESCALAB250Xi (Thermo Scientific, UK) equipped with mono-chromated Al K alpha (energy: 1486.68 eV). N_2 adsorption-desorption isotherms were recorded via a Micromeritics 3Flex analyzer based on the Brunauer-Emmett-Teller method.

5.2.5 Electrochemical measurements

The electrode slurry was prepared by mixing the active materials, carbon black and polyvinylidene difluoride (PVDF) with a weight ratio of 8:1:1 in N-Methyl-2-pyrrolidone (NMP). The B-KTO, S-KTO and S-KTO@C electrodes were fabricated by coating the mixed slurry onto copper foils and then dried at 100 °C under vacuum for 12 h. For potassium half-cell testing, 2032-type coin cells (CR2032) were assembled in an Ar-filled glove box, using the prepared electrodes and potassium metal foils separated by glass microfiber filters (Whatman,

Grade GF/D). An electrolyte of 1 M potassium bis(fluoroslufonyl)imide (KFSI) in 1:1 (volume ratio) ethylene carbonate (EC) and diethyl carbonate (DEC) was used for electrochemical measurements. Galvanostatic charge and discharge (GCD) tests were conducted on a computer-controlled NEWARE^{TM} battery tester. Cyclic voltammogram (CV) measurements were performed on a Biologic VMP3 electrochemical workstation at different scan rates in the voltage range from 0.01 V to 3.0 V. As for galvanostatic intermittent titration technique (GITT) experiments, the cells were initially activated at 0.1 C for 5 cycles and then were charged/discharged for 10 min at a pulse current density of 10 mA g^{-1}, followed by a relaxation for 3 h to reach the equilibrium potential state. This process was repeated multiple times until the cut-off potential was reached. Electrochemical impedance spectra (EIS) were obtained in the frequency range from 100 kHz to 10 mHz with a potential amplitude of 5 mV. For *ex situ* material characterizations, coin cells were dissembled in the glove box and washed with DEC for three times to remove residual potassium salts. These electrodes were directly used for *ex situ* XRD and XPS characterizations.

A potassium-ion hybrid capacitor (PIHC) was fabricated, using S-KTO@C as an anode and activated carbon (AC, specific surface area: 1904 m^2g^{-1}, produced by Nanjing XFNANO Materials Tech Co., Ltd.; model: XFP06) as a cathode. Before the assembly of PIHCs, the S-KTO@C anode and AC cathode were pre-activated for 5 cycles at a current density of 20 mA g^{-1} in potassium half-cells. The mass ratio of the anode versus cathode was designed to be 1.5:1. The electrolyte and the separator used in the PIHC device were 1 M KFSI in EC and DEC (1:1 in volume) and glass microfiber membranes, respectively. The energy (E) and power (P)

densities of the PIHC device were acquired via galvanostatic charge-discharge profiles, according to the following equations:

$$\mathrm{E} = \int_{t_1}^{t_2} UI/m dt \qquad \textbf{Equation 5.1}$$

$$\mathrm{P} = \mathrm{E}/(t_2 - t_1) \qquad \textbf{Equation 5.2}$$

Wherein *U* and *I* are the working voltage (V) and applied current (A), respectively. *m* stands for the total mass of the two electrodes, and t_1 and t_2 represent the begin and end time (s) of the discharge process.

5.2.6 *In situ* XRD measurements

The Swagelok cell for the *in situ* XRD measurement consists of the S-KTO@C electrode, associated with a Be window (positive part), and a K metal foil (negative part) was used for *in situ* XRD measurements. The charge/discharge current density was 0.1 C within the potential range from 0.01 V to 3.0 V. In addition, based on the Bruker D8 Discovery X-ray diffractometer with Cu Kα radiation, the scan step was 0.02° (2-theta = 10° - 50°), and the step time was 0.5 s. The first XRD pattern was from the fresh cell, and then XRD measurements were proceeded continuously along with the charge/discharge process.

5.3 Results and discussion

The synthesis route for the S-KTO@C sample is schematically illustrated in **Figure 5.1**a. A mixture of TiO_2, K_2CO_3 and glucose is used to prepare spherical precursors through a spray

drying process, followed by calcination at 700 °C under Ar atmosphere. Scanning electron microscopy (SEM) images of the as-prepared precursors show a spherical shape with an average diameter of ~12 μm. Each microsphere is an accumulation of many primary nanoparticles, as shown in **Figure 5.2**. Figure 5.1b, 5.1c and **Figure 5.3a** reveal the morphology of the obtained $K_2Ti_2O_5$ microsphere (S-KTO) after high-temperature calcination. As shown in the SEM images, the primary nanoparticles are transformed into nanorods. After CVD treatment, the surface of S-KTO@C microspheres remains smooth and clear without obvious carbon aggregations (Figure 5.1e, 5.1f and 5.3b). Moreover, the morphological features of S-KTO and S-KTO@C were further investigated via transmission electron microscopy (TEM). Figure 5.1d and **Figure 5.4**a show the TEM images of KTO nanorods with an interplanar spacing of 0.258 nm, which corresponds to the (-3 1 1) plane of $K_2Ti_2O_5$ (JCPDS No. 04-012-6258). In addition, TEM images in Figure 5.1g and 5.4b reveal that a homogeneous carbon-coating layer with a thickness of about 10 nm has been grown on the surface of the KTO nanorods after CVD treatment. Such a core-shell structure is expected to guarantee fast electron transport and also improve structural stability. Furthermore, the selected area electron diffraction (SAED) patterns of S-KTO and S-KTO@C indicate the incorporation of amorphous carbon after CVD process (**Figure 5.5**).[386] Energy-dispersive X-ray spectroscopy (EDS, **Figure 5.6**) elemental maps also illustrate the homogeneous distribution of K, Ti, O and C elements in the S-KTO@C material.

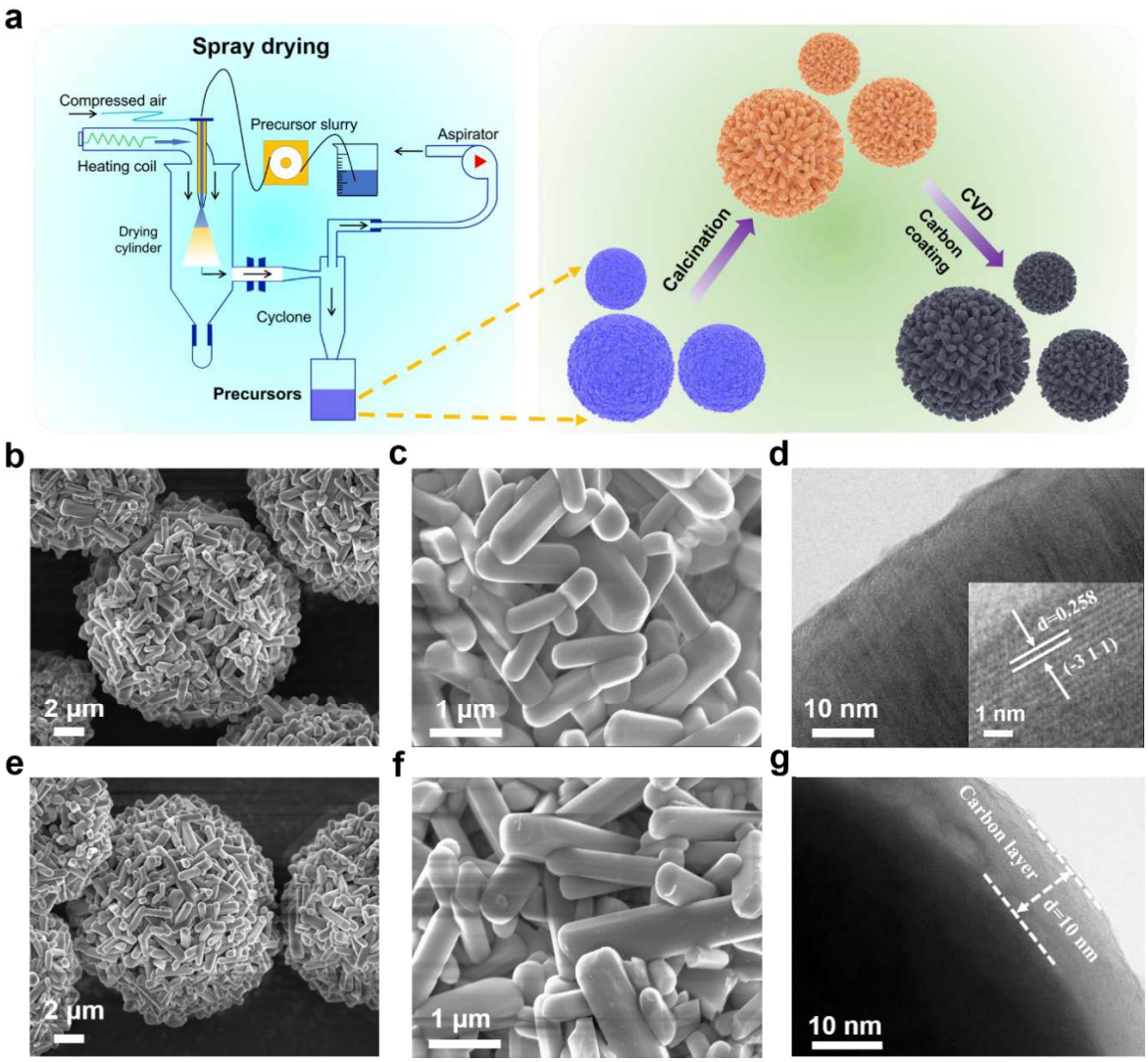

Figure 5.1 (a) Schematic illustration of the preparation process for S-KTO@C. (b, c) SEM images and (d) TEM images of S-KTO. The inset shows the lattice spacing of the S-KTO material. (e, f) SEM images and (g) TEM image of S-KTO@C.

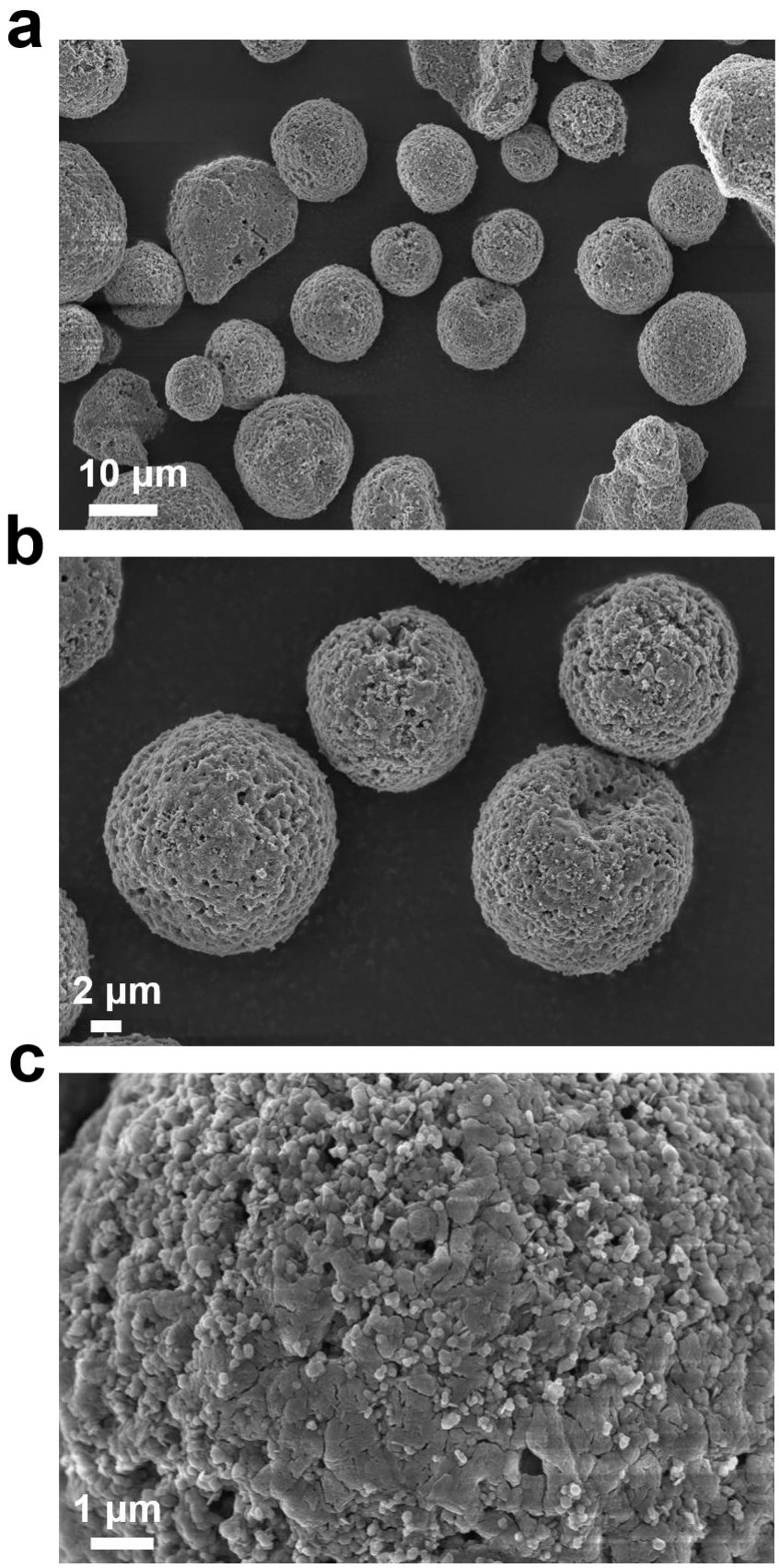

Figure 5.2 (a-c) SEM images of S-KTO precursors.

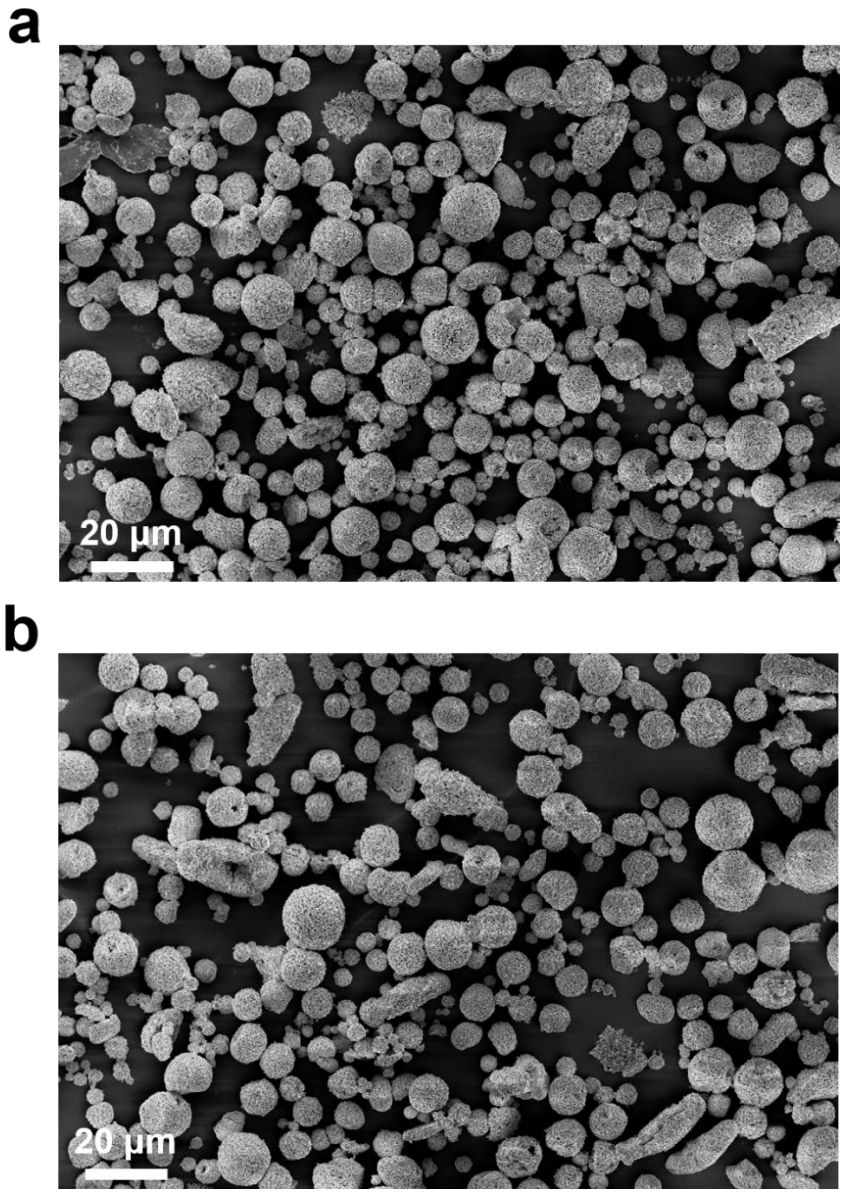

Figure 5.3 Low-magnification SEM images of (a) S-KTO and (b) S-KTO@C microspheres.

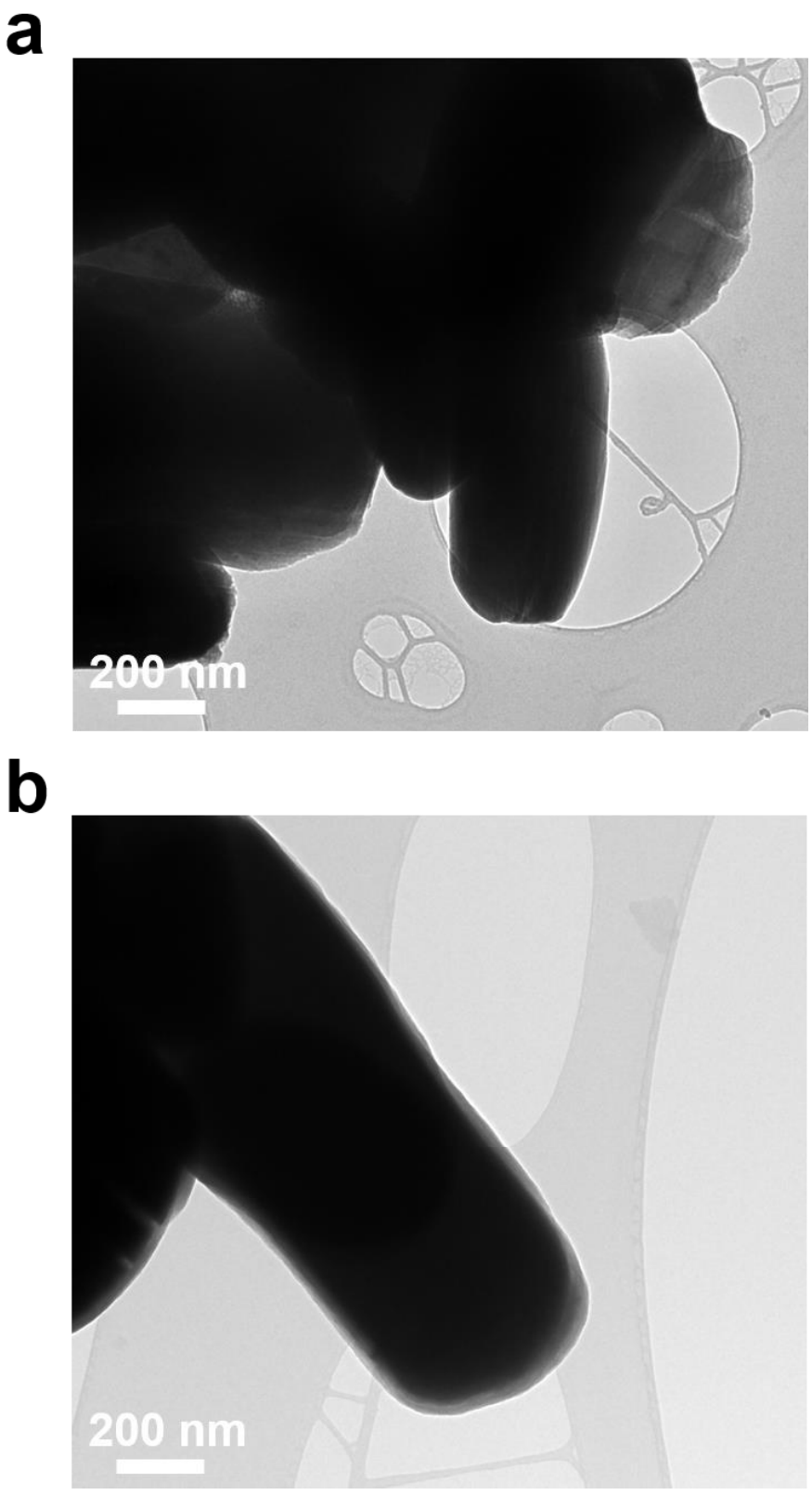

Figure 5.4 Low-magnification TEM images of (a) S-KTO and (b) S-KTO@C microspheres.

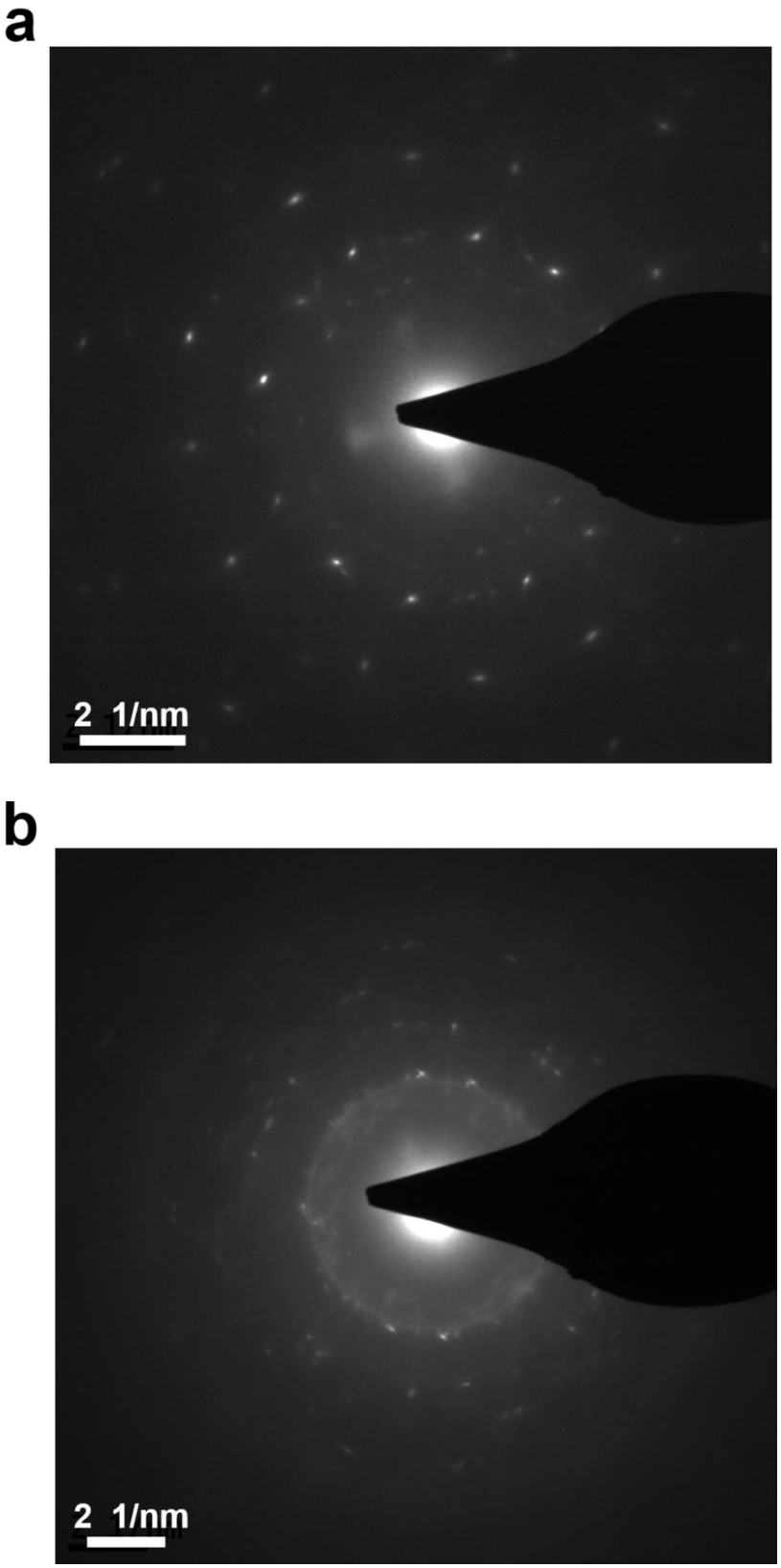

Figure 5.5 SAED patterns of (a) S-KTO and (b) S-KTO@C materials.

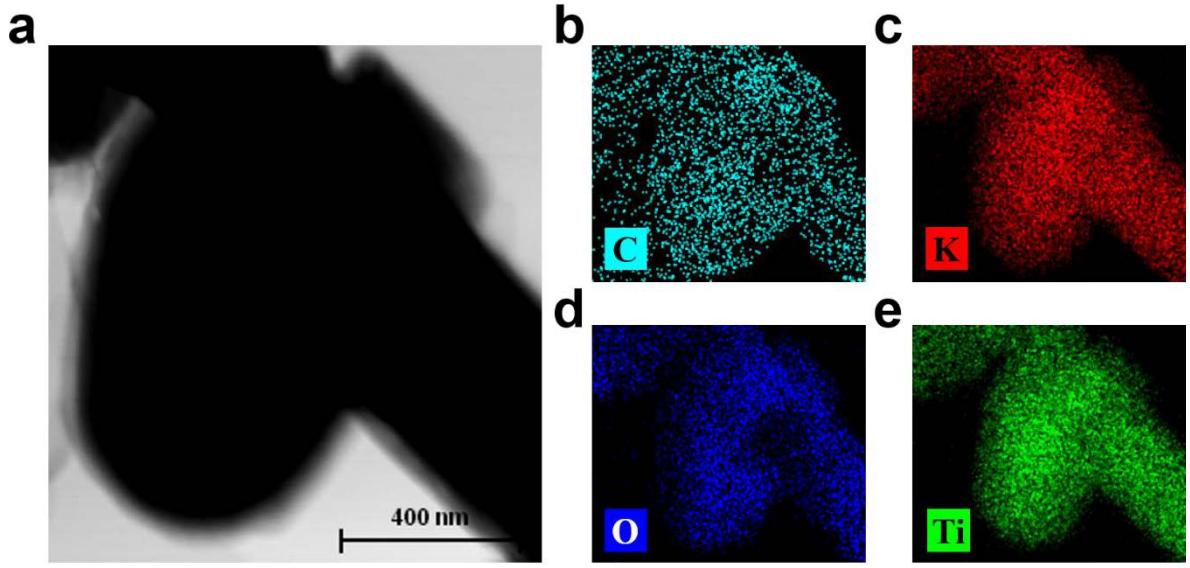

Figure 5.6 (a) TEM-EDS elemental maps for (b) C, (c) K, (d) O, and (e) Ti in the S-KTO@C material.

Figure 5.7a shows X-ray diffraction (XRD) results of the as-synthesized S-KTO and S-KTO@C samples. All the diffraction peaks can be well indexed to monoclinic $K_2Ti_2O_5$ (JCPDS No. 04-012-6258) with space group of *C2/m*, demonstrating the good crystallinity of the initial $K_2Ti_2O_5$ phase. The carbon content in the S-KTO@C determined by thermogravimetric analysis (TGA) is estimated to be 5.35% (Figure 5.7b). Raman spectroscopy presented in Figure 5.7c shows two representative D and G bands located at 1350 and 1584 cm^{-1}, respectively, indicating the typical carbon signal within S-KTO@C. The relative intensity ratio (I_D/I_G) is 1.00, which confirms the amorphous character of the carbon component.[387] X-ray photoelectron spectroscopy (XPS) analysis results for S-KTO and S-KTO@C are summarized in Figure 5.7d-f and **Figure 5.8**. In Figure 5.7d, two strong peaks located at 464.3 and 458.5 eV can be assigned to low-resolution Ti $2p_{1/2}$ and high-resolution Ti $2p_{3/2}$, respectively, confirming the existence

of Ti^{4+} in the material.[388] The O1s spectrum displays three characteristic peaks at 532.7, 531 and 529.3 eV as shown in Figure 5.7e. The slight increase of the O1s B peak intensity is attributed to the change of surface oxygen species induced by the surface coating.[30] Furthermore, two peaks at 295.8 and 293.1 eV correspond to the $K2p_{1/2}$ and $K2p_{3/2}$ characteristic peaks, respectively (Figure 5.7f). In addition, several shoulder peaks generated by adventitious carbon species are also observed in Figure 5.7f. Compared with the pure S-KTO sample, the peak intensity of C1s significantly increases after the carbon coating.[262] **Figure 5.9** shows the nitrogen adsorption-desorption isotherms of the two materials. The S-KTO@C material has a larger specific surface area (43.6 m^2 g^{-1}) than the uncoated S-KTO material (15.2 m^2 g^{-1}). For comparison, bulk $K_2Ti_2O_5$ (B-KTO) materials were prepared via a solid-state calcination process (**Figure 5.10**).

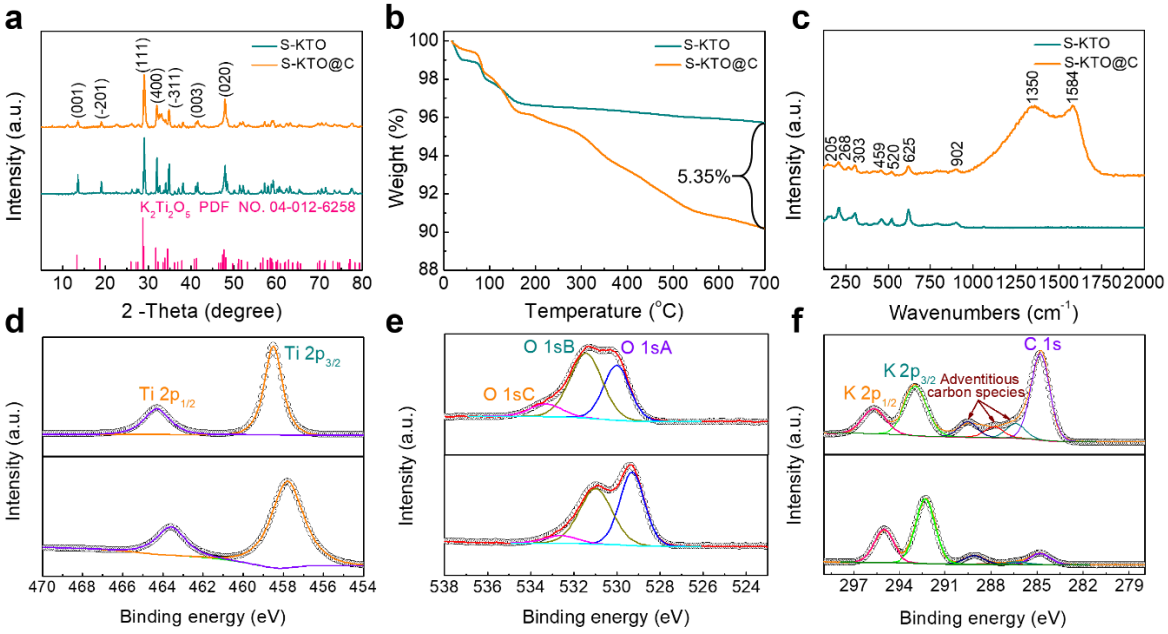

Figure 5.7 (a) XRD patterns, (b) TGA curves and (c) Raman spectra of S-KTO and S-KTO@C. (d-f) High-resolution XPS spectra of Ti 2p, O1s, K 2p and C 1s of S-KTO (lower) and S-KTO@C (upper).

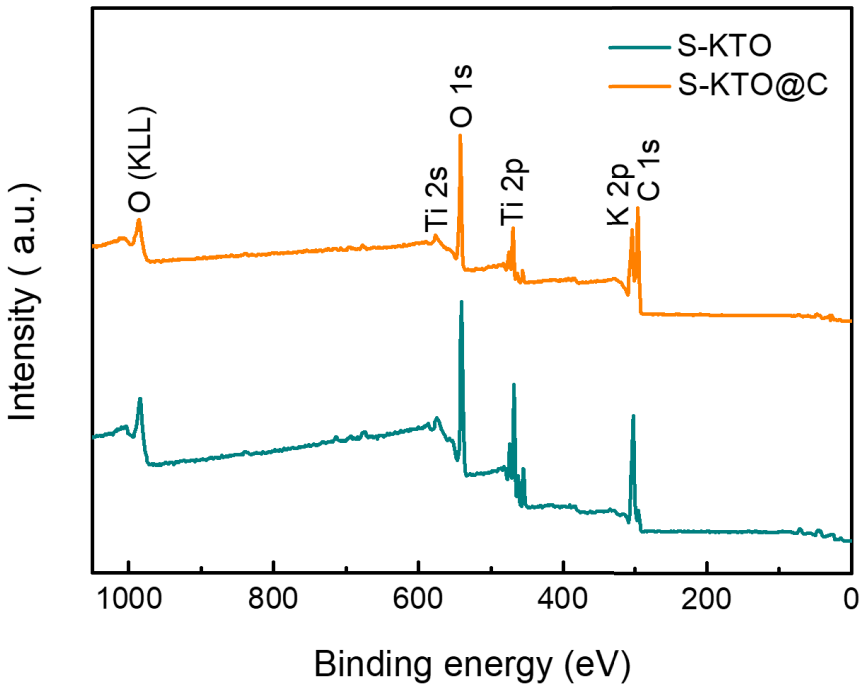

Figure 5.8 XPS spectra of the S-KTO and S-KTO@C materials.

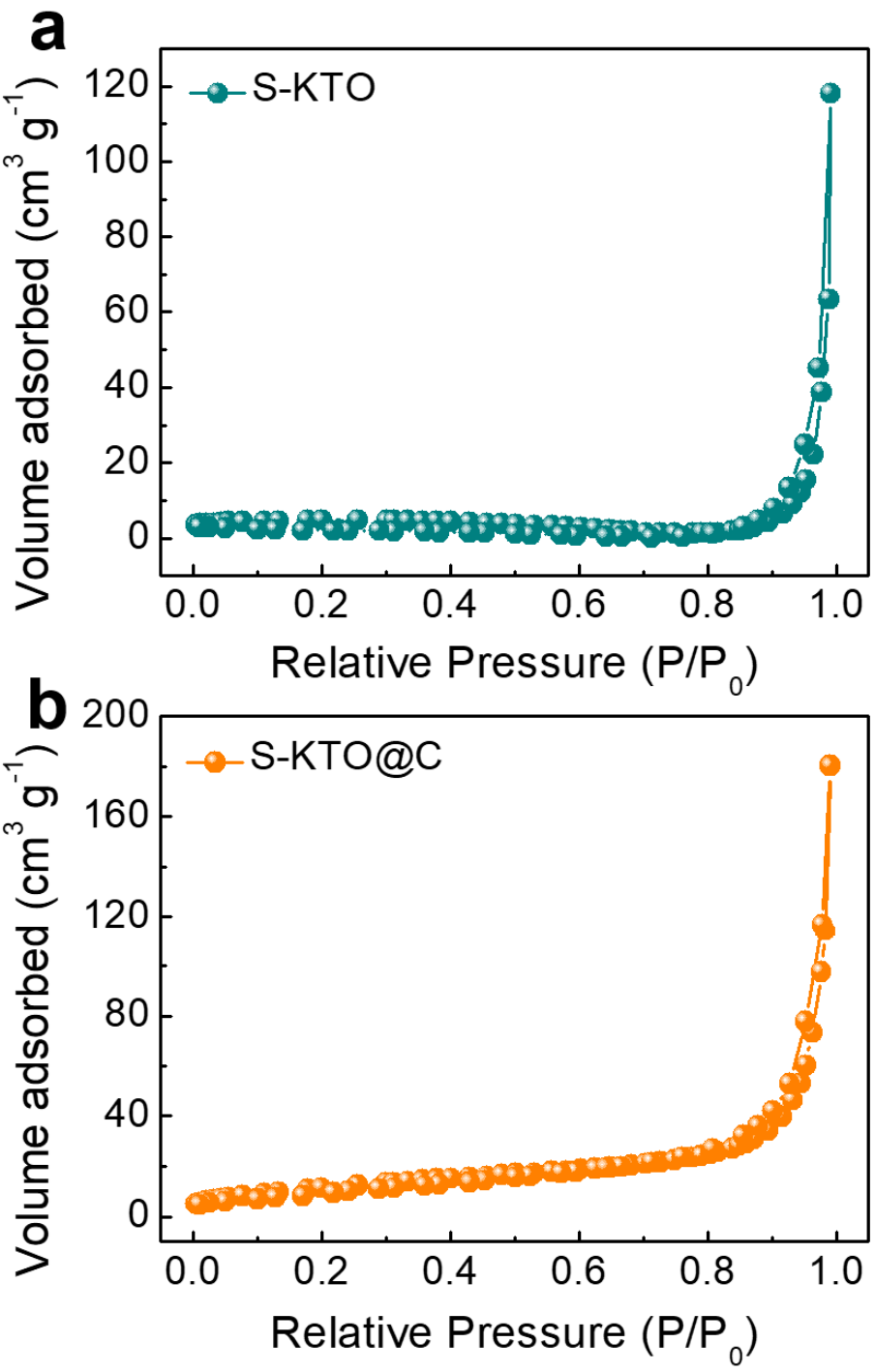

Figure 5.9 Nitrogen adsorption–desorption isotherms of the (a) S-KTO and (b) S-KTO@C materials.

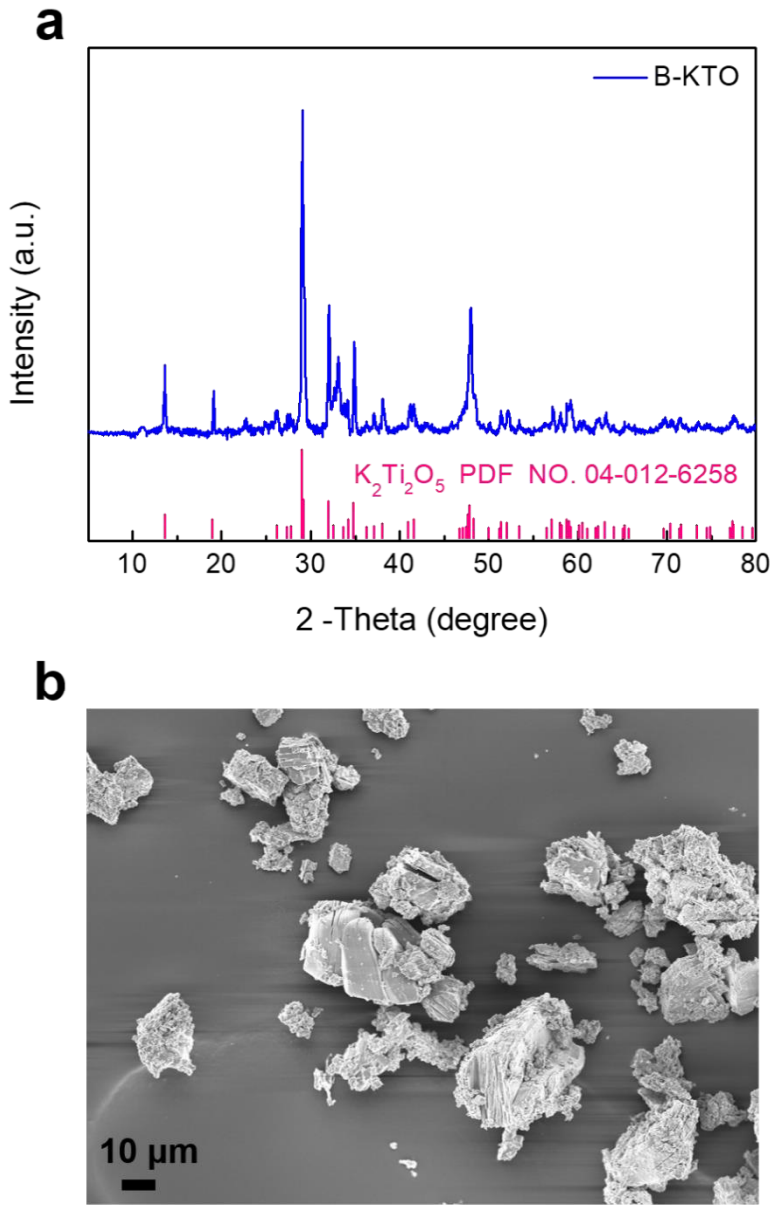

Figure 5.10 (a) XRD pattern and (b) SEM image of B-KTO.

The electrochemical performance of the as-synthesized materials was evaluated by galvanostatic charge and discharge (GCD) in the voltage range of 0.01-3.0 V. The theoretical capacity at 1 C (160 mAh g^{-1}) is calculated based on a two-electron transfer process of $K_2Ti_2O_5$ according to:

$$K_2Ti_2O_5 + 2K^+ + 2e^- \longleftrightarrow K_4Ti_2O_5 \qquad \textbf{Equation 5.3}$$

As can be seen from **Figure 5.11**a, 5.11b and **Figure 5.12**, the first discharge capacity for S-KTO, S-KTO@C and B-KTO electrodes are 348.7, 317.4 and 262.1 mAh g^{-1} with relatively low Coulombic efficiencies (CE) of 42.4, 48.9 and 21%, respectively. It is considered that the formation of solid electrolyte interphase (SEI) mainly accounts for the irreversible capacities.[259, 375-376] Subsequently, these three electrodes deliver reversible discharge capacities of 147, 155.1 and 74.8 mAh g^{-1} in the second cycle, corresponding to the insertion of 1.68, 1.88 and 0.91 K^+ per formula unit upon discharge ($Ti^{3+} \rightarrow Ti^{4+}$), respectively. Moreover, the average discharge voltage plateau of the S-KTO@C electrode is at 0.38 V, which is much lower than their counterparts in lithium ($Li_4Ti_5O_{12}$, 1.55 V)[9] and sodium (Na_xTiO_2, 0.8 V)[389] cells. The relatively lower operation voltage in PIBs than in LIBs and SIBs contributes to a higher energy density when designing full cells. Meanwhile, the higher potassiation voltage of the S-KTO@C electrode than graphite electrodes (~ 0.1 V)[390] and hard carbon electrodes (~ 0.25 V)[259] avoids the formation of K metal dendrites during cycling, effectively improving safety and prolonging service life. As the cycle continues, all three electrodes experience pronounced capacity losses in the initial 10 cycles. This is mainly ascribed to undesired side reactions and continuous growth of the SEI layer.[366, 369, 377] The S-KTO@C electrode shows the best capacity retention among all three electrodes after 100 cycles (Figure 5.11c).

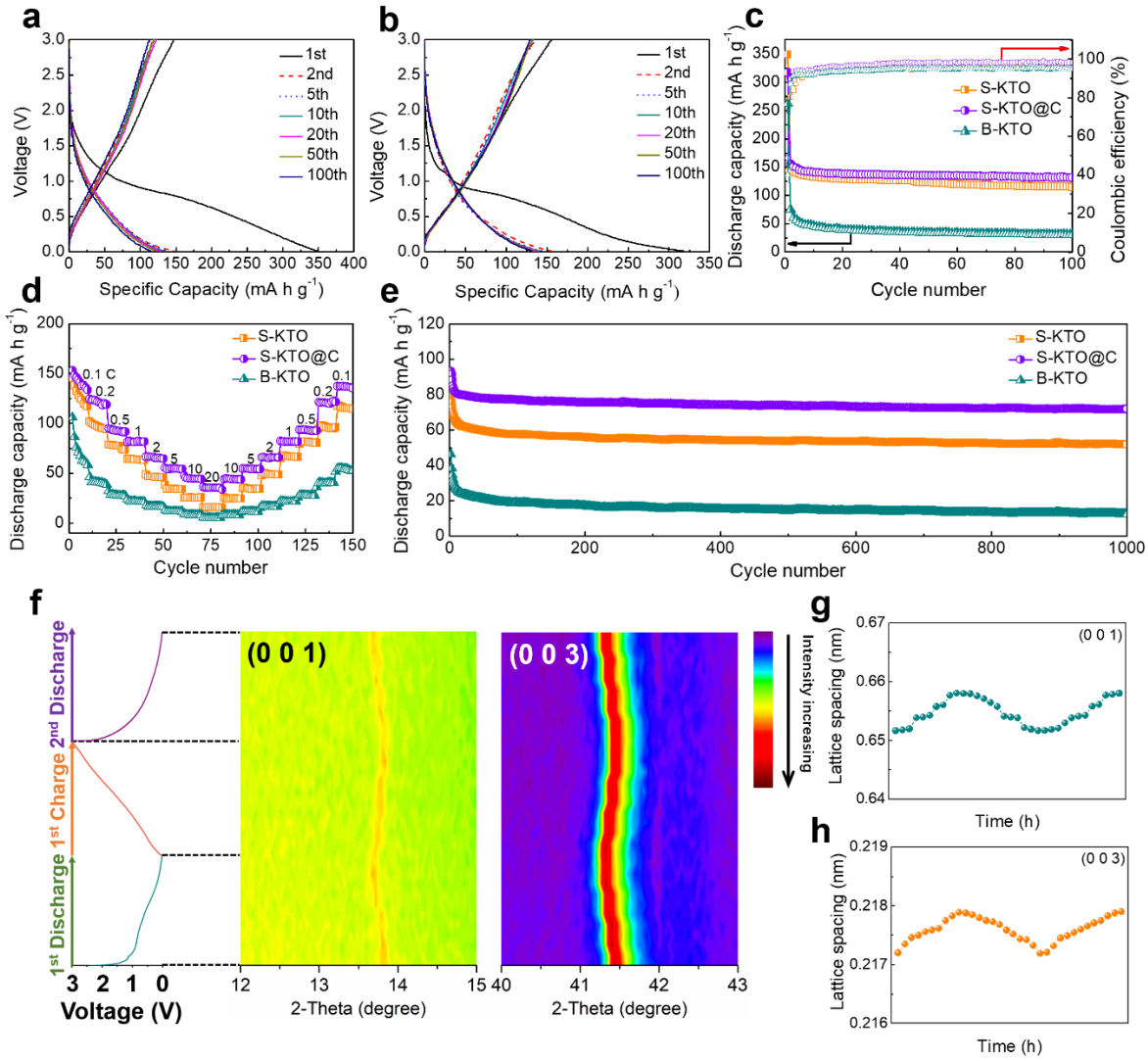

Figure 5.11 Galvanostatic charge and discharge voltage profiles of cells with (a) S-KTO and (b) S-KTO@C electrodes between 0.01 and 3 V (*vs.* K^+/K) at a current density of 0.1 C. (c) Cycling performance of S-KTO, S-KTO@C and B-KTO electrodes at a current density of 0.1 C for 100 cycles. (d) Rate performances of cells with S-KTO, S-KTO@C and B-KTO electrodes at various current densities. (e) Long-term cycling performance of cells with S-KTO, S-KTO@C and B-KTO electrodes at a current density of 1 C for 1000 cycles. (f) *In situ* XRD contour plots of a S-KTO@C electrode at a current density of 0.1 C. (g, h) The change of lattice spacings, corresponding to the (001) and (003) peaks *vs.* time.

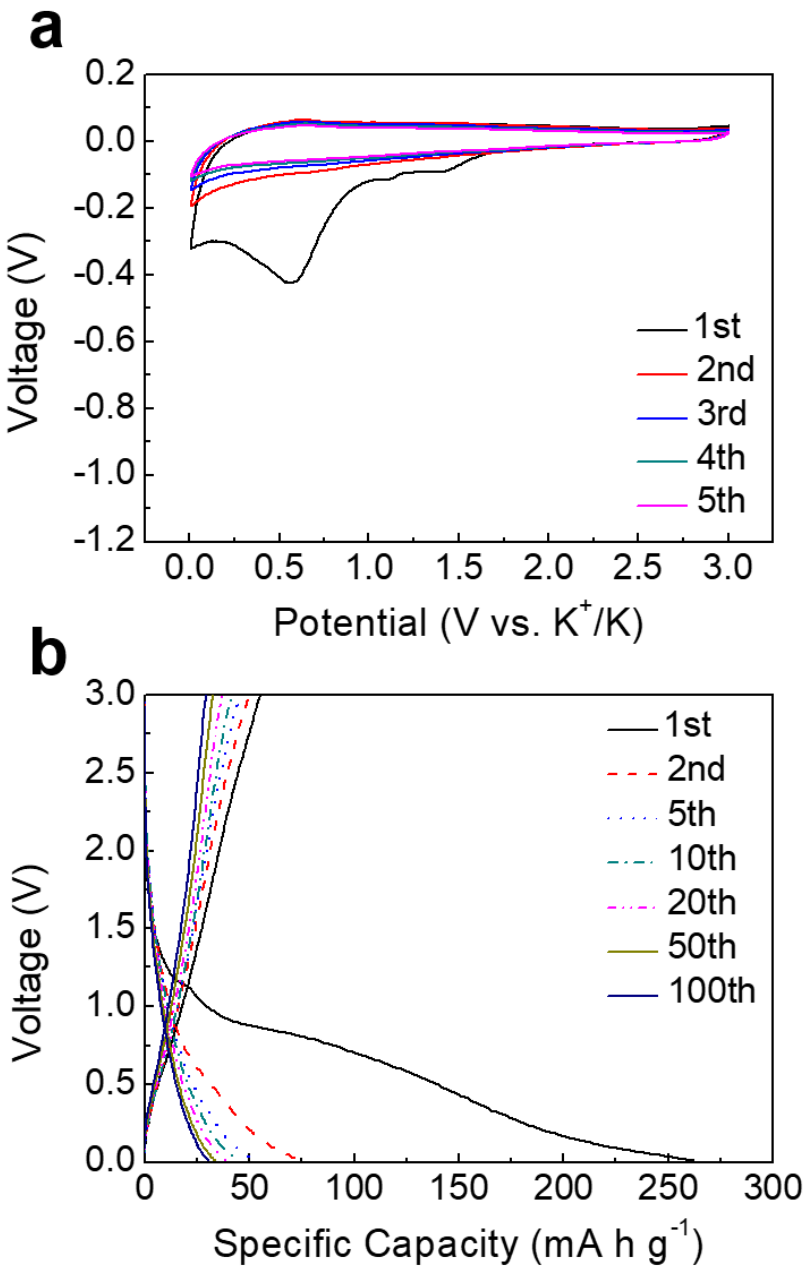

Figure 5.12 Electrochemical performances of the B-KTO sample: (a) CV curves and (b) GCD profiles under a current density of 0.1 C between 0.01 and 3 V (*vs.* K^+/K).

Electrochemical impedance spectra (EIS) obtained after the 1st and the 100th cycle show the S-KTO@C electrode has the smallest charge transfer resistance (R_{ct}) without any significantly

increasing after cycling (**Figure 5.13**). This result indicates that carbon-coating contributes to the enhanced reaction kinetics and improved interface stability. Furthermore, the S-KTO@C electrode also exhibits the best rate capability among the three electrodes as the current density is changed from 0.1 to 20 C (Figure 5.11d). When the discharge current is returned to the original value, the cell with the S-KTO@C electrode recovers to its initial capacity and remains stable, indicating outstanding electrochemical reversibility and stability. To further evaluate the long-term cycling stability, S-KTO, S-KTO@C and B-KTO anodes were cycled at 1 C for 1000 cycles (Figure 5.11e). Both S-KTO and S-KTO@C cells show good cycling stability with capacity retentions of 65.3% and 77.1%, respectively. In contrast, the B-KTO cell shows an extremely poor capacity retention of 26.5% after long-term cycling. These results demonstrate good cycling stability and excellent rate capability for the S-KTO@C electrode benefiting from both the structure design and carbon-coating. Specifically, the nanorod-assembled microstructure shortens the diffusion pathway for K^+ in the solid-state lattice and also facilitates the penetration of electrolyte inside the material. Meanwhile, the presence of an ultra-thin conductive carbon layer is beneficial for fast electron transport and establishes a stable interface between electrode and electrolyte.[367-368] Furthermore, the carbon-coating layer of S-KTO@C also reduces the risk of structural degradation and prevents the electrode from being jeopardized by side-products during cycling.[262, 264, 377]

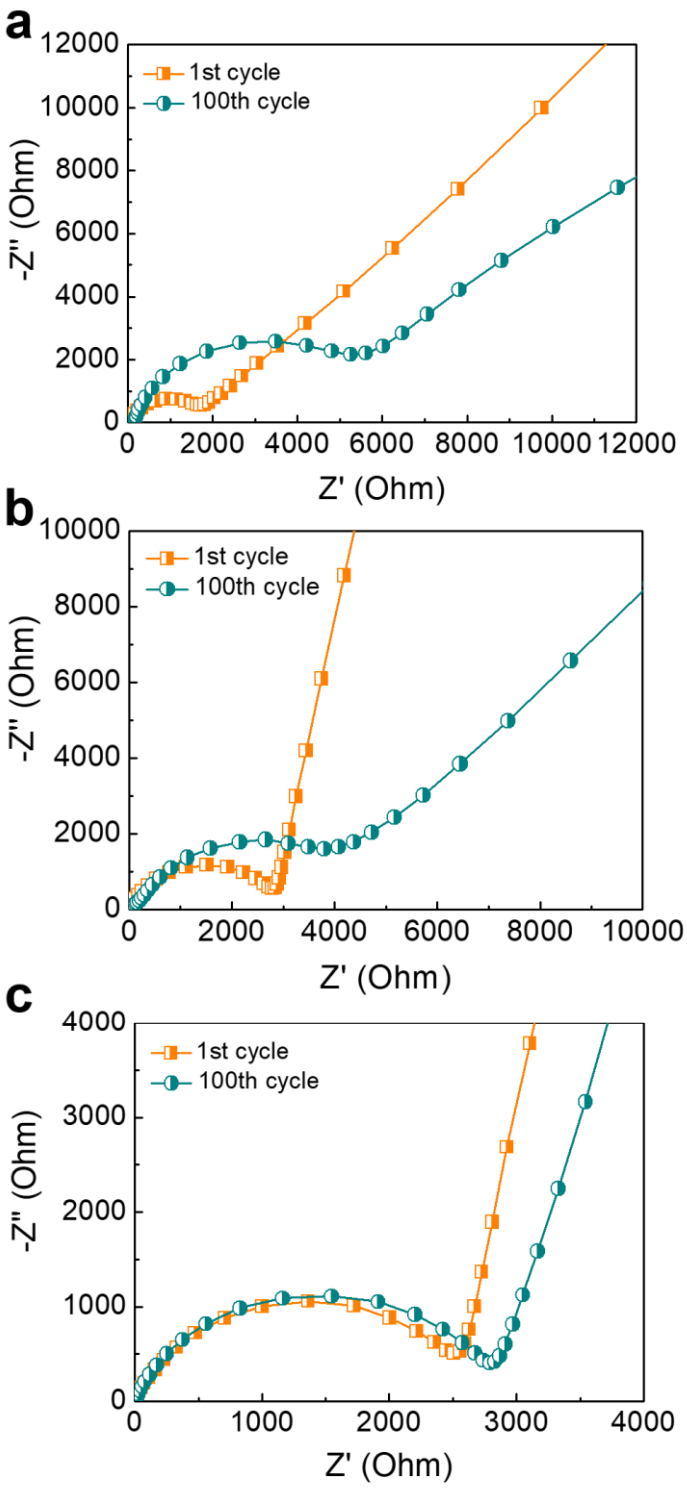

Figure 5.13 Electrochemical impedance spectra (EIS) of the cells with (a) B-KTO, (b) S-KTO and (c) S-KTO@C electrodes after the first (yellow) and 100th (green) cycle.

To fully understand the relationship between the structural evolution and the K-storage mechanism of S-KTO@C, *ex situ* XRD was performed to investigate the structural integrity of S-KTO@C materials after repeated cycles. As can be seen from **Figure 5.14**, three characteristic peaks representing (001), (-202) and (003) of monoclinic $K_2Ti_2O_5$ appear in the XRD patterns of both fresh S-KTO and S-KTO@C electrodes. After 100 cycles, these diffraction peaks almost disappear for S-KTO while remaining unchanged for S-KTO@C. In addition, SEM images demonstrate that the S-KTO electrode has been severely corroded, while S-KTO@C is able to withstand the harsh operating environment and maintain its original microstructure after repeatedly cycling (**Figure 5.15**). Furthermore, *ex situ* XPS was employed to investigate the change of the chemical states during (dis)charge. **Figure 5.16** shows the XPS spectra of Ti 2p and C 1s for S-KTO@C anode materials at different charge and discharge stages. Both Ti $2p_{1/2}$ and Ti $2p_{3/2}$ spectra are deconvoluted into two shoulder peaks in the first fully discharged state, corresponding to Ti^{3+} and Ti^{4+}, respectively, indicating the gradual reduction of Ti at the end of first discharge. However, the relative peak intensities of the Ti $2p_{1/2}$B and Ti $2p_{3/2}$B spectra decline after the electrode was subsequently charged to 3 V, implying oxidation of Ti. It can be speculated that Ti experiences a reversible transition between Ti^{3+} and Ti^{4+}.[391] Meanwhile, the chemical state of C 1s changes slightly before and after (dis)charge. This result confirms that the carbon species are stable during the K^+ (de)intercalation process.

Figure 5.11f and **Figure 5.17** show the *in situ* XRD patterns of the S-KTO@C electrode in a Swagelok cell cycled at 0.1 C. The characteristic diffraction peaks of (001) and (003) planes

located at 13.81° and 41.44°, respectively, shift continuously to a lower value during the 1st discharge process, demonstrating a gradual expansion of the lattice distances during the K^+ intercalation process (Figure 5.11g and 5.11h). The enlarged interlayer distances are attributed to the addition of the average charge on oxygen anions during K^+ intercalation.[376, 392] After the cell was then charged to 3.0 V, these peaks return to their original positions, implying the recovery of the corresponding lattice distances. Upon the second discharge process, the (001) and (003) peaks experience a similar trend with K^+ intercalation. The reversible evolution of diffraction peak positions with the regular change of lattice distances suggests a good reversibility of K^+ intercalation and deintercalation in S-KTO@C materials. Consequently, the S-KTO@C electrode demonstrates excellent long-term cycling stability.

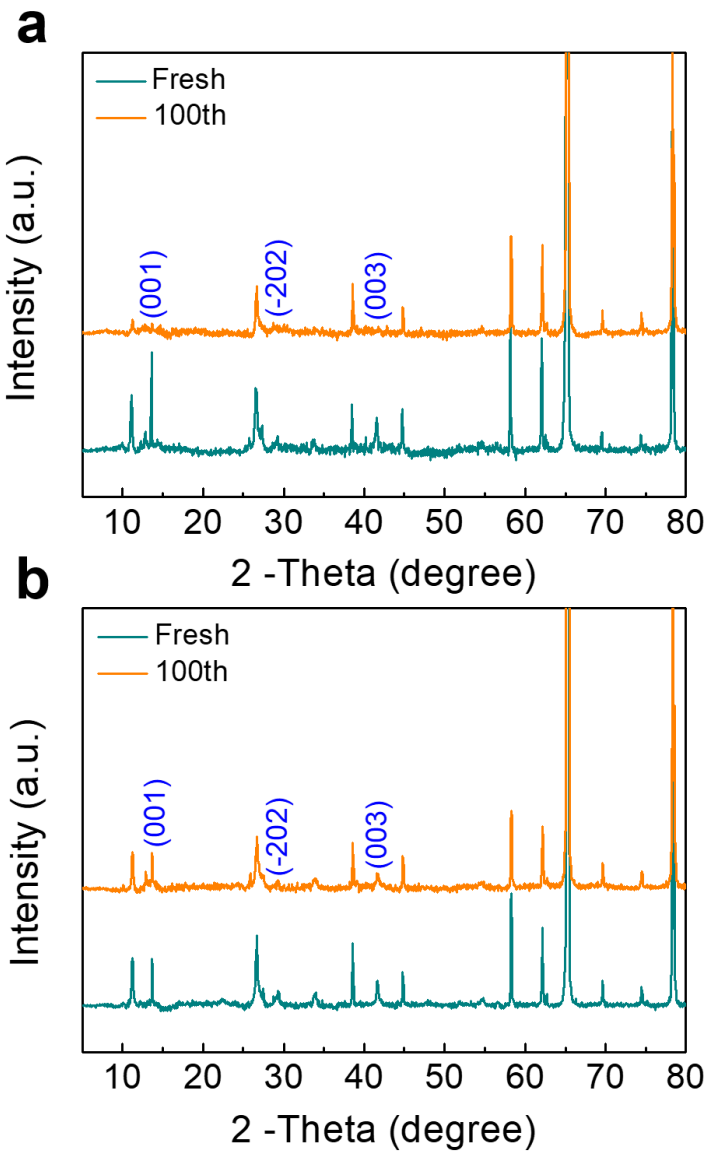

Figure 5.14 *Ex situ* XRD results of (a) S-KTO and (b) S-KTO@C electrodes before (green) and after (yellow) 100 cycles. The cells were cycled at 0.1 C.

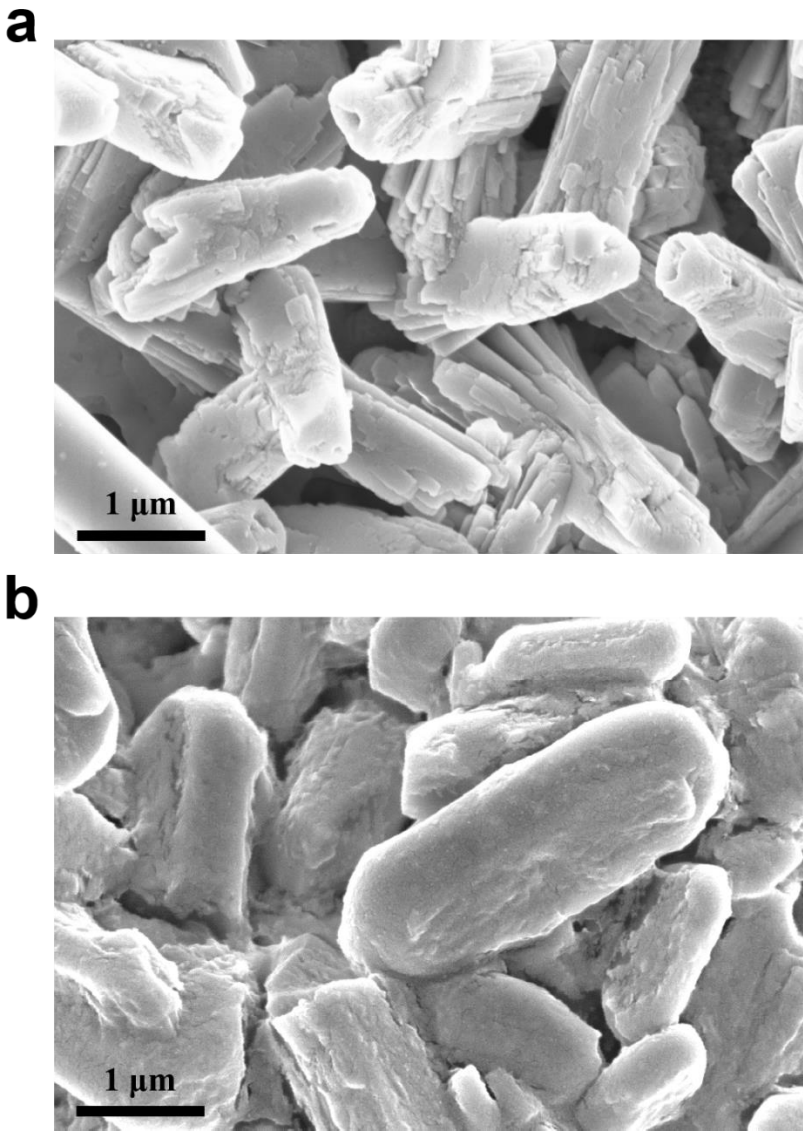

Figure 5.15 SEM images of (a) S-KTO and (b) S-KTO@C electrodes after 100 (dis)charge cycles.

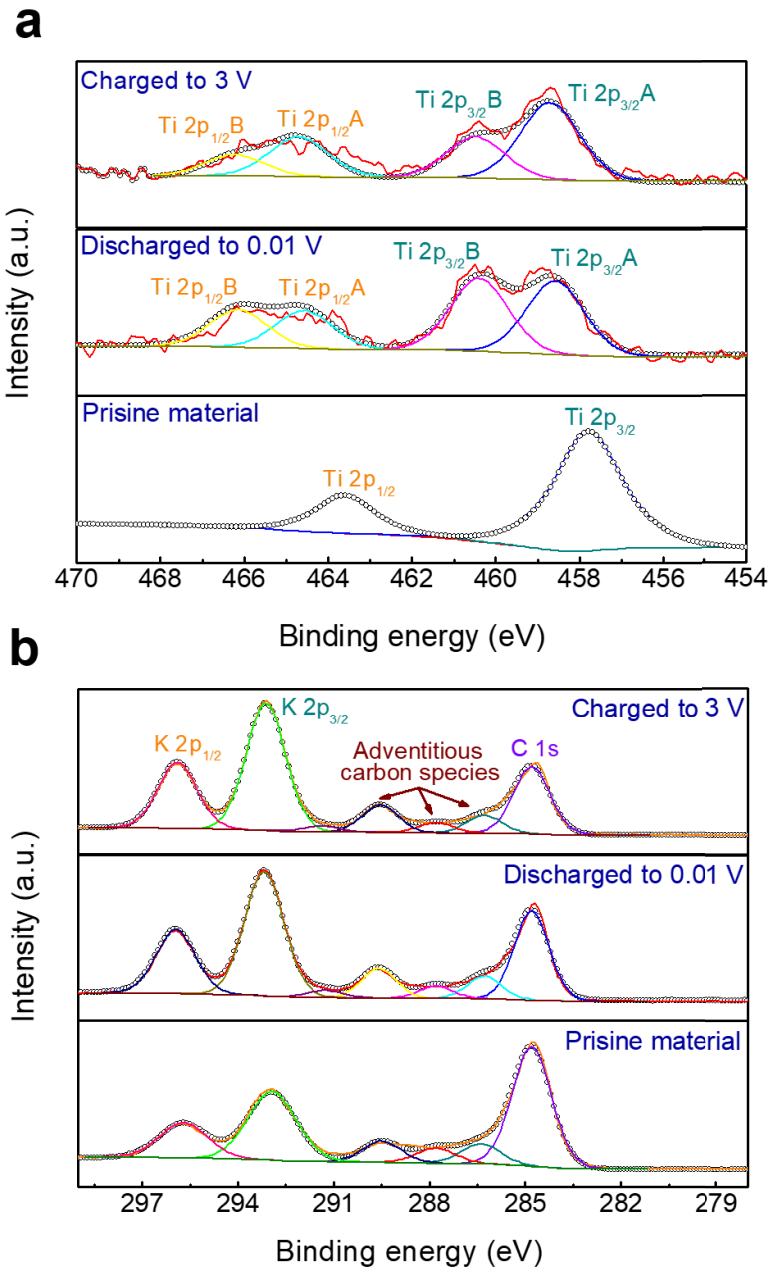

Figure 5.16 *Ex situ* XPS results of (a) Ti 2p and (b) C 1s for S-KTO@C electrodes at different charge/discharge states. The cells were (dis)charged at 0.1C.

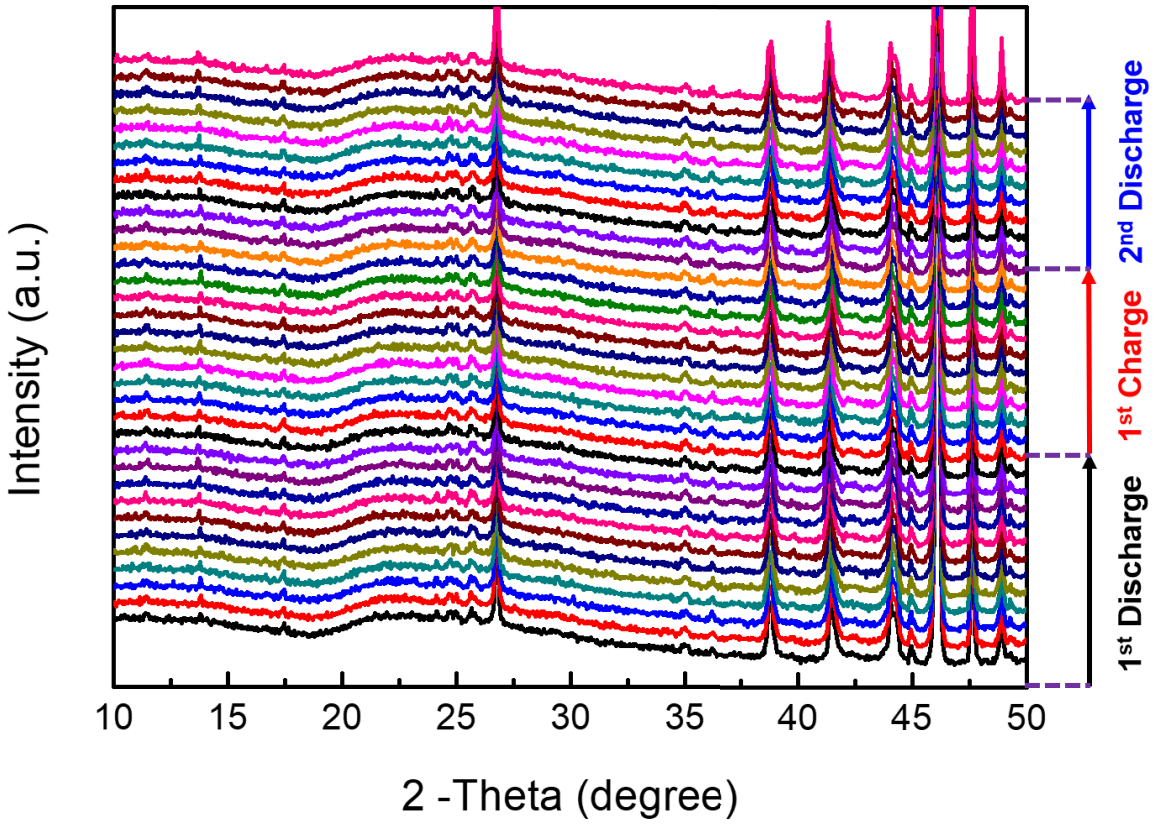

Figure 5.17 *In situ* XRD patterns of a S-KTO@C Swagelok cell cycled at 0.1 C.

To further identify the impact of carbon-coating and structure design on KTO anode materials, galvanostatic intermittent titration technique (GITT) was applied to evaluate the reaction kinetics of K^+ (de)intercalation into the KTO host. The voltage response *vs.* specific capacity (mAh g^{-1}) profiles after initial activation are displayed in **Figure 5.18**a, 5.18b **and 5.19**. The S-KTO@C electrode (Figure 5.18a) exhibits the smallest overpotential compared with the S-KTO (Figure 5.18b) and the B-KTO (Figure 5.19) electrodes during the (de)potassiation process. Additionally, their reaction resistances were obtained with respect to different

(dis)charge states. The resistances of the three electrodes rise dramatically to the maximum value at the end of the charging process (Figure 5.18c), whereas the discharge resistances drop to the lowest value when the cells are fully discharged (Figure 5.18d). In comparison to the S-KTO@C and S-KTO electrodes, the B-KTO electrode shows the largest resistance throughout the (dis)charge region, which is consistent with the large overpotential in Figure 5.19. Given the poor electrochemical performance of the B-KTO electrode, we therefore mainly study S-KTO and S-KTO@C electrodes in the following research.

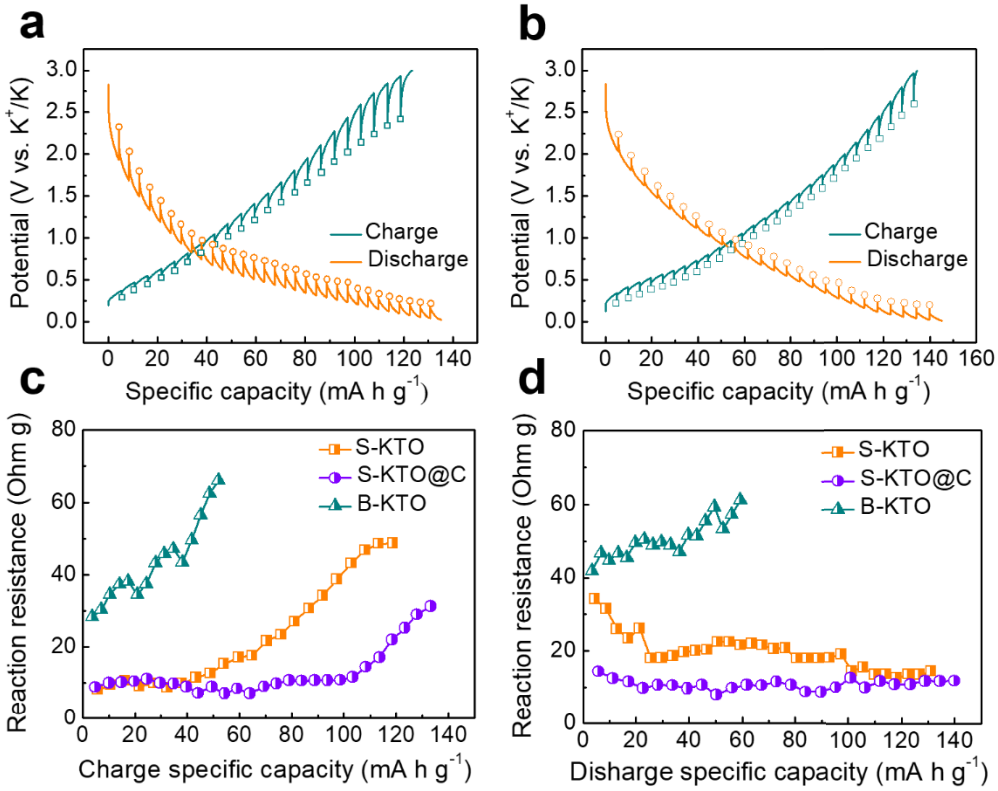

Figure 5.18 Galvanostatic intermittent titration technique (GITT) results for (a) S-KTO and (b) S-KTO@C electrodes measured at 0.1 C. (c) Charge reaction resistances and (d) discharge reaction resistances of S-KTO, S-KTO@C and B-KTO electrodes.

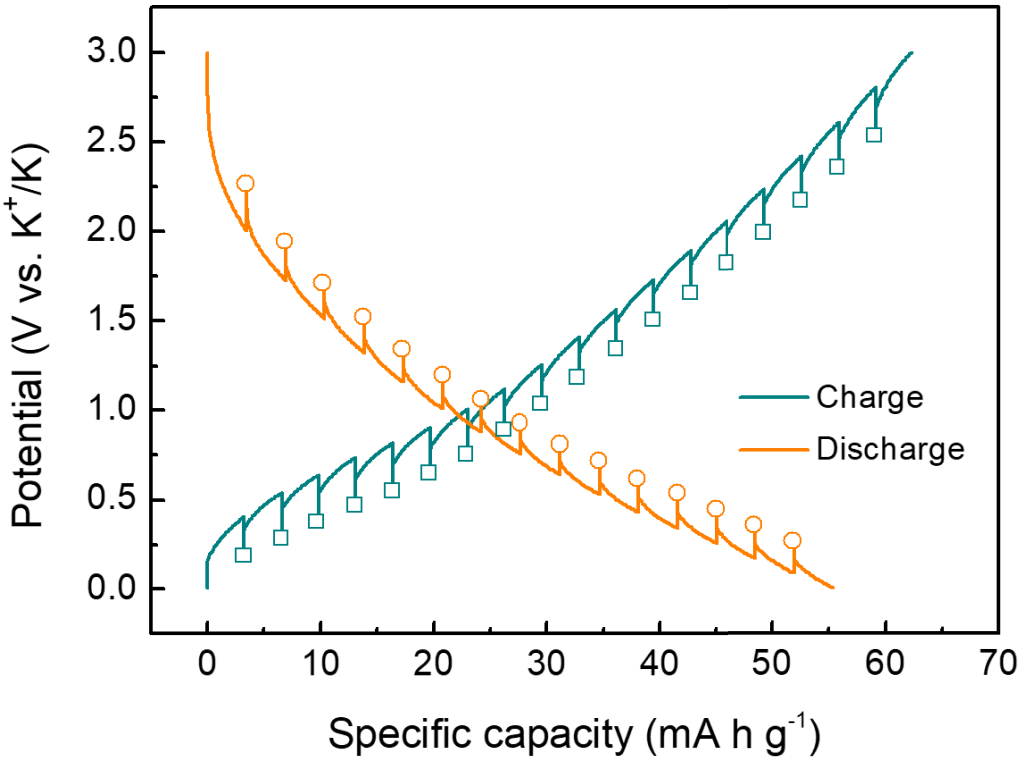

Figure 5.19 GITT profiles of the cell with a B-KTO electrode at a current density of 0.1 C.

In order to elucidate fast potassium storage behavior, it is necessary to understand the capacitive contribution of electrode materials during the (dis)charge/discharge process. **Figure 5.20**a and 5.20b show the cyclic voltammetry (CV) curves of the S-KTO and S-KTO@C electrodes recorded at 0.1 mV s^{-1}. Two strong and irreversible redox peaks appear at 1.13 and 0.70 V upon the first cathodic scan, corresponding to the formation of the SEI layer and irreversible electrolyte consumption. In the subsequent CV cycles, one pair of redox peaks located at 0.71 and 1.05 V indicates intercalation and deintercalation of K^+, respectively. However, these two peaks are inconspicuous in S-KTO@C due to the presence of amorphous

carbon. In view of this, we further analyze the relationship between the scan rate (v) and the measured current (i) according to the power-law relationship (**Figure 5.21**),[393-395]

$$i = av^b \quad \textbf{Equation 5.4}$$

where a and b are variable parameters. If the b value equals 1, the potassium storage is dominated by the surface-controlled process, and if the b value equals 0.5, the potassium storage is determined by the diffusion-controlled process. The b value can be calculated by drawing log(i)–log(v) linear plots:[396-397]

$$log\, i = b\, log\, v + log\, a \quad \textbf{Equation 5.5}$$

The as-obtained b values for the cathodic peaks (0.89 and 0.92) and anionic peaks (0.82 and 0.88) of S-KTO and S-KTO@C reveal that the material capacity can mainly be attributed to the surface-controlled process (**Figure 5.22**). In consideration of the percentage of different charge storage contributions, we quantitatively separate the total current response (i) into two parts: surface-controlled contribution (k_1v) and diffusion-controlled contribution ($k_2v^{1/2}$) through rewriting Equation 5.5.[394, 398-399]

$$i(V) = i_{capacitive} + i_{diffusion} = k_1v + k_2v^{1/2} \quad \textbf{Equation 5.6}$$

By plotting i(V)/$v^{1/2}$ versus $v^{1/2}$, we can confirm both k_1 and k_2 values and obtain the current per unit area. As shown in Figure 5.20c and 5.20d, the proportions of magenta areas (k_1v) contributed by the capacitive current are 32.4% and 48.6% for S-KTO and S-KTO@C, respectively, at a scan rate of 0.1 mV s^{-1}. These capacitive contributions grow with the scan rate and reach maximum values of 91.6% (S-KTO) and 95.2% (S-KTO@C) at a high scan rate of 5 mV s^{-1} (Figure 5.20e and 5.20f). These results indicate that the K^+ storage mechanisms of S-

KTO and S-KTO@C electrodes are dominated by the intercalation pseudocapacitive behavior at a high scan rate.[259, 397] Meanwhile, carbon-coating significantly increases the capacitive contribution to the total capacity of the S-KTO@C electrode.

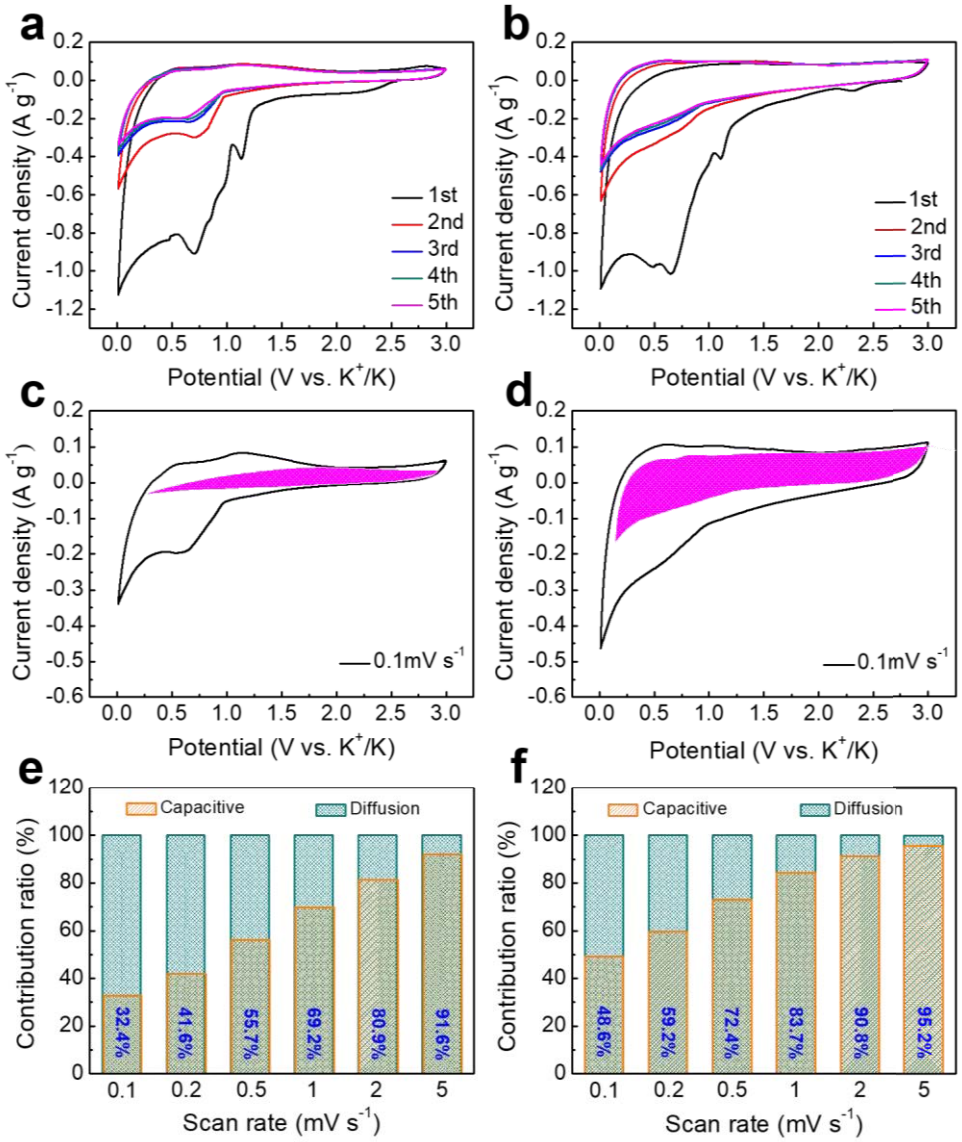

Figure 5.20 CV curves of K-half cells with (a) S-KTO and (b) S-KTO@C electrodes between 0.01 and 3 V (*vs.* K^+/K) at a scan rate of 0.1 mV s^{-1}. Quantitative analysis of the CV curves between the total current (black lines) and the surface capacitive current (pink regions) at a scan rate of 0.1 mV s^{-1} of (c) S-KTO and (d) S-KTO@C electrodes. The capacitive contribution histograms of the (e) S-KTO and (f) S-KTO@C electrodes at different scan rates.

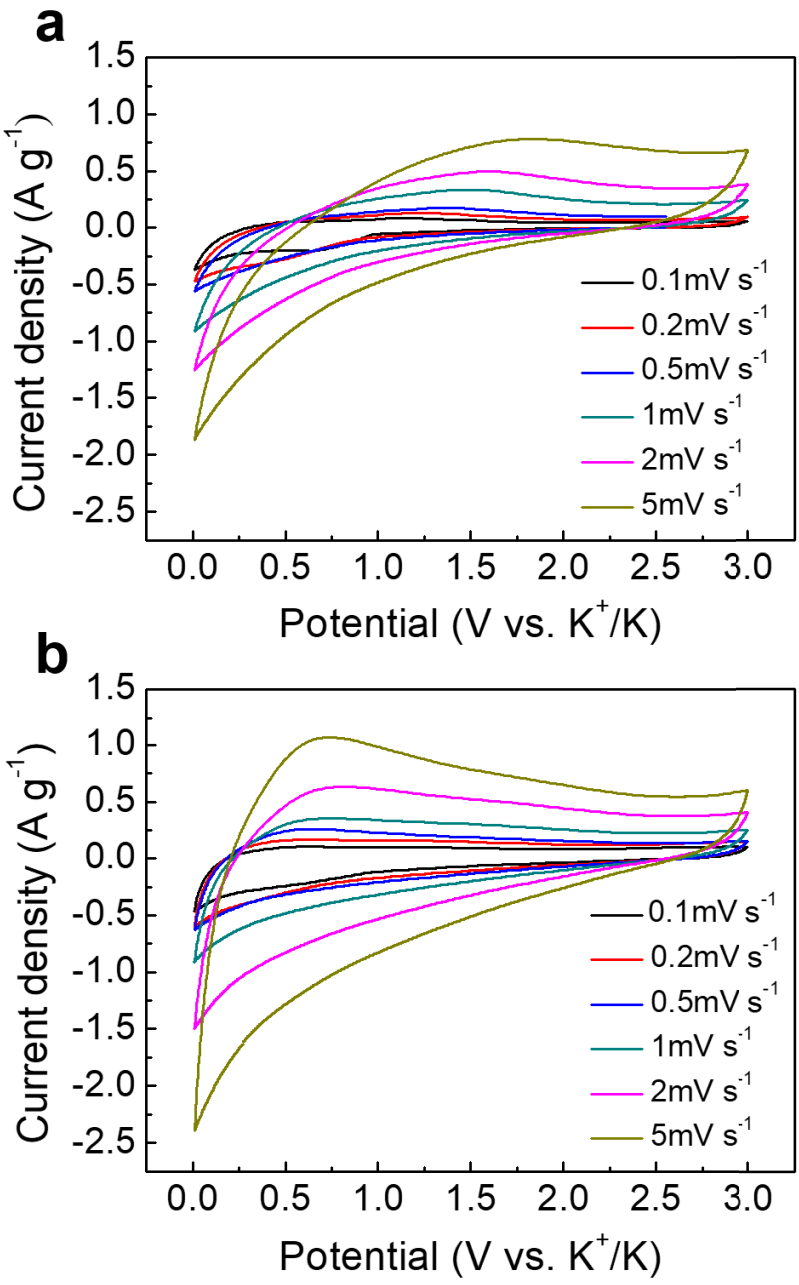

Figure 5.21 CV curves of (a) S-KTO and (b) S-KTO@C electrodes at different scan rates.

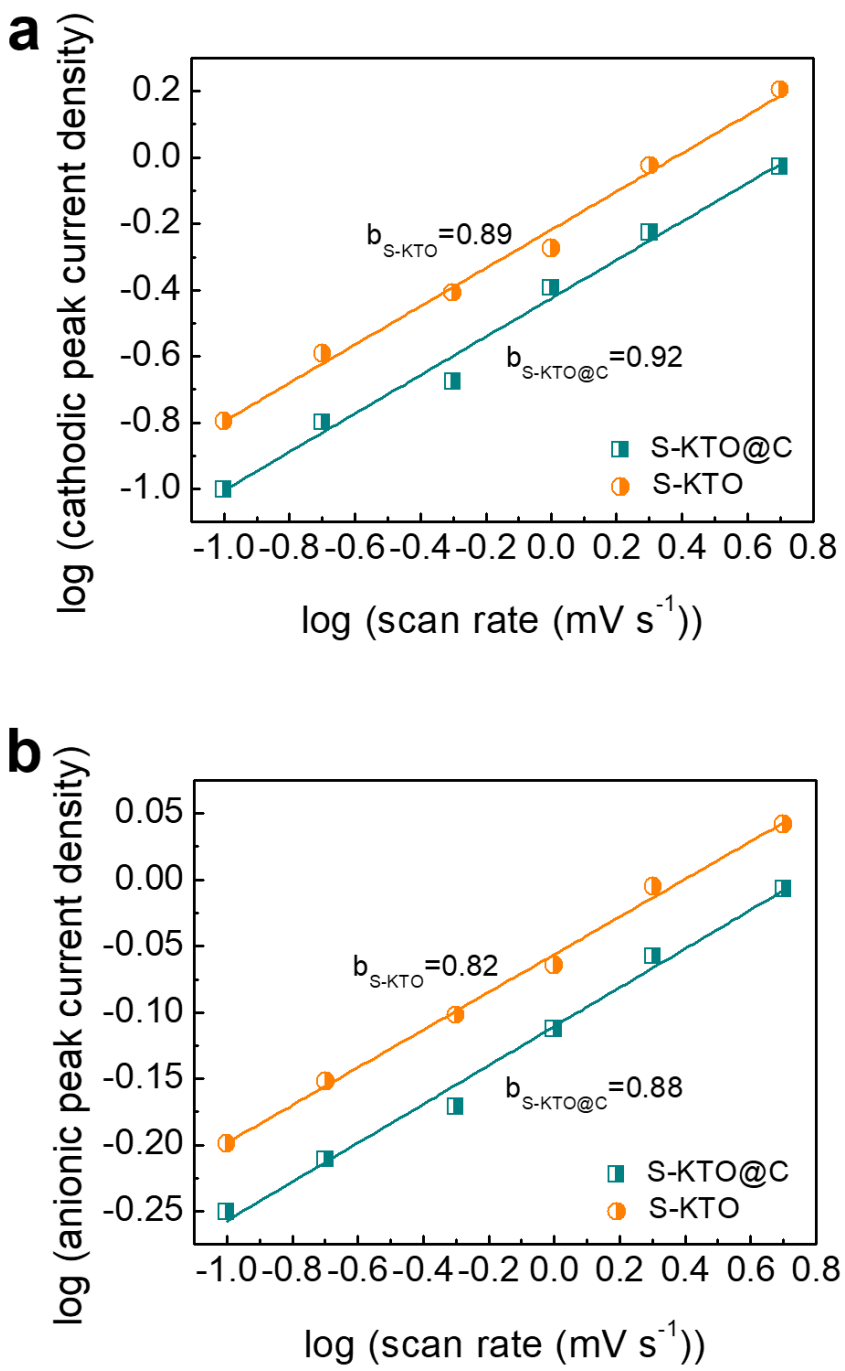

Figure 5.22 b-value analysis using the relationship between the (a) cathodic and (b) anodic peak currents versus scan rates.

As a proof of concept, potassium-ion hybrid capacitors (PIHCs) were fabricated, using the S-KTO@C (battery-type anode material) electrode and the commercial activated carbon (AC,

capacitor-type cathode material) electrode (**Figure 5.23**a). The electrolyte is 1 M potassium bis(fluoroslufonyl)imide (KFSI) in ethylene carbonate (EC) and diethyl carbonate (DEC) (1:1, volume ratio). AC has a very high specific surface area and abundant micropores and mesopores, which shows remarkable rate capability and good cycling stability as a cathode material for PIHCs.[400] These features make them suitable for rapid K^+ (de)absorbing (**Figures 5.24** and **5.25**). In order to optimize the electrochemical performance of the PIHCs, three mass ratios of anode to cathode were investigated. **Figure 5.26** reveals the electrochemical performance of the assembled PIHCs with different mass ratios of 1:1, 1.5:1 and 2:1. Obviously, the PIHC with the mass ratio of 1.5:1 shows the best electrochemical performances among all three devices. Therefore, we selected this ratio in the following study. Figure 5.23b reveals the CV profiles of fabricated PIHC in the voltage range from 0.01 to 3.5 V. Notably, the PIHC does not show noticeable voltage polarization even at a high working voltage of 3.5 V, indicating excellent electrochemical stability in such a wide voltage window. The fabricated device delivers an energy density of 57.4 Wh kg^{-1} and a maximum power output of 1.74 kW kg^{-1} (Figure 5.23c and 5.23d). Ragone plots of recently reported PIHCs, sodium-ion hybrid capacitors (SIHCs), lithium-ion hybrid capacitors (LIHCs) and zinc-ion hybrid capacitors (ZIHCs) were summarized in Figure 5.23e. The results clearly show that the S-KTO@C//AC PIHC is competitive to AC//AC symmetric supercapacitors (**Figure 5.27**) and other reported hybrid capacitors, such as soft carbon (SC)//AC PIHCs,[401] Prussian blue (PB)//AC PIHCs,[402] $Li_4Ti_5O_{12}$//AC LIHCs,[403] sodium titanate nanotubes (Na-TNTs)//AC SIHCs,[404] V_2O_5/CNT//AC SIHCs[405] and MnO_2//AC ZIHCs[400]. Moreover, the S-KTO@C//AC PIHC shows exceptional

cycling stability with a retention of 80.3% over 3000 cycles at a current density of 5 A g^{-1} (Figure 5.23f).

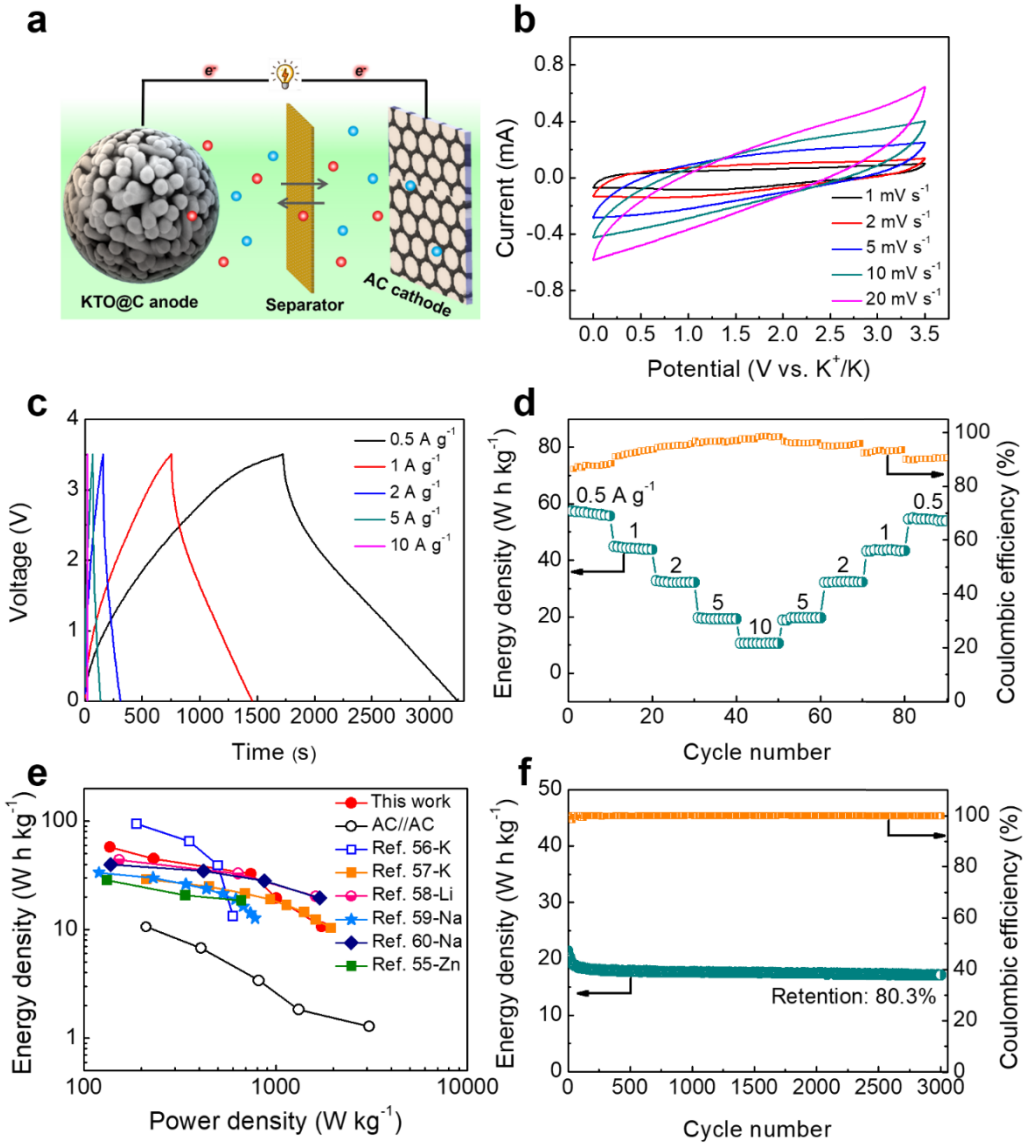

Figure 5.23 (a) Schematic illustration of a S-KTO@C//AC PIHC. (b) CV curves of the fabricated PIHC device at different scan rates. (c) GCD curves and (d) rate capability of the PIHC at different current densities. (e) Ragone plots in comparison with other works, including lithium-ion hybrid capacitors, sodium-ion hybrid capacitors, potassium-ion hybrid capacitors and zinc-ion hybrid capacitors. (f) Long-term cycling stability of the PIHC device at 5 A g^{-1} for 3000 cycles.

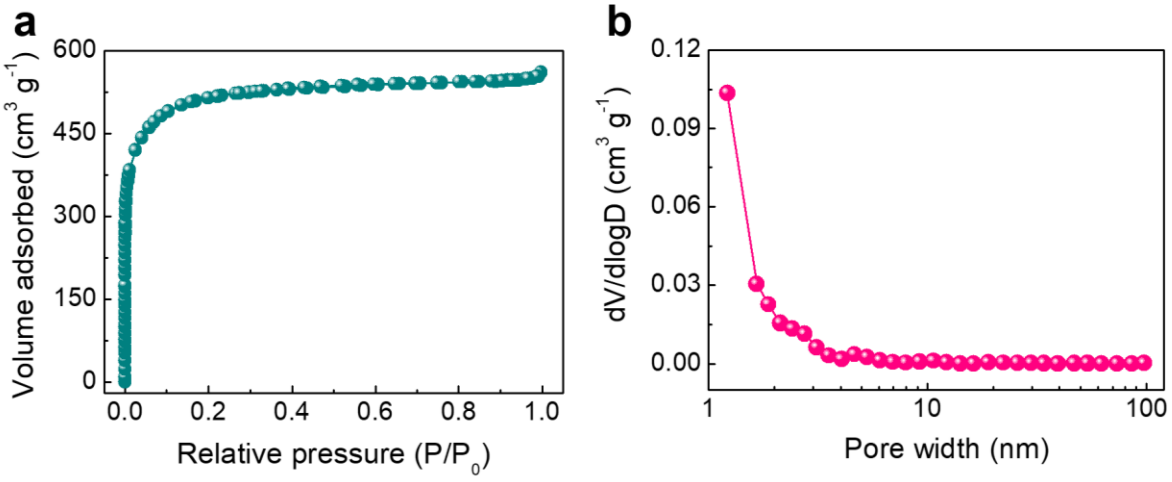

Figure 5.24 (a) The nitrogen adsorption/desorption isotherms and (b) corresponding pore size distribution of the employed AC.

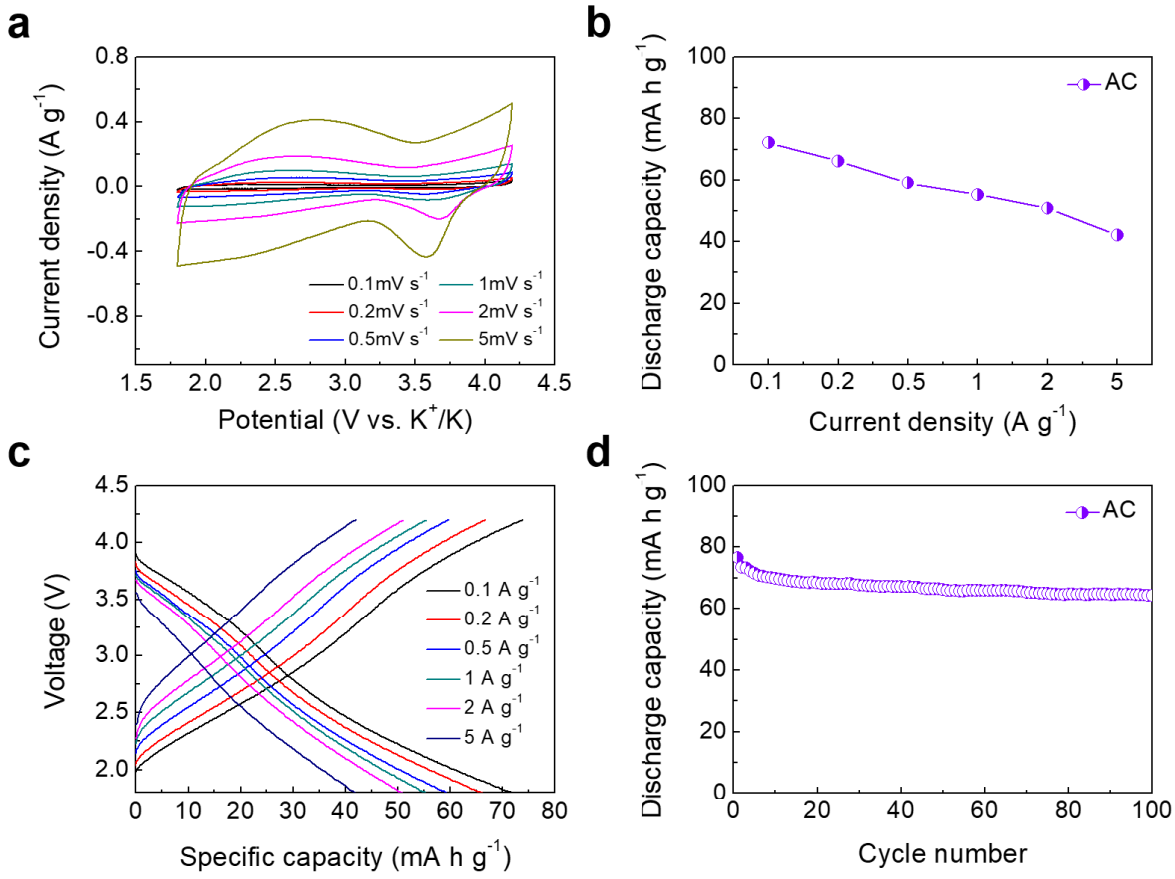

Figure 5.25 (a) CV curves of K-half cells with the AC electrode between 1.8 and 4.2 V (*vs.* K^+/K) at different scan rates. (b, c) Rate performances and relevant galvanostatic charge and

discharge voltage profiles of cells with the AC electrode at various current densities. (d) Cycling performance of cells with the AC electrode at a current density of 0.1 A g^{-1} for 100 cycles.

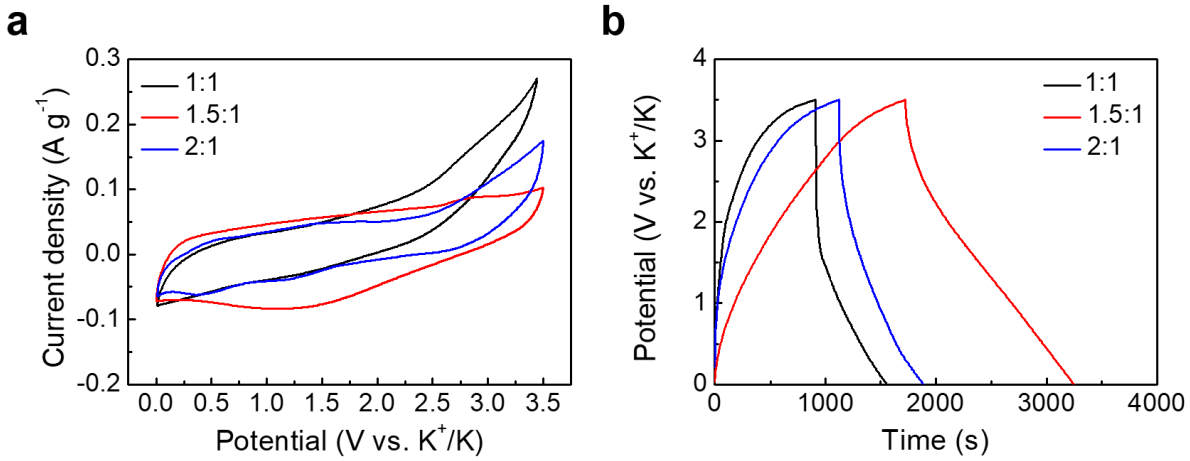

Figure 5.26 (a) CV curves and (b) galvanostatic charge and discharge voltage profiles of PIHCs with different mass ratios of anode to cathode.

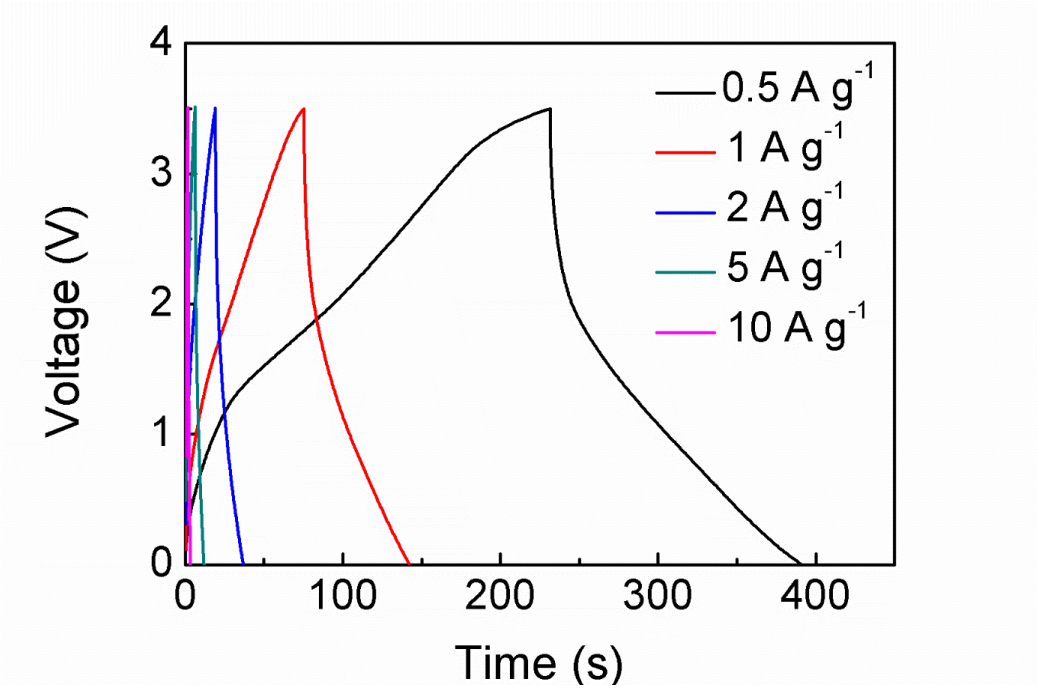

Figure 5.27 GCD curves of an AC//AC symmetric supercapacitor at different current densities.

5.4 Summary

In summary, S-KTO@C microspheres were synthesized via a spray drying method followed by a controlled CVD treatment. Material characterizations confirm that an ultrathin carbon layer with a thickness of 10 nm was successfully grown on the surface of KTO nanorods in S-KTO@C microspheres. When used as the anode material for PIBs, the as-synthesized S-KTO@C delivers a reversible discharge capacity of about 155.1 mAh g^{-1} at 0.1 C and outstanding capacity retention of 77.1% at 1 C after 1000 cycles, which is better than the pristine S-KTO and its bulk counterpart. *In situ* XRD characterization demonstrates that the S-KTO@C material undergoes reversible structural evolution during K^+ (de)intercalation. Quantitative analysis elucidates that potassium storage is dominated by a surface-controlled capacitive process at high current densities, which is attributed to both the porous microstructure and carbon-coating. By coupling with an activated carbon cathode, a well-designed potassium-ion hybrid capacitor was assembled. Such a device can operate at a cell voltage up to 3.5 V and deliver remarkable energy and power density with exceptional cycling stability. We believe that our work could provide valuable suggestions for the rational design of electrode materials and pave the way for the future development of potassium-ion batteries.

CHAPTER 6 PHOSPHORUS AND OXYGEN DUAL-DOPED POROUS CARBON SPHERES WITH ENHANCED REACTION KINETICS AS ANODE MATERIALS FOR HIGH-PERFORMANCE POTASSIUM-ION HYBRID CAPACITORS

6.1 Introduction

Rechargeable batteries, such as lithium-ion batteries (LIBs), have been widely utilized as the main power sources for portable electronic devices for decades.[4, 360, 406] Nevertheless, their poor rate capability and inferior cycle life struggle to meet the rapidly growing commercial market of electric vehicles (EVs) and grid-scale energy storage.[7, 407] Hence, there is an imperative demand for exploring complementary alternatives that are durable under long-term high-power operating conditions. Supercapacitors with ultrafast charge/discharge rates and exceptional durability have been demonstrated to be reliable to power high-speed trams but are significantly limited by their relatively low energy density for long-distance driving.[375, 408] Therefore, innovative energy storage devices are strongly desired to integrate high energy density with high power density. To this end, potassium-ion hybrid capacitors (PIHCs) have emerged as a promising choice for renewable energy storage. They employ both battery-type anodes and supercapacitor-type cathodes to bridge the gaps in lifespan, energy density and power density. Moreover, potassium is an abundant element in the earth's crust and shows a low standard redox potential (−2.94 V for K/K^+ vs. the standard hydrogen electrode, SHE). In addition, K^+ has a

smaller Stokes radius than that of Li^+ and Na^+, owing to its weaker Lewis acidity and smaller desolvation energy. This characteristic results in higher ionic conductivity of the electrolyte.[205, 267, 409-410] However, it remains a great challenge to discover suitable anode materials that support potassiation/depotassiation redox reactions. The size of K^+ (1.38 Å) is much larger than that of Li^+ (0.76 Å) and Na^+ (1.02 Å), which inevitably causes severe volume expansion of anode materials after repeated cycles, therefore, leading to performance degradation during electrochemical cycling. Furthermore, the sluggish diffusion kinetics of K^+ in the solid state of the anode materials also lowers its rate capability, which is vital in determining the power density of PIHCs.[200, 411]

Given the afore-mentioned problems, tremendous efforts have been made towards the development of high-performance anode materials.[268, 412-414] In comparison to other candidates such as transitional metal dichalcogenides, NASICON-structured compounds and alloying anodes, hard carbons stand out as one of the most promising anodes for potassium-based energy storage owing to their excellent rate capability, low cost and good chemical stability.[415-417] Despite some progresses in this field, they still suffer from many problems, such as an unsatisfactory depotassiation capacity (~250 mAh g^{-1}) and volume expansion.[409, 417-418] Moreover, the decomposition of carbonate-based electrolyte results in the formation of an organic-rich solid electrolyte interphase (SEI) on the surface of hard carbon anodes, which is unfavorable for the diffusion and transport of K^+.[267, 419]

In order to improve electrochemical performances of hard carbon anodes in PIHCs, nanostructural engineering has attracted great attention as an effective strategy.[417, 420-422] The

porous structure of hard carbons can buffer the large volume change upon potassiation and depotassiation, increase the contact area between the electrode and liquid electrolyte, and shorten the diffusion length for K^+ migration within the solid state.[423-424] Furthermore, the heteroatom (e.g., N, O, S and P) doping strategy has also been identified to be effective in enlarging the interlayer distance and improving the electronic conductivity of hard carbons.[397, 425-426] The introduction of heteroatoms induces a large number of defects, which can contribute to fast and efficient potassium adsorption storage in addition to the intercalation process. Such integration of adsorption-intercalation potassium storage mechanisms is beneficial to boost the rate performance through improved reaction kinetics.[425, 427-428] It has been reported that phosphorus-doping can enhance the electrochemical performances of carbonous anode materials in rechargeable alkaline-metal-ion batteries.[429-430] The strong affinity of P to alkaline metal ions provides additional capacitive contribution. Meanwhile, P-doping brings abundant defects and thereby promotes the improvement of electrochemical activity. Although P-doped carbon materials have been intensively investigated for LIBs and sodium-ion batteries (SIBs), there are few reports about P-doping in potassium-based energy storage devices and their specific functional mechanisms are unclear as well.[429-430]

Considering the advantages of both rational structure design and heteroatom doping, we synthesized phosphorus/oxygen dual-doped porous carbon spheres (P/O-PCSs) via a chemical vapor deposition (CVD) method, followed by a heteroatom doping process. The resultant three-dimensional (3D) porous structure serves as an open framework to alleviate the large volume expansion. Meanwhile, the introduction of heteroatoms gives rise to enlarged interlayer

distances and abundant active sites for K^+ storage, as evidenced by both experimental investigation and density functional theory (DFT) calculations. As battery-type anode materials, the as-synthesized P/O-PCS anode materials show a reversible discharge capacity of 401 mAh g^{-1} at 0.1 A g^{-1}, exceptional rate capability, and superior long-term cycling stability (89.8% after 10000 cycles). *In situ* Raman spectroscopy and *ex situ* XPS measurements reveal that the formation of P-C and P-O/P-OH bonds not only improves the structural stability, but also boosts the reaction kinetics of the hard carbon material during cycling. By coupling the P/O-PCS anode with a commercial activated carbon (AC) cathode, the fabricated potassium-ion hybrid capacitor exhibits remarkable electrochemical performances as a state-of-the-art energy storage device for long-term and large-scale energy storage.

6.2 Experimental section

6.2.1 Synthesis of $MnCO_3$ microspheres

The $MnCO_3$ precursors were obtained via a chemical precipitation method. Firstly, 1 mmol manganese sulfate monohydrate ($MnSO_4 \cdot H_2O$, 99.9%, Sigma–Aldrich) was dissolved in 100 mL distilled water and stirred for 1 h. Subsequently, 1 mmol sodium bicarbonate ($NaHCO_3$, 99.9%, Sigma–Aldrich) was dissolved in 100 mL distilled water and mixed with the $MnSO_4$ solution under vigorous stirring for 30 min. The formed precipitate was washed with ethanol and distilled water for several times and dried at 80 °C under vacuum overnight.

6.2.2 Synthesis of porous carbon sphere (PCS)

The $MnCO_3$ microspheres were placed in a quartz tube furnace and preheated to 650 °C under 50 sccm Ar gas flow ($MnCO_3 \rightarrow MnO + CO_2$). Then, acetylene (10 vol.% in Ar) was introduced for chemical vapor deposition (CVD) with a flow rate of 50 sccm for 1 h. After the furnace was naturally cooled down to room temperature, the as-synthesized MnO/C composite was etched by 2 M HCl to completely remove the MnO template and washed by ethanol and dried at 80 °C under vacuum for 20 h to obtain the PCS.

6.2.3 Synthesis of oxygen/phosphorus dual-doped porous carbon sphere (P/O-PCS)

The as-synthesized PCS and sodium hypophosphite monohydrate ($NaH_2PO_2 \bullet H_2O$, 99.9%, Sigma–Aldrich) were mixed with a mass ratio of 1:5 and then placed in a tube furnace and heated to 350 ºC for 2 h in Ar atmosphere. The obtained sample was purified with 0.1 M HCl solution and ethanol, followed by drying at 80 °C under vacuum overnight.

6.2.4 Materials characterization

The structure of the as-prepared sample was measured via a Bruker D8 Discovery X-ray diffractometer with Cu Kα radiation (2-Theta = 5° - 80°), and Raman spectra was carried out with a Renishaw inVia Raman spectrometer system (Gloucestershire, UK) in conjunction with a 17 mW Renishaw He-Ne laser source at 633 nm. The morphology was revealed by field-emission scanning electron microscopy (FE-SEM, Zeiss Supra 55VP) and transmission electron microscopy (TEM, field emission CM200, Fei) equipped with an energy-dispersive X-ray

spectrometer. The Brunauer-Emmett-Teller surface area analysis was performed based on a Micromeritics 3Flex analyzer. X-ray photoelectron spectroscopy (XPS) was conducted on an ESCALAB250Xi (Thermo Scientific, UK) associated with mono-chromated Al K alpha (energy: 1486.68 eV).

6.2.5 Electrochemical measurements

The anode was prepared by mixing the active materials, carbon black and polyvinylidene difluoride (PVDF) with a weight ratio of 8:1:1 in N-Methyl-2-pyrrolidone (NMP). Subsequently, the formed slurry was directly coated onto copper foils and dried at 100 °C under vacuum overnight. 2032-type coin cells (CR2032) were assembled in an Ar-filled glove box, using the prepared anodes and potassium metal foils. Glass microfiber filters (Whatman, Grade GF/D) and 1 M potassium bis(fluoroslufonyl)imide (KFSI) in ethylene carbonate (EC) and diethyl carbonate (DEC) with a volume ration of 1:1 were used as separators and electrolyte, respectively. Galvanostatic charge and discharge tests were conducted on a computer controlled NEWARE^{TM} battery tester. Cyclic voltammogram (CV) and electrochemical impedance spectra (EIS) measurements were obtained on a Biologic VMP3 electrochemical workstation. As for *ex situ* material characterizations, coin cells were cycled and dissembled in a glove box. These electrodes were used for *ex situ* measurements after washing with DEC solvent to remove impurities.

The relationship between the applied current (i) and the scan rate (v) in the CV analysis was calculated based on the power-law relationship:

$$i = av^b$$ **Equation 6.1**

Wherein a and b are variable parameters. If b equals 1, the potassium storage is mainly determined by the surface-dominated capacitive contribution process, while if b equals 0.5, the potassium storage is dominated by the diffusion-controlled process. The fitted b value can be obtained from the slope of log(i) –log(v) plots:

$$logi = blogv + loga$$ **Equation 6.2**

Moreover, the current response from the different potassium storage behavior can be quantitatively defined through:

$$i(V) = i_{capacitive} + i_{diffusion} = k_1 v + k_2 v^{1/2}$$ **Equation 6.3**

In this case, $k_1 v$ represents surface-driven contribution while $k_2 v^{1/2}$ indicates diffusion-controlled contribution.

Galvanostatic intermittent titration technique (GITT) was performed with a pulse current of 20 mA g^{-1} for 30 min, followed by a rest interval for 6 h. This process was repeated several times until the pre-set potential was reached. Before testing, all the cells were cycled at 50 mA g^{-1} for 5 cycles for activation. The ionic diffusion coefficient (D_k) is calculated by the following Equation (4):

$$D_k = \frac{4}{\pi}\left(\frac{IV_m}{Z_A FS}\right)^2 \left[\frac{\left(\frac{dE}{d\delta}\right)}{\left(\frac{dE}{d\tau^{1/2}}\right)}\right]^2$$ **Equation 6.4**

where I and V_m correspond to the impulse current and molar volume of anode materials, respectively. Z_A is the charge transfer amount of K^+. F represents the Faraday constant and t

stands for the duration time of the applied current. S is the active surface area between electrode and electrolyte. The slope of Coulometric titration profiles suggests dE/dδ, while $dE/d\tau^{1/2}$ is derived from relation curves between response time and voltage. If the cell voltage is linearly proportional to $\tau^{1/2}$, D_k can be acquired by simplifying the Equation (4) based on Fick's second law:

$$D_k = \frac{4}{\pi\tau}\left(\frac{n_m V_m}{S}\right)^2 \left(\frac{\Delta E_s}{\Delta E_\tau}\right)^2 \quad \textbf{Equation 6.5}$$

wherein, ΔEs, ΔEτ and n_m are the change of equilibrium potential, difference of cell voltage and the number of moles, respectively, at each current pulse step.

The temperature-dependent electrochemical impedance spectroscopy (EIS) is employed to calculate the K^+ activation energy according to the Arrhenius equation:

$$k = \frac{T}{R_s} = A\, exp\left(-\frac{E_{act}}{RT}\right) \quad \textbf{Equation 6.6}$$

Where k, T, R_s are the rate constant, the absolute temperature, and the transfer resistance, respectively. A represents the pre-exponential constant, R stands for the standard gas constant and E_{act} is the activation energy.

A potassium-ion hybrid capacitor (PIHC) was assembled using as-synthesized P/O-PCS as an anode and the activated carbon (AC, produced by Nanjing XFNANO Materials Tech Co., Ltd.; model: XFP06) as a cathode. The designed weight ratio of the cathode versus anode was 1:2. 1 M KFSI in EC and DEC (1:1 in volume) and glass microfiber membranes were employed as electrolytes and separators, respectively. Before fabricating a PIHC, both the P/O-PCS anode and the AC cathode were cycled 3 times in potassium half-cells for activation. The energy (E) and power (P) densities of the PIHC device were calculated based on the following equations:

$$E = \int_{t_1}^{t_2} UI/mdt$$ **Equation 6.7**

$$P = E/t$$ **Equation 6.8**

Where *I* and *U* are the charge/discharge current (A) and potential window (V), respectively. *m* represents the mass of the two electrodes, and *t* (s) is the discharge time.

6.2.6 *In situ* Raman measurements

The *in situ* Raman cell was fabricated according to a typical two-electrode configuration. In this case, a K metal foil (negative part) was placed on the glass slide as the counter and reference electrode, covered by a glass microfiber filter as the separator. Then, 50 μL of 1 M KFSI in EC and DEC (1:1 in volume) was slowly dropped on the separator. The electrode (positive part) was fabricated by coating the mixed slurry (active materials, carbon black, and PVDF with a mass ratio of 9:0.5:0.5) onto the stainless-steel mesh and placed on the top of separator. A piece of transparent quartz window (0.5 mm in thickness) was fixed on the top of the cell as an optical window to ensure internal tightness. The whole assembly process was done in an argon-filled glovebox, and the applied current was 50 mA g^{-1} with a working voltage ranging from 0.01 V to 3.0 V.

6.2.7 DFT calculations

All density functional theory (DFT) calculations were performed using Perdew-Burke-Ernzerhof (PBE) generalized gradient exchange approximation correlational functional and the projected augmented wave (PAW) pseudopotentials as implemented Vienna ab initio Package (VASP). The planewave cutoff energy was set at 500 eV. All structures were built by using a

supercell of 5×5×1 of the graphene unit cell. The Brillouin-zones were sampled with a k-point mesh of 3×3×1 in most calculations while 9×9×1 for the calculations of density of states. A vacuum layer of at least 20 Å in the non-periodic direction (z-axis) was used to avoid interactions between neighboring layers. Structures were relaxed when the energy difference was less than 10^{-4} eV. The adsorption energy of K in adsorption sites was calculated using the equation of $E_{ads} = E_{total}-E_{sub}-E_K$, where E_{tot} is the total energy of compounds obtained from DFT calculations, E_K is the energy of K atoms and E_{sub} is the energy of each substrate. Spin-polarizations were included in all calculations and the dispersion correction was included by DFT-D3. The nudged elastic band (NEB) method was used to estimate the diffusion barrier of K atoms, and the convergence criterion of forces were set as 0.02 eVÅ^{-1}.

6.3 Results and discussion

The synthesis process of P/O-PCS is illustrated in **Figure 6.1**a. Manganese carbonate ($MnCO_3$) microspheres with a diameter of about 1.5 μm (**Figure 6.2**a-c) were first prepared as precursors through a chemical co-precipitation method. After a CVD process, these precursors were transformed into carbon-coated manganese (II) monoxide (MnO) microspheres. As shown in **Figure 6.3**a-c, the transformation of $MnCO_3$ into MnO generates porous structures, and the decomposition of acetylene (C_2H_2) results in the formation of an ultrathin and uniform carbon coating layer on the surface of the porous MnO microspheres. Furthermore, porous carbon spheres (PCSs) were obtained by the removal of the MnO template via acid etching. **Figure**

6.4a-c indicates a typical 3D porous architecture of the as-prepared PCSs, which consists of many interconnected channels. The highly porous and open feature of PCS was further confirmed by high-resolution transmission electron microscopy (HRTEM). **Figure 6.5**a and 6.5b verifies that all the pores inside PCS are interconnected with each other to construct an open 3D framework, which is beneficial for the impregnation of electrolytes and shortens the diffusion pathway for K^+. The thickness of the carbon wall is approximately 5 nm, with an interlayer distance of 0.36 nm, corresponding to the (002) plane of the hard carbon structure. (Figure 6.5c and 6.5d). Finally, P/O-PCS was obtained by mixing PCS with sodium hypophosphite (NaH_2PO_2) through further calcination under an Ar atmosphere. Figure 6.1b and 6.1c reveals that the primary nanostructural characteristics of PCS were clearly preserved after heteroatom doping. Figure 6.1d shows that the interlayer distance of P/O-PCS (0.38 nm) is slightly larger than that of PCS (0.36 nm). This enlarged interplanar spacing is mainly ascribed to the heteroatom doping effect.[430] From the selected area electron diffraction (SAED) results (**Figure 6.6**a and 6.6b), it is evident that both PCS and P/O-PCS have a disordered carbon structure with low graphitization. Energy-dispersive X-ray spectroscopy (EDS) mapping images (**Figure 6.7**a–d) confirm the homogenous distribution of P and O over the entire material.

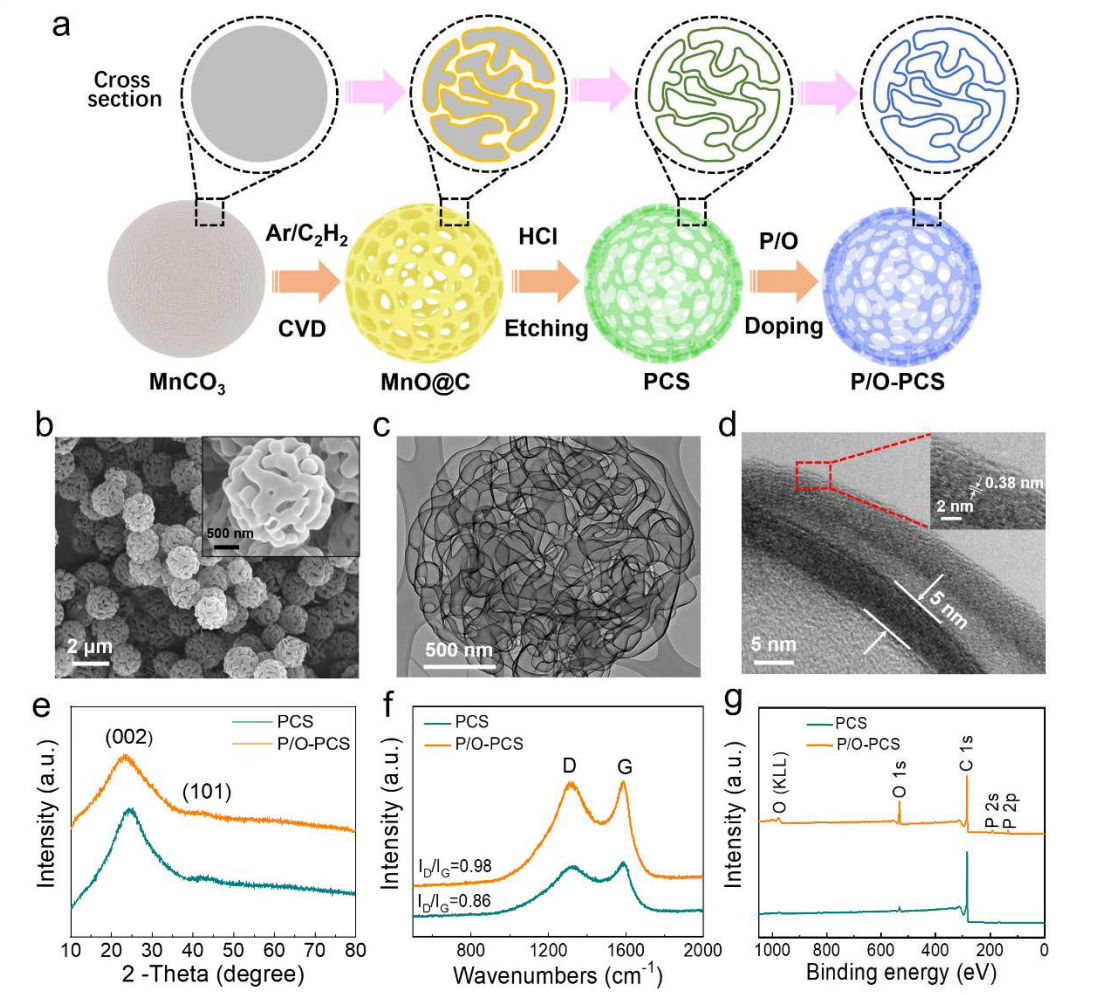

Figure 6.1 (a) The synthesis process of the P/O-PCS material. (b-d) SEM and TEM images of as-prepared P/O-PCS. (e) XRD patterns, (f) Raman spectra and (g) XPS spectra of PCS and P/O-PCS.

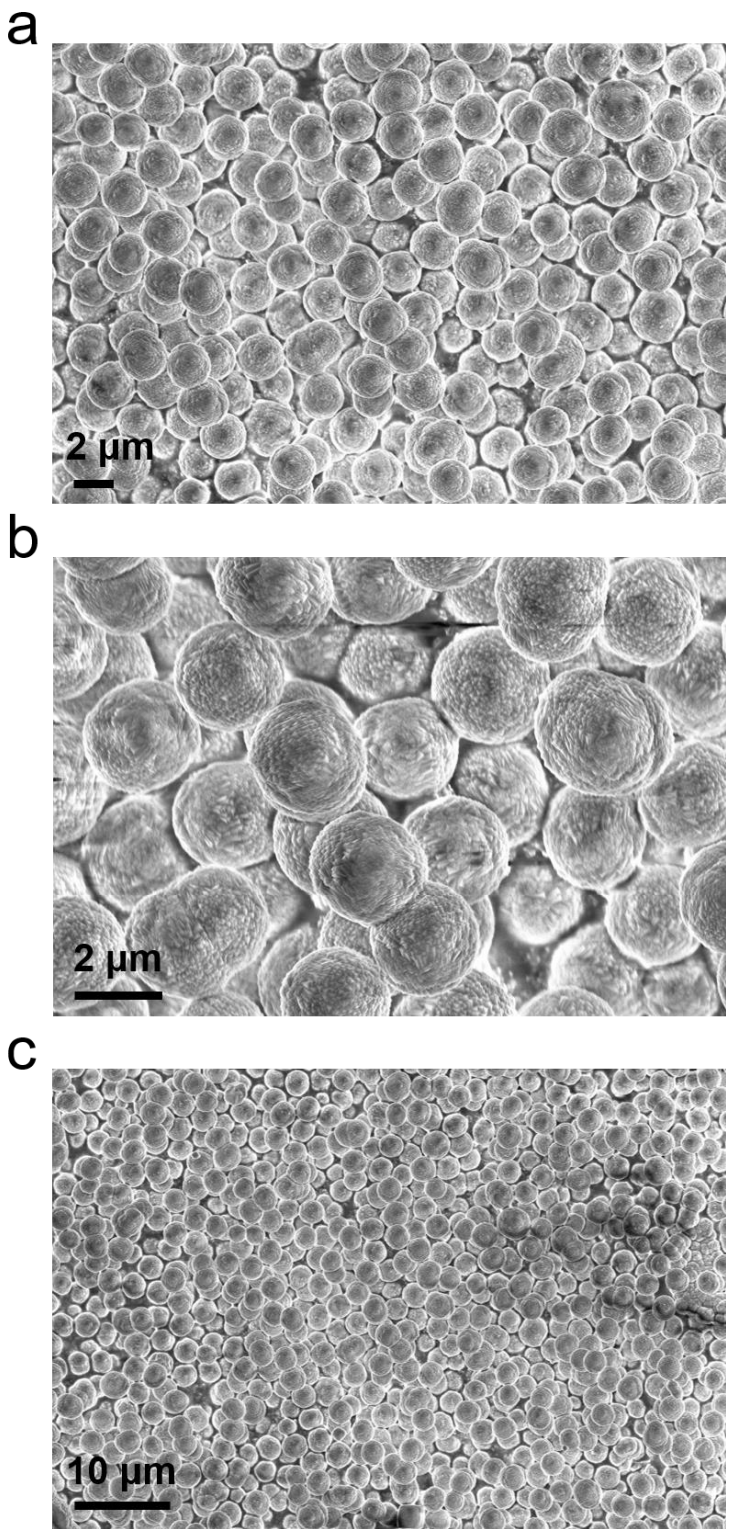

Figure 6.2 (a-c) SEM images of $MnCO_3$ precursors.

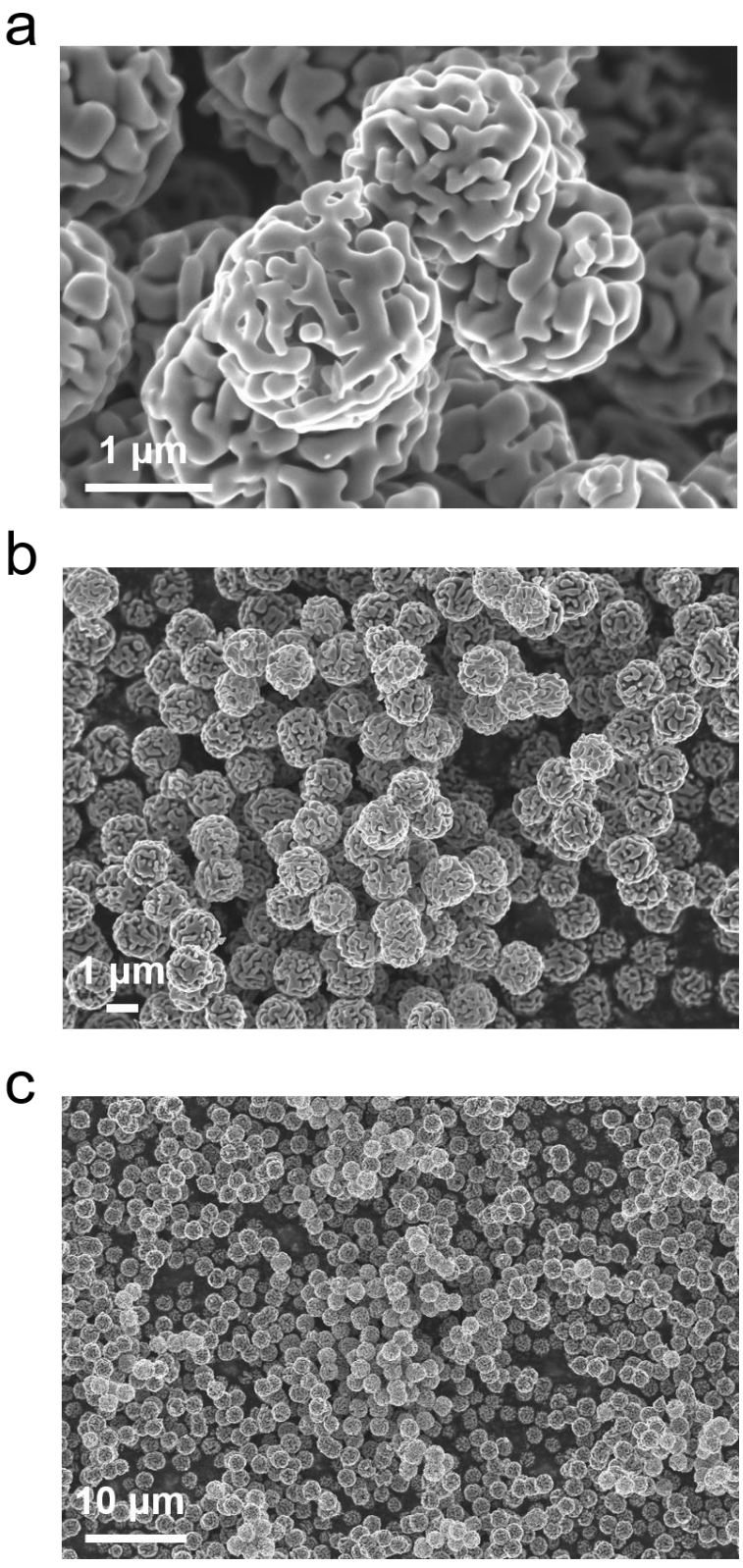

Figure 6.3 (a-c) SEM images of MnO@carbon composites.

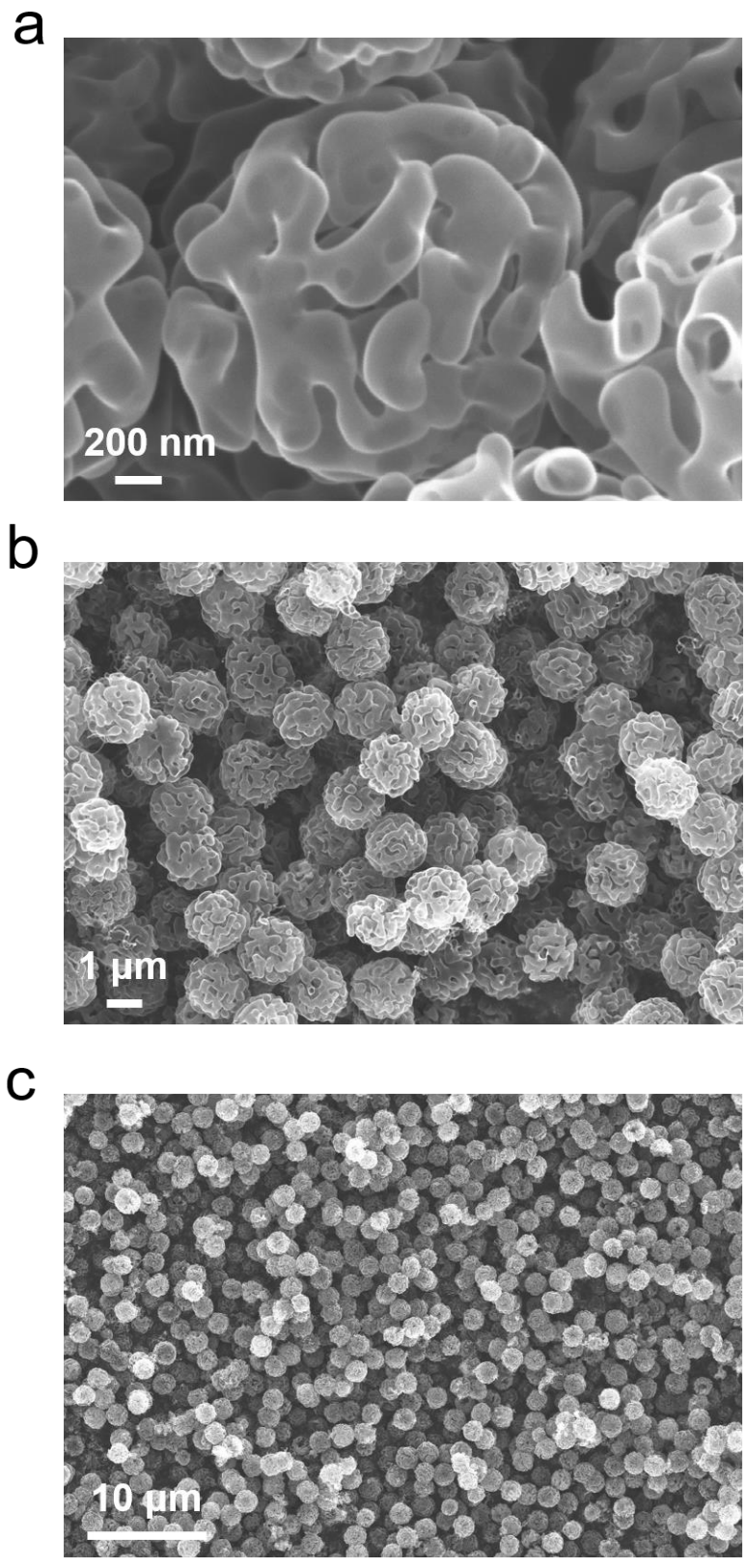

Figure 6.4 (a-c) SEM images of PCS materials.

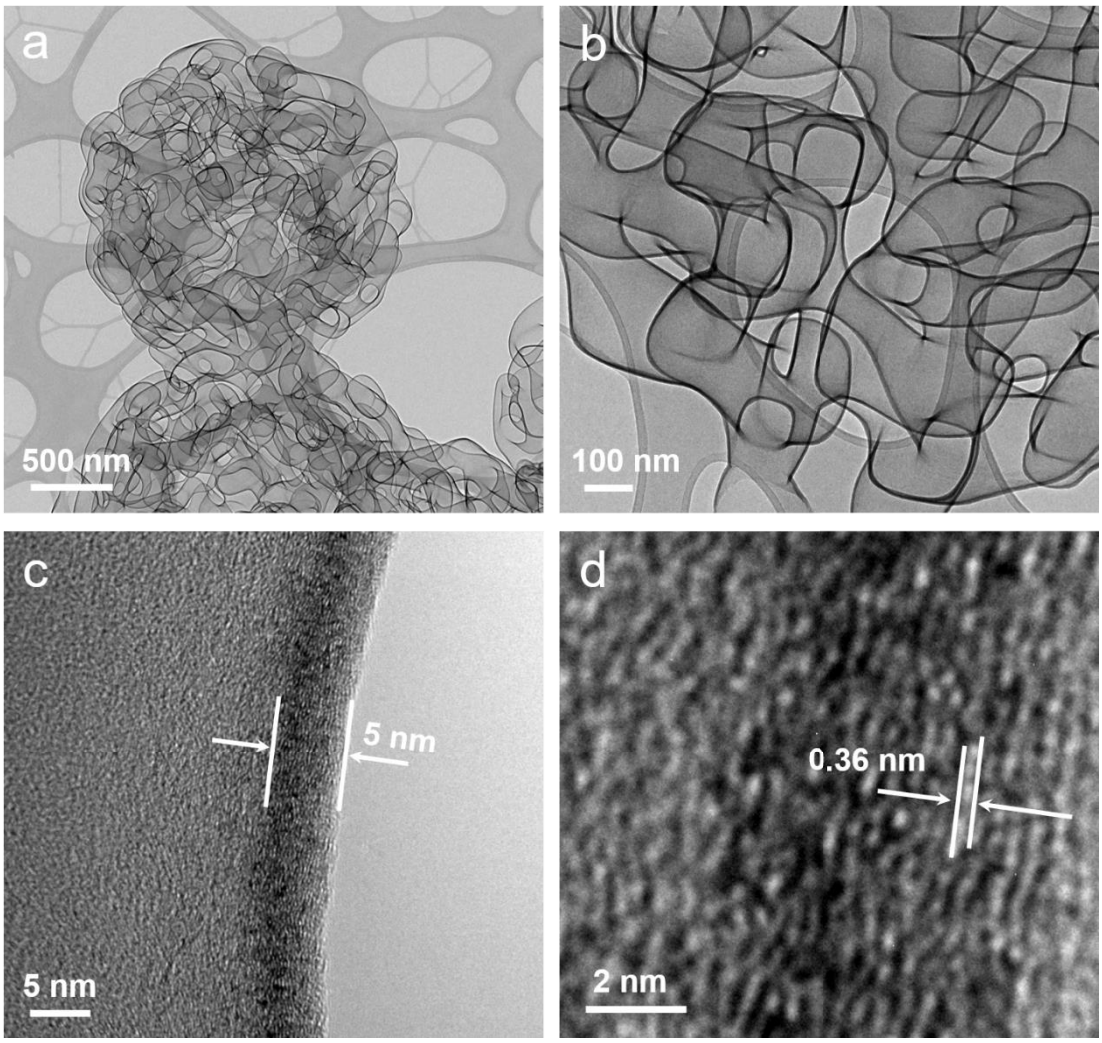

Figure 6.5 (a, b) Low-magnification and (c, d) high-magnification TEM images of PCS.

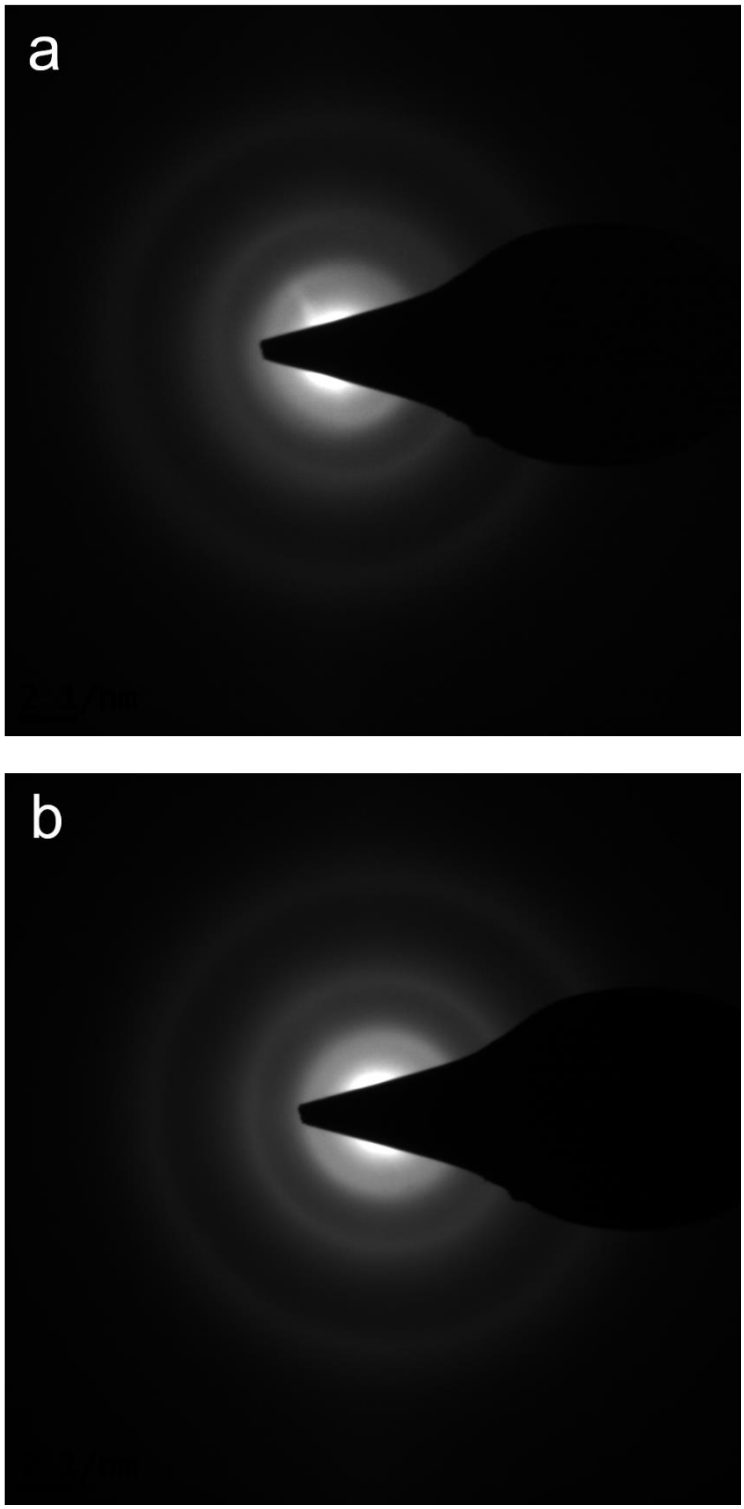

Figure 6.6 SAED patterns of (a) PCS and (b) P/O-PCS materials.

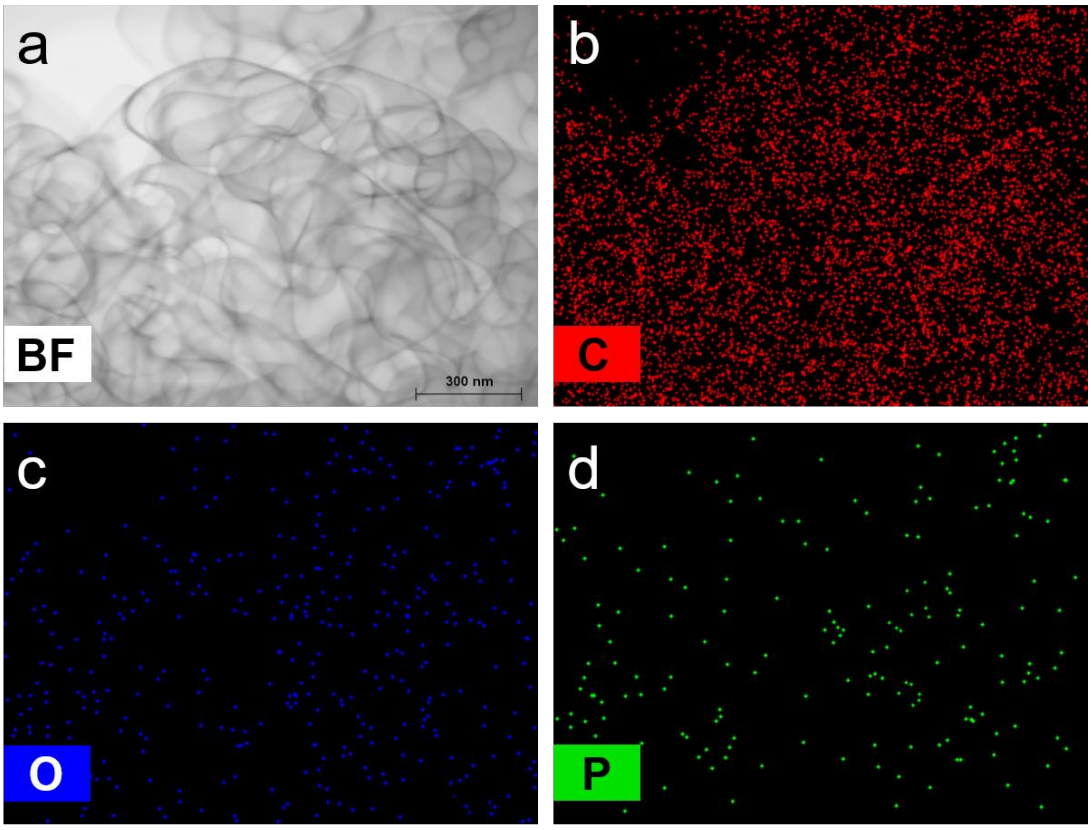

Figure 6.7 (a) TEM-EDS elemental maps for (b) C, (c) O and (d) P in the P/O-PCS material.

The structure of the as-synthesized materials was further characterized by X-ray diffraction (XRD). As shown in Figure 6.1e, two broad and weak diffraction peaks can be well indexed to disordered (002) and (101) carbon planes. In contrast to the pristine PCS, the (002) diffraction peak of P/O-PCS shifts slightly to a lower position, indicating the expanded interlayer distance after elemental doping, which agrees well with the TEM results. Raman spectra (Figure 6.1f) display two characteristic peaks located at 1340 cm^{-1} and 1580 cm^{-1}, representing the disorder-induced D-band and in-plane stretched G-band, respectively. The intensity ratio (I_D/I_G) of P/O-PCS increases from 0.86 to 0.98 after P/O dual doping, implying more defects and active sites have been introduced into the carbon matrix. Moreover, nitrogen adsorption–desorption isotherms were obtained to calculate the surface area, as shown in **Figure 6.8**. All profiles

clearly exhibit IV type isotherms with H3 type hysteresis loops, confirming the meso/macroporous structure.[397] In addition, P/O-PCS has a slightly larger specific surface area (246 $m^2 g^{-1}$) than that of PCS (221 $m^2 g^{-1}$). This further indicates the introduction of defects in P/O-PCS, which could contribute to fast-ionic diffusion channels and the reduced transport distance of K^+. The chemical compositions of PCS and P/O-PCS were examined by X-ray photoelectron spectroscopy (XPS) analysis. Compared to the pristine PCS, the overall survey spectra in Figure 6.1g depict the strong O and additional P signals in P/O-PCS. Moreover, the high-resolution C 1s and O 1s spectra in **Figure 6.9**a and 6.9b indicate the existence of P-C and P-O/P-OH bands. This result is further verified by the high-resolution P 2p spectra presented in Figure 6.9c, where two fitting peaks located at 134.6 eV and 130.5 eV can be assigned to P-O/P-OH and P-C bands, respectively. The presence of P species, with an atomic percentage of 1.1%, confirms the success of the heteroatom doping strategy (**Table 6.1**). Meanwhile, a surge in O peak intensity of P/O-PCS also unravels the incorporation of a large number of oxygen-rich defects into the structure,[430] which is consistent with both the TEM and Raman findings.

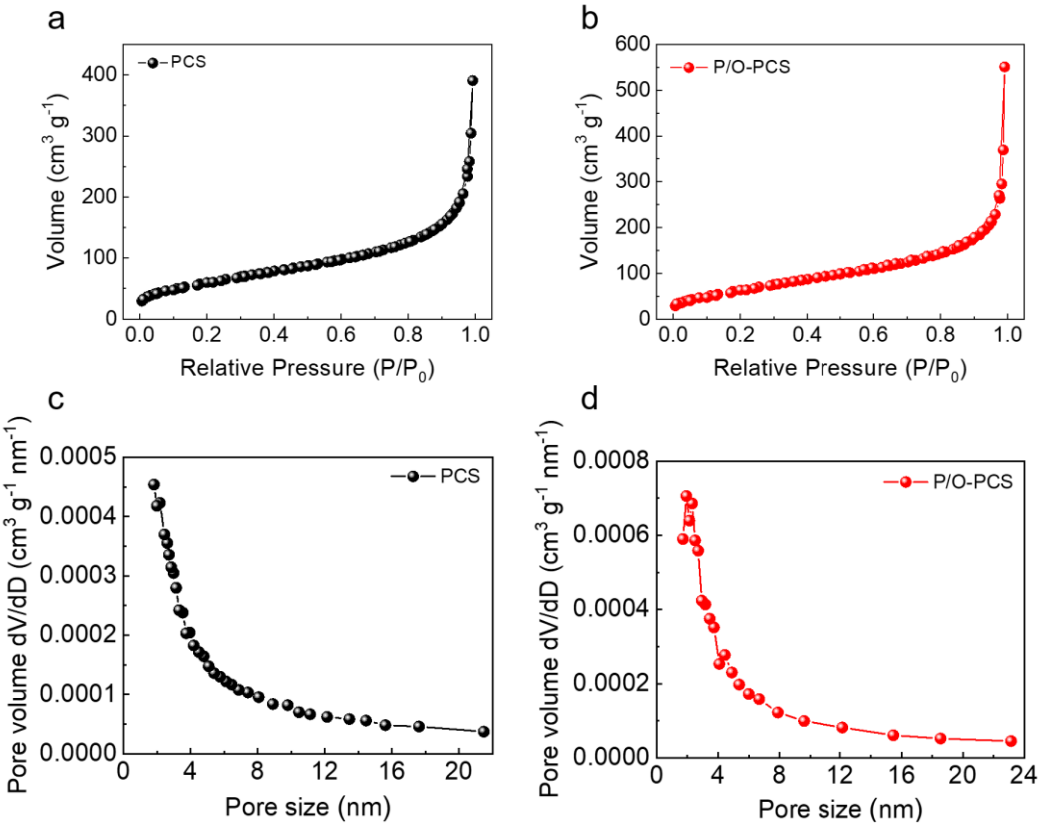

Figure 6.8 Nitrogen adsorption–desorption isotherms of (a) PCS and (b) P/O-PCS materials. Pore size distribution for the (c) PCS and (d) P/O-PCS materials.

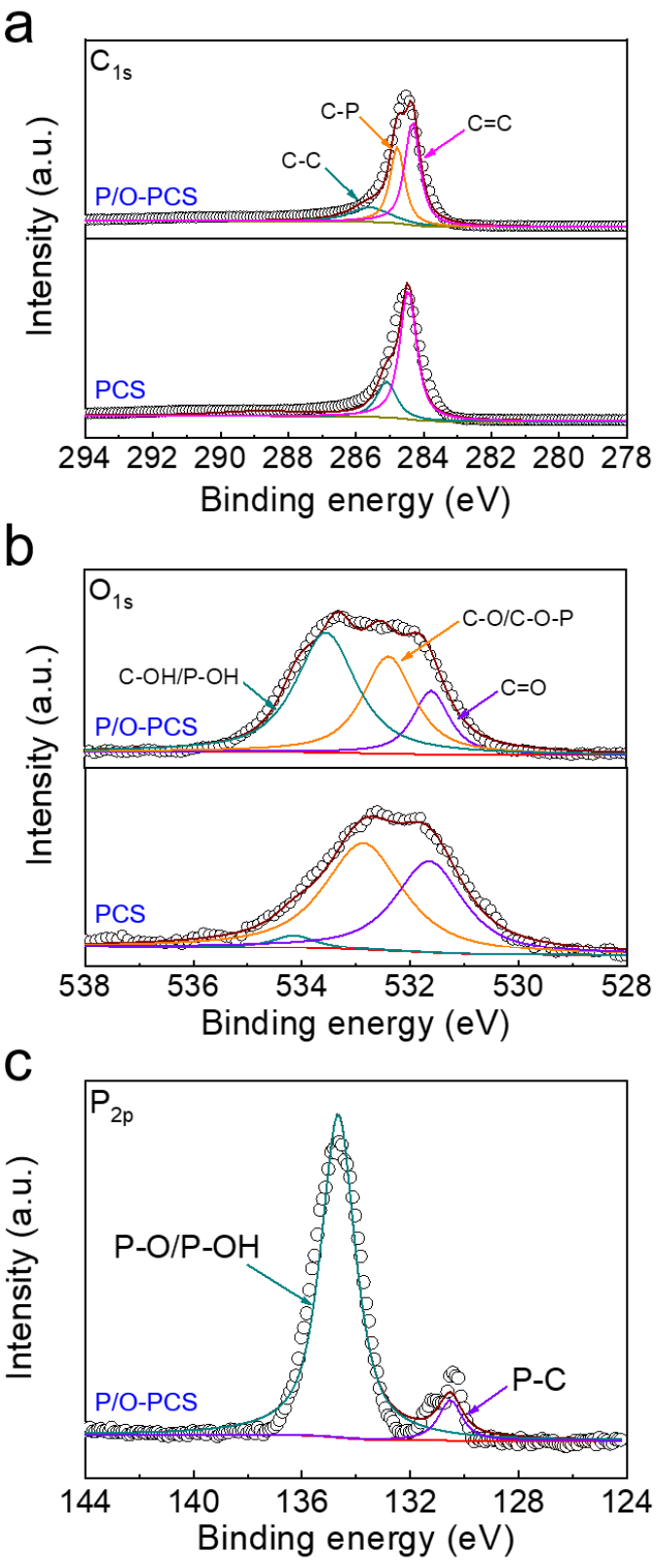

Figure 6.9 High-resolution XPS spectra of (a) C, (b) O and (c) P for PCS and P/O-PCS materials.

Table 6.1 Atomic percentage of different chemical compositions in PCS and P/O-PCS based on the EDS analysis.

Elements	PCS	P/O-PCS
C	89.8%	80.7%
O	10.2%	18.2%
P		1.1%

The potassium storage performance of the as-prepared PCS and P/O-PCS was evaluated by cyclic voltammetry (CV) measurements within the voltage range of 0.01–3.0 V (**Figure 6.11**). During the first cycle, both electrodes show a broad and irreversible cathodic peak at about 0.5 V, which is derived from the formation of the SEI layer accompanied by the decomposition of the carbonate electrolyte.[412, 421] Furthermore, a pair of redox peaks around 0.65 V and 0.6 V is also observed in the low potential region, corresponding to intercalation and deintercalation of K^+ into carbon layers (Figure 6.11a and 6.11b). Notably, P/O-PCS shows an extra pair of redox peaks located at 0.45 V and 1.25 V (Figure 6.11c and 6.11d), representing unique P-based redox reactions involved in the potassium storage process.[430] In the subsequent cycle, all CV curves overlap with each other, demonstrating excellent electrochemical reversibility. Figure 6.10a and 6.10b displays galvanostatic charge and discharge profiles of two electrodes at a current density of 0.1 A g^{-1}. The initial Coulombic efficiencies (ICE) of PCS and P/O-PCS are 42% and 40%, respectively. The irreversible capacity loss that occurs in the first cycle is ascribed to the formation of the SEI layer and irreversible trapping of K^+ inside the carbon structure.[421] Apart from that, P/O-PCS delivers a higher depotassiation capacity of 401 mAh g^{-1} compared

to the pristine PCS (346 mAh g^{-1}). Moreover, as shown in Figure 6.10c, both electrodes exhibit outstanding capacity retention (83% for PCS and 85% for P/O-PCS after 300 cycles). Postmodern SEM analysis (**Figure 6.12**) show that both electrodes are able to maintain their original microstructure after repeated cycles. The enhanced electrochemical performance and structural stability of P/O-PCS could be ascribed to the synergistic effect of structural engineering and the P/O heteroatom doping approach, which is beneficial to buffer the large volume expansion, shorten diffusion paths of K^+ and promote rapid potassium adsorption storage. Electrochemical impedance spectra (EIS) were carried out to measure the interfacial resistance of two electrodes after 300 cycles. As shown in **Figure 6.13**, P/O-PCS shows a smaller charge transfer resistance (R_{ct}) value than that of PCS at the end of the 300th cycle.[431-432] This phenomenon is originated from the improved interfacial stability between the electrode and electrolyte after heteroatom doping.

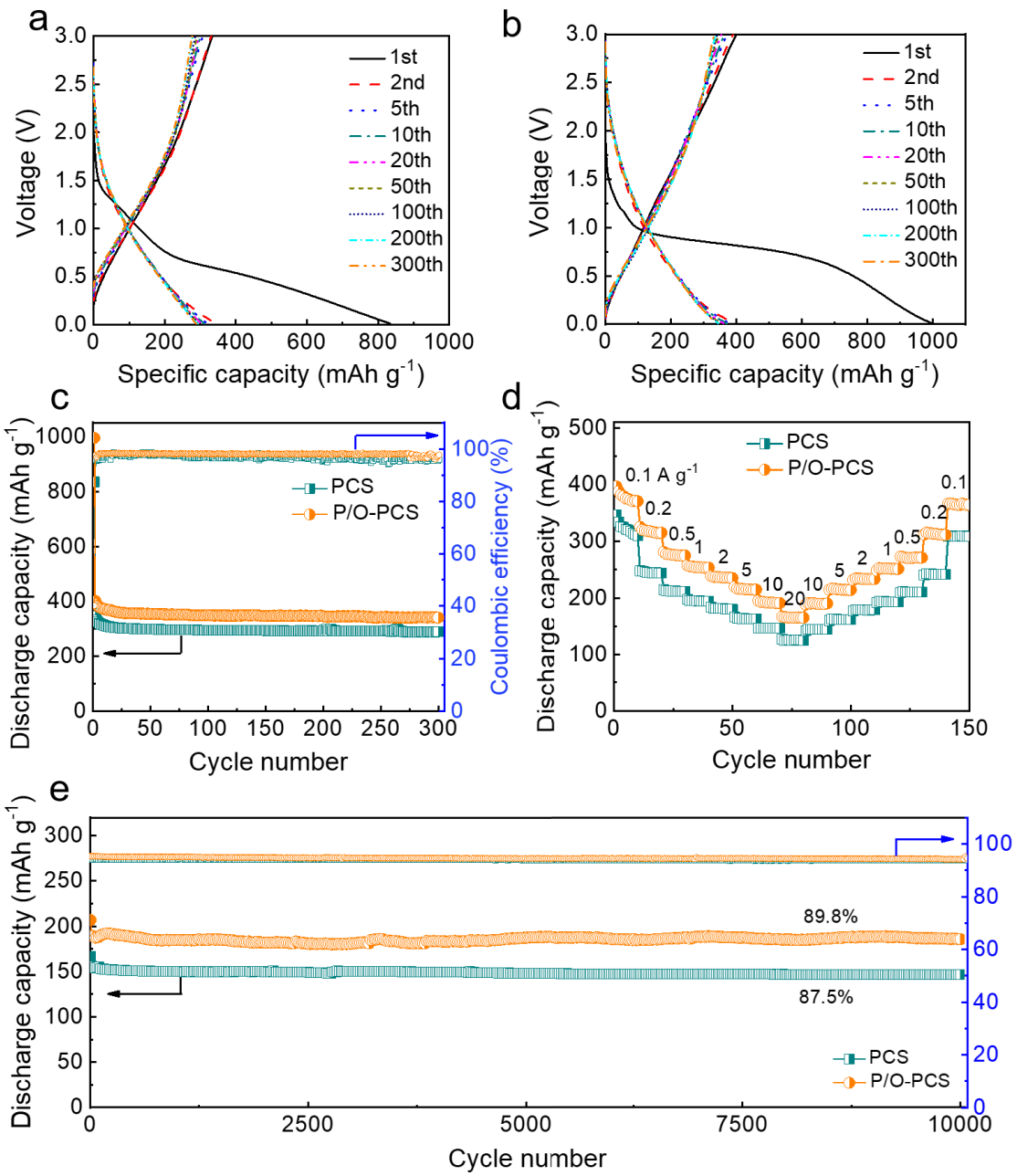

Figure 6.10 Galvanostatic charge and discharge voltage profiles of (a) PCS and (b) P/O-PCS electrodes between 0.01 and 3 V (*vs.* K^+/K) at a current density of 0.1 A g^{-1}. (c) Cycle life of PCS and P/O-PCS electrodes at 0.1 A g^{-1} for 100 cycles. (d) Rate capability of PCS and P/O-PCS electrodes at various current densities (0.1 A g^{-1} – 20 A g^{-1}). (e) Long-term cycling stability of PCS and P/O-PCS electrodes at 20 A g^{-1} for 10000 cycles.

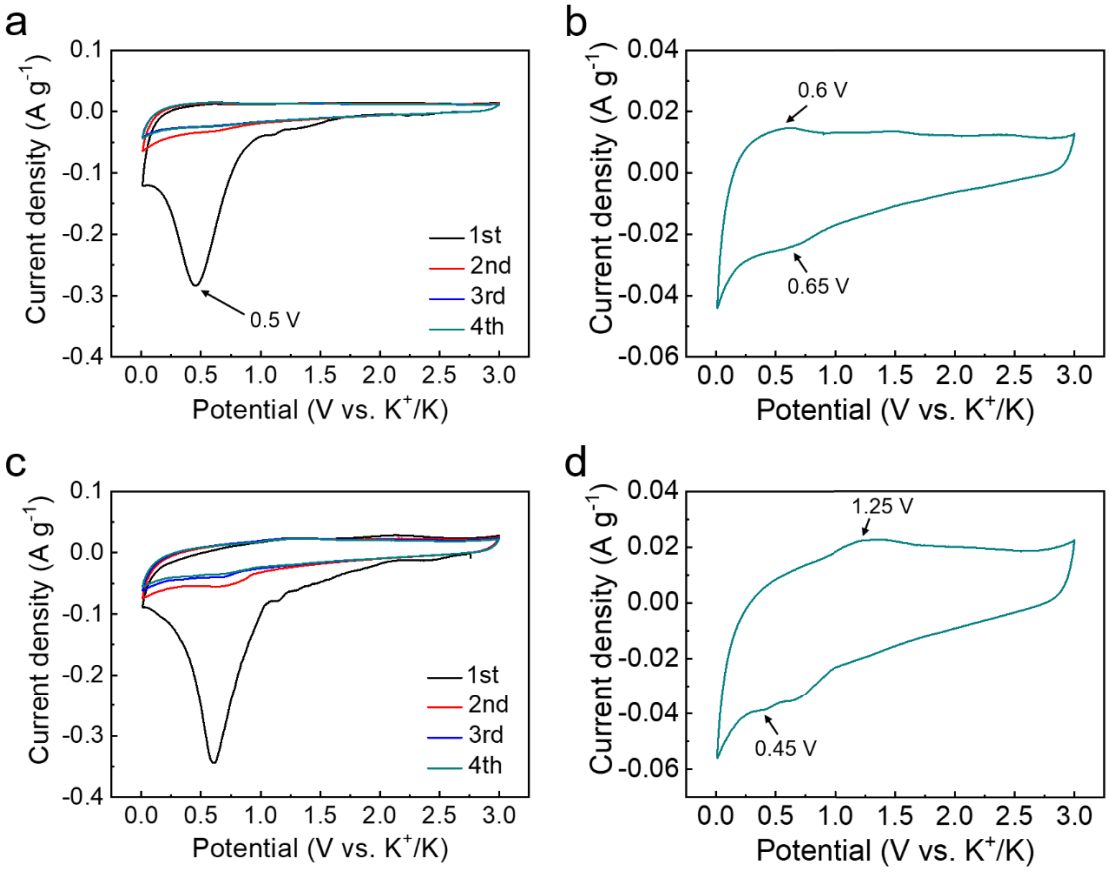

Figure 6.11 CV curves of (a) PCS and (c) P/O-PCS electrodes at a scan rate of 0.1 mV s^{-1} between 0.01 and 3 V (vs. K^+/K). The CV profiles of (b) PCS and (d) P/O-PCS after the fourth cycle.

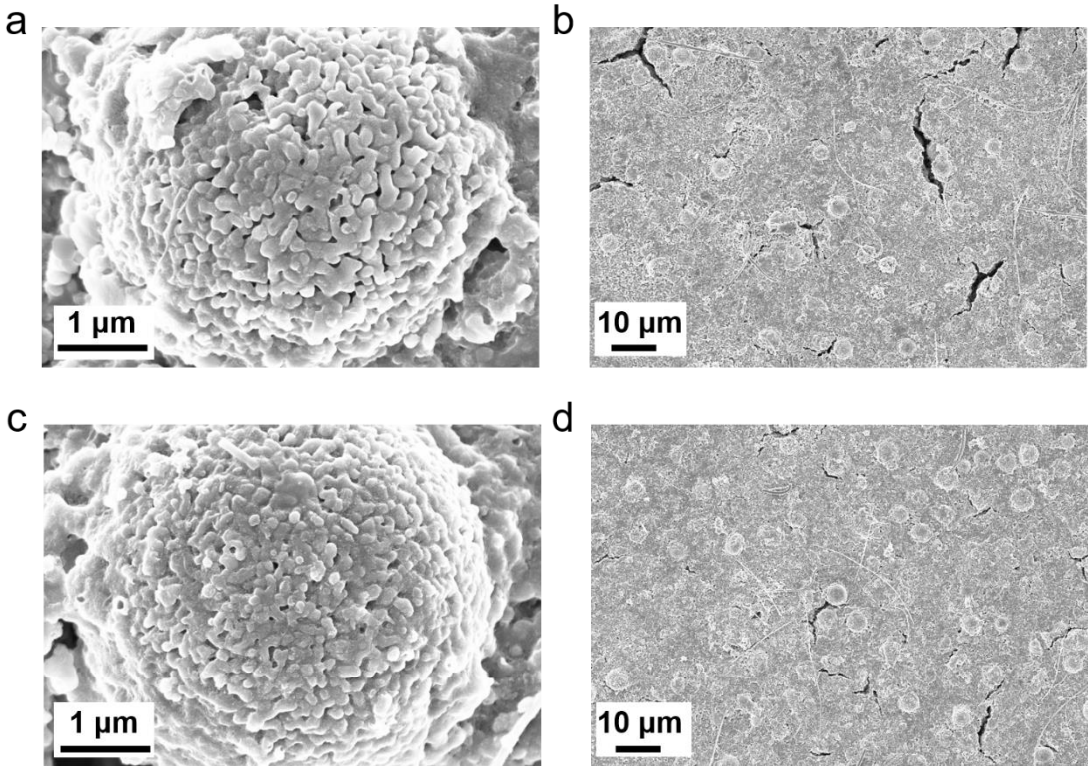

Figure 6.12 SEM images of (a, b) PCS and (c, d) P/O-PCS electrodes at different magnifications before and after 300 cycles.

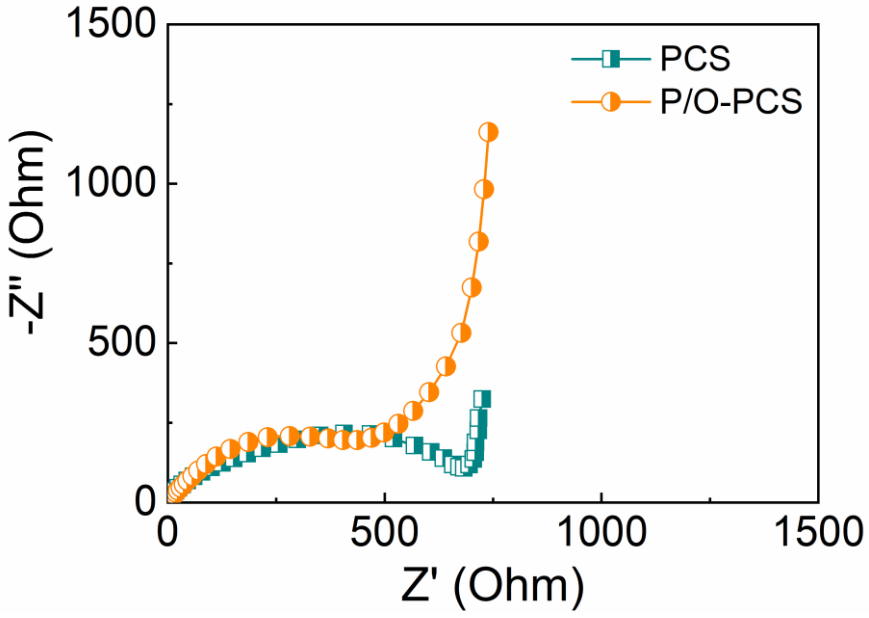

Figure 6.13 Electrochemical impedance spectra (EIS) of the cells with PCS and P/O-PCS electrodes after the 300th cycle.

We further increase the current density to investigate the rate performance of PCS and P/O-PCS electrodes (Figure 6.10d and **Figure 6.14**). As expected, P/O-PCS delivers high specific capacities of 403, 326, 281, 258, 239, 220 and 195 mAh g^{-1} at current densities of 0.1, 0.2, 0.5, 1, 2, 5 and 10 A g^{-1}, respectively. Even at a very high current rate of 20 A g^{-1}, P/O-PCS still shows a discharge capacity of 168 mAh g^{-1}, which is much higher than previously reported anode materials in the half cell (**Figure 6.15**).[397, 428, 433-437] When the discharge current density is reduced back to 0.1 A g^{-1}, the discharge capacity of P/O-PCS restores to almost its original level, illustrating good electrochemical reversibility. Figure 6.10e manifests the long-term cycling stability of the as-prepared electrodes. P/O-PCS shows superior capacity retention of 89.8% even after 10000 cycles, which is one of the best results among state-of-the-art anode materials (**Figure 6.16**).[397, 412, 416, 422, 425, 433, 436, 438-441] To further understand the influence of heteroatom doping on potassium storage behavior, CV analysis was performed to study the reaction mechanism of two electrodes at different scan rates (**Figure 6.17**). As indicated in **Figure 6.18**, *b* values of carbon-based redox peaks are very close to 0.5, implying a diffusion-dominated process. Whereas the CV peaks derived from the phosphorus-based redox reaction in P/O-PCS show *b* values of 0.91 and 1.02 for cathodic and anodic peaks, respectively, manifesting a surface-dominated capacitive contribution. The mixed potassium storage mechanism of both diffusive and capacitive reactions significantly enhances the reaction kinetics of the P/O-PCS anode material. **Figure 6.19**a and 6.19b illustrates the representative CV profiles separated by different potassium storage behaviors at a scan rate of 0.1 mV s^{-1}.

Although the two electrodes show typical intercalation-type charge storage at the low scan rate, the portion of the capacitive contribution, especially at the low (0.01-0.5 V) and high (2.5-3 V) voltage range, is largely increased in P/O-PCS. This phenomenon demonstrates the enhanced surface absorption process caused by P/O heteroatom doping. Meanwhile, the percentage of capacitive charges surges to 82.4% for PCS and 85.1% for P/O-PCS (Figure 6.19c and 6.19d) at a scan rate of 5 mV s^{-1}, revealing an overwhelming surface-controlled capacitive reaction at higher rate.

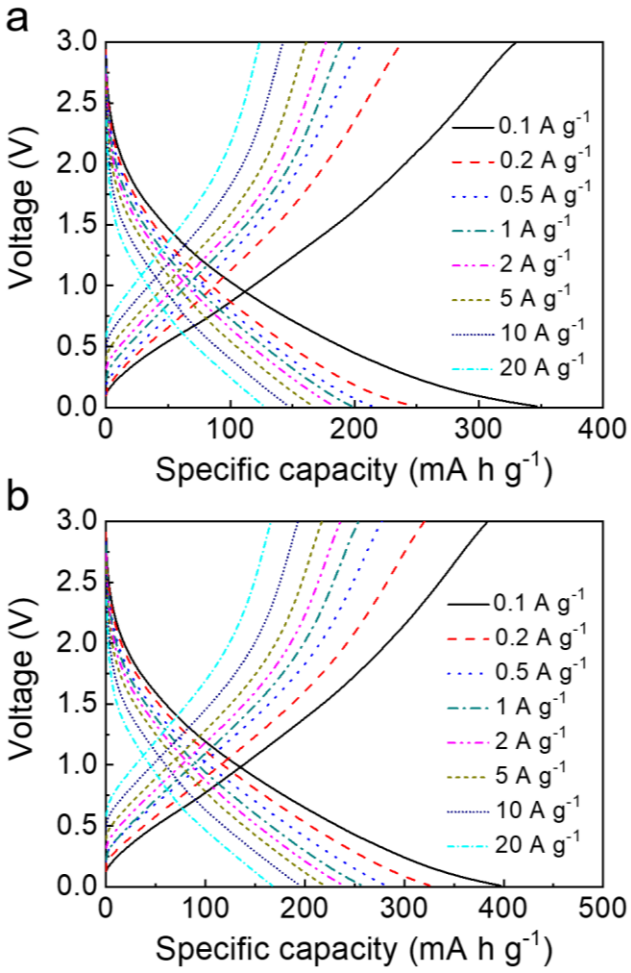

Figure 6.14 GCD profiles of (a) PCS and (b) P/O-PCS electrodes under different current densities between 0.01 and 3 V (*vs.* K^+/K).

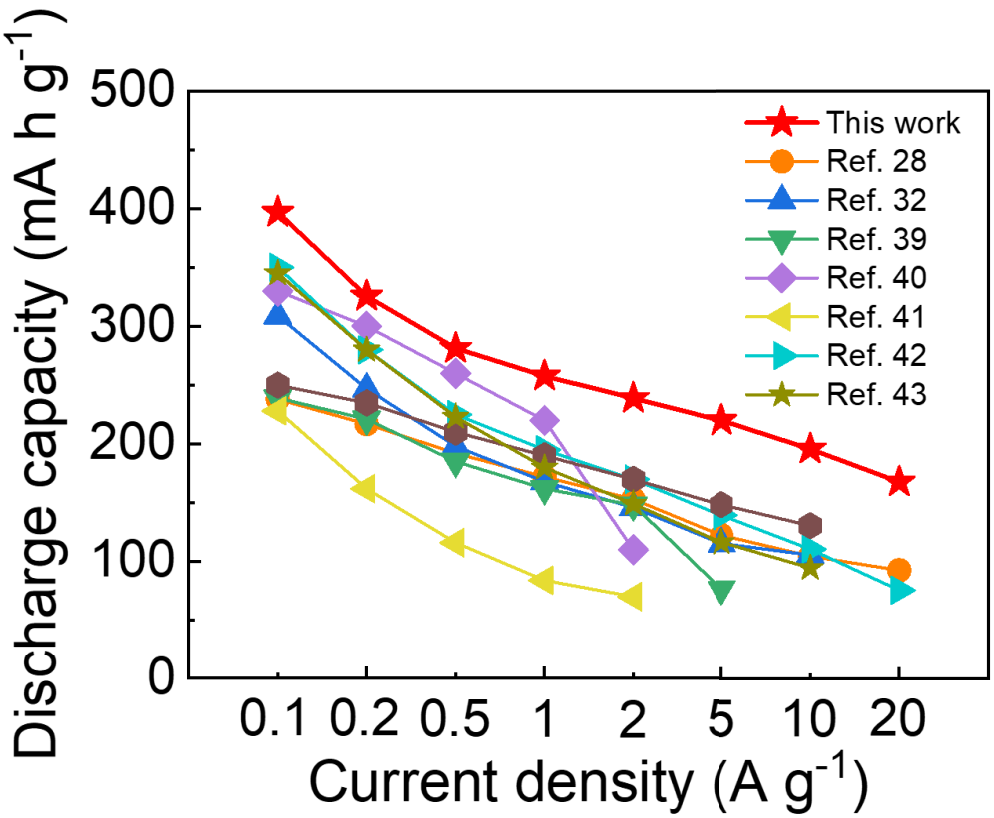

Figure 6.15 Comparison of rate capability of P/O-PCS with the reported anode materials for potassium-based energy storage devices.[397, 428, 433-437]

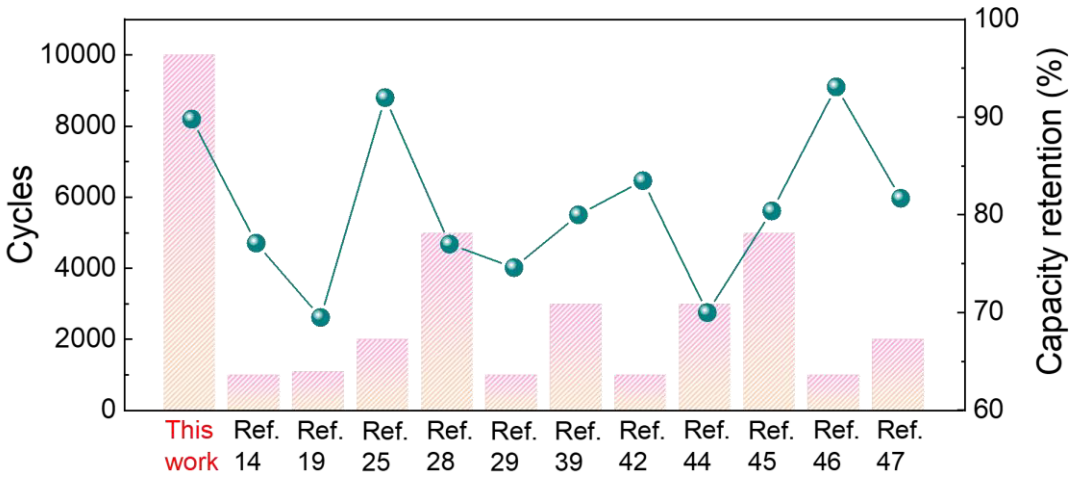

Figure 6.16 Comparisons of cycle number versus corresponding capacity retention of various anode materials for potassium-based energy storage devices.[397, 412, 416, 422, 425, 433, 436, 438-441]

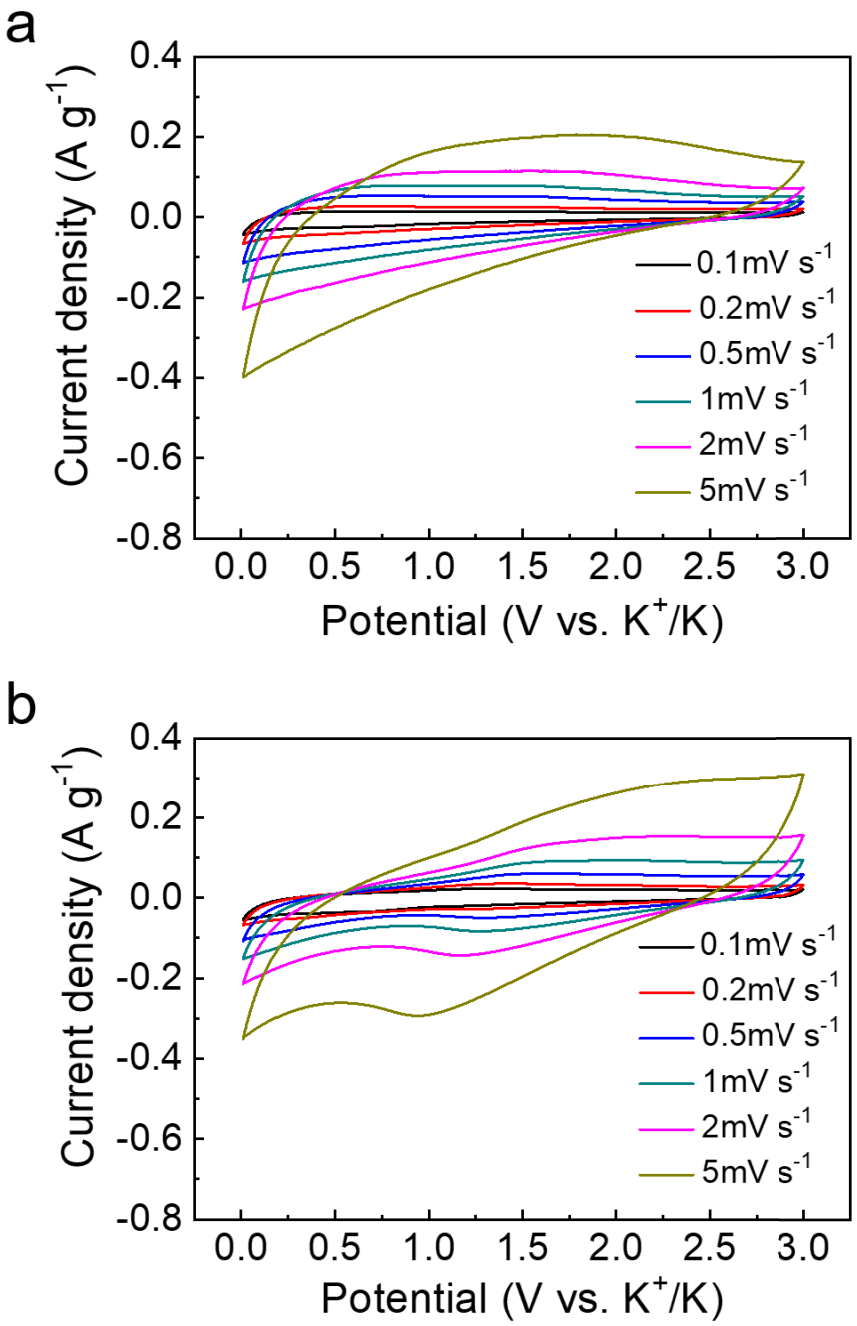

Figure 6.17 CV curves of (a) PCS and (b) P/O-PCS electrodes at different scan rates between 0.01 and 3 V (*vs.* K^+/K).

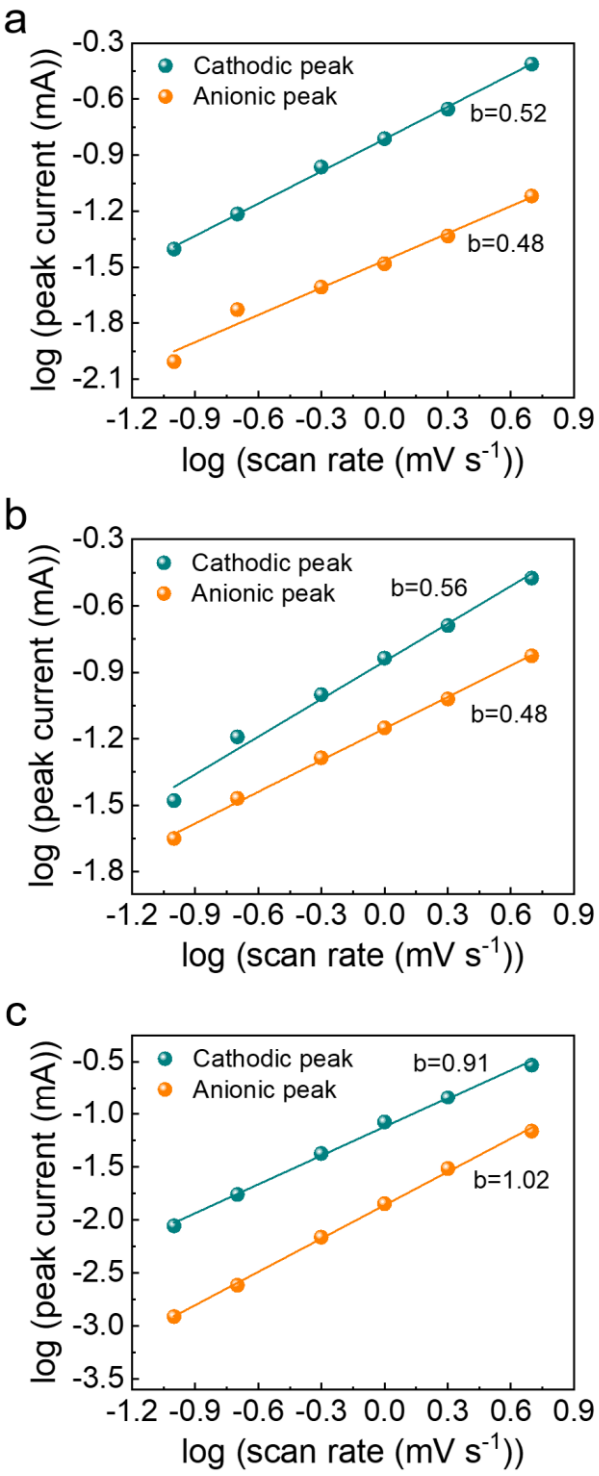

Figure 6.18 b-value analysis using the relationship between the peak currents and scan rates: (a, b) carbon-derived redox peaks in PCS and P/O-PCS, (c) P-based redox peaks in P/O-PCS.

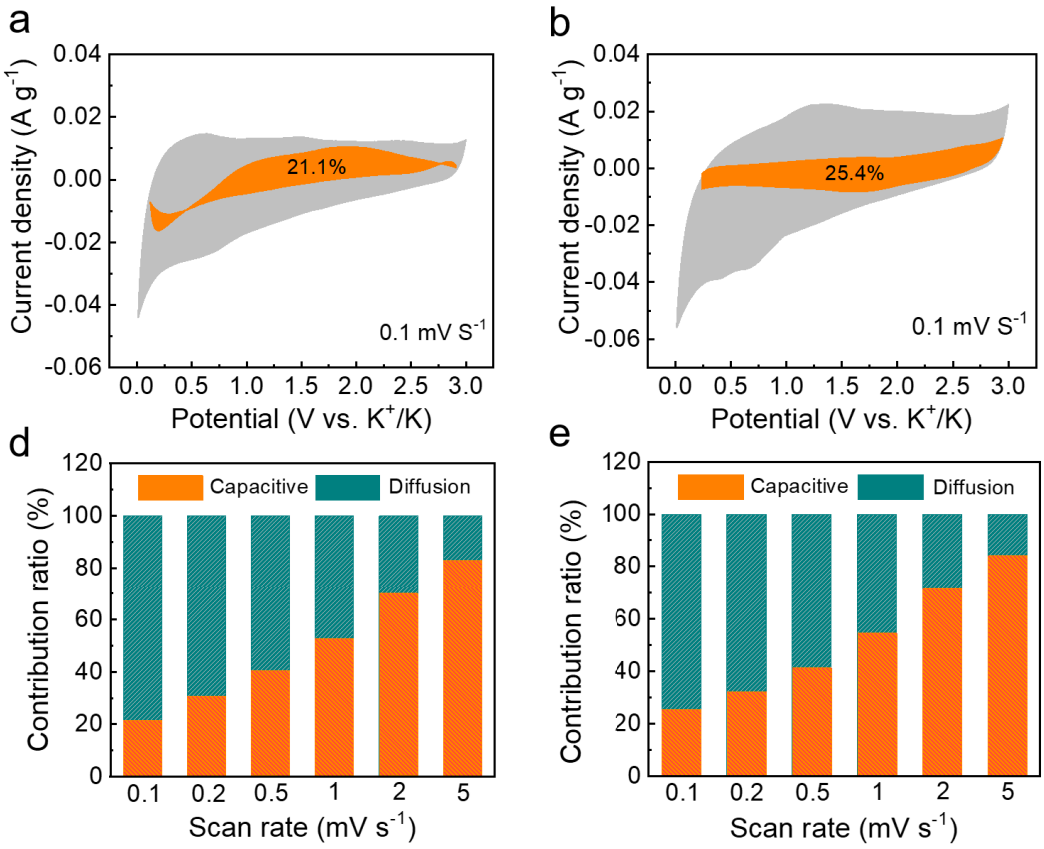

Figure 6.19 CV curves and surface-controlled capacitive contributions of (a) PCS and (b) P/O-PCS electrodes shown in the orange regions (0.1 mV/s). The capacitive contribution histograms of (c) PCS and (d) P/O-PCS electrodes at scan rates from 0.1 to 5 mV/s.

To gain more insight into the effect of heteroatom doping on reaction kinetics, the galvanostatic intermittent titration technique (GITT) was employed for further electrochemical testing. The overpotential and reaction resistances of P/O-PCS for potassiation and depotassiation are lower than those of PCS (**Figure 6.20** and **Figure 6.21**a-d). Moreover, the calculated diffusion coefficients (D_k, Figure 6.21e and 6.21f) of P/O-PCS are between 10^{-10} and 10^{-9} cm^2 s^{-1}, which are much higher than the corresponding values for PCS (10^{-10} and 10^{-11} cm^2

s^{-1}). The lower resistances and increased D_k confirm that the introduction of P/O heteroatoms reduces the diffusion barrier for K^+ and thereby enhances the reaction kinetics. The high D_k are competitive to many other anode materials for potassium-based energy storage devices.[397, 412, 428, 439]

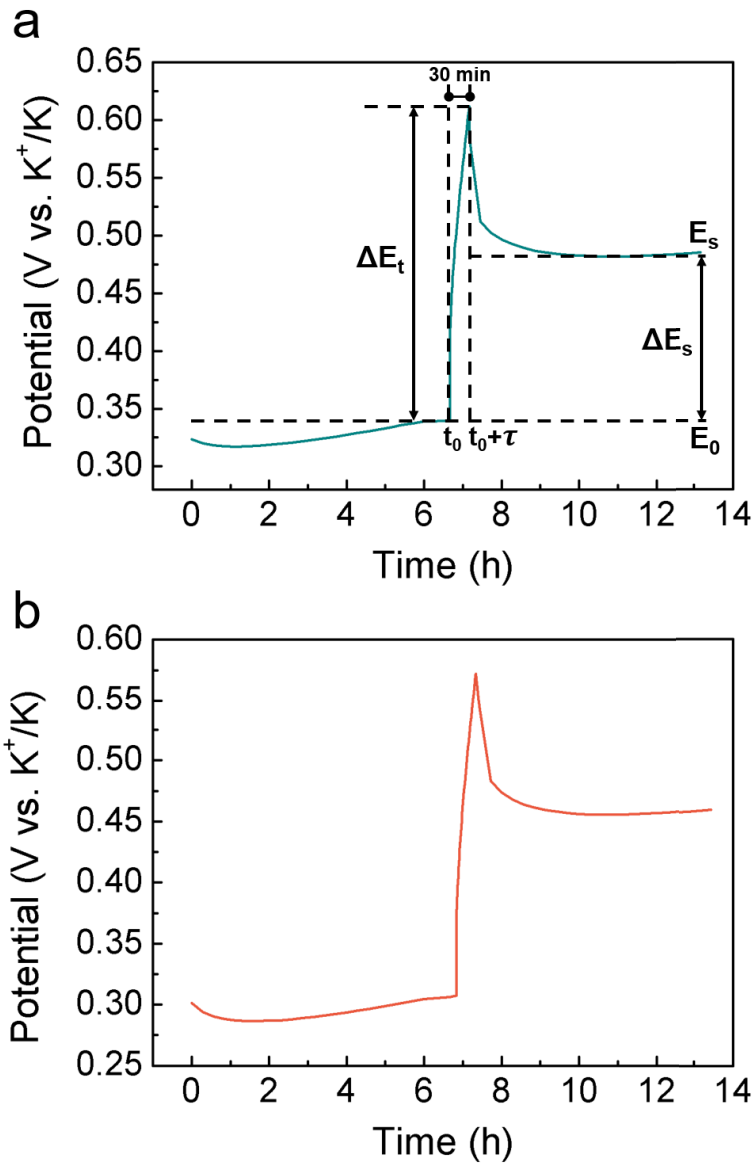

Figure 6.20 Current step diagram of (a) PCS and (b) P/O-PCS at 0.6 V versus K^+/K in the first depotassiation process.

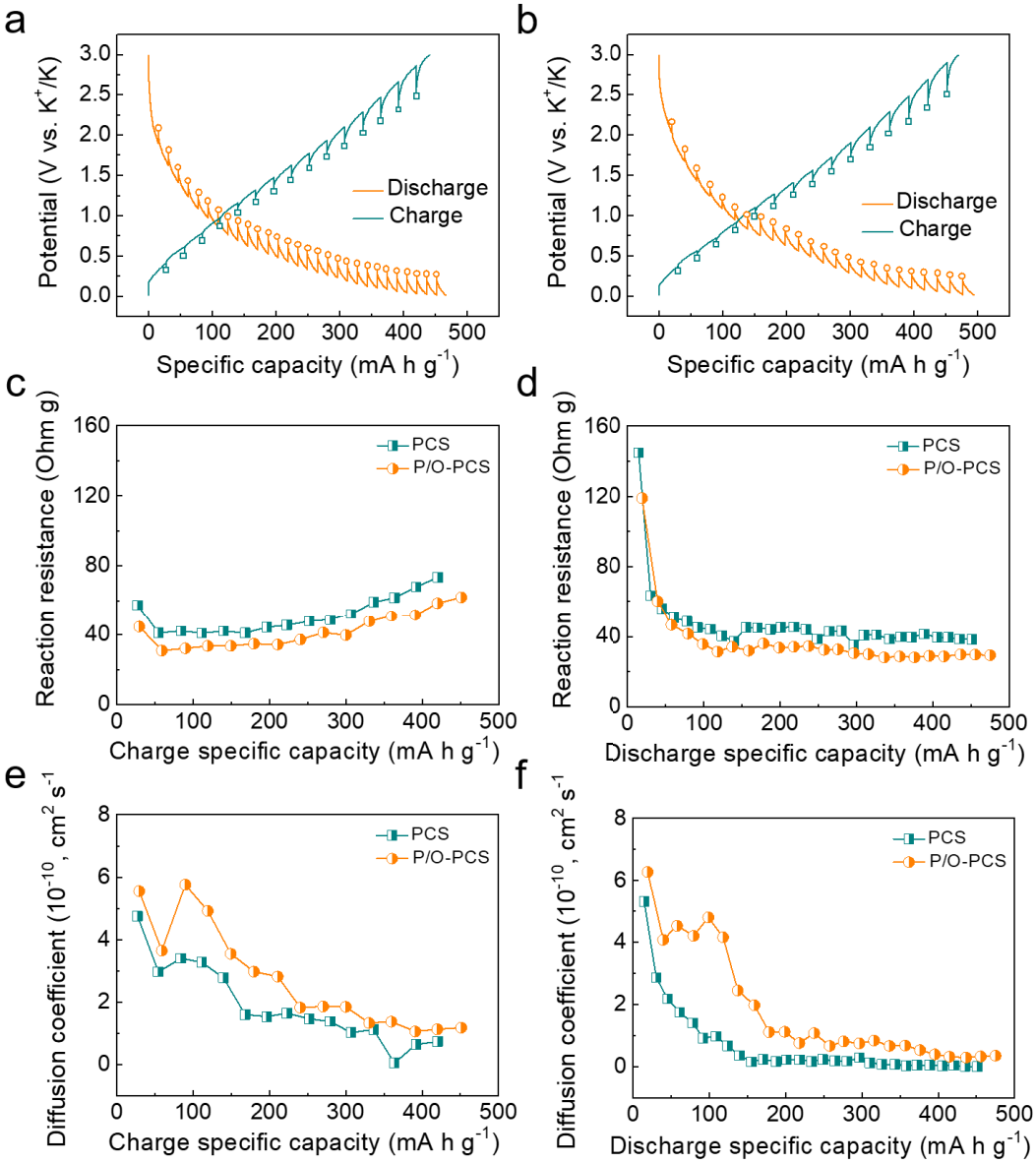

Figure 6.21 Galvanostatic intermittent titration technique results for (a) PCS and (b) P/O@PCS electrodes measured at 20 mA g^{-1}. (c) Charge and (d) discharge reaction resistances of PCS and (b) P/O@PCS. The variation of diffusion coefficients for PCS and P/O@PCS upon (e) potassiation and (f) depotassiation.

The structural evolution of PCS and P/O-PCS during potassiation and depotassiation was carefully studied by *in situ* Raman spectroscopy. From **Figure 6.22**a, in the first discharge

(potassiation) process, the peak intensities of both D band and G band gradually reduce at the end of discharge, indicating the formation of potassiation compounds (KC_x).[429-430] Then, the intensities of D band and G band gradually restore in the following charge process. Compared to PCS, the intensities of the characteristic Raman peaks in P/O-PCS show better recovery ability, suggesting remarkable structural reversibility. Apart from that, the intensity ratio (I_D/I_G) of P/O-PCS remains nearly unchanged after the first full cycle (from 0.79 to 0.8), while this value significantly increases for PCS under the same condition (from 0.82 to 1.02, **Figure 6.23**a and 6.23b). The I_D/I_G values obtained from *in situ* Raman spectroscopy are lower than that from Raman results in Figure 6.1f, which is due to the presence of carbon black in the electrodes. These results indicate that heteroatom doping is essential to promote the stabilization of the hard carbon structure and therefore improves its reversibility for potassium storage. One reason for this is the enhanced surface or near-surface potassium absorption contribution. The previous work mentioned that K^+ intercalation in the hard carbon induces irreversible rearrangement of carbon layers and results in a partial short-range graphitic stacking (Figure 6.22b).[442] However, after modification, some potassium ions are preferentially absorbed on the introduced P/O functional groups, serving as a "buffer zone". Hence, the amount of potassium ions intercalated into carbon layers is reduced, which avoids further structural collapse and mitigates the irreversible transformation to a large extent. Therefore, the reversible potassium absorption mechanism appears to be kinetically faster and less destructive than the traditional intercalation behavior.

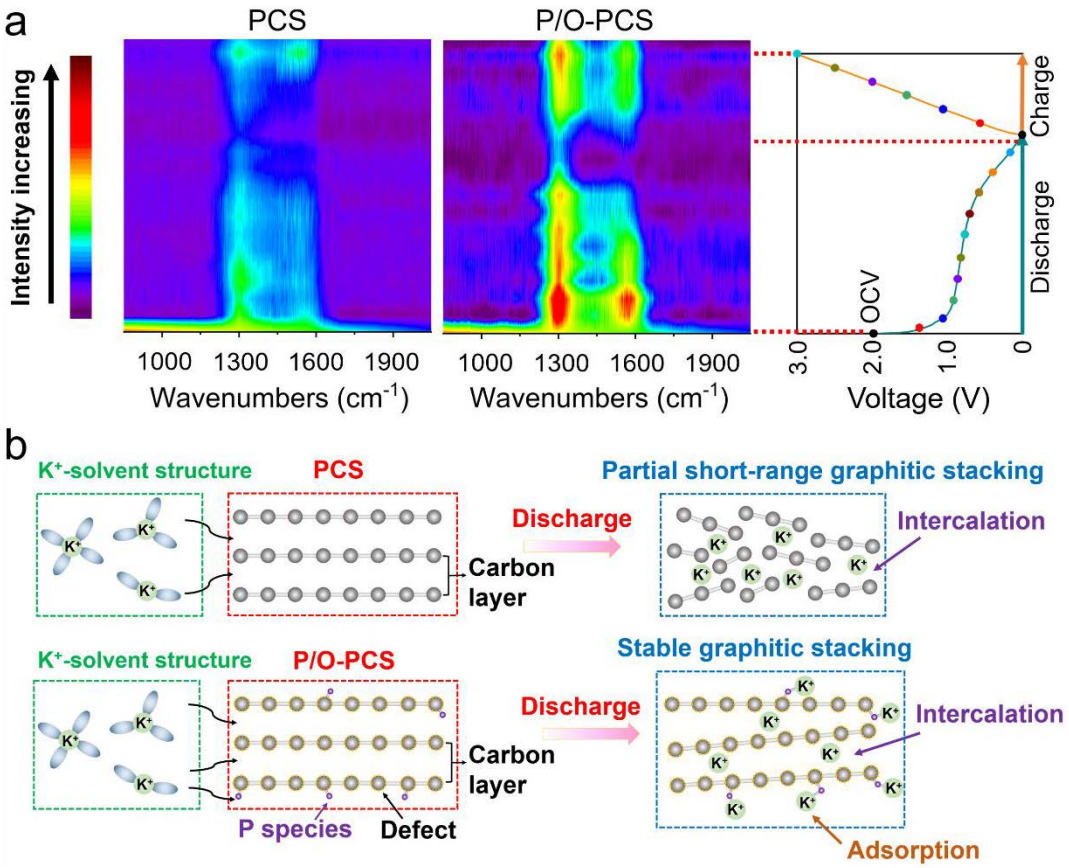

Figure 6.22 *In situ* Raman spectra of (a) PCS and (b) P/O-PCS electrodes in the first electrochemical cycle from bottom to top. (c) Scheme of the P/O dual doping strategy with respect to the potassium storage mechanism.

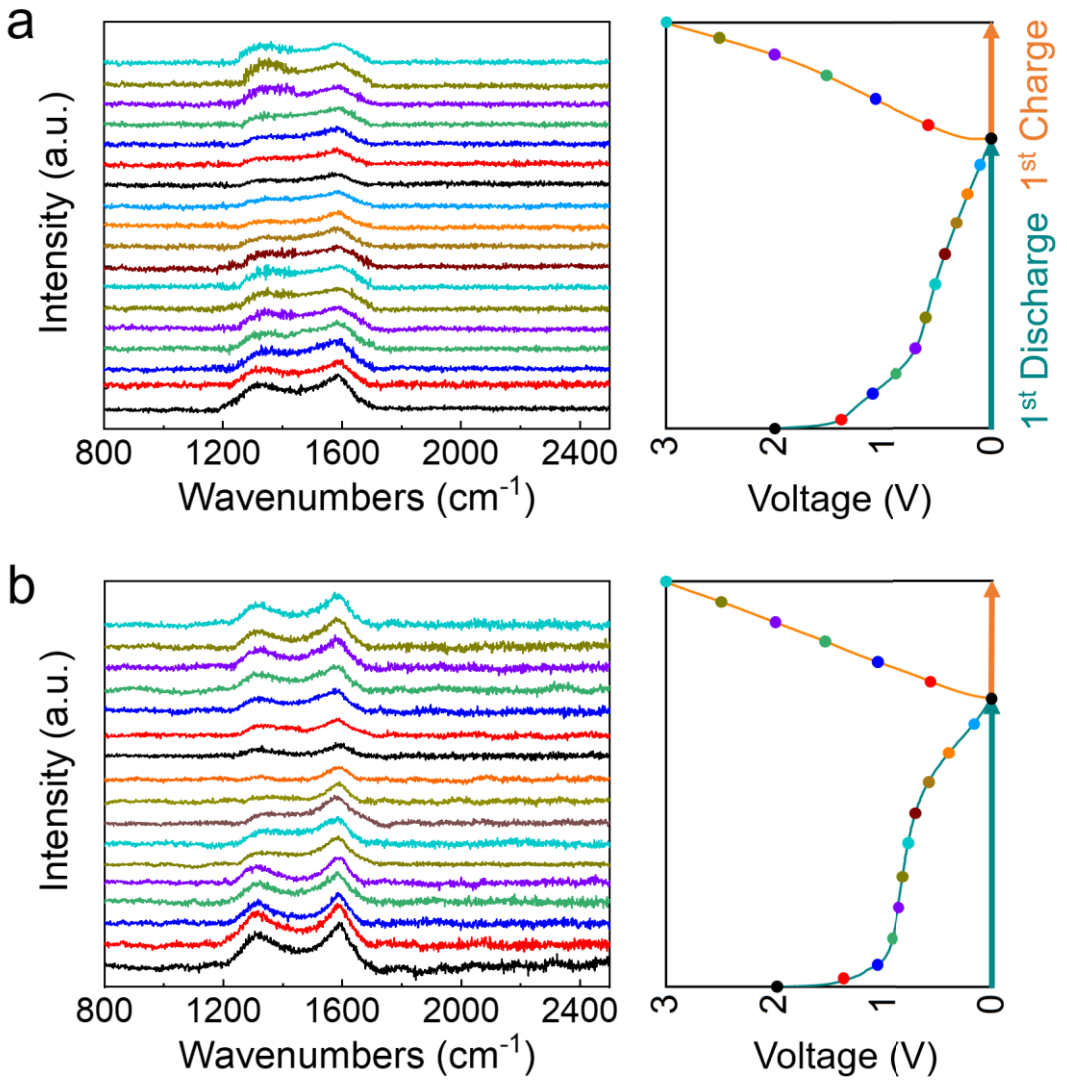

Figure 6.23 *In situ* Raman patterns and relevant GCD profiles of (a) PCS and (b) P/O-PCS electrodes cycled at 0.2 A g^{-1}.

The decomposition of electrolyte components usually forms a SEI on the surface of anode materials in alkali metal-ion batteries.[431] As heteroatom doping may trigger compositional variation of SEI layers upon cycling, SEI compositions on the electrode surface were further investigated through *ex situ* XPS. **Figure 6.24**a and 6.24b presents a summary of the XPS analysis results of PCS and P/O-PCS electrodes before and after the first full cycle. The strong

K signals are mainly derived from the potassiation process, while S signals are the evidence of the decomposition of potassium bis(fluoroslufonyl)imide (KFSI). **Figure 6.25**a and 6.25b further reveals the evolution of S chemical states. Four characteristic peaks appear after cycling, which can be assigned to the formation of inorganic sulfide-based compounds. Moreover, the formation of obvious S-F and K-F bonds is also observed in Figure 6.25c and 6.25d. These species are derived from decomposition of KFSI-based electrolyte on the interface, which is related to the stability of the SEI layers. High-resolution C_{1s} spectra show that less organic species, such as RO-COOK, were generated on the surface of the P/O-PCS electrode compared with the PCS electrode (Figure 6.25e and 6.25f). The presence of heteroatom doping species can trigger the decomposition of KFSI anions rather than carbonate solvents, leading to the formation of more sulfide species during the initial potassiation process. According to previous reports, an inorganic-rich SEI layer is beneficial to the interfacial stability of carbon materials, which contributes to the enhanced cycling stability.[71, 413, 431] In addition, the P-C bond in P/O-PCS becomes stronger and shifts to a lower position at the end of the first cycle, implying that the P-C bond tends to react with K^+ to form a more stable structure (Figure 6.24c). This result is consistent with the *in situ* Raman findings. In order to further understand the merits of inorganic dominated SEI components, the temperature-dependent EIS measurement was performed from 298 to 333 K to evaluate the activation energy (E_{act}) of the two electrodes. As shown in **Figure 6.26**a-c, the P/O-PCS electrode shows a decreased energy barrier (60.2 kJ mol^{-1}) compared to the PCS electrode (83.2 kJ mol^{-1}), indicating the improved K^+ transport kinetics of the as-formed SEI. Therefore, an integrated inorganic rich SEI layer via heteroatom

doping not only favors enhanced mechanical strength to accommodate volume expansion, but also boosts the transport and diffusion of K^+.[419]

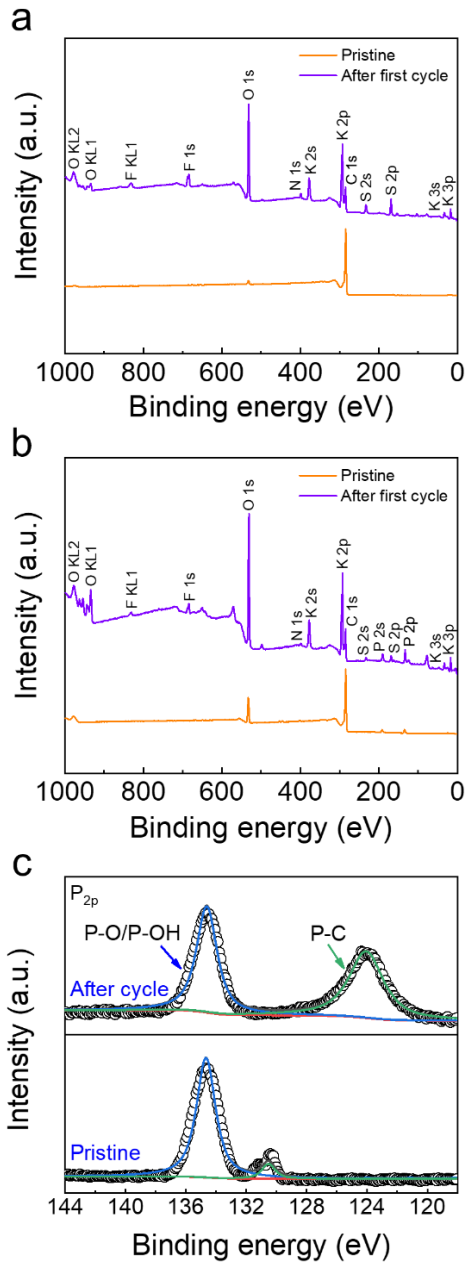

Figure 6.24 *Ex situ* XPS analysis of (a) PCS and (b) P/O-PCS electrodes before and after the first full cycle. (c) High-resolution spectra of P_{2p} characteristic peaks after cycling. The cells were cycled at 0.1 A g^{-1}.

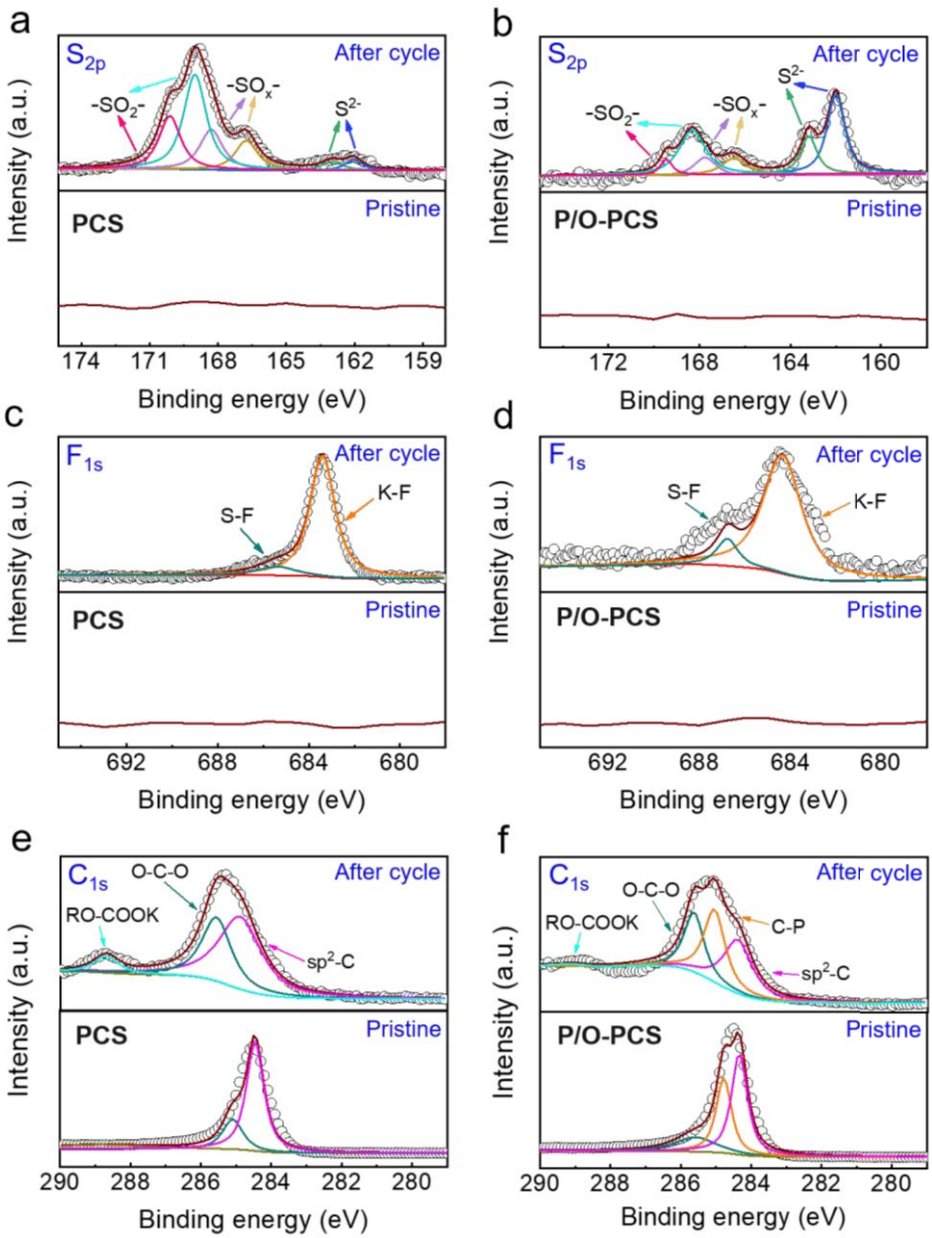

Figure 6.25 High-resolution XPS spectra of (a, b) S_{2p}, (c, d) F_{1s} and (e, f) C_{1s} characteristic peaks for PCS and P/O-PCS before and after cycling. The cells were cycled at 0.1 A g^{-1}.

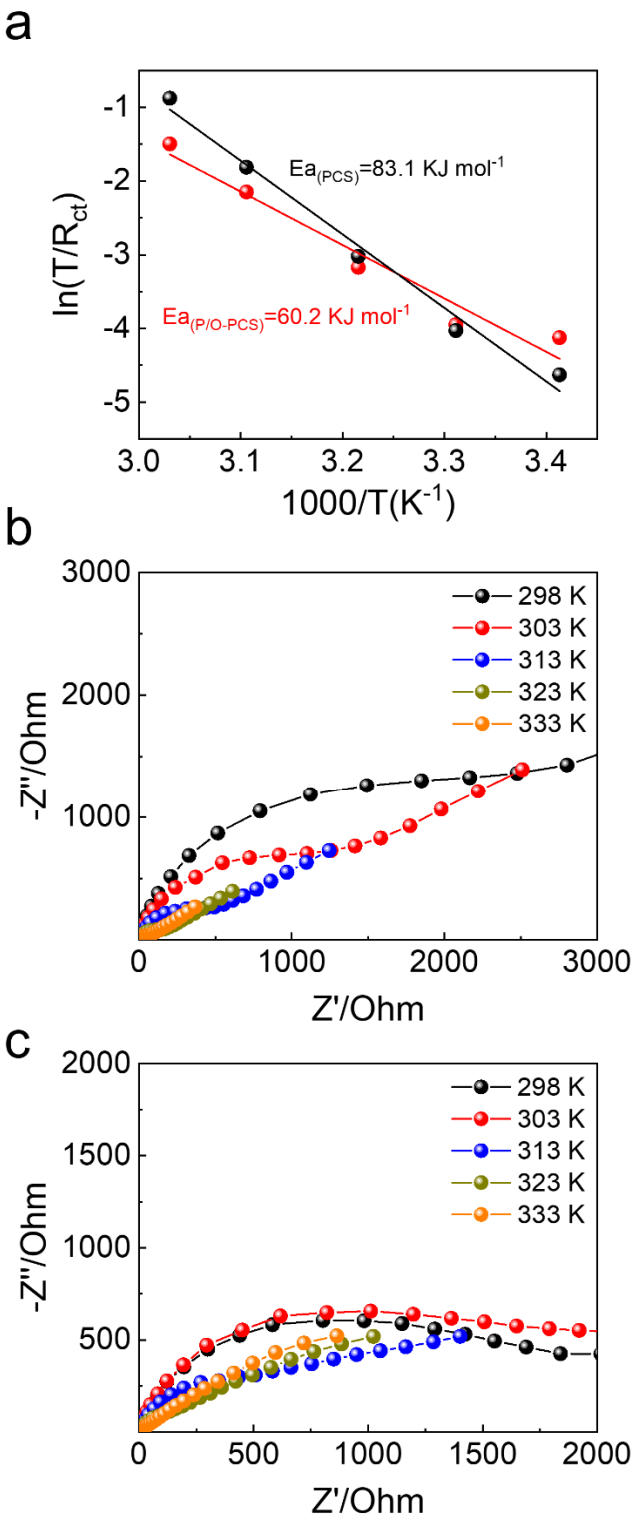

Figure 6.26 (a) The activation energies of PCS and P/O-PCS electrodes obtained from the temperature-dependent EIS test. The temperature-dependent EIS measurements of (b) PCS and (c) P/O-PCS electrodes.

DFT calculations were carried out to understand the impact of P/O heteroatom doping on K^+ storage. On the basis of experimental observations, five structures were constructed in our calculations: (1) pure-graphene (Pure-G), (2) graphene with a single carbon vacancy (SV-G), (3) graphene with a double carbon vacancy (DV-G), (4) graphene with one C atom replaced by a P-OH group (P(OH)-G), (5) graphene with two neighboring C atoms replaced by a P-$(OH)_2$ group (P$(OH)_2$-G). **Figure 6.27**a-j shows the calculated adsorption energy (E_{ads}) of K atoms on different structures. For each structure, two different adsorption sites were considered and discussed. One is the K atom adsorption on defective sites (Figure 6.27b-e), while the other is on non-defective sites (Figure 6.27g-j). It should be noted that there are no defective sites in Pure-G, and the adsorption energies of K atoms on Pure-G, defective sites of SV-G, DV-G, P(OH)-G and P$(OH)_2$-G are -0.12, -1.21, -1.19, -0.32 and -1.94 eV, respectively (Figure 6.27a-e). Considering the defect concentration in experiments is limited, the K atom adsorption on those non-defective sites of the defective structures is also of great importance. Figure 6.27g-j shows K atom adsorption on non-defective sites of SV-G, DV-G, P(OH)-G and P$(OH)_2$-G, with adsorption energies of -0.82, -0.82, -0.14 and -1.15 eV, respectively. The calculation demonstrates that the presence of P/OH doping species and oxygen-rich defects in PCS can significantly increase the binding strength of K atoms, which is similar to those of previous reports on P-doped carbon materials and favors the capacitance performance.[429-430, 443] The stronger binding of K atoms on SV-G, DV-G and P$(OH)_2$-G configurations can be attributed to the enhancement of density of states (DOS) near the Fermi level. As shown in Figure 6.27k,

$P(OH)_2$-G shows the strongest binding to K atoms than that of other four theoretical models. The strong binding energy on the $P(OH)_2$-G surface can also be proven from the charge density difference (CDD) analysis. **Figure 6.28** reveals that charge transfer from a K atom to $P(OH)_2$-G is the easiest among the other above-mentioned structures.

Another factor affecting the electrochemical performance of P/O-PCS is the diffusion rate of K^+ on the electrode surface. Figure 6.27l shows the calculated diffusion barriers for K atoms on Pure-G, SV-G, DV-G, P(OH)-G and $P(OH)_2$-G. Obviously, Pure-G has a low diffusion barrier of 0.08 eV, demonstrating its fast diffusion kinetics. As for SV-G, DV-G, P(OH)-G and $P(OH)_2$-G structures, two diffusion barriers were considered for each configuration: (1) K atoms diffuse from a defective site to a non-defective site; (2) K atoms diffuse between two neighboring non-defective sites. Specifically, the diffusion barrier of K atoms along a defective site to a non-defective site is much higher than that between non-defective sites. For example, based on the $P(OH)_2$-G structure, a K atom that diffuses from a defective site to a non-defective site (1→2, Figure 6.27e and 6.27j) shows a barrier energy of 0.83 eV, while a much lower barrier energy (0.11 eV) is achieved when K atoms diffuse between two non-defective sites (2→3, Figure 6.27e and 6.27j). Similar diffusion behavior has also been observed in other defective structures, and the calculated diffusion barriers between two non-defective sites are ~0.08 eV (Figure 6.27l). This means the diffusion of K atoms on non-defective sites of these structures can be very fast. Considering the ratio of defects on these structures is very low, the diffusion of K atoms on the non-defective sites should dominate the diffusion kinetics. Although the diffusion of K atoms on all the five structures has a quite similar diffusion barrier,

the binding of K atoms on the non-defective sites of $P(OH)_2$-G is much stronger than that on the other structures, indicating the $P(OH)_2$-G structure has high K^+ storage capability as well as the fast diffusion of K atoms. Therefore, P/O heteroatom doping can promote adsorption of K^+ and tune the electronic structure of the carbon configuration to ensure fast and efficient electron transfer.

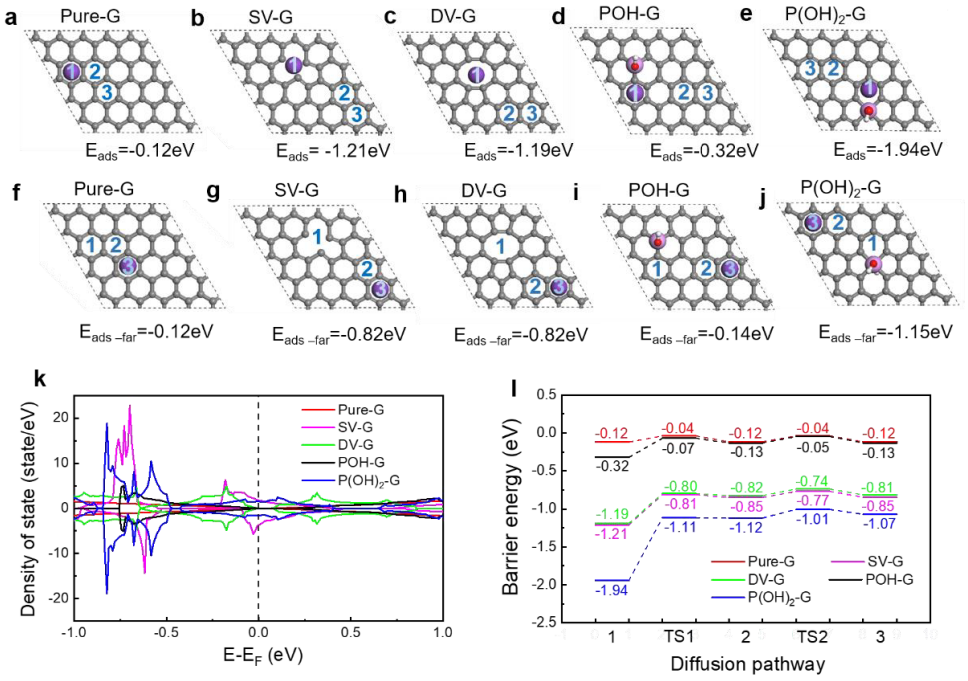

Figure 6.27 Theoretical calculations of K atom adsorption and diffusion in different configurations. The optimized geometry of K atom adsorption on (a) Pure-G, and defective sites of (b) SV-G, (c) DV-G, (d) POH-G, (e) $P(OH)_2$-G as well as the corresponding adsorption energy (E_{ads}). The optimized geometry of K atom adsorption on (f) Pure-G, and non-defective sites of (g) SV-G, (h) DV-G, (i) POH-G, (j) $P(OH)_2$-G as well as the corresponding adsorption energy ($E_{ads\text{-}far}$). The light blue numbers (1→3) represent migration path of K atom in different configurations. (k) The density of states (DOS) of different configurations. (l) the adsorption energies and diffusion barriers of K atom in different configurations.

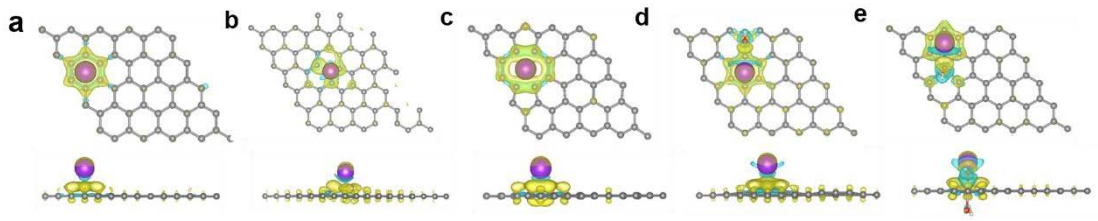

Figure 6.28 (a-e) The charge density difference (CDD) analysis of different configurations.

Considering the exceptionally high reaction kinetics and potassium storage capability of the as-synthesized P/O-PCS anode material, a green and high-power potassium-ion hybrid capacitor (PIHC) device was fabricated, using P/O-PCS as the anode material and the commercial activated carbon (AC) as the cathode material (**Figure 6.29**a). Before assembling the PIHC, the electrochemical properties of AC, including charge and discharge curves, cycling and rate performances, were systematically investigated (**Figure 6.30**a-c), which shows excellent electrochemical performances as a cathode for PIHCs. The optimal mass ration of 1:2 (anode to cathode) was selected to achieve maximum output power (Figure 6.30d). CV profiles shown in **Figure 6.31** demonstrate that the assembled PIHC is electrochemically stable at the given voltage range (0.01 V to 4 V). Figure 6.29b exhibits typical CV curves of PIHC at different scan rates in the potential range from 0.01 V to 4 V. All CV profiles present quasi-rectangular shapes, indicating the combination of both battery-type and capacitor-type potassium storage mechanisms in PIHC. Furthermore, charge and discharge curves are also present in **Figure 6.32**. The P/O-PCS//AC device exhibits a high energy density of 158 Wh kg^{-1} at a power density of 223 W kg^{-1}, and still maintains an energy density of 11 Wh kg^{-1} even at an ultrahigh power density of 1.38 kW kg^{-1} (Figure 6.29c). Such excellent rate capability and

energy output are superior to many reported state-of-the-art hybrid capacitors, as summarized in Figure 6.29d.[375, 400, 404-405, 408, 433, 439, 444-446] In addition, the constructed device also shows an exceedingly high-capacity retention of 94.5% after 30000 cycles at 5 A g^{-1} with a Coulombic efficiency above 99% (Figure 6.29e). Meanwhile, light-emitting diode (LED) arrays can be successfully illuminated by two lab-assembled PIHCs connected in series (see the inset in Figure 6.29e).

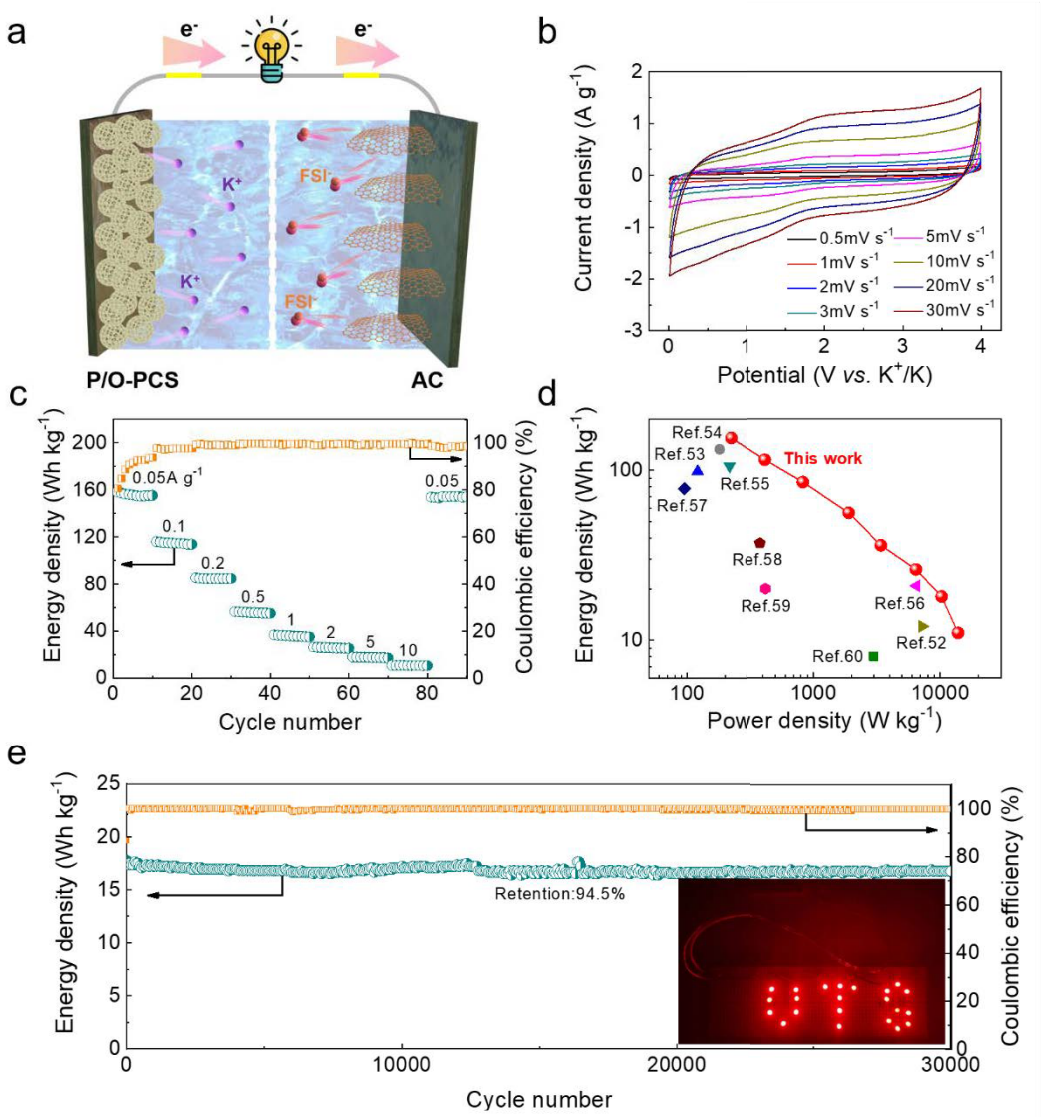

Figure 6.29 (a) Schematic illustration of the as-prepared P/O-PCS//AC device. Electrochemical performances of the P/O-PCS//AC device. (b) CV curves of the P/O-PCS//AC at different scan rates. (c) Rate performance of the as-prepared P/O-PCS//AC (0.05 to 10 A g^{-1}). (d) Ragone plots of different hybrid capacitors according to previous works.[375, 400, 404-405, 408, 433, 439, 444-446] (e) Long-term cycle performance of the P/O-PCS//AC device at 5 A g^{-1} up to 30000 cycles. The inset displays the illuminated LED arrays powered by our fabricated P/O-PCS//AC device.

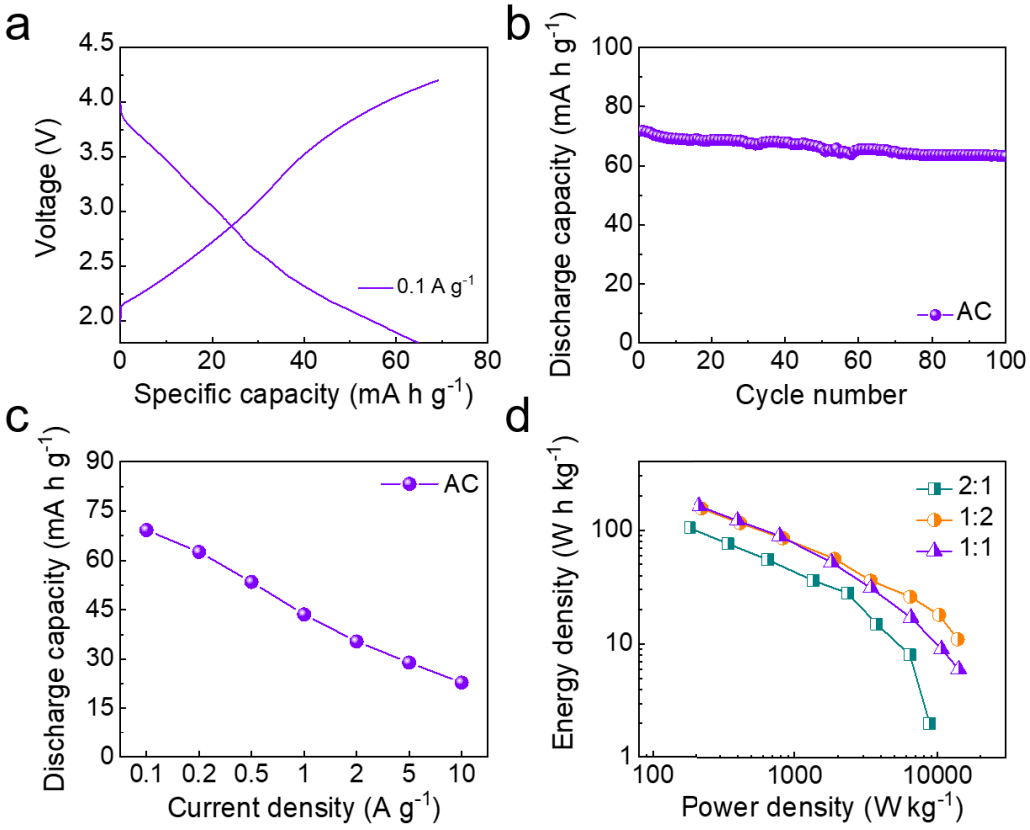

Figure 6.30 Electrochemical performances of the AC cathode in K-half cells. (a) Galvanostatic charge and discharge voltage profiles of the AC cathode within the potential range from 1.8 to 4.2 V (*vs.* K^+/K) at a current density of 0.1 A g^{-1}. (b) Cycling performance of the AC cathode at a current density of 0.1 A g^{-1} for 100 cycles. (c) Rate performance of the AC cathode at various current densities. (d) Ragone plots of P/O-PCS//AC with different mass ratios of anode to cathode.

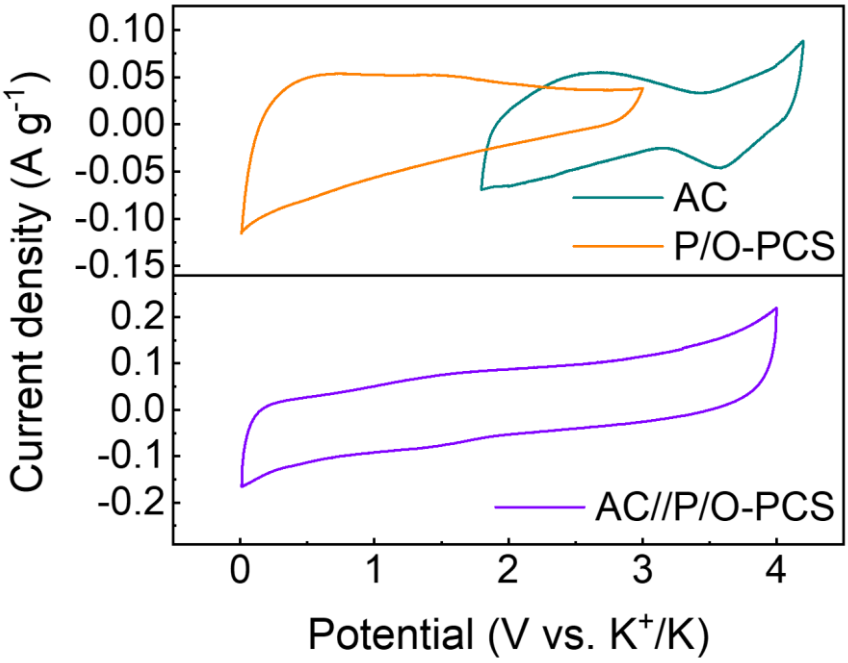

Figure 6.31 CV curves of the P/O-PCS anode and the AC cathode in half cells (top) and PIHCs (bottom) at 0.5 mV s^{-1}.

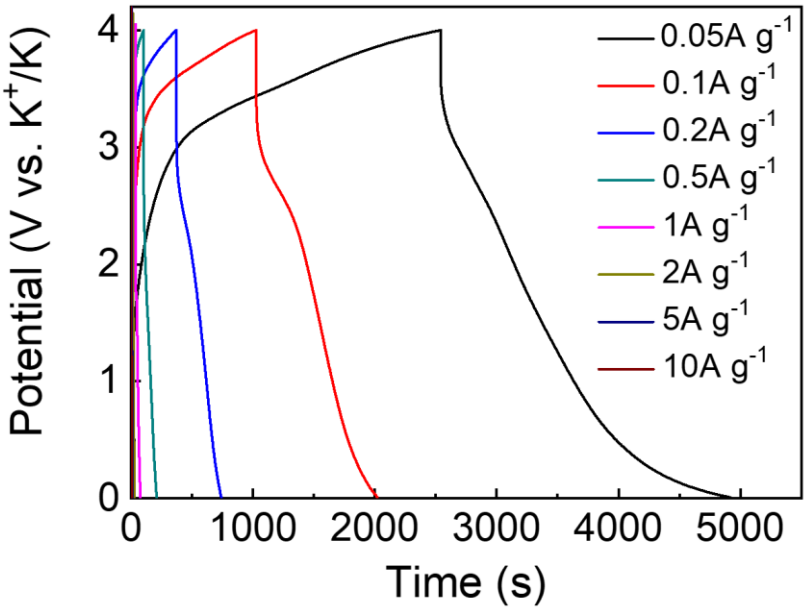

Figure 6.32 GCD curves of a P/O-PCS//AC PIHC at different current densities.

6.4 Summary

In summary, phosphorus/oxygen dual-doped porous carbon spheres show excellent potassium storage capability when used as anode materials for PIHCs. Benefiting from the 3D interconnected porous structure and P/O heteroatom doping, the P/O-PCS anode displays a high specific capacity of 401 mAh g^{-1} at 0.1 A g^{-1}, exceptional rate capability and ultralong cycling lifespan (89.8% after 10000 cycles). In particular, an enhanced surface-dominated potassium adsorption process is achieved through heteroatom doping. Moreover, *in situ* Raman investigation and DFT calculations reveal that the formation of P-C and P-O/P-OH bonds improves the structural stability and reaction kinetics of the hard carbon anode during potassiation and depotassiation. Meanwhile, P/O-PCS with enlarged interlayer distances provides abundant active sites and oxygen-rich defects for redox reactions. When couple the battery-type P/O-PCS anode with a capacitor-type AC cathode, the as-developed potassium-ion hybrid capacitor device demonstrates impressive electrochemical performances, which inspires the future development of novel potassium-based energy storage devices.

CHAPTER 7 CONCLUSIONS

7.1 General conclusion

This doctoral thesis reported on the synthesis of advanced electrode materials for lithium-ion and potassium-ion batteries. For lithium-ion batteries, lithium-rich manganese-based layered oxides hold great promise for next-generation cathode materials owing to their high specific energy density, but still face severe issues such as capacity loss and voltage decay. Surface coating has been confirmed as a reliable method to handle these problems to a large extent and, therefore, promotes industrial applications of lithium-rich cathode materials. For potassium-ion batteries, the surface coating strategy can be well applied to potassium cathode materials and overcome drawbacks including serious side reactions and sluggish kinetics behavior. Meanwhile, the presence of a uniform and robust coating layer can prevent anode materials from being attacked by parasitic products and thereby enhancing the interfacial stability. Apart from surface modification, heteroatom doping also plays a significant role in improving rate capability and cycling stability of anode materials such as hard carbons. All of these findings provide valuable and meaningful guidelines for designing next-generation electrode materials for state of art renewable energy storage devices.

7.2 Aegis of lithium-rich cathode materials via heterostructured $LiAlF_4$ coating for high-performance lithium-ion batteries

In this work, an effective $LiAlF_4$ coating strategy was proposed to overcome obstacles such as structural instability and voltage decay. The as-developed lithium-rich cathode material shows outstanding performance including a high reversible capacity (246 mAh g^{-1} at 0.1C), excellent rate capability (133 mAh g^{-1} at 5C), and ultralong cycling stability (3000 cycles). In comparison to those of pristine and AlF_3 coated lithium-rich cathode materials, the improved performances can be ascribed to the introduction of the lithium-ion-conductive nanolayer and the presence of nonbonding O^{n-} species in the active material lattice, which enable rapid and effective Li^+ transport and diffusion. This work provides a new strategy to develop high-performance lithium-rich cathode materials for high-energy-density lithium-ion batteries.

7.3 Construction of hierarchical $K_{1.39}Mn_3O_6$ spheres via AlF_3 coating for high-performance potassium-ion batteries

In this work, the preparation process of hierarchical $K_{1.39}Mn_3O_6$ microspheres cathode materials is reported for potassium-ion batteries. In addition, a facile AlF_3 surface coating strategy was employed to further improve the electrochemical performance of $K_{1.39}Mn_3O_6$ microspheres. The as-synthesized AlF_3 coated $K1_{.39}Mn_3O_6$ cathode materials deliver a reversible discharge capacity (~110 mAh g^{-1} at 10 mA g^{-1}), excellent rate capability and long-term cycling stability. Galvanostatic intermittent titration technique results demonstrate that the increased diffusion kinetics of potassium-ion insertion and extraction during discharge and

charge processes benefit from both the hierarchical sphere structure and surface modification. Furthermore, *ex situ* X-ray diffraction measurements reveal that the irreversible structure evolution can be significantly mitigated via AlF_3 surface coating. This work sheds light on rational design of high-performance cathode materials for potassium-ion batteries.

7.4 $K_2Ti_2O_5$@C microspheres with enhanced K^+ intercalation pseudocapacitance ensuring fast potassium storage and long-term cycling stability

This work reported on carbon-coated $K_2Ti_2O_5$ microspheres (S-KTO@C) synthesized via an economic spray drying method. Taking advantage of both the porous microstructure and carbon coating, S-KTO@C shows superior rate capability and cycling stability as an anode material for PIBs. Furthermore, the intimate integration of carbon coating through chemical vapor deposition technology significantly enhances the K^+ intercalation pseudocapacitive behavior. As a proof of concept, a potassium-ion hybrid capacitor is constructed with the S-KTO@C (battery-type anode material) and the activated carbon (capacitor-type cathode material). The assembled device shows a high energy density, high power density, and excellent capacity retention. This work can pave the way for the development of high-performance potassium-based energy storage devices.

7.5 Phosphorus and oxygen dual-doped porous carbon spheres with enhanced reaction kinetics as anode materials for high-performance potassium-ion hybrid capacitors

This work reported the synthesis of phosphorus/oxygen dual-doped porous carbon spheres, which possess expanded interlayer distances, abundant redox active sites and oxygen-rich defects. The as-developed battery-type anode material shows high discharge capacity (401 mAh g^{-1} at 0.1 A g^{-1}), outstanding rate capability, and ultralong cycling stability (89.8% after 10000 cycles). *In situ* Raman spectroscopy and density functional theory calculations further confirm that the formation of P-C and P-O/P-OH bonds not only improves structural stability, but also contributes to a rapid surface-controlled potassium adsorption process. As a proof of concept, a potassium-ion hybrid capacitor was assembled by a dual-doped porous carbon sphere anode and an activated carbon cathode. It shows superior electrochemical performances, which opens a new avenue for innovative potassium-based energy storage technology.

7.6 Outlooks and perspectives

The pursuit for high-performance electrode materials has long been one of the hottest issues in the field of rechargeable batteries. Nevertheless, the journey of discovery is always a game of compromise, which cannot balance all the concerns involving in electrode material design. Therefore, how to fulfill the demand of practical applications without sacrificing too many its inherent advantages should be given the priority.

The request for high-energy-density lithium-ion batteries stimulates people's interest on layered lithium-rich cathode materials. Despite their appealing advantages such as high specific capacity, the obvious drawbacks of lithium-rich cathode materials still cannot be ignored. Hence, future research should focus on the development of innovative improvement strategies such as surface coating and elemental doping, which suppresses irreversible anionic redox reactions and unwanted voltage decay during cycling. Although these strategies may be suitable for large-scale productions, their negative aspects are equally notable. For example, both of these two techniques only decelerate performance degradation. As the cycling goes on, the irreversible structural transformation and microstructural defects still exist and eventually worsen the electrochemical performance of lithium-rich cathode materials. Therefore, the goal will not be achieved through improving lithium-rich cathode materials alone. Other factors, such as the electrode manufacturing process, suitable electrolyte and the battery assembly process, also ultimately determine electrochemical performances of lithium-ion batteries. When it comes to practical applications, critical issues to obtain high-density lithium-rich oxide electrodes should be addressed. These include: (1) an increase of reactive surface areas and corresponding side reactions due to the particle-fracture under high pressure calendaring. (2) The formation of a thick CEI layer onto the cathode resulting rapid energy degradation upon cycling. These issues are easily to be ignored in lab research conducted commonly using low-density lithium-rich oxide electrodes and set higher demands for the electrodes manufacturing process.

The rise and development of potassium-ion batteries not only brings about a plethora of opportunities but also faces unprecedented challenges for design electrode materials. Unlike the traditional lithium-ion battery system, the fundamental reaction mechanism of potassium-based energy storage devices is still unclear and the research on potassium-ion batteries is in its infancy. As for cathode materials, most of layered structure cathode materials experience continuous phase transitions that lead to inferior structural stability and rate performance. Although surface coating can significantly improve the electrochemical properties of manganese-based layered cathode materials, its functional mechanism cannot be well interpreted by previous experience derived from the lithium-ion battery system. To this end, the future work is expected to disclose the relationship between the electrochemical behavior and reaction mechanism upon cycling and focus on the following aspects: (1) Rational design of cathode materials, including composition optimization, microstructure design, surface functionalization and nanoengineering. (2) Employing advanced characterization techniques such as *in situ* synchrotron XRD, electron paramagnetic resonance (EPR) and the resonant inelastic X-ray scattering (RIXS). (3) Taking into account good compatibility between cathode materials and electrolytes.

For the future development of anode materials for potassium-ion batteries, there is plenty of room for discussion and investigation in terms of their crystal structure and reaction mechanisms. Most of them have achieved exceptional electrochemical performances such as high discharge capacity and ultralong cycling stability. Nevertheless, it is important to note that the low ICE (less than 50%) and volumetric densities are rarely discussed, which negatively

affects the overall energy density of the battery. Improvement strategies such as surface modification and heteroatom doping have positive effects on anode materials and seem to be helpful to handle these issues. However, similar to the situation described in cathode materials, the lack of a fundamental understanding of reaction mechanism hinders their further development. Given the complicated and uncertain reaction process of electrode materials during electrochemical cycling, the recent development of cutting-edge characterization technologies such as operando synchrotron XRD, *in situ* TEM, and *in situ* Raman would be a great help for understanding the de/intercalation behavior of K^+ along with the corresponding structural evolution during successive cycling periods. It suggests that an anode material with more capacitive contribution can offer a better rate capacity and good cycling performance. Hence, the preparation of anode materials including abundant surface-active sites and shortened diffusion path is of significant importance. More attention should be paid to the commercialized practical application of anode materials for PIBs in the future.

Appendix A: Abbreviations/Symbols

Abbreviations/Symbols	Full name
a.u.	Arbitrary unit
Ar	Argon
M	Molar concentration
μm	Micrometer
nm	Nanometer
I	Arbitrary unit
g	Gram
h	Hour
V	Voltage
A	Ampere
°C	Degree Celsius
Ω	Ohm
Li	Lithium
K	Potassium

Appendix B: Scholarship & Awards

-2017 UTS International Research Scholarship (IRS).

-2017 Rail Manufacturing Cooperative Research Centre (RMCRC) Project Scholarship.

-2016 National Scholarship for Postgraduate students, Ministry of Education (**top 100**).

-2016 Innovation personal Scholarship, Huang Shanglian Academy Youth Innovation Award, Chongqing University (**Only 12 individuals each year**).

-2015 Haotian Scholarship for Postgraduate students, Chongqing University (**top 1%**).

-2015-2016 University Scholarship in Chongqing University (top 10%).

-2014 Outstanding Graduate, Xihua University (20%).

-2012-2014 University Scholarship in Xihua University.

Appendix C: Conferences

1. Preliminary program of 2019 International Symposium on Frontier Materials, Australia, Sydney, 17-18 November 2019.

2. 2019 International Conference on Electrochemical Energy, Australia, Sydney, 4-8 August 2019.

3. International Conference for Energy Storage and Conversion, Australia, Sydney, 16-18 July 2018.

REFERENCES

1. Obama, B., The irreversible momentum of clean energy. *Science* **2017,** *355* (6321), 126-129.

2. York, R., Do alternative energy sources displace fossil fuels? *Nature Clim. Change* **2012,** *2* (6), 441.

3. Tarascon, J.-M.; Armand, M., Issues and challenges facing rechargeable lithium batteries. In *Materials For Sustainable Energy: A Collection of Peer-Reviewed Research and Review Articles from Nature Publishing Group*, World Scientific: **2011**; pp 171-179.

4. Goodenough, J. B.; Park, K.-S., The Li-ion Rechargeable Battery: A Perspective. *J. Am. Chem. Soc.* **2013,** *135* (4), 1167-1176.

5. Bruce, P. G.; Scrosati, B.; Tarascon, J. M., Nanomaterials for Rechargeable Lithium Batteries. *Angew. Chem. Int. Ed.* **2008,** *47* (16), 2930-2946.

6. Kang, K.; Meng, Y. S.; Bréger, J.; Grey, C. P.; Ceder, G., Electrodes with High Power and High Capacity for Rechargeable Lithium Batteries. *Science* **2006,** *311* (5763), 977-980.

7. Whittingham, M. S., Lithium Batteries and Cathode Materials. *Chem. Rev.* **2004,** *104* (10), 4271-4302.

8. Sun, Y. K.; Myung, S. T.; Park, B. C.; Prakash, J.; Belharouak, I.; Amine, K., High-energy cathode material for long-life and safe lithium batteries. *Nat. Mater.* **2009,** *8* (4), 320-324.

9. Xu, B.; Qian, D.; Wang, Z.; Meng, Y. S., Recent progress in cathode materials research for advanced lithium ion batteries. *Mater. Sci. Eng. R Rep.* **2012,** *73* (5-6), 51-65.

10. Mizushima, K.; Jones, P.; Wiseman, P.; Goodenough, J. B., $LixCoO_2$ ($0< x<-1$): A new cathode material for batteries of high energy density. *Mater. Res. Bull.* **1980,** *15* (6), 783-789.

11. Armstrong, A. R.; Bruce, P. G., Synthesis of layered $LiMnO_2$ as an electrode for rechargeable lithium batteries. *Nature* **1996,** *381* (6582), 499-500.

12. Padhi, A. K.; Nanjundaswamy, K. S.; Goodenough, J. B., Phospho-olivines as Positive-Electrode Materials for Rechargeable Lithium Batteries. *J. Electrochem. Soc.* **1997,** *144* (4), 1188-1194.

13. Lu, Z.; MacNeil, D.; Dahn, J., Layered $Li[Ni_xCo_{1-2x}Mn_x]O_2$ Cathode Materials for Lithium-Ion Batteries. *Electrochem. Solid-State Lett.* **2001,** *4* (12), A200-A203.

14. Bianchini, M.; Roca-Ayats, M.; Hartmann, P.; Brezesinski, T.; Janek, J., There and Back Again—The Journey of $LiNiO_2$ as a Cathode Active Material. *Angew. Chem. Int. Ed.* **2019,** *58* (31), 10434-10458.

15. Liu, J.; Bao, Z.; Cui, Y.; Dufek, E. J.; Goodenough, J. B.; Khalifah, P.; Li, Q.; Liaw, B. Y.; Liu, P.; Manthiram, A.; Meng, Y. S.; Subramanian, V. R.; Toney, M. F.; Viswanathan, V. V.; Whittingham, M. S.; Xiao, J.; Xu, W.; Yang, J.; Yang, X.-Q.; Zhang, J.-G., Pathways for practical high-energy long-cycling lithium metal batteries. *Nat. Energy* **2019,** *4* (3), 180-186.

16. Manthiram, A., A reflection on lithium-ion battery cathode chemistry. *Nat. Commun.* **2020,** *11* (1), 1550.

17. Yu, H.; Zhou, H., High-Energy Cathode Materials (Li_2MnO_3-$LiMO_2$) for Lithium-Ion Batteries. *J. Phys. Chem. Lett.* **2013,** *4* (8), 1268-1280.

18. Yabuuchi, N.; Yoshii, K.; Myung, S.-T.; Nakai, I.; Komaba, S., Detailed Studies of a High-Capacity Electrode Material for Rechargeable Batteries, Li_2MnO_3−$LiCo_{1/3}Ni_{1/3}Mn_{1/3}O_2$. *J. Am. Chem. Soc.* **2011,** *133* (12), 4404-4419.

19. Deng, H.; Belharouak, I.; Sun, Y.-K.; Amine, K., $Li_xNi_{0.25}Mn_{0.75}O_y$ ($0.5 \leq x \leq 2$, $2 \leq y \leq 2.75$) compounds for high-energy lithium-ion batteries. *J. Mater. Chem.* **2009,** *19* (26), 4510-4516.

20. Zheng, J.; Myeong, S.; Cho, W.; Yan, P.; Xiao, J.; Wang, C.; Cho, J.; Zhang, J. G., Li-and Mn-Rich Cathode Materials: Challenges to Commercialization. *Adv. Energy Mater.* **2017,** *7* (6), 1601284.

21. Assat, G.; Tarascon, J.-M., Fundamental understanding and practical challenges of anionic redox activity in Li-ion batteries. *Nat. Energy* **2018,** *3* (5), 373-386.

22. Lee, J.; Kitchaev, D. A.; Kwon, D. H.; Lee, C. W.; Papp, J. K.; Liu, Y. S.; Lun, Z.; Clement, R. J.; Shi, T.; McCloskey, B. D.; Guo, J.; Balasubramanian, M.; Ceder, G., Reversible Mn^{2+}/Mn^{4+} double redox in lithium-excess cathode materials. *Nature* **2018,** *556* (7700), 185-190.

23. Sun, C.; Rajasekhara, S.; Goodenough, J. B.; Zhou, F., Monodisperse Porous $LiFePO_4$ Microspheres for a High Power Li-Ion Battery Cathode. *J. Am. Chem. Soc.* **2011,** *133* (7), 2132-2135.

24. Wang, Y.; Wang, Y.; Hosono, E.; Wang, K.; Zhou, H., The Design of a $LiFePO_4$/carbon Nanocomposite With a Core–Shell Structure and Its Synthesis by an In Situ Polymerization Restriction Method. *Angew. Chem. Int. Ed.* **2008,** *47* (39), 7461-7465.

25. Huang, H.; Yin, S.-C.; Nazar, L. F., Approaching Theoretical Capacity of $LiFePO_4$ at Room Temperature at High Rates. *Electrochem. Solid-State Lett.* **2001,** *4* (10), A170-A172.

26. Yan, P.; Zheng, J.; Liu, J.; Wang, B.; Cheng, X.; Zhang, Y.; Sun, X.; Wang, C.; Zhang, J.-G., Tailoring grain boundary structures and chemistry of Ni-rich layered cathodes for enhanced cycle stability of lithium-ion batteries. *Nat. Energy* **2018,** *3*, 600-605.

27. Chen, S.; He, T.; Su, Y.; Lu, Y.; Bao, L.; Chen, L.; Zhang, Q.; Wang, J.; Chen, R.; Wu, F., Ni-Rich $LiNi_{0.8}Co_{0.1}Mn_{0.1}O_2$ Oxide Coated by Dual-Conductive Layers as High Performance Cathode Material for Lithium-Ion Batteries. *ACS Appl. Mater. Interfaces* **2017,** *9* (35), 29732-29743.

28. Cho, J.; Kim, T.-J.; Kim, J.; Noh, M.; Park, B., Synthesis, Thermal, and Electrochemical Properties of $AlPO_4$-Coated $LiNi_{0.8}Co_{0.1}Mn_{0.1}O_2$ Cathode Materials for a Li-Ion Cell. *J. Electrochem. Soc.* **2004,** *151* (11), A1899-A1904.

29. Jiang, K. C.; Wu, X.-L.; Yin, Y.-X.; Lee, J.-S.; Kim, J.; Guo, Y.-G., Superior Hybrid Cathode Material Containing Lithium-Excess Layered Material and Graphene for Lithium-Ion Batteries. *ACS Appl. Mater. Interfaces* **2012,** *4* (9), 4858-4863.

30. Zhao, S.; Sun, B.; Yan, K.; Zhang, J.; Wang, C.; Wang, G., Aegis of Lithium-Rich Cathode Materials via Heterostructured $LiAlF_4$ Coating for High-Performance Lithium-Ion Batteries. *ACS Appl. Mater. Interfaces* **2018,** *10* (39), 33260-33268.

31. Sun, Y. K.; Lee, M. J.; Yoon, C. S.; Hassoun, J.; Amine, K.; Scrosati, B., The Role of AlF_3 Coatings in Improving Electrochemical Cycling of Li-Enriched Nickel-Manganese Oxide Electrodes for Li-Ion Batteries. *Adv. Mater.* **2012,** *24* (9), 1192-1196.

32. Shi, J.-L.; Xiao, D.-D.; Ge, M.; Yu, X.; Chu, Y.; Huang, X.; Zhang, X.-D.; Yin, Y.-X.; Yang, X.-Q.; Guo, Y.-G.; Gu, L.; Wan, L.-J., High-Capacity Cathode Material with High Voltage for Li-Ion Batteries. *Adv. Mater.* **2018,** *30* (9), 1705575.

33. Rossouw, M.; Thackeray, M., Lithium manganese oxides from Li_2MnO_3 for rechargeable lithium battery applications. *Mater. Res. Bull.* **1991,** *26* (6), 463-473.

34. Yamada, A., Lattice instability in Li $(Li_xMn_{2-x})O_4$. *J. Solid State Chem.* **1996,** *122* (1), 160-165.

35. Lu, Z.; Dahn, J. R., Understanding the Anomalous Capacity of Li/Li$[Ni_xLi_{(1/3-2x/3)}Mn_{(2/3-x/3)}]O_2$ Cells Using In Situ X-Ray Diffraction and Electrochemical Studies. *J. Electrochem. Soc.* **2002,** *149* (7), A815-A822.

36. Yang, X.; Tang, W.; Liu, Z.; Makita, Y.; Ooi, K., Synthesis of lithium-rich $Li_xMn_2O_4$ spinels by lithiation and heat-treatment of defective spinels. *J. Mater. Chem.* **2002,** *12* (3), 489-495.

37. Meng, Y. S.; Ceder, G.; Grey, C. P.; Yoon, W. S.; Jiang, M.; Bréger, J.; Shao-Horn, Y., Cation Ordering in Layered O3 Li$[Ni_xLi_{1/3-2x/3}Mn_{2/3-x/3}]O_2$ ($0 \leq x \leq 1/2$) Compounds. *Chem. Mater.* **2005,** *17* (9), 2386-2394.

38. Zhang, X.; Jiang, W.; Mauger, A.; Gendron, F.; Julien, C., Minimization of the cation mixing in $Li_{1+x}(NMC)_{1-x}O_2$ as cathode material. *J. Power Sources* **2010,** *195* (5), 1292-1301.

39. Deng, Z.; Manthiram, A., Influence of Cationic Substitutions on the Oxygen Loss and Reversible Capacity of Lithium-Rich Layered Oxide Cathodes. *J. Phys. Chem. C* **2011,** *115* (14), 7097-7103.

40. Xiao, P.; Deng, Z. Q.; Manthiram, A.; Henkelman, G., Calculations of Oxygen Stability in Lithium-Rich Layered Cathodes. *J. Phys. Chem. C* **2012,** *116* (44), 23201-23204.

41. Boulineau, A.; Simonin, L.; Colin, J. F.; Bourbon, C.; Patoux, S., First Evidence of Manganese-Nickel Segregation and Densification upon Cycling in Li-Rich Layered Oxides for Lithium Batteries. *Nano Lett.* **2013,** *13* (8), 3857-3863.

42. Fell, C. R.; Qian, D.; Carroll, K. J.; Chi, M.; Jones, J. L.; Meng, Y. S., Correlation Between Oxygen Vacancy, Microstrain, and Cation Distribution in Lithium-Excess Layered Oxides During the First Electrochemical Cycle. *Chem. Mater.* **2013,** *25* (9), 1621-1629.

43. Sathiya, M.; Rousse, G.; Ramesha, K.; Laisa, C. P.; Vezin, H.; Sougrati, M. T.; Doublet, M. L.; Foix, D.; Gonbeau, D.; Walker, W.; Prakash, A. S.; Ben Hassine, M.; Dupont, L.; Tarascon, J. M., Reversible anionic redox chemistry in high-capacity layered-oxide electrodes. *Nat. Mater.* **2013,** *12* (9), 827-835.

44. Luo, K.; Roberts, M. R.; Hao, R.; Guerrini, N.; Pickup, D. M.; Liu, Y. S.; Edstrom, K.; Guo, J.; Chadwick, A. V.; Duda, L. C.; Bruce, P. G., Charge-compensation in 3d-transition-metal-oxide intercalation cathodes through the generation of localized electron holes on oxygen. *Nat. Chem.* **2016,** *8* (7), 684-691.

45. Seo, D. H.; Lee, J.; Urban, A.; Malik, R.; Kang, S.; Ceder, G., The structural and chemical origin of the oxygen redox activity in layered and cation-disordered Li-excess cathode materials. *Nat. Chem.* **2016,** *8* (7), 692-697.

46. Assat, G.; Foix, D.; Delacourt, C.; Iadecola, A.; Dedryvere, R.; Tarascon, J. M., Fundamental interplay between anionic/cationic redox governing the kinetics and thermodynamics of lithium-rich cathodes. *Nat. Commun.* **2017,** *8* (1), 2219.

47. Hu, E.; Yu, X.; Lin, R.; Bi, X.; Lu, J.; Bak, S.; Nam, K.-W.; Xin, H. L.; Jaye, C.; Fischer, D. A.; Amine, K.; Yang, X.-Q., Evolution of redox couples in Li- and Mn-rich cathode materials and mitigation of voltage fade by reducing oxygen release. *Nat. Energy* **2018,** *3* (8), 690-698.

48. Singer, A.; Zhang, M.; Hy, S.; Cela, D.; Fang, C.; Wynn, T. A.; Qiu, B.; Xia, Y.; Liu, Z.; Ulvestad, A.; Hua, N.; Wingert, J.; Liu, H.; Sprung, M.; Zozulya, A. V.; Maxey, E.; Harder, R.; Meng, Y. S.; Shpyrko, O. G., Nucleation of dislocations and their dynamics in layered oxide cathode materials during battery charging. *Nat. Energy* **2018,** *3* (8), 641-647.

49. Assat, G.; Glazier, S. L.; Delacourt, C.; Tarascon, J.-M., Probing the thermal effects of voltage hysteresis in anionic redox-based lithium-rich cathodes using isothermal calorimetry. *Nat. Energy* **2019,** *4* (8), 647-656.

50. Hong, J.; Gent, W. E.; Xiao, P.; Lim, K.; Seo, D.-H.; Wu, J.; Csernica, P. M.; Takacs, C. J.; Nordlund, D.; Sun, C.-J.; Stone, K. H.; Passarello, D.; Yang, W.; Prendergast, D.; Ceder, G.; Toney, M. F.; Chueh, W. C., Metal–oxygen decoordination stabilizes anion redox in Li-rich oxides. *Nat. Mater.* **2019,** *18*, 256–265.

51. Radin, M. D.; Vinckeviciute, J.; Seshadri, R.; Van der Ven, A., Manganese oxidation as the origin of the anomalous capacity of Mn-containing Li-excess cathode materials. *Nat. Energy* **2019,** *4*, 639–646.

52. Manthiram, A.; Knight, J. C.; Myung, S. T.; Oh, S. M.; Sun, Y. K., Nickel-Rich and Lithium-Rich Layered Oxide Cathodes: Progress and Perspectives. *Adv. Energy Mater.* **2016,** *6* (1), 1501010.

53. Hy, S.; Liu, H.; Zhang, M.; Qian, D.; Hwang, B.-J.; Meng, Y. S., Performance and design considerations for lithium excess layered oxide positive electrode materials for lithium-ion batteries. *Energy Environ. Sci.* **2016,** *9* (6), 1931-1954.

54. Yu, H.; Kim, H.; Wang, Y.; He, P.; Asakura, D.; Nakamura, Y.; Zhou, H., High-energy 'composite' layered manganese-rich cathode materials via controlling Li_2MnO_3 phase activation for lithium-ion batteries. *Phys. Chem. Chem. Phys.* **2012,** *14* (18), 6584-6595.

55. Wang, J.; He, X.; Paillard, E.; Laszczynski, N.; Li, J.; Passerini, S., Lithium-and Manganese-Rich Oxide Cathode Materials for High-Energy Lithium Ion Batteries. *Adv. Energy Mater.* **2016,** *6* (21), 1600906.

56. Erickson, E. M.; Schipper, F.; Penki, T. R.; Shin, J.-Y.; Erk, C.; Chesneau, F.-F.; Markovsky, B.; Aurbach, D., Recent Advances and Remaining Challenges for Lithium Ion Battery Cathodes II. Lithium-rich, $xLi_2MnO_3 \cdot (1\text{-}x)\ LiNi_aCo_bMn_cO_2$. *J. Electrochem. Soc.* **2017,** *164* (1), A6341-A6348.

57. Thackeray, M. M.; Kang, S.-H.; Johnson, C. S.; Vaughey, J. T.; Benedek, R.; Hackney, S., Li_2MnO_3-stabilized $LiMO_2$ (M= Mn, Ni, Co) electrodes for lithium-ion batteries. *J. Mater. Chem.* **2007,** *17* (30), 3112-3125.

58. Ammundsen, B.; Paulsen, J., Novel Lithium-Ion Cathode Materials Based on Layered Manganese Oxides. *Adv. Mater.* **2001,** *13* (12-13), 943-956.

59. Kikkawa, J.; Akita, T.; Tabuchi, M.; Shikano, M.; Tatsumi, K.; Kohyama, M., Formation and Disappearance of Spinel Nanograins in $Li_{1.2-x}Mn_{0.4}Fe_{0.4}O_2$ ($0 \leq x \leq 0.99$) during Extraction and Insertion of Li Ions. *J. Electrochem. Soc.* **2009,** *156* (11), A839-A845.

60. Luo, K.; Roberts, M. R.; Hao, R.; Guerrini, N.; Liberti, E.; Allen, C. S.; Kirkland, A. I.; Bruce, P. G., One-Pot Synthesis of Lithium-Rich Cathode Material with Hierarchical Morphology. *Nano Lett.* **2016,** *16* (12), 7503-7508.

61. Wu, Z.; Ji, S.; Zheng, J.; Hu, Z.; Xiao, S.; Wei, Y.; Zhuo, Z.; Lin, Y.; Yang, W.; Xu, K.; Amine, K.; Pan, F., Prelithiation Activates $Li(Ni_{0.5}Mn_{0.3}Co_{0.2})O_2$ for High Capacity and Excellent Cycling Stability. *Nano Lett.* **2015,** *15* (8), 5590-5596.

62. Bareno, J.; Lei, C. H.; Wen, J. G.; Kang, S. H.; Petrov, I.; Abraham, D. P., Local Structure of Layered Oxide Electrode Materials for Lithium-Ion Batteries. *Adv. Mater.* **2010,** *22* (10), 1122-1127.

63. Ammundsen, B.; Paulsen, J.; Davidson, I.; Liu, R.-S.; Shen, C.-H.; Chen, J.-M.; Jang, L.-Y.; Lee, J.-F., Local Structure and First Cycle Redox Mechanism of Layered $Li_{1.2}Cr_{0.4}Mn_{0.4}O_2$ Cathode Material. *J. Electrochem. Soc.* **2002,** *149* (4), A431.

64. Kikkawa, J.; Akita, T.; Tabuchi, M.; Shikano, M.; Tatsumi, K.; Kohyama, M., Fe-rich and Mn-rich nanodomains in $Li_{1.2}Mn_{0.4}Fe_{0.4}O_2$ positive electrode materials for lithium-ion batteries. *Appl. Phys. Lett.* **2007,** *91* (5), 054103.

65. Thackeray, M. M.; Kang, S. H.; Johnson, C. S.; Vaughey, J. T.; Hackney, S. A., Comments on the structural complexity of lithium-rich $Li_{1+x}M_{1-x}O_2$ electrodes (M=Mn, Ni, Co) for lithium batteries. *Electrochem. Commun.* **2006,** *8* (9), 1531-1538.

66. Jarvis, K. A.; Deng, Z.; Allard, L. F.; Manthiram, A.; Ferreira, P. J., Atomic Structure of a Lithium-Rich Layered Oxide Material for Lithium-Ion Batteries: Evidence of a Solid Solution. *Chem. Mater.* **2011,** *23* (16), 3614-3621.

67. Yoon, W.-S.; Iannopollo, S.; Grey, C. P.; Carlier, D.; Gorman, J.; Reed, J.; Ceder, G., Local Structure and Cation Ordering in O3 Lithium Nickel Manganese Oxides with Stoichiometry $Li[Ni_xMn_{(2-x)/3}]Li_{(1-2x)/3}]O_2$. *Electrochem. Solid-State Lett.* **2004,** *7* (7), A167.

68. Lu, Z.; Chen, Z.; Dahn, J. R., Lack of Cation Clustering in $Li[Ni_xLi_{1/3-2x/3}Mn_{2/3-x/3}]O_2$ ($0 < x \leq 1/2$) and $Li[Cr_xLi_{(1-x)/3}Mn_{(2-2x)/3}]O_2$ ($0 < x < 1$). *Chem. Mater.* **2003,** *15* (16), 3214-3220.

69. Armstrong, A. R.; Holzapfel, M.; Novák, P.; Johnson, C. S.; Kang, S.-H.; Thackeray, M. M.; Bruce, P. G., Demonstrating Oxygen Loss and Associated Structural Reorganization in the Lithium Battery Cathode $Li[Ni_{0.2}Li_{0.2}Mn_{0.6}]O_2$. *J. Am. Chem. Soc.* **2006,** *128* (26), 8694-8698.

70. Hua, W.; Wang, S.; Knapp, M.; Leake, S. J.; Senyshyn, A.; Richter, C.; Yavuz, M.; Binder, J. R.; Grey, C. P.; Ehrenberg, H., Structural insights into the formation and voltage degradation of lithium-and manganese-rich layered oxides. *Nat. Commun.* **2019,** *10* (1), 1-11.

71. Wu, F.; Li, W.; Chen, L.; Su, Y.; Bao, L.; Bao, W.; Yang, Z.; Wang, J.; Lu, Y.; Chen, S., Renovating the electrode-electrolyte interphase for layered lithium-& manganese-rich oxides. *Energy Stor. Mater.* **2020**, 28, 383-392.

72. Robertson, A. D.; Bruce, P. G., Overcapacity of $Li[Ni_xLi_{1/3-2x/3}Mn_{2/3-x/3}]O_2$ Electrodes. *Electrochem. Solid-State Lett.* **2004,** *7* (9), A294.

73. Armstrong, A. R.; Bruce, P. G., Electrochemistry Beyond Mn^{4+} in $Li_xMn_{1-y}Li_yO_2$. *Electrochem. Solid-State Lett.* **2004,** *7* (1), A1-A4.

74. Armstrong, A. R.; Robertson, A. D.; Bruce, P. G., Overcharging manganese oxides: Extracting lithium beyond Mn^{4+}. *J. Power Sources* **2005,** *146* (1-2), 275-280.

75. La Mantia, F.; Rosciano, F.; Tran, N.; Novák, P., Direct evidence of oxygen evolution from $Li_{1+x}(Ni_{1/3}Mn_{1/3}Co_{1/3})_{1-x}O_2$ at high potentials. *J. Appl. Electrochem.* **2008,** *38* (7), 893-896.

76. Chen, H.; Islam, M. S., Lithium Extraction Mechanism in Li-Rich Li_2MnO_3 Involving Oxygen Hole Formation and Dimerization. *Chem. Mater.* **2016,** *28* (18), 6656-6663.

77. Gu, M.; Belharouak, I.; Zheng, J.; Wu, H.; Xiao, J.; Genc, A.; Amine, K.; Thevuthasan, S.; Baer, D. R.; Zhang, J.-G., Formation of the Spinel Phase in the Layered Composite Cathode Used in Li-Ion Batteries. *ACS Nano* **2012,** *7* (1), 760-767.

78. Yan, P.; Zheng, J.; Gu, M.; Xiao, J.; Zhang, J.-G.; Wang, C.-M., Intragranular cracking as a critical barrier for high-voltage usage of layer-structured cathode for lithium-ion batteries. *Nat. Commun.* **2017,** *8*, 14101.

79. Chen, C.-J.; Pang, W. K.; Mori, T.; Peterson, V. K.; Sharma, N.; Lee, P.-H.; Wu, S.-h.; Wang, C.-C.; Song, Y.-F.; Liu, R.-S., The Origin of Capacity Fade in the $Li_2MnO_3 \cdot LiMO_2$ (M= Li, Ni, Co, Mn) Microsphere Positive Electrode: An Operando Neutron Diffraction and Transmission X-ray Microscopy Study. *J. Am. Chem. Soc.* **2016,** *138* (28), 8824-8833.

80. Pearce, P. E.; Perez, A. J.; Rousse, G.; Saubanère, M.; Batuk, D.; Foix, D.; McCalla, E.; Abakumov, A. M.; Van Tendeloo, G.; Doublet, M.-L., Evidence for anionic redox activity in a tridimensional-ordered Li-rich positive electrode β-Li_2IrO_3. *Nat. Mater.* **2017,** *16* (5), 580-586.

81. Koga, H.; Croguennec, L.; Ménétrier, M.; Douhil, K.; Belin, S.; Bourgeois, L.; Suard, E.; Weill, F.; Delmas, C., Reversible Oxygen Participation to the Redox Processes Revealed for $Li_{1.20}Mn_{0.54}Co_{0.13}Ni_{0.13}O_2$. *J. Electrochem. Soc.* **2013,** *160* (6), A786-A792.

82. Li, X.; Qiao, Y.; Guo, S.; Xu, Z.; Zhu, H.; Zhang, X.; Yuan, Y.; He, P.; Ishida, M.; Zhou, H., Direct Visualization of the Reversible O^{2-}/O^{-} Redox Process in Li-Rich Cathode Materials. *Adv. Mater.* **2018,** *30* (14), 1705197.

83. Xu, B.; Fell, C. R.; Chi, M.; Meng, Y. S., Identifying surface structural changes in layered Li-excess nickel manganese oxides in high voltage lithium ion batteries: A joint experimental and theoretical study. *Energy Environ. Sci.* **2011,** *4* (6), 2223-2233.

84. Gu, M.; Belharouak, I.; Genc, A.; Wang, Z.; Wang, D.; Amine, K.; Gao, F.; Zhou, G.; Thevuthasan, S.; Baer, D. R.; Zhang, J. G.; Browning, N. D.; Liu, J.; Wang, C., Conflicting Roles of Nickel in Controlling Cathode Performance in Lithium Ion Batteries. *Nano Lett.* **2012,** *12* (10), 5186-5191.

85. Gu, M.; Genc, A.; Belharouak, I.; Wang, D.; Amine, K.; Thevuthasan, S.; Baer, D. R.; Zhang, J.-G.; Browning, N. D.; Liu, J.; Wang, C., Nanoscale Phase Separation, Cation Ordering, and Surface Chemistry in Pristine $Li_{1.2}Ni_{0.2}Mn_{0.6}O_2$ for Li-Ion Batteries. *Chem. Mater.* **2013,** *25* (11), 2319-2326.

86. Yan, P.; Zheng, J.; Zheng, J.; Wang, Z.; Teng, G.; Kuppan, S.; Xiao, J.; Chen, G.; Pan, F.; Zhang, J.-G.; Wang, C.-M., Ni and Co Segregations on Selective Surface Facets and Rational Design of Layered Lithium Transition-Metal Oxide Cathodes. *Adv. Energy Mater.* **2016,** *6* (9), 1502455.

87. Gu, L.; Xiao, D.; Hu, Y. S.; Li, H.; Ikuhara, Y., Atomic-Scale Structure Evolution in a Quasi-Equilibrated Electrochemical Process of Electrode Materials for Rechargeable Batteries. *Adv. Mater.* **2015,** *27* (13), 2134-2149.

88. Lin, F.; Markus, I. M.; Nordlund, D.; Weng, T. C.; Asta, M. D.; Xin, H. L.; Doeff, M. M., Surface reconstruction and chemical evolution of stoichiometric layered cathode materials for lithium-ion batteries. *Nat. Commun.* **2014,** *5*, 3529.

89. Zheng, J.; Gu, M.; Genc, A.; Xiao, J.; Xu, P.; Chen, X.; Zhu, Z.; Zhao, W.; Pullan, L.; Wang, C.; Zhang, J. G., Mitigating Voltage Fade in Cathode Materials by Improving the Atomic Level Uniformity of Elemental Distribution. *Nano Lett.* **2014,** *14* (5), 2628-2635.

90. Xiao, L.; Xiao, J.; Yu, X.; Yan, P.; Zheng, J.; Engelhard, M.; Bhattacharya, P.; Wang, C.; Yang, X.-Q.; Zhang, J.-G., Effects of structural defects on the electrochemical activation of Li_2MnO_3. *Nano Energy* **2015,** *16*, 143-151.

91. Reed, J.; Ceder, G., Role of Electronic Structure in the Susceptibility of Metastable Transition-Metal Oxide Structures to Transformation. *Chem. Rev.* **2004,** *104* (10), 4513-4534.

92. Goodenough, J. B.; Kim, Y., Challenges for Rechargeable Li Batteries. *Chem. Mater.* **2010,** *22* (3), 587-603.

93. Ohzuku, T.; Nagayama, M.; Tsuji, K.; Ariyoshi, K., High-capacity lithium insertion materials of lithium nickel manganese oxides for advanced lithium-ion batteries: toward rechargeable capacity more than 300 mAh g^{-1}. *J. Mater. Chem.* **2011,** *21* (27), 10179-10188.

94. Hu, E.; Yu, X.; Lin, R.; Bi, X.; Lu, J.; Bak, S.; Nam, K.-W.; Xin, H. L.; Jaye, C.; Fischer, D. A.; Amine, K.; Yang, X.-Q., Evolution of redox couples in Li- and Mn-rich cathode materials and mitigation of voltage fade by reducing oxygen release. *Nat. Energy* **2018,** *3* (8), 690-698.

95. Assat, G.; Foix, D.; Delacourt, C.; Iadecola, A.; Dedryvere, R.; Tarascon, J. M., Fundamental interplay between anionic/cationic redox governing the kinetics and thermodynamics of lithium-rich cathodes. *Nat. Commun.* **2017,** *8* (1), 2219.

96. Hy, S.; Liu, H.; Zhang, M.; Qian, D.; Hwang, B.-J.; Meng, Y. S., Performance and design considerations for lithium excess layered oxide positive electrode materials for lithium ion batteries. *Energy Environ. Sci.* **2016,** *9* (6), 1931-1954.

97. Ye, D.; Wang, B.; Chen, Y.; Han, G.; Zhang, Z.; Hulicova-Jurcakova, D.; Zou, J.; Wang, L., Understanding the stepwise capacity-increase of high energy low-Co Li-rich cathode materials for lithium ion batteries. *J. Mater. Chem. A* **2014,** *2* (44), 18767-18774.

98. Ozawa, K.; Nakao, Y.; Mochiku, T.; Cheng, Z.; Wang, L.; Iwai, H.; Tsuchiya, Y.; Fujii, H.; Igawa, N., Electrochemical Characteristics of Layered $Li_{1.95}Mn_{0.9}Co_{0.15}O_3$(C2/m) as a Lithium-Battery Cathode. *J. Electrochem. Soc.* **2012,** *159* (3), A300-A304.

99. Park, M.-S.; Lee, J.-W.; Choi, W.; Im, D.; Doo, S.-G.; Park, K.-S., On the surface modifications of high-voltage oxide cathodes for lithium-ion batteries: new insight and significant safety improvement. *J. Mater. Chem.* **2010,** *20* (34), 7208-7213.

100. Cho, J.; Kim, Y. J.; Kim, T. J.; Park, B., Zero-Strain Intercalation Cathode for Rechargeable Li-Ion Cell. *Angew. Chem. Int. Ed.* **2001,** *40* (18), 3367-3369.

101. Li, C.; Zhang, H.; Fu, L.; Liu, H.; Wu, Y.; Rahm, E.; Holze, R.; Wu, H., Cathode materials modified by surface coating for lithium ion batteries. *Electrochim. Acta* **2006,** *51* (19), 3872-3883.

102. Chen, Z.; Qin, Y.; Amine, K.; Sun, Y.-K., Role of surface coating on cathode materials for lithium-ion batteries. *J. Mater. Chem.* **2010,** *20* (36), 7606-7612.

103. Zheng, J.; Myeong, S.; Cho, W.; Yan, P.; Xiao, J.; Wang, C.; Cho, J.; Zhang, J. G., Li- and Mn-Rich Cathode Materials: Challenges to Commercialization. *Adv. Energy Mater.* **2017,** *7* (6), 1601284.

104. Zheng, J.; Gu, M.; Xiao, J.; Polzin, B. J.; Yan, P.; Chen, X.; Wang, C.; Zhang, J.-G., Functioning Mechanism of AlF_3 Coating on the Li-and Mn-rich Cathode Materials. *Chem. Mater.* **2014,** *26* (22), 6320-6327.

105. Jung, S. C.; Han, Y.-K., How Do Li Atoms Pass through the Al_2O_3 Coating Layer during Lithiation in Li-ion Batteries? *J. Phys. Chem. Lett.* **2013,** *4* (16), 2681-2685.

106. Zhang, X. D.; Shi, J. L.; Liang, J. Y.; Yin, Y. X.; Zhang, J. N.; Yu, X. Q.; Guo, Y. G., Suppressing Surface Lattice Oxygen Release of Li-Rich Cathode Materials via Heterostructured Spinel $Li_4Mn_5O_{12}$ Coating. *Adv. Mater.* **2018,** *30* (29), 1801751.

107. Bian, X.; Fu, Q.; Qiu, H.; Du, F.; Gao, Y.; Zhang, L.; Zou, B.; Chen, G.; Wei, Y., High-Performance $Li(Li_{0.18}Ni_{0.15}Co_{0.15}Mn_{0.52})O_2@Li_4M_5O_{12}$ Heterostructured Cathode Material Coated with a Lithium Borate Oxide Glass Layer. *Chem. Mater.* **2015,** *27* (16), 5745-5754.

108. Bian, X.; Fu, Q.; Pang, Q.; Gao, Y.; Wei, Y.; Zou, B.; Du, F.; Chen, G., Multi-Functional Surface Engineering for Li-Excess Layered Cathode Material Targeting Excellent Electrochemical and Thermal Safety Properties. *ACS Appl. Mater. Interfaces* **2016,** *8* (5), 3308-3318.

109. Liu, H.; Qian, D.; Verde, M. G.; Zhang, M.; Baggetto, L.; An, K.; Chen, Y.; Carroll, K. J.; Lau, D.; Chi, M.; Veith, G. M.; Meng, Y. S., Understanding the Role of NH_4F and Al_2O_3 Surface Co-modification on Lithium-Excess Layered Oxide $Li_{1.2}Ni_{0.2}Mn_{0.6}O_2$. *ACS Appl. Mater. Interfaces* **2015,** *7* (34), 19189-19200.

110. Sun, Y. K.; Lee, M. J.; Yoon, C. S.; Hassoun, J.; Amine, K.; Scrosati, B., The Role of AlF_3 Coatings in Improving Electrochemical Cycling of Li-Enriched Nickel-Manganese Oxide Electrodes for Li-Ion Batteries. *Adv. Mater.* **2012,** *24* (9), 1192-1196.

111. Zhang, X.; Belharouak, I.; Li, L.; Yu, L.; Axelbaum, R. L., Structural and electrochemical study of Al_2O_3 and TiO_2 Coated $Li_{1.2}Ni_{0.13}Mn_{0.54}Co_{0.13}O_2$ cathode material using ALD. *Adv. Energy Mater.* **2013,** *3* (10), 1299-1307.

112. Zheng, F.; Yang, C.; Xiong, X.; Xiong, J.; Hu, R.; Chen, Y.; Liu, M., Nanoscale Surface Modification of Lithium-Rich Layered-Oxide Composite Cathodes for Suppressing Voltage Fade. *Angew. Chem. Int. Ed.* **2015,** *54* (44), 13058-13062.

113. Yu, R.; Lin, Y.; Huang, Z., Investigation on the enhanced electrochemical performances of $Li_{1.2}Ni_{0.13}Co_{0.13}Mn_{0.54}O_2$ by surface modification with ZnO. *Electrochim. Acta* **2015,** *173*, 515-522.

114. Guo, S.; Yu, H.; Liu, P.; Liu, X.; Li, D.; Chen, M.; Ishida, M.; Zhou, H., Surface coating of lithium–manganese-rich layered oxides with delaminated MnO_2 nanosheets as cathode materials for Li-ion batteries. *J. Mater. Chem. A* **2014,** *2* (12), 4422-4428.

115. Wang, Q. Y.; Liu, J.; Murugan, A. V.; Manthiram, A., High capacity double-layer surface modified $Li[Li_{0.2}Mn_{0.54}Ni_{0.13}Co_{0.13}]O_2$ cathode with improved rate capability. *J. Mater. Chem.* **2009,** *19* (28), 4965-4972.

116. Wang, Z.; Liu, E.; He, C.; Shi, C.; Li, J.; Zhao, N., Effect of amorphous $FePO_4$ coating on structure and electrochemical performance of $Li_{1.2}Ni_{0.13}Co_{0.13}Mn_{0.54}O_2$ as cathode material for Li-ion batteries. *J. Power Sources* **2013,** *236*, 25-32.

117. Bing, L.; Zhang, Q.; He, S.; Sato, Y.; Zheng, J.; Li, D., Improved electrochemical properties of $Li_{1.2}Ni_{0.18}Mn_{0.59}Co_{0.03}O_2$ by surface modification with $LiCoPO_4$. *Electrochim. Acta* **2011,** *56* (19), 6748-6751.

118. Liu, Y.; Wang, Q.; Lu, Y.; Yang, B.; Su, M.; Gao, Y.; Dou, A.; Pan, J., Enhanced electrochemical performances of layered cathode material $Li_{1.5}Ni_{0.25}Mn_{0.75}O_{2.5}$ by coating with $LiAlO_2$. *J. Alloys Compd.* **2015,** *638*, 1-6.

119. Liu, X.; Liu, J.; Huang, T.; Yu, A., CaF_2-coated $Li_{1.2}Mn_{0.54}Ni_{0.13}Co_{0.13}O_2$ as cathode materials for Li-ion batteries. *Electrochim. Acta* **2013,** *109* (11), 52-58.

120. Li, C.-D.; Xu, J.; Xia, J.-S.; Liu, W.; Xiong, X.; Zheng, Z.-A., Influences of FeF_3 coating layer on the electrochemical properties of $Li[Li_{0.2}Mn_{0.54}Ni_{0.13}Co_{0.13}]O_2$ cathode materials for lithium-ion batteries. *Solid State Ion* **2016,** *292*, 75-82.

121. Sun, S.; Wan, N.; Wu, Q.; Zhang, X.; Pan, D.; Bai, Y.; Lu, X., Surface-modified $Li[Li_{0.2}Ni_{0.17}Co_{0.07}Mn_{0.56}]O_2$ nanoparticles with MgF_2 as cathode for Li-ion battery. *Solid State Ion* **2015,** *278*, 85-90.

122. Song, B.; Zhou, C.; Chen, Y.; Liu, Z.; Lai, M. O.; Xue, J.; Lu, L., Role of carbon coating in improving electrochemical performance of Li-rich $Li(Li_{0.2}Mn_{0.54}Ni_{0.13}Co_{0.13})O_2$ cathode. *RSC Adv.* **2014,** *4* (83), 44244-44252.

123. Xia, Q.; Zhao, X.; Xu, M.; Ding, Z.; Liu, J.; Chen, L.; Ivey, D. G.; Wei, W., A Li-rich Layered@Spinel@Carbon heterostructured cathode material for high capacity and high rate

lithium-ion batteries fabricated via an in situ synchronous carbonization-reduction method. *J. Mater. Chem. A* **2015,** *3* (7), 3995-4003.

124. Mun, J.; Park, J.-H.; Choi, W.; Benayad, A.; Park, J.-H.; Lee, J.-M.; Doo, S.-G.; Oh, S. M., New dry carbon nanotube coating of over-lithiated layered oxide cathode for lithium-ion batteries. *J. Mater. Chem. A* **2014,** *2* (46), 19670-19677.

125. Xue, Q.; Li, J.; Xu, G.; Zhou, H.; Wang, X.; Kang, F., In situ polyaniline modified cathode material $Li[Li_{0.2}Mn_{0.54}Ni_{0.13}Co_{0.13}]O_2$ with high rate capacity for lithium ion batteries. *J. Mater. Chem. A* **2014,** *2* (43), 18613–18623.

126. Ying, J.; Wan, C.; Jiang, C., Surface treatment of $LiNi_{0.8}Co_{0.2}O_2$ cathode material for lithium secondary batteries. *J. Power Sources* **2001,** *102* (1), 162-166.

127. Hashem, A. M. A.; Abdel-Ghany, A. E.; Eid, A. E.; Trottier, J.; Zaghib, K.; Mauger, A.; Julien, C. M., Study of the surface modification of $LiNi_{1/3}Co_{1/3}Mn_{1/3}O_2$ cathode material for lithium-ion battery. *J. Power Sources* **2011,** *196* (20), 8632-8637.

128. Myung, S.-T.; Amine, K.; Sun, Y.-K., Surface modification of cathode materials from nano- to microscale for rechargeable lithium-ion batteries. *J. Mater. Chem.* **2010,** *20* (34), 7074-7095.

129. Han, S.; Qiu, B.; Wei, Z.; Xia, Y.; Liu, Z., Surface structural conversion and electrochemical enhancement by heat treatment of chemical pre-delithiation processed lithium-rich layered cathode material. *J. Power Sources* **2014,** *268*, 683-691.

130. Qiu, B.; Zhang, M.; Wu, L.; Wang, J.; Xia, Y.; Qian, D.; Liu, H.; Hy, S.; Chen, Y.; An, K.; Zhu, Y.; Liu, Z.; Meng, Y. S., Gas-solid interfacial modification of oxygen activity in layered oxide cathodes for lithium-ion batteries. *Nat. Commun.* **2016,** *7*, 12108.

131. Erickson, E. M.; Sclar, H.; Schipper, F.; Liu, J.; Tian, R.; Ghanty, C.; Burstein, L.; Leifer, N.; Grinblat, J.; Talianker, M., High-Temperature Treatment of Li-Rich Cathode Materials with Ammonia: Improved Capacity and Mean Voltage Stability during Cycling. *Adv. Energy Mater.* **2017,** *7* (18), 1700708.

132. Lin, T.; Schulli, T. U.; Hu, Y.; Zhu, X.; Gu, Q.; Luo, B.; Cowie, B.; Wang, L., Faster Activation and Slower Capacity/Voltage Fading: A Bifunctional Urea Treatment on Lithium-Rich Cathode Materials. *Adv. Funct. Mater.* **2021,** *11* (2), 2000943.

133. Chen, Q.; Pei, Y.; Chen, H.; Song, Y.; Zhen, L.; Xu, C.-Y.; Xiao, P.; Henkelman, G., Highly reversible oxygen redox in layered compounds enabled by surface polyanions. *Nat. Commun.* **2020,** *11* (1), 3411.

134. Zhu, Z.; Gao, R.; Waluyo, I.; Dong, Y.; Hunt, A.; Lee, J.; Li, J., Stabilized Co-Free Li-Rich Oxide Cathode Particles with An Artificial Surface Prereconstruction. *Adv. Energy Mater.* **2020,** *10* (35), 2001120.

135. Wang, Y.; Yang, Z.; Qian, Y.; Gu, L.; Zhou, H., New Insights into Improving Rate Performance of Lithium-Rich Cathode Material. *Adv. Mater.* **2015,** *27* (26), 3915-3920.

136. Qing, R. P.; Shi, J. L.; Xiao, D. D.; Zhang, X. D.; Yin, Y. X.; Zhai, Y. B.; Gu, L.; Guo, Y. G., Enhancing the Kinetics of Li-Rich Cathode Materials through the Pinning Effects of Gradient Surface Na^+ Doping. *Adv. Energy Mater.* **2016,** *6* (6), 1501914.

137. Li, Q.; Li, G.; Fu, C.; Luo, D.; Fan, J.; Li, L., K^+-Doped $Li_{1.2}Mn_{0.54}Co_{0.13}Ni_{0.13}O_2$: A Novel Cathode Material with an Enhanced Cycling Stability for Lithium-Ion Batteries. *ACS Appl. Mater. Interfaces* **2014,** *6* (13), 10330-10341.

138. Jin, X.; Xu, Q.; Liu, H.; Yuan, X.; Xia, Y., Excellent rate capability of Mg doped $Li[Li_{0.2}Ni_{0.13}Co_{0.13}Mn_{0.54}]O_2$ cathode material for lithium-ion battery. *Electrochim. Acta* **2014,** *136*, 19-26.

139. Nayak, P. K.; Grinblat, J.; Levi, M.; Levi, E.; Kim, S.; Choi, J. W.; Aurbach, D., Al Doping for Mitigating the Capacity Fading and Voltage Decay of Layered Li and Mn-Rich Cathodes for Li-Ion Batteries. *Adv. Energy Mater.* **2016,** *6* (8), 1502398.

140. Song, B.; Zhou, C.; Wang, H.; Liu, H.; Liu, Z.; Lai, M. O.; Lu, L., Advances in Sustain Stable Voltage of Cr-Doped Li-Rich Layered Cathodes for Lithium Ion Batteries. *J. Electrochem. Soc.* **2014,** *161* (10), A1723-A1730.

141. Liu, S.; Liu, Z.; Shen, X.; Li, W.; Gao, Y.; Banis, M. N.; Li, M.; Chen, K.; Zhu, L.; Yu, R.; Wang, Z.; Sun, X.; Lu, G.; Kong, Q.; Bai, X.; Chen, L., Surface Doping to Enhance

Structural Integrity and Performance of Li-Rich Layered Oxide. *Adv. Energy Mater.* **2018,** *8* (31), 1802105.

142. He, Z.; Wang, Z.; Chen, H.; Huang, Z.; Li, X.; Guo, H.; Wang, R., Electrochemical performance of zirconium doped lithium rich layered $Li_{1.2}Mn_{0.54}Ni_{0.13}Co_{0.13}O_2$ oxide with porous hollow structure. *J. Power Sources* **2015,** *299*, 334-341.

143. Zhang, H.-Z.; Li, F.; Pan, G.-L.; Li, G.-R.; Gao, X.-P., The Effect of Polyanion-Doping on the Structure and Electrochemical Performance of Li-Rich Layered Oxides as Cathode for Lithium-Ion Batteries. *J. Electrochem. Soc.* **2015,** *162* (9), A1899-A1904.

144. Zhang, H.; Qiao, Q.; Li, G.; Gao, X., PO_4^{3-} polyanion-doping for stabilizing Li-rich layered oxides as cathode materials for advanced lithium-ion batteries. *J. Mater. Chem. A* **2014,** *2* (20), 7454-7460.

145. Liu, D.; Fan, X.; Li, Z.; Liu, T.; Sun, M.; Qian, C.; Ling, M.; Liu, Y.; Liang, C., A cation/anion co-doped $Li_{1.12}Na_{0.08}Ni_{0.2}Mn_{0.6}O_{1.95}F_{0.05}$ cathode for lithium ion batteries. *Nano Energy* **2019,** *58*, 786-796.

146. Chen, G.; An, J.; Meng, Y.; Yuan, C.; Matthews, B.; Dou, F.; Shi, L.; Zhou, Y.; Song, P.; Wu, G.; Zhang, D., Cation and anion Co-doping synergy to improve structural stability of Li- and Mn-rich layered cathode materials for lithium-ion batteries. *Nano Energy* **2019,** *57*, 157-165.

147. Liu, Y.; Ning, D.; Zheng, L.; Zhang, Q.; Gu, L.; Gao, R.; Zhang, J.; Franz, A.; Schumacher, G.; Liu, X., Improving the electrochemical performances of Li-rich $Li_{1.20}Ni_{0.13}Co_{0.13}Mn_{0.54}O_2$ through a cooperative doping of Na^+ and PO_4^{3-} with Na_3PO_4. *J. Power Sources* **2018,** *375*, 1-10.

148. Zheng, Z.; Guo, X.-D.; Zhong, Y.-J.; Hua, W.-B.; Shen, C.-H.; Chou, S.-L.; Yang, X.-S., Host Structural Stabilization of $Li_{1.232}Mn_{0.615}Ni_{0.154}O_2$ through K-Doping Attempt: toward Superior Electrochemical Performances. *Electrochim. Acta* **2016,** *188*, 336-343.

149. Yu, R.; Wang, X.; Fu, Y.; Wang, L.; Cai, S.; Liu, M.; Bing, L.; Gang, W.; Di, W.; Ren, Q., Effect of magnesium doping on properties of lithium-rich layered oxide cathodes based on a one-step co-precipitation strategy. *J. Mater. Chem. A* **2016,** *4* (13), 4941-4951.

150. Ramesha, R. N.; Laisa, C. P.; Ramesha, K., Improving Electrochemical Stability by Transition Metal Cation Doping for Manganese in Lithium-rich Layered Cathode, $Li_{1.2}Ni_{0.13}Co_{0.13}Mn_{0.54-x}M_xO_2$ (M=Co, Cr and Fe). *Electrochim. Acta* **2017,** *249*, 377-386.

151. Wu, F.; Kim, G.-T.; Kuenzel, M.; Zhang, H.; Asenbauer, J.; Geiger, D.; Kaiser, U.; Passerini, S., Elucidating the Effect of Iron Doping on the Electrochemical Performance of Cobalt-Free Lithium-Rich Layered Cathode Materials. *Adv. Energy Mater.* **2019,** *9* (43), 1902445.

152. Li, N.; An, R.; Su, Y.; Wu, F.; Bao, L.; Chen, L.; Zheng, Y.; Shou, H.; Chen, S., The role of yttrium content in improving electrochemical performance of layered lithium-rich cathode materials for Li-ion batteries. *J. Mater. Chem. A* **2013,** *1* (34), 9760-9767.

153. Yu, R.; Wang, G.; Liu, M.; Zhang, X.; Wang, X.; Shu, H.; Yang, X.; Huang, W., Mitigating voltage and capacity fading of lithium-rich layered cathodes by lanthanum doping. *J. Power Sources* **2016,** *335*, 65-75.

154. Qiao, Q.-Q.; Qin, L.; Li, G.-R.; Wang, Y.-L.; Gao, X.-P., Sn-stabilized Li-rich layered $Li(Li_{0.17}Ni_{0.25}Mn_{0.58})O_2$ oxide as a cathode for advanced lithium-ion batteries. *J. Mater. Chem. A* **2015,** *3* (34), 17627-17634.

155. Feng, X.; Gao, Y.; Ben, L.; Yang, Z.; Wang, Z.; Chen, L., Enhanced electrochemical performance of Ti-doped $Li_{1.2}Mn_{0.54}Co_{0.13}Ni_{0.13}O_2$ for lithium-ion batteries. *J. Power Sources* **2016,** *317*, 74-80.

156. Song, B.; Lai, M. O.; Lu, L., Influence of Ru substitution on Li-rich$0.55Li_2MnO_3 \cdot 0.45LiNi_{1/3}Co_{1/3}Mn_{1/3}O_2$ cathode for Li-ion batteries. *Electrochim. Acta* **2012,** *80*, 187-195.

157. Zang, Y.; Ding, C.-X.; Wang, X.-C.; Wen, Z.-Y.; Chen, C.-H., Molybdenum-doped lithium-rich layered-structured cathode material $Li_{1.2}Ni_{0.2}Mn_{0.6}O_2$ with high specific capacity and improved rate performance. *Electrochim. Acta* **2015,** *168*, 234-239.

158. Huang, J.; Liu, H.; Tao, H.; Ying, S. M.; Jian, L., Enhancing the electrochemical performance of Li-rich layered oxide $Li_{1.13}Ni_{0.3}Mn_{0.57}O_2$ via WO_3 doping and accompanying spontaneous surface phase formation. *J. Power Sources* **2018,** *375*, 21-28.

159. Liu, J.; Wang, S.; Ding, Z.; Zhou, R.; Xia, Q.; Zhang, J.; Chen, L.; Wei, W.; Wang, P., The Effect of Boron Doping on Structure and Electrochemical Performance of Lithium-Rich Layered Oxide Materials. *ACS Appl. Mater. Interfaces* **2016,** *8* (28), 18008-18017.

160. Guo, B.; Zhao, J.; Fan, X.; Zhang, W.; Li, S.; Yang, Z.; Chen, Z.; Zhang, W., Aluminum and fluorine co-doping for promotion of stability and safety of lithium-rich layered cathode material. *Electrochim. Acta* **2017,** *236*, 171-179.

161. Zheng, J.; Gu, M.; Genc, A.; Xiao, J.; Xu, P.; Chen, X.; Zhu, Z.; Zhao, W.; Pullan, L.; Wang, C.; Zhang, J. G., Mitigating Voltage Fade in Cathode Materials by Improving the Atomic Level Uniformity of Elemental Distribution. *Nano Lett.* **2014,** *14* (5), 2628-2635.

162. Wang, D.; Belharouak, I.; Koenig, G. M.; Zhou, G.; Amine, K., Growth mechanism of $Ni_{0.3}Mn_{0.7}CO_3$ precursor for high capacity Li-ion battery cathodes. *J. Mater. Chem.* **2011,** *21* (25), 9290-9295.

163. Liu, J.; Chen, H.; Xie, J.; Sun, Z.; Wu, N.; Wu, B., Electrochemical performance studies of Li-rich cathode materials with different primary particle sizes. *J. Power Sources* **2014,** *251*, 208-214.

164. Zheng, J. M.; Wu, X. B.; Yang, Y., A comparison of preparation method on the electrochemical performance of cathode material $Li[Li_{0.2}Mn_{0.54}Ni_{0.13}Co_{0.13}]O_2$ for lithium-ion battery. *Electrochim. Acta* **2011,** *56* (8), 3071-3078.

165. Wang, J.; Yuan, G.; Zhang, M.; Qiu, B.; Xia, Y.; Liu, Z., The structure, morphology, and electrochemical properties of $Li_{1+x}Ni_{1/6}Co_{1/6}Mn_{4/6}O_{2.25+x/2}$ ($0.1 \leq x \leq 0.7$) cathode materials. *Electrochim. Acta* **2012,** *66*, 61-66.

166. Liu, S.; Liu, Z.; Shen, X.; Wang, X.; Liao, S.-C.; Yu, R.; Wang, Z.; Hu, Z.; Chen, C.-T.; Yu, X.; Yang, X.; Chen, L., Li–Ti Cation Mixing Enhanced Structural and Performance Stability of Li-Rich Layered Oxide. *Adv. Energy Mater.* **2019,** *9* (32), 1901530.

167. Knight, J. C.; Nandakumar, P.; Kan, W. H.; Manthiram, A., Effect of Ru substitution on the first charge–discharge cycle of lithium-rich layered oxides. *J. Mater. Chem. A* **2015,** *3* (5), 2006-2011.

168. House, R. A.; Jin, L.; Maitra, U.; Tsuruta, K.; Somerville, J. W.; Förstermann, D. P.; Massel, F.; Duda, L.; Roberts, M. R.; Bruce, P. G., Lithium manganese oxyfluoride as a new cathode material exhibiting oxygen redox. *Energy Environ. Sci.* **2018,** *11* (4), 926-932.

169. Saha, S.; Assat, G.; Sougrati, M. T.; Foix, D.; Li, H.; Vergnet, J.; Turi, S.; Ha, Y.; Yang, W.; Cabana, J.; Rousse, G.; Abakumov, A. M.; Tarascon, J.-M., Exploring the bottlenecks of anionic redox in Li-rich layered sulfides. *Nat. Energy* **2019,** *4*, 977-987.

170. Liu, P.; Zhang, H.; He, W.; Xiong, T.; Cheng, Y.; Xie, Q.; Ma, Y.; Zheng, H.; Wang, L.; Zhu, Z.-Z.; Peng, Y.; Mai, L.; Peng, D.-L., Lithium Deficiencies Engineering in Li-Rich Layered Oxide $Li_{1.098}Mn_{0.533}Ni_{0.113}Co_{0.138}O_2$ for High-Stability Cathode. *J. Am. Chem. Soc.* **2019,** *141* (27), 10876-10882.

171. Zhu, Z.; Yu, D.; Yang, Y.; Su, C.; Huang, Y.; Dong, Y.; Waluyo, I.; Wang, B.; Hunt, A.; Yao, X.; Lee, J.; Xue, W.; Li, J., Gradient Li-rich oxide cathode particles immunized against oxygen release by a molten salt treatment. *Nat. Energy* **2019,** *4* (12), 1049-1058.

172. Wu, F.; Li, N.; Su, Y.; Shou, H.; Bao, L.; Yang, W.; Zhang, L.; An, R.; Chen, S., Spinel/Layered Heterostructured Cathode Material for High-Capacity and High-Rate Li-Ion Batteries. *Adv. Mater.* **2013,** *25* (27), 3722-3726.

173. Fu, F.; Xu, G.-L.; Wang, Q.; Deng, Y.-P.; Li, X.; Li, J.-T.; Huang, L.; Sun, S.-G., Synthesis of single crystalline hexagonal nanobricks of $LiNi_{1/3}Co_{1/3}Mn_{1/3}O_2$ with high percentage of exposed {010} active facets as high rate performance cathode material for lithium-ion battery. *J. Mater. Chem. A* **2013,** *1* (12), 3860-3864.

174. Liu, Y.; Wang, J.; Wu, J.; Ding, Z.; Yao, P.; Zhang, S.; Chen, Y., 3D Cube-Maze-Like Li-Rich Layered Cathodes Assembled from 2D Porous Nanosheets for Enhanced Cycle Stability and Rate Capability of Lithium-Ion Batteries. *Adv. Energy Mater.* **2020,** *10* (5), 1903139.

175. Abouimrane, A.; Odom, S. A.; Tavassol, H.; Schulmerich, M. V.; Wu, H.; Bhargava, R.; Gewirth, A. A.; Moore, J. S.; Amine, K., 3-Hexylthiophene as a Stabilizing Additive for High Voltage Cathodes in Lithium-Ion Batteries. *J. Electrochem. Soc.* **2013,** *160* (2), A268-A271.

176. Zhu, Y.; Li, Y.; Bettge, M.; Abraham, D. P., Positive Electrode Passivation by LiDFOB Electrolyte Additive in High-Capacity Lithium-Ion Cells. *J. Electrochem. Soc.* **2012,** *159* (12), A2109-A2117.

177. Tan, S.; Zhang, Z.; Li, Y.; Li, Y.; Zheng, J.; Zhou, Z.; Yang, Y., Tris (hexafluoro-iso-propyl) phosphate as an SEI-Forming Additive on Improving the Electrochemical Performance of the $Li[Li_{0.2}Mn_{0.56}Ni_{0.16}Co_{0.08}]O_2$ Cathode Material. *J. Electrochem. Soc.* **2013,** *160* (2), A285-A292.

178. Zheng, J.; Xiao, J.; Gu, M.; Zuo, P.; Wang, C.; Zhang, J.-G., Interface modifications by anion receptors for high energy lithium ion batteries. *J. Power Sources* **2014,** *250*, 313-318.

179. Li, Z. D.; Zhang, Y. C.; Xiang, H. F.; Ma, X. H.; Yuan, Q. F.; Wang, Q. S.; Chen, C. H., Trimethyl phosphite as an electrolyte additive for high-voltage lithium-ion batteries using lithium-rich layered oxide cathode. *J. Power Sources* **2013,** *240*, 471-475.

180. Zhou, Z.; Ma, Y.; Wang, L.; Zuo, P.; Cheng, X.; Du, C.; Yin, G.; Gao, Y., Triphenyl phosphite as an electrolyte additive to improve the cyclic stability of lithium-rich layered oxide cathode for lithium-ion batteries. *Electrochim. Acta* **2016,** *216*, 44-50.

181. Zhuang, Y.; Du, F.; Zhu, L.; Cao, H.; Dai, H.; Adkins, J.; Zhou, Q.; Zheng, J., Trimethylsilyl (trimethylsiloxy) acetate as a novel electrolyte additive for improvement of electrochemical performance of lithium-rich $Li_{1.2}Ni_{0.2}Mn_{0.6}O_2$ cathode in lithium-ion batteries. *Electrochim. Acta* **2018,** *290*, 220-227.

182. Pires, J.; Castets, A.; Timperman, L.; Santos-Peña, J.; Dumont, E.; Levasseur, S.; Tessier, C.; Dedryvère, R.; Anouti, M., Tris(2,2,2-trifluoroethyl) phosphite as an electrolyte additive for high-voltage lithium-ion batteries using lithium-rich layered oxide cathode. *J. Power Sources* **2015,** *296*, 413-425.

183. Li, J.; Xing, L.; Zhang, R.; Chen, M.; Wang, Z.; Xu, M.; Li, W., Tris(trimethylsilyl)borate as an electrolyte additive for improving interfacial stability of high voltage layered lithium-rich oxide cathode/carbonate-based electrolyte. *J. Power Sources* **2015,** *285*, 360-366.

184. Zhang, J.; Wang, J.; Yang, J.; NuLi, Y., Artificial interface deriving from sacrificial tris (trimethylsilyl) phosphate additive for lithium rich cathode materials. *Electrochim. Acta* **2014,** *117*, 99-104.

185. Lee, S. J.; Han, J.-G.; Park, I.; Song, J.; Cho, J.; Kim, J.-S.; Choi, N.-S., Effect of lithium bis (oxalato) borate additive on electrochemical performance of $Li_{1.17}Ni_{0.17}Mn_{0.5}Co_{0.17}O_2$ cathodes for lithium-ion batteries. *J. Electrochem. Soc.* **2014,** *161* (14), A2012-A2019.

186. Han, J. G.; Park, I.; Cha, J.; Park, S.; Park, S.; Myeong, S.; Cho, W.; Kim, S. S.; Hong, S. Y.; Cho, J., Interfacial Architectures Derived by Lithium Difluoro (bisoxalato) Phosphate for Lithium-Rich Cathodes with Superior Cycling Stability and Rate Capability. *ChemElectroChem* **2017,** *4* (1), 56-65.

187. Hong, P.; Xu, M.; Zheng, X.; Zhu, Y.; Liao, Y.; Xing, L.; Huang, Q.; Wan, H.; Yang, Y.; Li, W., Effect of ethylene glycol bis (propionitrile) ether (EGBE) on the performance and interfacial chemistry of lithium-rich layered oxide cathode. *J. Power Sources* **2016,** *329*, 216-224.

188. Lou, S.; Ma, Y.; Zhou, Z.; Huo, H.; Zuo, P.; Cheng, X.; Qu, X.; Gao, Y.; Du, C.; Yin, G., Unravelling the Enhanced High-Temperature Performance of Lithium-Rich Oxide Cathode with Methyl Diphenylphosphinite as Electrolyte Additive. *ChemElectroChem* **2018,** *5* (12), 1569-1575.

189. Zheng, X.; Wang, X.; Cai, X.; Xing, L.; Xu, M.; Liao, Y.; Li, X.; Li, W., Constructing a Protective Interface Film on Layered Lithium-Rich Cathode Using an Electrolyte Additive with Special Molecule Structure. *ACS Appl. Mater. Interfaces* **2016,** *8* (44), 30116-30125.

190. Li, Y.; Lian, F.; Ma, L.; Liu, C.; Yang, L.; Sun, X.; Chou, K., Fluoroethylene Carbonate as Electrolyte Additive for Improving the electrochemical performances of High-Capacity $Li_{1.16}[Mn_{0.75}Ni_{0.25}]_{0.84}O_2$ Material. *Electrochim. Acta* **2015,** *168*, 261-270.

191. Yang, J.; Li, P.; Zhong, F.; Feng, X.; Chen, W.; Ai, X.; Yang, H.; Xia, D.; Cao, Y., Suppressing Voltage Fading of Li-Rich Oxide Cathode via Building a Well-Protected and

Partially-Protonated Surface by Polyacrylic Acid Binder for Cycle-Stable Li-Ion Batteries. *Adv. Energy Mater.* **2020**, 1904264.

192. Liu, J.; Wang, J.; Ni, Y.; Zhang, Y.; Luo, J.; Cheng, F.; Chen, J., Spinel/Lithium-Rich Manganese Oxide Hybrid Nanofibers as Cathode Materials for Rechargeable Lithium-Ion Batteries. *Small Methods* **2019,** *3* (12), 1900350.

193. Singer, A.; Zhang, M.; Hy, S.; Cela, D.; Fang, C.; Wynn, T. A.; Qiu, B.; Xia, Y.; Liu, Z.; Ulvestad, A.; Hua, N.; Wingert, J.; Liu, H.; Sprung, M.; Zozulya, A. V.; Maxey, E.; Harder, R.; Meng, Y. S.; Shpyrko, O. G., Nucleation of dislocations and their dynamics in layered oxide cathode materials during battery charging. *Nat. Energy* **2018,** *3* (8), 641-647.

194. Ito, A.; Li, D.; Ohsawa, Y.; Sato, Y., A new approach to improve the high-voltage cyclic performance of Li-rich layered cathode material by electrochemical pre-treatment. *J. Power Sources* **2008,** *183* (1), 344-346.

195. Goodenough, J. B.; Park, K.-S., The Li-Ion Rechargeable Battery: A Perspective. *J. Am. Chem. Soc.* **2013,** *135* (4), 1167-1176.

196. Vaalma, C.; Buchholz, D.; Weil, M.; Passerini, S., A cost and resource analysis of sodium-ion batteries. *Nat. Rev. Mater.* **2018,** *3* (4), 18013.

197. Speirs, J.; Contestabile, M.; Houari, Y.; Gross, R., The future of lithium availability for electric vehicle batteries. *Renew. Sust. Energ. Rev.* **2014,** *35*, 183-193.

198. Olivetti, E. A.; Ceder, G.; Gaustad, G. G.; Fu, X., Lithium-Ion Battery Supply Chain Considerations: Analysis of Potential Bottlenecks in Critical Metals. *Joule* **2017,** *1* (2), 229-243.

199. Zubi, G.; Dufo-López, R.; Carvalho, M.; Pasaoglu, G., The lithium-ion battery: State of the art and future perspectives. *Renew. Sust. Energ. Rev.* **2018,** *89*, 292-308.

200. Pramudita, J. C.; Sehrawat, D.; Goonetilleke, D.; Sharma, N., An Initial Review of the Status of Electrode Materials for Potassium-Ion Batteries. *Adv. Energy Mater.* **2017,** *7* (24), 1602911.

201. Zhang, J.; Liu, T.; Cheng, X.; Xia, M.; Zheng, R.; Peng, N.; Yu, H.; Shui, M.; Shu, J., Development status and future prospect of non-aqueous potassium ion batteries for large scale energy storage. *Nano Energy* **2019,** *60*, 340-361.

202. Zhang, W.; Liu, Y.; Guo, Z., Approaching high-performance potassium-ion batteries via advanced design strategies and engineering. *Sci. Adv.* **2019,** *5* (5), eaav7412.

203. Komaba, S.; Hasegawa, T.; Dahbi, M.; Kubota, K., Potassium intercalation into graphite to realize high-voltage/high-power potassium-ion batteries and potassium-ion capacitors. *Electrochem. Commun.* **2015,** *60*, 172-175.

204. Vaalma, C.; Buchholz, D.; Passerini, S., Non-aqueous potassium-ion batteries: a review. *Curr Opin Electrochem* **2018,** *9*, 41-48.

205. Kim, H.; Kim, J. C.; Bianchini, M.; Seo, D.-H.; Rodriguez-Garcia, J.; Ceder, G., Recent Progress and Perspective in Electrode Materials for K-Ion Batteries. *Advanced Energy Materials* **2018,** *8* (9), 1702384.

206. Hosaka, T.; Kubota, K.; Hameed, A. S.; Komaba, S., Research Development on K-Ion Batteries. *Chem. Rev.* **2020,** *120* (14), 6358-6466.

207. Wu, X.; Leonard, D. P.; Ji, X., Emerging Non-Aqueous Potassium-Ion Batteries: Challenges and Opportunities. *Chem. Mater.* **2017,** *29* (12), 5031-5042.

208. Kim, H.; Seo, D.-H.; Kim, J. C.; Bo, S.-H.; Liu, L.; Shi, T.; Ceder, G., Investigation of Potassium Storage in Layered P3-Type $K_{0.5}MnO_2$ Cathode. *Adv. Mater.* **2017,** *29* (37), 1702480.

209. Zhao, S.; Yan, K.; Munroe, P.; Sun, B.; Wang, G., Construction of Hierarchical $K_{1.39}Mn_3O_6$ Spheres via AlF_3 Coating for High-Performance Potassium-Ion Batteries. *Adv. Energy Mater.* **2019,** *9* (10), 1803757.

210. Hwang, J.-Y.; Kim, J.; Yu, T.-Y.; Myung, S.-T.; Sun, Y.-K., Development of P3-$K_{0.69}CrO_2$ as an ultra-high-performance cathode material for K-ion batteries. *Energy Environ. Sci.* **2018,** *11* (10), 2821-2827.

211. Zhang, X.; Yang, Y.; Qu, X.; Wei, Z.; Sun, G.; Zheng, K.; Yu, H.; Du, F., Layered P2-Type $K_{0.44}Ni_{0.22}Mn_{0.78}O_2$ as a High-Performance Cathode for Potassium-Ion Batteries. *Adv. Funct. Mater.* **2019,** *29* (49), 1905679.

212. Xue, L.; Li, Y.; Gao, H.; Zhou, W.; Lü, X.; Kaveevivitchai, W.; Manthiram, A.; Goodenough, J. B., Low-Cost High-Energy Potassium Cathode. *J. Am. Chem. Soc.* **2017,** *139* (6), 2164-2167.

213. Su, D.; McDonagh, A.; Qiao, S.-Z.; Wang, G., High-Capacity Aqueous Potassium-Ion Batteries for Large-Scale Energy Storage. *Adv. Mater.* **2017,** *29* (1), 1604007.

214. Huang, B.; Liu, Y.; Lu, Z.; Shen, M.; Zhou, J.; Ren, J.; Li, X.; Liao, S., Prussian Blue [$K_2FeFe(CN)_6$] Doped with Nickel as a Superior Cathode: An Efficient Strategy To Enhance Potassium Storage Performance. *ACS Sustain. Chem. Eng.* **2019,** *7* (19), 16659-16667.

215. Park, W. B.; Han, S. C.; Park, C.; Hong, S. U.; Han, U.; Singh, S. P.; Jung, Y. H.; Ahn, D.; Sohn, K.-S.; Pyo, M., KVP_2O_7 as a Robust High-Energy Cathode for Potassium-Ion Batteries: Pinpointed by a Full Screening of the Inorganic Registry under Specific Search Conditions. *Adv. Energy Mater.* **2018,** *8* (13), 1703099.

216. Kim, H.; Seo, D.-H.; Bianchini, M.; Clément, R. J.; Kim, H.; Kim, J. C.; Tian, Y.; Shi, T.; Yoon, W.-S.; Ceder, G., A New Strategy for High-Voltage Cathodes for K-Ion Batteries: Stoichiometric $KVPO_4F$. *Adv. Energy Mater.* **2018,** *8* (26), 1801591.

217. Lin, X.; Huang, J.; Tan, H.; Huang, J.; Zhang, B., $K_3V_2(PO_4)_2F_3$ as a robust cathode for potassium-ion batteries. *Energy Stor. Mater.* **2019,** *16*, 97-101.

218. Tian, B.; Zheng, J.; Zhao, C.; Liu, C.; Su, C.; Tang, W.; Li, X.; Ning, G.-H., Carbonyl-based polyimide and polyquinoneimide for potassium-ion batteries. *J. Mater. Chem. A* **2019,** *7* (16), 9997-10003.

219. Chen, Y.; Luo, W.; Carter, M.; Zhou, L.; Dai, J.; Fu, K.; Lacey, S.; Li, T.; Wan, J.; Han, X.; Bao, Y.; Hu, L., Organic electrode for non-aqueous potassium-ion batteries. *Nano Energy* **2015,** *18*, 205-211.

220. Tang, M.; Wu, Y.; Chen, Y.; Jiang, C.; Zhu, S.; Zhuo, S.; Wang, C., An organic cathode with high capacities for fast-charge potassium-ion batteries. *J. Mater. Chem. A* **2019,** *7* (2), 486-492.

221. He, G.; Nazar, L. F., Crystallite Size Control of Prussian White Analogues for Nonaqueous Potassium-Ion Batteries. *ACS Energy Lett.* **2017,** *2* (5), 1122-1127.

222. Vaalma, C.; Giffin, G. A.; Buchholz, D.; Passerini, S., Non-Aqueous K-Ion Battery Based on Layered $K_{0.3}MnO_2$ and Hard Carbon/Carbon Black. *J. Electrochem. Soc.* **2016,** *163* (7), A1295-A1299.

223. Deng, L.; Niu, X.; Ma, G.; Yang, Z.; Zeng, L.; Zhu, Y.; Guo, L., Layered Potassium Vanadate $K_{0.5}V_2O_5$ as a Cathode Material for Nonaqueous Potassium Ion Batteries. *Adv. Funct. Mater.* **2018,** *28* (49), 1800670.

224. Jian, Z.; Liang, Y.; Rodríguez-Pérez, I. A.; Yao, Y.; Ji, X., Poly(anthraquinonyl sulfide) cathode for potassium-ion batteries. *Electrochem. Commun.* **2016,** *71*, 5-8.

225. Xing, Z.; Jian, Z.; Luo, W.; Qi, Y.; Bommier, C.; Chong, E. S.; Li, Z.; Hu, L.; Ji, X., A perylene anhydride crystal as a reversible electrode for K-ion batteries. *Energy Stor. Mater.* **2016,** *2*, 63-68.

226. Deng, T.; Fan, X.; Luo, C.; Chen, J.; Chen, L.; Hou, S.; Eidson, N.; Zhou, X.; Wang, C., Self-Templated Formation of P2-type $K_{0.6}CoO_2$ Microspheres for High Reversible Potassium-Ion Batteries. *Nano Lett.* **2018,** *18* (2), 1522-1529.

227. Shadike, Z.; Shi, D.-R.; Tian, W.; Cao, M.-H.; Yang, S.-F.; Chen, J.; Fu, Z.-W., Long life and high-rate Berlin green $FeFe(CN)_6$ cathode material for a non-aqueous potassium-ion battery. *J. Mater. Chem. A* **2017,** *5* (14), 6393-6398.

228. Zhang, L.; Zhang, B.; Wang, C.; Dou, Y.; Zhang, Q.; Liu, Y.; Gao, H.; Al-Mamun, M.; Pang, W. K.; Guo, Z.; Dou, S. X.; Liu, H. K., Constructing the best symmetric full K-ion battery with the NASICON-type $K_3V_2(PO_4)_3$. *Nano Energy* **2019,** *60*, 432-439.

229. Zhao, Q.; Wang, J.; Lu, Y.; Li, Y.; Liang, G.; Chen, J., Oxocarbon Salts for Fast Rechargeable Batteries. *Angew. Chem. Int. Ed.* **2016,** *55* (40), 12528-12532.

230. Masese, T.; Yoshii, K.; Yamaguchi, Y.; Okumura, T.; Huang, Z.-D.; Kato, M.; Kubota, K.; Furutani, J.; Orikasa, Y.; Senoh, H.; Sakaebe, H.; Shikano, M., Rechargeable potassium-ion batteries with honeycomb-layered tellurates as high voltage cathodes and fast potassium-ion conductors. *Nat. Commun.* **2018,** *9* (1), 3823.

231. Qian, J.; Wu, C.; Cao, Y.; Ma, Z.; Huang, Y.; Ai, X.; Yang, H., Prussian Blue Cathode Materials for Sodium-Ion Batteries and Other Ion Batteries. *Adv. Energy Mater.* **2018,** *8* (17), 1702619.

232. Wu, X.; Jian, Z.; Li, Z.; Ji, X., Prussian white analogues as promising cathode for non-aqueous potassium-ion batteries. *Electrochem. Commun.* **2017,** *77*, 54-57.

233. Xiao, P.; Song, J.; Wang, L.; Goodenough, J. B.; Henkelman, G., Theoretical Study of the Structural Evolution of a $Na_2FeMn(CN)_6$ Cathode upon Na Intercalation. *Chem. Mater.* **2015,** *27* (10), 3763-3768.

234. Wang, L.; Song, J.; Qiao, R.; Wray, L. A.; Hossain, M. A.; Chuang, Y.-D.; Yang, W.; Lu, Y.; Evans, D.; Lee, J.-J.; Vail, S.; Zhao, X.; Nishijima, M.; Kakimoto, S.; Goodenough, J. B., Rhombohedral Prussian White as Cathode for Rechargeable Sodium-Ion Batteries. *J. Am. Chem. Soc.* **2015,** *137* (7), 2548-2554.

235. Bie, X.; Kubota, K.; Hosaka, T.; Chihara, K.; Komaba, S., A novel K-ion battery: hexacyanoferrate(ii)/graphite cell. *J. Mater. Chem. A* **2017,** *5* (9), 4325-4330.

236. Song, J.; Wang, L.; Lu, Y.; Liu, J.; Guo, B.; Xiao, P.; Lee, J.-J.; Yang, X.-Q.; Henkelman, G.; Goodenough, J. B., Removal of Interstitial H_2O in Hexacyanometallates for a Superior Cathode of a Sodium-Ion Battery. *J. Am. Chem. Soc.* **2015,** *137* (7), 2658-2664.

237. Ling, C.; Chen, J.; Mizuno, F., First-Principles Study of Alkali and Alkaline Earth Ion Intercalation in Iron Hexacyanoferrate: The Important Role of Ionic Radius. *J. Phys. Chem. C* **2013,** *117* (41), 21158-21165.

238. Xue, L.; Gao, H.; Zhou, W.; Xin, S.; Park, K.; Li, Y.; Goodenough, J. B., Liquid K–Na Alloy Anode Enables Dendrite-Free Potassium Batteries. *Adv. Mater.* **2016,** *28* (43), 9608-9612.

239. Ren, W.; Qin, M.; Zhu, Z.; Yan, M.; Li, Q.; Zhang, L.; Liu, D.; Mai, L., Activation of Sodium Storage Sites in Prussian Blue Analogues via Surface Etching. *Nano Lett.* **2017,** *17* (8), 4713-4718.

240. Wang, R. Y.; Wessells, C. D.; Huggins, R. A.; Cui, Y., Highly Reversible Open Framework Nanoscale Electrodes for Divalent Ion Batteries. *Nano Lett.* **2013,** *13* (11), 5748-5752.

241. Imanishi, N.; Morikawa, T.; Kondo, J.; Yamane, R.; Takeda, Y.; Yamamoto, O.; Sakaebe, H.; Tabuchi, M., Lithium intercalation behavior of iron cyanometallates. *J. Power Sources* **1999,** *81-82*, 530-534.

242. Asakura, D.; Li, C. H.; Mizuno, Y.; Okubo, M.; Zhou, H.; Talham, D. R., Bimetallic Cyanide-Bridged Coordination Polymers as Lithium Ion Cathode Materials: Core@Shell Nanoparticles with Enhanced Cyclability. *J. Am. Chem. Soc.* **2013,** *135* (7), 2793-2799.

243. Zhou, A.; Cheng, W.; Wang, W.; Zhao, Q.; Xie, J.; Zhang, W.; Gao, H.; Xue, L.; Li, J., Hexacyanoferrate-Type Prussian Blue Analogs: Principles and Advances Toward High-Performance Sodium and Potassium Ion Batteries. *Adv. Energy Mater.* **2020,** *30* (13), 1909192.

244. Eftekhari, A., Potassium secondary cell based on Prussian blue cathode. *J. Power Sources* **2004,** *126* (1), 221-228.

245. You, Y.; Wu, X.-L.; Yin, Y.-X.; Guo, Y.-G., High-quality Prussian blue crystals as superior cathode materials for room-temperature sodium-ion batteries. *Energy Environ. Sci.* **2014,** *7* (5), 1643-1647.

246. Liu, Z.; Su, H.; Yang, Y.; Wu, T.; Sun, S.; Yu, H., Advances and perspectives on transitional metal layered oxides for potassium-ion battery. *Energy Stor. Mater.* **2021,** *34*, 211-228.

247. Kim, H.; Seo, D.-H.; Urban, A.; Lee, J.; Kwon, D.-H.; Bo, S.-H.; Shi, T.; Papp, J. K.; McCloskey, B. D.; Ceder, G., Stoichiometric Layered Potassium Transition Metal Oxide for Rechargeable Potassium Batteries. *Chem. Mater.* **2018,** *30* (18), 6532-6539.

248. Deng, T.; Fan, X.; Luo, C.; Chen, J.; Chen, L.; Hou, S.; Eidson, N.; Zhou, X.; Wang, C., Self-Templated Formation of P2-type $K_{0.6}CoO_2$ Microspheres for High Reversible Potassium-Ion Batteries. *Nano Lett* **2018,** *18* (2), 1522-1529.

249. Kim, H.; Kim, J. C.; Bo, S. H.; Shi, T.; Kwon, D. H.; Ceder, G., K-Ion Batteries Based on a P2-Type $K_{0.6}CoO_2$ Cathode. *Adv. Energy Mater.* **2017,** *7* (17), 1700098.

250. Deng, T.; Fan, X.; Chen, J.; Chen, L.; Luo, C.; Zhou, X.; Yang, J.; Zheng, S.; Wang, C., Layered P2-Type $K_{0.65}Fe_{0.5}Mn_{0.5}O_2$ Microspheres as Superior Cathode for High-Energy Potassium-Ion Batteries. *Adv. Funct. Mater.* **2018,** *28* (28), 1800219.

251. Zhao, Z.; Liu, H.; Gao, W.; Xue, W.; Liu, Z.; Huang, J.; Pan, X.; Huang, Y., Surface-Engineered PtNi-O Nanostructure with Record-High Performance for Electrocatalytic Hydrogen Evolution Reaction. *J. Am. Chem. Soc.* **2018,** *140* (29), 9046-9050.

252. Yang, J.; Ju, Z.; Jiang, Y.; Xing, Z.; Xi, B.; Feng, J.; Xiong, S., Enhanced Capacity and Rate Capability of Nitrogen/Oxygen Dual-Doped Hard Carbon in Capacitive Potassium-Ion Storage. *Adv. Mater.* **2018,** *30* (4), 1700104.

253. Wu, X.; Chen, Y.; Xing, Z.; Lam, C. W. K.; Pang, S.-S.; Zhang, W.; Ju, Z., Advanced Carbon-Based Anodes for Potassium-Ion Batteries. *Adv. Energy Mater.* **2019,** *9* (21), 1900343.

254. Fan, L.; Ma, R.; Zhang, Q.; Jia, X.; Lu, B., Graphite Anode for a Potassium-Ion Battery with Unprecedented Performance. *Angew. Chem. Int. Ed.* **2019,** *58* (31), 10500-10505.

255. Jian, Z.; Luo, W.; Ji, X., Carbon electrodes for K-ion batteries. *J. Am. Chem. Soc.* **2015,** *137* (36), 11566-11569.

256. Luo, W.; Wan, J.; Ozdemir, B.; Bao, W.; Chen, Y.; Dai, J.; Lin, H.; Xu, Y.; Gu, F.; Barone, V., Potassium Ion Batteries with Graphitic Materials. *Nano Lett.* **2015,** *15* (11), 7671-7677.

257. Jian, Z.; Xing, Z.; Bommier, C.; Li, Z.; Ji, X., Hard Carbon Microspheres: Potassium-Ion Anode Versus Sodium-Ion Anode. *Adv. Energy Mater.* **2016,** *6* (3), 1501874.

258. Qian, Y.; Jiang, S.; Li, Y.; Yi, Z.; Zhou, J.; Li, T.; Han, Y.; Wang, Y.; Tian, J.; Lin, N.; Qian, Y., *In Situ* Revealing the Electroactivity of P-O and P-C Bonds in Hard Carbon for High-Capacity and Long-Life Li/K-Ion Batteries. *Adv. Energy Mater.* **2019,** *9* (34), 1901676.

259. Chen, J.; Yang, B.; Hou, H.; Li, H.; Liu, L.; Zhang, L.; Yan, X., Disordered, Large Interlayer Spacing, and Oxygen-Rich Carbon Nanosheets for Potassium Ion Hybrid Capacitor. *Adv. Energy Mater.* **2019,** *9* (19), 1803894.

260. Chen, M.; Wang, W.; Liang, X.; Gong, S.; Liu, J.; Wang, Q.; Guo, S.; Yang, H., Sulfur/Oxygen Codoped Porous Hard Carbon Microspheres for High-Performance Potassium-Ion Batteries. *Adv. Energy Mater.* **2018,** *8* (19), 1800171.

261. Liu, Y.; Lu, Y.-X.; Xu, Y.-S.; Meng, Q.-S.; Gao, J.-C.; Sun, Y.-G.; Hu, Y.-S.; Chang, B.-B.; Liu, C.-T.; Cao, A.-M., Pitch-Derived Soft Carbon as Stable Anode Material for Potassium Ion Batteries. *Adv. Mater.* **2020,** *32* (17), 2000505.

262. Ge, J.; Fan, L.; Wang, J.; Zhang, Q.; Liu, Z.; Zhang, E.; Liu, Q.; Yu, X.; Lu, B., $MoSe_2$/N-Doped Carbon as Anodes for Potassium-Ion Batteries. *Adv. Energy Mater.* **2018,** *8* (29), 1801477.

263. Wang, W.; Jiang, B.; Qian, C.; Lv, F.; Feng, J.; Zhou, J.; Wang, K.; Yang, C.; Yang, Y.; Guo, S., Pistachio-Shuck-Like $MoSe_2$/C Core/Shell Nanostructures for High-Performance Potassium-Ion Storage. *Adv. Mater.* **2018,** *30* (30), e1801812.

264. Huang, H.; Cui, J.; Liu, G.; Bi, R.; Zhang, L., Carbon-Coated $MoSe_2$/MXene Hybrid Nanosheets for Superior Potassium Storage. *ACS Nano* **2019,** *13* (3), 3448-3456.

265. Sultana, I.; Rahman, M. M.; Mateti, S.; Ahmadabadi, V. G.; Glushenkov, A. M.; Chen, Y., K-ion and Na-ion storage performances of Co_3O_4–Fe_2O_3 nanoparticle-decorated super P carbon black prepared by a ball milling process. *Nanoscale* **2017,** *9* (10), 3646-3654.

266. Liu, Y.; Tai, Z.; Zhang, J.; Pang, W. K.; Zhang, Q.; Feng, H.; Konstantinov, K.; Guo, Z.; Liu, H. K., Boosting potassium-ion batteries by few-layered composite anodes prepared via solution-triggered one-step shear exfoliation. *Nat. Commun.* **2018,** *9* (1), 3645.

267. Hwang, J.-Y.; Myung, S.-T.; Sun, Y.-K., Recent Progress in Rechargeable Potassium Batteries. *Adv. Funct. Mater.* **2018,** *28* (43), 1802938.

268. Zheng, J.; Yang, Y.; Fan, X.; Ji, G.; Ji, X.; Wang, H.; Hou, S.; Zachariah, M. R.; Wang, C., Extremely stable antimony–carbon composite anodes for potassium-ion batteries. *Energy Environ. Sci.* **2019,** *12* (2), 615-623.

269. Xiong, P.; Wu, J.; Zhou, M.; Xu, Y., Bismuth–Antimony Alloy Nanoparticle@Porous Carbon Nanosheet Composite Anode for High-Performance Potassium-Ion Batteries. *ACS Nano* **2020,** *14* (1), 1018-1026.

270. Chen, K.-T.; Tuan, H.-Y., Bi–Sb Nanocrystals Embedded in Phosphorus as High-Performance Potassium Ion Battery Electrodes. *ACS Nano* **2020,** *14* (9), 11648-11661.

271. Wu, Y.; Huang, H.-B.; Feng, Y.; Wu, Z.-S.; Yu, Y., The Promise and Challenge of Phosphorus-Based Composites as Anode Materials for Potassium-Ion Batteries. *Adv. Mater.* **2019,** *31* (50), 1901414.

272. Zhang, W.; Mao, J.; Li, S.; Chen, Z.; Guo, Z., Phosphorus-Based Alloy Materials for Advanced Potassium-ion Battery Anode. *J. Am. Chem. Soc.* **2017,** *139* (9), 3316-3319.

273. Obama, B., The Irreversible Momentum of Clean Energy. *Science* **2017,** *355* (631), 127-129.

274. Shafizadeh, F., Alternative Energy Sources. *Science* **1980,** *209* (4459), 917-917.

275. Tarascon, J. M.; Armand, M., Issues and Challenges Facing Rechargeable Lithium Batteries. *Nature* **2001,** *414* (6861), 359-367.

276. Bruce, P. G.; Scrosati, B.; Tarascon, J.-M., Nanomaterials for Rechargeable Lithium Batteries. *Angew. Chem. Int. Ed.* **2008,** *47* (16), 2930-2946.

277. Kittner, N.; Lill, F.; Kammen, D. M., Energy Storage Deployment and Innovation for the Clean Energy Transition. *Nat. Energy* **2017,** *2* (9), 17125.

278. Armand, M.; Tarascon, J. M., Building Better Batteries. *Nature* **2008,** *451* (7179), 652-657.

279. Evarts, E. C., Lithium Batteries To the Limits of Lithium. *Nature* **2015,** *526* (7575), S93-S95.

280. Tang, W.; Liu, L. L.; Tian, S.; Li, L.; Yue, Y. B.; Wu, Y. P.; Guan, S. Y.; Zhu, K., Nano-$LiCoO_2$ as Cathode Material of Large Capacity and High Rate Capability for Aqueous Rechargeable Lithium Batteries. *Electrochem. Commun.* **2010,** *12* (11), 1524-1526.

281. Cho, J.; Kim, T. J.; Kim, J.; Noh, M.; Park, B., Synthesis, Thermal, and Electrochemical Properties of $AlPO_4$-Coated $LiNi_{0.8}Co_{0.1}Mn_{0.1}O_2$ Cathode Materials for a Li-Ion Cell. *J. Electrochem. Soc.* **2004,** *151* (11), A1899-A1904.

282. Reddy, M. V.; Rao, G. V. S.; Chowdari, B. V. R., Metal Oxides and Oxysalts as Anode Materials for Li Ion Batteries. *Chem. Rev.* **2013,** *113* (7), 5364-5457.

283. Yan, K.; Sun, B.; Munroe, P.; Wang, G., Three-Dimensional Pie-Like Current Collectors for Dendrite-Free Lithium Metal Anodes. *Energy Stor. Mater.* **2018,** *11*, 127-133.

284. Yu, H.; Zhou, H., High-Energy Cathode Materials (Li_2MnO_3–$LiMO_2$) for Lithium-Ion Batteries. *J. Phys. Chem. Lett.* **2013,** *4* (8), 1268-1280.

285. Yabuuchi, N.; Yoshii, K.; Myung, S.-T.; Nakai, I.; Komaba, S., Detailed Studies of a High-Capacity Electrode Material for Rechargeable Batteries, Li_2MnO_3−$LiCo_{1/3}Ni_{1/3}Mn_{1/3}O_2$. *J. Am. Chem. Soc.* **2011,** *133* (12), 4404-4419.

286. Yu, X.; Lyu, Y.; Gu, L.; Wu, H.; Bak, S.-M.; Zhou, Y.; Amine, K.; Ehrlich, S. N.; Li, H.; Nam, K.-W.; Yang, X.-Q., Understanding the Rate Capability of High-Energy-Density Li-Rich Layered $Li_{1.2}Ni_{0.15}Co_{0.1}Mn_{0.55}O_2$ Cathode Materials. *Adv. Energy. Mater.* **2014,** *4* (5), 1300950.

287. Xu, J.; Dou, S.; Liu, H.; Dai, L., Cathode Materials for Next Generation Lithium Ion Batteries. *Nano Energy* **2013,** *2* (4), 439-442.

288. Assat, G.; Foix, D.; Delacourt, C.; Iadecola, A.; Dedryvère, R.; Tarascon, J.-M., Fundamental Interplay Between Anionic/Cationic Redox Governing the Kinetics and Thermodynamics of Lithium-Rich Cathodes. *Nat. Commun.* **2017,** *8* (1), 2219.

289. Sathiya, M.; Abakumov, A. M.; Foix, D.; Rousse, G.; Ramesha, K.; Saubanère, M.; Doublet, M. L.; Vezin, H.; Laisa, C. P.; Prakash, A. S.; Gonbeau, D.; VanTendeloo, G.; Tarascon, J. M., Origin of Voltage Decay in High-Capacity Layered Oxide Electrodes. *Nat. Mater.* **2014,** *14* (2), 230-238.

290. Zheng, J.; Gu, M.; Xiao, J.; Zuo, P.; Wang, C.; Zhang, J.-G., Corrosion/Fragmentation of Layered Composite Cathode and Related Capacity/Voltage Fading during Cycling Process. *Nano Lett.* **2013,** *13* (8), 3824-3830.

291. Xiao, B.; Liu, H.; Liu, J.; Sun, Q.; Wang, B.; Kaliyappan, K.; Zhao, Y.; Banis, M. N.; Liu, Y.; Li, R.; Sham, T.-K.; Botton, G. A.; Cai, M.; Sun, X., Nanoscale Manipulation of Spinel Lithium Nickel Manganese Oxide Surface by Multisite Ti Occupation as High-Performance Cathode. *Adv. Mater.* **2017,** *29* (47), 1703764.

292. Liu, W.; Li, X.; Xiong, D.; Hao, Y.; Li, J.; Kou, H.; Yan, B.; Li, D.; Lu, S.; Koo, A.; Adair, K.; Sun, X., Significantly Improving Cycling Performance of Cathodes in Lithium Ion Batteries: The Effect of Al_2O_3 and $LiAlO_2$ Coatings on $LiNi_{0.6}Co_{0.2}Mn_{0.2}O_2$. *Nano Energy* **2018,** *44*, 111-120.

293. Zheng, J.; Gu, M.; Xiao, J.; Polzin, B. J.; Yan, P.; Chen, X.; Wang, C.; Zhang, J.-G., Functioning Mechanism of AlF_3 Coating on the Li- and Mn-Rich Cathode Materials. *Chem. Mater.* **2014,** *26* (22), 6320-6327.

294. Deng, S.; Xiao, B.; Wang, B.; Li, X.; Kaliyappan, K.; Zhao, Y.; Lushington, A.; Li, R.; Sham, T.-K.; Wang, H.; Sun, X., New Insight into Atomic-Scale Engineering of Electrode Surface for Long-Life and Safe High Voltage Lithium Ion Cathodes. *Nano Energy* **2017,** *38*, 19-27.

295. Chen, D.; Zheng, F.; Li, L.; Chen, M.; Zhong, X.; Li, W.; Lu, L., Effect of Li_3PO_4 Coating of Layered Lithium-Rich Oxide on Electrochemical Performance. *J. Power Sources* **2017,** *341*, 147-155.

296. Zheng, F.; Yang, C.; Xiong, X.; Xiong, J.; Hu, R.; Chen, Y.; Liu, M., Nanoscale Surface Modification of Lithium-Rich Layered-Oxide Composite Cathodes for Suppressing Voltage Fade. *Angew. Chem. Int. Ed.* **2015,** *54* (44), 13058-13062.

297. Bian, X.; Fu, Q.; Qiu, H.; Du, F.; Gao, Y.; Zhang, L.; Zou, B.; Chen, G.; Wei, Y., High-Performance $Li(Li_{0.18}Ni_{0.15}Co_{0.15}Mn_{0.52})O_2@Li_4M_5O_{12}$ Heterostructured Cathode Material Coated with a Lithium Borate Oxide Glass Layer. *Chem. Mater.* **2015,** *27* (16), 5745-5754.

298. Bian, X.; Fu, Q.; Pang, Q.; Gao, Y.; Wei, Y.; Zou, B.; Du, F.; Chen, G., Multi-Functional Surface Engineering for Li-Excess Layered Cathode Material Targeting Excellent Electrochemical and Thermal Safety Properties. *ACS Appl. Mater. Interfaces* **2016,** *8* (5), 3308-3318.

299. Xie, J.; Sendek, A. D.; Cubuk, E. D.; Zhang, X.; Lu, Z.; Gong, Y.; Wu, T.; Shi, F.; Liu, W.; Reed, E. J.; Cui, Y., Atomic Layer Deposition of Stable $LiAlF_4$ Lithium Ion Conductive Interfacial Layer for Stable Cathode Cycling. *ACS Nano* **2017,** *11* (7), 7019-7027.

300. Koga, H.; Croguennec, L.; Ménétrier, M.; Mannessiez, P.; Weill, F.; Delmas, C., Different Oxygen Redox Participation for Bulk and Surface: A Possible Global Explanation for the Cycling Mechanism of $Li_{1.20}Mn_{0.54}Co_{0.13}Ni_{0.13}O_2$. *J. Power Sources* **2013,** *236*, 250-258.

301. Li, G. R.; Feng, X.; Ding, Y.; Ye, S. H.; Gao, X. P., AlF_3-Coated $Li(Li_{0.17}Ni_{0.25}Mn_{0.58})O_2$ as Cathode Material for Li-Ion Batteries. *Electrochim. Acta* **2012,** *78*, 308-315.

302. Luo, K.; Roberts, M. R.; Hao, R.; Guerrini, N.; Liberti, E.; Allen, C. S.; Kirkland, A. I.; Bruce, P. G., One-Pot Synthesis of Lithium-Rich Cathode Material with Hierarchical Morphology. *Nano Lett.* **2016,** *16* (12), 7503-7508.

303. Assat, G.; Tarascon, J.-M., Fundamental Understanding and Practical Challenges of Anionic Redox Activity in Li-Ion Batteries. *Nat. Energy* **2018,** *3*, 373–386.

304. Li, X.; Qiao, Y.; Guo, S.; Xu, Z.; Zhu, H.; Zhang, X.; Yuan, Y.; He, P.; Ishida, M.; Zhou, H., Direct Visualization of the Reversible O^{2-}/O^{-} Redox Process in Li-Rich Cathode Materials. *Adv. Mater.* **2018,** *30* (14), 1705197.

305. Pearce, P. E.; Perez, A. J.; Rousse, G.; Saubanère, M.; Batuk, D.; Foix, D.; McCalla, E.; Abakumov, A. M.; Van Tendeloo, G.; Doublet, M.-L.; Tarascon, J.-M., Evidence for Anionic Redox Activity in a Tridimensional-Ordered Li-Rich Positive Electrode β-Li_2IrO_3. *Nat. Mater.* **2017,** *16* (5), 580-586.

306. Dedryvère, R.; Laruelle, S.; Grugeon, S.; Gireaud, L.; Tarascon, J. M.; Gonbeau, D., XPS Identification of the Organic and Inorganic Components of the Electrode/Electrolyte Interface Formed on a Metallic Cathode. *J. Electrochem. Soc.* **2005,** *152* (4), A689-A696.

307. Luo, D.; Li, G.; Fu, C.; Zheng, J.; Fan, J.; Li, Q.; Li, L., A New Spinel-Layered Li-Rich Microsphere as a High-Rate Cathode Material for Li-Ion Batteries. *Adv. Energy. Mater.* **2014,** *4* (11), 1400062.

308. Zheng, J.; Myeong, S.; Cho, W.; Yan, P.; Xiao, J.; Wang, C.; Cho, J.; Zhang, J.-G., Li- and Mn-Rich Cathode Materials: Challenges to Commercialization. *Adv. Energy. Mater.* **2017,** *7* (6), 1601284.

309. Armstrong, A. R.; Holzapfel, M.; Novak, P.; Johnson, C. S.; Kang, S. H.; Thackeray, M. M.; Bruce, P. G., Demonstrating Oxygen Loss and Associated Structural Reorganization in the Lithium Battery Cathode $Li[Ni_{0.2}Li_{0.2}Mn_{0.6}]O_2$. *J. Am. Chem. Soc.* **2006,** *128* (26), 8694-8698.

310. Zuo, Y.; Li, B.; Jiang, N.; Chu, W.; Zhang, H.; Zou, R.; Xia, D., A High-Capacity O2-Type Li-Rich Cathode Material with a Single-Layer Li_2MnO_3 Superstructure. *Adv. Mater.* **2018,** *30* (16), 1707255.

311. Lee, J.; Kitchaev, D. A.; Kwon, D.-H.; Lee, C.-W.; Papp, J. K.; Liu, Y.-S.; Lun, Z.; Clément, R. J.; Shi, T.; McCloskey, B. D.; Guo, J.; Balasubramanian, M.; Ceder, G., Reversible Mn^{2+}/Mn^{4+} Double Redox in Lithium-Excess Cathode Materials. *Nature* **2018,** *556* (7700), 185-190.

312. Qiu, B.; Wang, J.; Xia, Y.; Wei, Z.; Han, S.; Liu, Z., Enhanced Electrochemical Performance with Surface Coating by Reactive Magnetron Sputtering on Lithium-Rich Layered Oxide Electrodes. *ACS Appl. Mater. Interfaces* **2014,** *6* (12), 9185-9193.

313. Wang, G.; Wang, X.; Yi, L.; Wang, L.; Yu, R.; Liu, M.; Wang, D.; Ren, Q.; Yang, X., The Effects of $LiTi_2(PO_4)_3$ Modification on the Performance of Spherical $Li_{1.5}Ni_{0.25}Mn_{0.75}O_{2+\delta}$ Cathode Material. *RSC Adv.* **2016,** *6* (52), 46325-46335.

314. Li, B.; Wang, J.; Cao, Z.; Zhang, P.; Zhao, J., The Role of SnO_2 Surface Coating in the Electrochemical Performance of $Li_{1.2}Mn_{0.54}Co_{0.13}Ni_{0.13}O_2$ Cathode Materials. *J. Power Sources* **2016,** *325*, 84-90.

315. Perez, A. J.; Beer, R.; Lin, Z.; Salager, E.; Taberna, P.-L.; Abakumov, A. M.; Simon, P.; Tarascon, J.-M., Proton Ion Exchange Reaction in Li_3IrO_4: A Way to New $H_{3+x}IrO_4$ Phases Electrochemically Active in Both Aqueous and Nonaqueous Electrolytes. *Adv. Energy. Mater.* **2018,** *8*, 1702855.

316. Kretschmer, K.; Sun, B.; Xie, X.; Chen, S.; Wang, G., A Free-Standing $LiFePO_4$–Carbon Paper Hybrid Cathode for Flexible Lithium-Ion Batteries. *Green Chem.* **2016,** *18* (9), 2691-2698.

317. Goodenough, J. B.; Park, K. S., The Li-Ion Rechargeable Battery: A Perspective. *J. Am. Chem. Soc.* **2013,** *135* (4), 1167-1176.

318. Jian, Z.; Luo, W.; Ji, X., Carbon Electrodes for K-Ion Batteries. *J. Am. Chem. Soc.* **2015,** *137* (36), 11566-11569.

319. Luo, W.; Wan, J.; Ozdemir, B.; Bao, W.; Chen, Y.; Dai, J.; Lin, H.; Xu, Y.; Gu, F.; Barone, V., Potassium Ion Batteries with Graphitic Materials. *Nano Lett.* **2015,** *15* (11), 7671-7677.

320. Pramudita, J. C.; Sehrawat, D.; Goonetilleke, D.; Sharma, N., An Initial Review of the Status of Electrode Materials for Potassium-Ion Batteries. *Adv. Energy Mater.* **2017,** *7* (24), 1602911.

321. Ge, J.; Fan, L.; Wang, J.; Zhang, Q.; Liu, Z.; Zhang, E.; Liu, Q.; Yu, X.; Lu, B., $MoSe_2$/N-Doped Carbon as Anodes for Potassium-Ion Batteries. *Adv. Energy Mater.* **2018**, *8* (29), 1801477.

322. Xu, Y.; Zhang, C.; Zhou, M.; Fu, Q.; Zhao, C.; Wu, M.; Lei, Y., Highly nitrogen doped carbon nanofibers with superior rate capability and cyclability for potassium ion batteries. *Nat. Commun.* **2018,** *9* (1), 1720.

323. Liu, L.; Chen, Y.; Xie, Y.; Tao, P.; Li, Q.; Yan, C., Understanding of the Ultrastable K-Ion Storage of Carbonaceous Anode. *Adv. Funct. Mater.* **2018,** *28* (29), 1801989.

324. Deng, L.; Yang, Z.; Tan, L.; Zeng, L.; Zhu, Y.; Guo, L., Investigation of the Prussian Blue Analog $Co_3[Co(CN)_6]_2$ as an Anode Material for Nonaqueous Potassium-Ion Batteries. *Adv. Mater.* **2018,** *30* (31), e1802510.

325. Wang, W.; Jiang, B.; Qian, C.; Lv, F.; Feng, J.; Zhou, J.; Wang, K.; Yang, C.; Yang, Y.; Guo, S., Pistachio-Shuck-Like $MoSe_2$/C Core/Shell Nanostructures for High-Performance Potassium-Ion Storage. *Adv. Mater.* **2018,** *30* (30), e1801812.

326. Xing, Z.; Jian, Z.; Luo, W.; Qi, Y.; Bommier, C.; Chong, E. S.; Li, Z.; Hu, L.; Ji, X., A perylene anhydride crystal as a reversible electrode for K-ion batteries. *Energy Stor. Mater.* **2016,** *2*, 63-68.

327. Zhang, W.; Mao, J.; Li, S.; Chen, Z.; Guo, Z., Phosphorus-Based Alloy Materials for Advanced Potassium-ion Battery Anode. *J. Am. Chem. Soc.* **2017,** *139* (9), 3316-3319.

328. Zhang, Q.; Wang, Z.; Zhang, S.; Zhou, T.; Mao, J.; Guo, Z., Cathode Materials for Potassium-Ion Batteries: Current Status and Perspective. *Electrochem. Energy Rev.* **2018,** 1, 1-34.

329. Mizushima, K.; Jones, P.; Wiseman, P.; Goodenough, J. B., Li_xCoO_2 (0< x<1): A new cathode material for batteries of high energy density. *Mater. Res. Bull.* **1980,** *15* (6), 783-789.

330. Wu, X.; Leonard, D. P.; Ji, X., Emerging Non-Aqueous Potassium-Ion Batteries: Challenges and Opportunities. *Chem. Mater.* **2017,** *29* (12), 5031-5042.

331. Delmas, C., Sodium and Sodium-Ion Batteries: 50 Years of Research. *Adv. Energy Mater.* **2018**, *8* (17), 1703137.

332. Liu, C.; Luo, S.; Huang, H.; Wang, Z.; Hao, A.; Zhai, Y.; Wang, Z., $K_{0.67}Ni_{0.17}Co_{0.17}Mn_{0.66}O_2$: A cathode material for potassium-ion battery. *Electrochem. Commun.* **2017,** *82*, 150-154.

333. Vaalma, C.; Giffin, G. A.; Buchholz, D.; Passerini, S., Non-Aqueous K-Ion Battery Based on Layered $K_{0.3}MnO_2$ and Hard Carbon/Carbon Black. *J. Electrochem. Soc.* **2016,** *163* (7), A1295-A1299.

334. Wang, X.; Xu, X.; Niu, C.; Meng, J.; Huang, M.; Liu, X.; Liu, Z.; Mai, L., Earth Abundant Fe/Mn-Based Layered Oxide Interconnected Nanowires for Advanced K-Ion Full Batteries. *Nano Lett.* **2016,** *17* (1), 544-550.

335. Kim, H.; Seo, D. H.; Kim, J. C.; Bo, S. H.; Liu, L.; Shi, T.; Ceder, G., Investigation of Potassium Storage in Layered P3-Type $K_{0.5}MnO_2$ Cathode. *Adv. Mater.* **2017,** *29* (37) 1702480.

336. Deng, T.; Fan, X.; Chen, J.; Chen, L.; Luo, C.; Zhou, X.; Yang, J.; Zheng, S.; Wang, C., Layered P2-Type $K_{0.65}Fe_{0.5}Mn_{0.5}O_2$ Microspheres as Superior Cathode for High-Energy Potassium-Ion Batteries. *Adv. Funct. Mater.* **2018,** *28* (28), 1800219.

337. Deng, T.; Fan, X.; Luo, C.; Chen, J.; Chen, L.; Hou, S.; Eidson, N.; Zhou, X.; Wang, C., Self-Templated Formation of P2-type $K_{0.6}CoO_2$ Microspheres for High Reversible Potassium-Ion Batteries. *Nano Lett.* **2018,** *18* (2), 1522-1529.

338. Hwang, J.-Y.; Kim, J.; Yu, T.-Y.; Myung, S.-T.; Sun, Y.-K., Development of P3-$K_{0.69}CrO_2$ as an ultra-high-performance cathode material for K-ion batteries. *Energy Environ. Sci.* **2018,** *11* (10), 2821-2827.

339. Kim, H.; Kim, J. C.; Bianchini, M.; Seo, D.-H.; Rodriguez-Garcia, J.; Ceder, G., Recent Progress and Perspective in Electrode Materials for K-Ion Batteries. *Adv. Energy Mater.* **2018,** *8* (9), 1702384.

340. Li, C.; Zhang, H.; Fu, L.; Liu, H.; Wu, Y.; Rahm, E.; Holze, R.; Wu, H., Cathode materials modified by surface coating for lithium ion batteries. *Electrochim. Acta* **2006,** *51* (19), 3872-3883.

341. Cho, J.; Kim, Y. J.; Kim, T.-J.; Park, B., Zero-Strain Intercalation Cathode for Rechargeable Li-Ion Cell. *Angew. Chem. Int. Ed.* **2001,** *40* (18), 3367-3369.

342. Xiao, B.; Liu, H.; Liu, J.; Sun, Q.; Wang, B.; Kaliyappan, K.; Zhao, Y.; Banis, M. N.; Liu, Y.; Li, R.; Sham, T. K.; Botton, G. A.; Cai, M.; Sun, X., Nanoscale Manipulation of Spinel Lithium Nickel Manganese Oxide Surface by Multisite Ti Occupation as High-Performance Cathode. *Adv. Mater.* **2017,** *29* (47), 1703764.

343. Wu, F.; Zhang, X.; Zhao, T.; Li, L.; Xie, M.; Chen, R., Multifunctional $AlPO_4$ Coating for Improving Electrochemical Properties of Low-Cost $Li[Li_{0.2}Fe_{0.1}Ni_{0.15}Mn_{0.55}]O_2$ Cathode Materials for Lithium-Ion Batteries. *ACS Appl. Mater. Inter.* **2015,** *7* (6), 3773-3781.

344. Sun, Y. K.; Lee, M. J.; Yoon, C. S.; Hassoun, J.; Amine, K.; Scrosati, B., The Role of AlF_3 Coatings in Improving Electrochemical Cycling of Li-Enriched Nickel-Manganese Oxide Electrodes for Li-Ion Batteries. *Adv. Mater.* **2012,** *24* (9), 1192-1196.

345. Xie, J.; Sendek, A. D.; Cubuk, E. D.; Zhang, X.; Lu, Z.; Gong, Y.; Wu, T.; Shi, F.; Liu, W.; Reed, E. J., Atomic Layer Deposition of Stable $LiAlF_4$ Lithium Ion Conductive Interfacial Layer for Stable Cathode Cycling. *ACS Nano* **2017,** *11* (7), 7019-7027.

346. Zhao, S.; Sun, B.; Yan, K.; Zhang, J.; Wang, C.; Wang, G., Aegis of Lithium-Rich Cathode Materials via Heterostructured $LiAlF_4$ Coating for High-Performance Lithium-Ion Batteries. *ACS Appl. Mater. Inter.* **2018,** *10* (39), 33260-33268.

347. Park, B.-C.; Kim, H.-B.; Myung, S.-T.; Amine, K.; Belharouak, I.; Lee, S.-M.; Sun, Y.-K., Improvement of structural and electrochemical properties of AlF_3-coated Li $[Ni_{1/3}Co_{1/3}Mn_{1/3}]O_2$ cathode materials on high voltage region. *J. Power Sources* **2008,** *178* (2), 826-831.

348. Bruce, P. G.; Scrosati, B.; Tarascon, J. M., Nanomaterials for Rechargeable Lithium Batteries. *Angew. Chem. Int. Ed.* **2008,** *47* (16), 2930-2946.

349. Ren, Y.; Armstrong, A. R.; Jiao, F.; Bruce, P. G., Influence of Size on the Rate of Mesoporous Electrodes for Lithium Batteries. *J. Am. Chem. Soc.* **2009,** *132* (3), 996-1004.

350. Sun, C.; Rajasekhara, S.; Goodenough, J. B.; Zhou, F., Monodisperse Porous $LiFePO_4$ Microspheres for a High Power Li-Ion Battery Cathode. *J. Am. Chem. Soc.* **2011,** *133* (7), 2132-2135.

351. Chu, Q.; Wang, X.; Zhang, X.; Li, Q.; Liu, X., Buckled Layers in $K_{0.66}Mn_2O_4 \cdot 0.28H_2O$ and $K_{0.99}Mn_3O_6 \cdot 1.25H_2O$ Synthesized at High Pressure: Implication for the Mechanism of Layer-to-Tunnel Transformation in Manganese Oxides. *Inorg. Chem.* **2011,** *50* (6), 2049-2051.

352. Baddour-Hadjean, R.; Pereira-Ramos, J.-P., Raman Microspectrometry Applied to the Study of Electrode Materials for Lithium Batteries. *Chem. Rev.* **2009,** *110* (3), 1278-1319.

353. Gao, A.; Li, M.; Guo, N.; Qiu, D.; Li, Y.; Wang, S.; Lu, X.; Wang, F.; Yang, R., K-Birnessite Electrode Obtained by Ion Exchange for Potassium-Ion Batteries: Insight into the Concerted Ionic Diffusion and K Storage Mechanism. *Adv. Energy Mater.* **2018**, *9* (1), 1802739.

354. Liu, W.; Li, X.; Xiong, D.; Hao, Y.; Li, J.; Kou, H.; Yan, B.; Li, D.; Lu, S.; Koo, A., Significantly improving cycling performance of cathodes in lithium-ion batteries: the effect of Al_2O_3 and $LiAlO_2$ coatings on $LiNi_{0.6}Co_{0.2}Mn_{0.2}O_2$. *Nano Energy* **2018,** *44*, 111-120.

355. Deng, L.; Niu, X.; Ma, G.; Yang, Z.; Zeng, L.; Zhu, Y.; Guo, L., Layered Potassium Vanadate $K_{0.5}V_2O_5$ as a Cathode Material for Nonaqueous Potassium Ion Batteries. *Adv. Funct. Mater.* **2018**, *28* (49), 1800670.

356. Weppner, W.; Huggins, R. A., Determination of the Kinetic Parameters of Mixed-Conducting Electrodes and Application to the System Li_3Sb. *J. Electrochem. Soc.* **1977,** *124* (10), 1569-1578.

357. Shen, Z.; Cao, L.; Rahn, C. D.; Wang, C.-Y., Least Squares Galvanostatic Intermittent Titration Technique (LS-GITT) for Accurate Solid Phase Diffusivity Measurement. *J. Electrochem. Soc.* **2013,** *160* (10), A1842-A1846.

358. Xiao, N.; McCulloch, W. D.; Wu, Y., Reversible Dendrite-Free Potassium Plating and Stripping Electrochemistry for Potassium Secondary Batteries. *J. Am. Chem. Soc.* **2017,** *139* (28), 9475-9478.

359. Berthelot, R.; Carlier, D.; Delmas, C., Electrochemical investigation of the P2-Na_xCoO_2 phase diagram. *Nat. Mater.* **2011,** *10* (1), 74-80.

360. Kittner, N.; Lill, F.; Kammen, D. M., Energy storage deployment and innovation for the clean energy transition. *Nat. Energy* **2017,** *2* (9), 17125.

361. Etacheri, V.; Marom, R.; Elazari, R.; Salitra, G.; Aurbach, D., Challenges in the development of advanced Li-ion batteries: a review. *Energy Environ. Sci.* **2011,** *4* (9), 3243-3262.

362. Yabuuchi, N.; Kubota, K.; Dahbi, M.; Komaba, S., Research Development on Sodium-Ion Batteries. *Chem. Rev.* **2014,** *114* (23), 11636-11682.

363. Dunn, B.; Kamath, H.; Tarascon, J.-M., Electrical Energy Storage for the Grid: A Battery of Choices. *Science* **2011,** *334* (6058), 928-935.

364. Hwang, J. Y.; Myung, S. T.; Sun, Y. K., Recent Progress in Rechargeable Potassium Batteries. *Adv. Funct. Mater.* **2018,** *28* (43), 1802938.

365. Chen, J.; Yang, B.; Li, H.; Ma, P.; Lang, J.; Yan, X., Candle soot: onion-like carbon, an advanced anode material for a potassium-ion hybrid capacitor. *J. Mater. Chem. A* **2019,** *7* (15), 9247-9252.

366. Yang, C.; Feng, J.; Lv, F.; Zhou, J.; Lin, C.; Wang, K.; Zhang, Y.; Yang, Y.; Wang, W.; Li, J., Metallic Graphene-Like VSe_2 Ultrathin Nanosheets: Superior Potassium-Ion Storage and Their Working Mechanism. *Adv. Mater.* **2018,** *30* (27), 1800036.

367. Wei, Z.; Wang, D.; Li, M.; Gao, Y.; Wang, C.; Chen, G.; Du, F., Fabrication of Hierarchical Potassium Titanium Phosphate Spheroids: A Host Material for Sodium-Ion and Potassium-Ion Storage. *Adv. Energy Mater.* **2018,** *8* (27), 1801102.

368. Zhang, Z.; Li, M.; Gao, Y.; Wei, Z.; Zhang, M.; Wang, C.; Zeng, Y.; Zou, B.; Chen, G.; Du, F., Fast Potassium Storage in Hierarchical $Ca_{0.5}Ti_2(PO_4)_3$@C Microspheres Enabling High-Performance Potassium-Ion Capacitors. *Adv. Funct. Mater.* **2018,** *28* (36), 1802684.

369. Deng, L.; Yang, Z.; Tan, L.; Zeng, L.; Zhu, Y.; Guo, L., Investigation of the Prussian Blue Analog $Co_3[Co(CN)_6]_2$ as an Anode Material for Nonaqueous Potassium-Ion Batteries. *Adv. Mater.* **2018,** *30* (31), 1802510.

370. Sultana, I.; Ramireddy, T.; Rahman, M. M.; Chen, Y.; Glushenkov, A. M., Tin-based composite anodes for potassium-ion batteries. *Chem. Commun.* **2016,** *52* (59), 9279-9282.

371. Zhu, G.-N.; Wang, Y.-G.; Xia, Y.-Y., Ti-based compounds as anode materials for Li-ion batteries. *Energy Environ. Sci.* **2012,** *5* (5), 6652-6667.

372. Mei, Y.; Huang, Y.; Hu, X., Nanostructured Ti-based anode materials for Na-ion batteries. *J. Mater. Chem. A* **2016,** *4* (31), 12001-12013.

373. Zhao, L.; Hu, Y. S.; Li, H.; Wang, Z.; Chen, L., Porous $Li_4Ti_5O_{12}$ Coated with N-Doped Carbon from Ionic Liquids for Li-Ion Batteries. *Adv. Mater.* **2011,** *23* (11), 1385-1388.

374. Kishore, B.; Venkatesh, G.; Munichandraiah, N., $K_2Ti_4O_9$: A Promising Anode Material for Potassium Ion Batteries. *J. Electrochem. Soc.* **2016,** *163* (13), A2551-A2554.

375. Dong, S.; Li, Z.; Xing, Z.; Wu, X.; Ji, X.; Zhang, X., Novel Potassium-Ion Hybrid Capacitor Based on an Anode of $K_2Ti_6O_{13}$ Microscaffolds. *ACS Appl. Mater. Interfaces* **2018,** *10* (18), 15542-15547.

376. Xu, S. M.; Ding, Y. C.; Liu, X.; Zhang, Q.; Wang, K. X.; Chen, J. S., Boosting Potassium Storage Capacity Based on Stress-Induced Size-Dependent Solid-Solution Behavior. *Adv. Energy Mater.* **2018,** *8* (32), 1802175.

377. Zhao, S.; Yan, K.; Munroe, P.; Sun, B.; Wang, G., Construction of Hierarchical $K_{1.39}Mn_3O_6$ Spheres via AlF_3 Coating for High-Performance Potassium-Ion Batteries. *Adv. Energy Mater.* **2019,** *9* (10), 1803757.

378. Ren, Y.; Armstrong, A. R.; Jiao, F.; Bruce, P. G., Influence of Size on the Rate of Mesoporous Electrodes for Lithium Batteries. *J. Am. Chem. Soc.* **2009,** *132* (3), 996-1004.

379. Jung, H.-G.; Jang, M. W.; Hassoun, J.; Sun, Y.-K.; Scrosati, B., A high-rate long-life $Li_4Ti_5O_{12}$/$Li[Ni_{0.45}Co_{0.1}Mn_{1.45}]O_4$ lithium-ion battery. *Nat. Commun.* **2011,** *2*, 516.

380. Zhang, W. M.; Wu, X. L.; Hu, J. S.; Guo, Y. G.; Wan, L. J., Carbon Coated Fe_3O_4 Nanospindles as a Superior Anode Material for Lithium-Ion Batteries. *Adv. Funct. Mater.* **2008,** *18* (24), 3941-3946.

381. Guo, Y. G.; Hu, J. S.; Wan, L. J., Nanostructured Materials for Electrochemical Energy Conversion and Storage Devices. *Adv. Mater.* **2008,** *20* (15), 2878-2887.

382. Li, H.; Zhou, H., Enhancing the performances of Li-ion batteries by carbon-coating: present and future. *Chem. Commun.* **2012,** *48* (9), 1201-1217.

383. Zhu, G.-N.; Liu, H.-J.; Zhuang, J.-H.; Wang, C.-X.; Wang, Y.-G.; Xia, Y.-Y., Carbon-coated nano-sized $Li_4Ti_5O_{12}$ nanoporous micro-sphere as anode material for high-rate lithium-ion batteries. *Energy Environ. Sci.* **2011,** *4* (10), 4016-4022.

384. Jian, Z.; Zhao, L.; Pan, H.; Hu, Y.-S.; Li, H.; Chen, W.; Chen, L., Carbon coated $Na_3V_2(PO_4)_3$ as novel electrode material for sodium ion batteries. *Electrochem. Commun.* **2012,** *14* (1), 86-89.

385. Kim, H.; Kim, H.; Ding, Z.; Lee, M. H.; Lim, K.; Yoon, G.; Kang, K., Recent Progress in Electrode Materials for Sodium-Ion Batteries. *Adv. Energy Mater.* **2016,** *6* (19), 1600943.

386. Cho, Y.-D.; Fey, G. T.-K.; Kao, H.-M., The effect of carbon coating thickness on the capacity of $LiFePO_4$/C composite cathodes. *J. Power Sources* **2009,** *189* (1), 256-262.

387. Li, D.; Ren, X.; Ai, Q.; Sun, Q.; Zhu, L.; Liu, Y.; Liang, Z.; Peng, R.; Si, P.; Lou, J., Facile Fabrication of Nitrogen-Doped Porous Carbon as Superior Anode Material for Potassium-Ion Batteries. *Adv. Energy Mater.* **2018,** *8* (34), 1802386.

388. Li, Y.; Yang, C.; Zheng, F.; Pan, Q.; Liu, Y.; Wang, G.; Liu, T.; Hu, J.; Liu, M., Design of TiO_2eC hierarchical tubular heterostructures for high performance potassium ion batteries. *Nano Energy* **2019,** *59*, 582-590.

389. Chen, C.; Wen, Y.; Hu, X.; Ji, X.; Yan, M.; Mai, L.; Hu, P.; Shan, B.; Huang, Y., Na^+ intercalation pseudocapacitance in graphene-coupled titanium oxide enabling ultra-fast sodium storage and long-term cycling. *Nat. Commun.* **2015,** *6*, 6929.

390. Fan, L.; Ma, R.; Zhang, Q.; Jia, X.; Lu, B., Graphite Anode for Potassium Ion Battery with Unprecedented Performance. *Angew. Chem. Int. Ed.* **2019,** *131*, 10610.

391. Wu, L.; Bresser, D.; Buchholz, D.; Giffin, G. A.; Castro, C. R.; Ochel, A.; Passerini, S., Unfolding the Mechanism of Sodium Insertion in Anatase TiO_2 Nanoparticles. *Adv. Energy Mater.* **2015,** *5* (2), 1401142.

392. Xia, Q.; Huang, Y.; Xiao, J.; Wang, L.; Lin, Z.; Li, W.; Liu, H.; Gu, Q.; Liu, H. K.; Chou, S. L., Phosphorus-Modulation-Triggered Surface Disorder in Titanium Dioxide Nanocrystals Enables Exceptional Sodium-Storage Performance. *Angew. Chem. Int. Ed.* **2019,** *58* (12), 4022-4026.

393. Augustyn, V.; Simon, P.; Dunn, B., Pseudocapacitive oxide materials for high-rate electrochemical energy storage. *Energy Environ. Sci.* **2014,** *7* (5), 1597-1614.

394. Wang, H.; Zhu, C.; Chao, D.; Yan, Q.; Fan, H. J., Nonaqueous Hybrid Lithium-Ion and Sodium-Ion Capacitors. *Adv. Mater.* **2017,** *29* (46), 1702093.

395. Brezesinski, T.; Wang, J.; Tolbert, S. H.; Dunn, B., Ordered mesoporous α-MoO_3 with iso-oriented nanocrystalline walls for thin-film pseudocapacitors. *Nat. Mater.* **2010,** *9* (2), 146-151.

396. Su, D.; McDonagh, A.; Qiao, S. Z.; Wang, G., High-Capacity Aqueous Potassium-Ion Batteries for Large-Scale Energy Storage. *Adv. Mater.* **2017,** *29* (1), 1604007.

397. Xu, Y.; Zhang, C.; Zhou, M.; Fu, Q.; Zhao, C.; Wu, M.; Lei, Y., Highly nitrogen doped carbon nanofibers with superior rate capability and cyclability for potassium ion batteries. *Nat. Commun.* **2018,** *9* (1), 1720.

398. Liu, J.; Wang, J.; Xu, C.; Jiang, H.; Li, C.; Zhang, L.; Lin, J.; Shen, Z. X., Advanced Energy Storage Devices: Basic Principles, Analytical Methods, and Rational Materials Design. *Adv. Sci.* **2018,** *5* (1), 1700322.

399. Augustyn, V.; Come, J.; Lowe, M. A.; Kim, J. W.; Taberna, P.-L.; Tolbert, S. H.; Abruña, H. D.; Simon, P.; Dunn, B., High-rate electrochemical energy storage through Li^+ intercalation pseudocapacitance. *Nat. Mater.* **2013,** *12* (6), 518-522.

400. Ma, X.; Cheng, J.; Dong, L.; Liu, W.; Mou, J.; Zhao, L.; Wang, J.; Ren, D.; Wu, J.; Xu, C.; Kang, F., Multivalent ion storage towards high-performance aqueous zinc-ion hybrid supercapacitors. *Energy Stor. Mater.* **2019,** *20*, 335-342.

401. Fan, L.; Lin, K.; Wang, J.; Ma, R.; Lu, B., A Nonaqueous Potassium-Based Battery–Supercapacitor Hybrid Device. *Adv. Mater.* **2018,** *30* (20), 1800804.

402. Zhou, L.; Zhang, M.; Wang, Y.; Zhu, Y.; Fu, L.; Liu, X.; Wu, Y.; Huang, W., Cubic Prussian blue crystals from a facile one-step synthesis as positive electrode material for superior potassium-ion capacitors. *Electrochim. Acta* **2017,** *232*, 106-113.

403. Kim, H.; Park, K. Y.; Cho, M. Y.; Kim, M. H.; Hong, J.; Jung, S. K.; Roh, K. C.; Kang, K., High-Performance Hybrid Supercapacitor Based on Graphene-Wrapped $Li_4Ti_5O_{12}$ and Activated Carbon. *ChemElectroChem* **2014,** *1* (1), 125-130.

404. Yin, J.; Qi, L.; Wang, H., Sodium Titanate Nanotubes as Negative Electrode Materials for Sodium-Ion Capacitors. *ACS Appl. Mater. Inter.* **2012,** *4* (5), 2762-2768.

405. Chen, Z.; Augustyn, V.; Jia, X.; Xiao, Q.; Dunn, B.; Lu, Y., High-Performance Sodium-Ion Pseudocapacitors Based on Hierarchically Porous Nanowire Composites. *ACS Nano* **2012,** *6* (5), 4319-4327.

406. Winter, M.; Barnett, B.; Xu, K., Before Li Ion Batteries. *Chem. Rev.* **2018,** *118* (23), 11433-11456.

407. Goodenough, J. B.; Kim, Y., Challenges for Rechargeable Li Batteries. *Chem. Mater.* **2010,** *22* (3), 587-603.

408. Fan, L.; Lin, K.; Wang, J.; Ma, R.; Lu, B., A Nonaqueous Potassium-Based Battery–Supercapacitor Hybrid Device. *Adv. Mater.* **2018,** *30* (20), 1800804.

409. Hosaka, T.; Kubota, K.; Hameed, A. S.; Komaba, S., Research Development on K-Ion Batteries. *Chem. Rev.* **2020,** *120* (14), 6358-6466.

410. Xue, L.; Li, Y.; Gao, H.; Zhou, W.; Lü, X.; Kaveevivitchai, W.; Manthiram, A.; Goodenough, J. B., Low-Cost High-Energy Potassium Cathode. *J. Am. Chem. Soc.* **2017,** *139* (6), 2164-2167.

411. Zhao, S.; Yan, K.; Munroe, P.; Sun, B.; Wang, G., Construction of Hierarchical $K_{1.39}Mn_3O_6$ Spheres via AlF_3 Coating for High-Performance Potassium-Ion Batteries. *Adv. Energy Mater.* **2019,** *9* (10), 1803757.

412. Zhao, S.; Dong, L.; Sun, B.; Yan, K.; Zhang, J.; Wan, S.; He, F.; Munroe, P.; Notten, P. H. L.; Wang, G., $K_2Ti_2O_5$@C Microspheres with Enhanced K^+ Intercalation Pseudocapacitance Ensuring Fast Potassium Storage and Long-Term Cycling Stability. *Small* **2020,** *16* (4), 1906131.

413. Fan, L.; Ma, R.; Zhang, Q.; Jia, X.; Lu, B., Graphite Anode for a Potassium-Ion Battery with Unprecedented Performance. *Angew. Chem. Int. Ed.* **2019,** *58* (31), 10500-10505.

414. Zhang, W.; Pang, W. K.; Sencadas, V.; Guo, Z., Understanding High-Energy-Density Sn_4P_3 Anodes for Potassium-Ion Batteries. *Joule* **2018,** *2* (8), 1534-1547.

415. Liu, L.; Chen, Y.; Xie, Y.; Tao, P.; Li, Q.; Yan, C., Understanding of the Ultrastable K-Ion Storage of Carbonaceous Anode. *Adv. Funct. Mater.* **2018,** *28* (29), 1801989.

416. Yang, J.; Ju, Z.; Jiang, Y.; Xing, Z.; Xi, B.; Feng, J.; Xiong, S., Enhanced Capacity and Rate Capability of Nitrogen/Oxygen Dual-Doped Hard Carbon in Capacitive Potassium-Ion Storage. *Adv. Mater.* **2018,** *30* (4), 1700104.

417. Wu, X.; Chen, Y.; Xing, Z.; Lam, C. W. K.; Pang, S.-S.; Zhang, W.; Ju, Z., Advanced Carbon-Based Anodes for Potassium-Ion Batteries. *Adv. Energy Mater.* **2019,** *9* (21), 1900343.

418. Jian, Z.; Xing, Z.; Bommier, C.; Li, Z.; Ji, X., Hard Carbon Microspheres: Potassium-Ion Anode Versus Sodium-Ion Anode. *Adv. Energy Mater.* **2016,** *6* (3), 1501874.

419. Wang, H.; Yu, D.; Wang, X.; Niu, Z.; Chen, M.; Cheng, L.; Zhou, W.; Guo, L., Electrolyte Chemistry Enables Simultaneous Stabilization of Potassium Metal and Alloying Anode for Potassium-Ion Batteries. *Angew. Chem. Int. Ed.* **2019,** *58* (46), 16451-16455.

420. Lai, X.; Halpert, J. E.; Wang, D., Recent advances in micro-/nano-structured hollow spheres for energy applications: From simple to complex systems. *Energy Environ. Sci.* **2012,** *5* (2), 5604-5618.

421. Ding, J.; Zhang, H.; Zhou, H.; Feng, J.; Zheng, X.; Zhong, C.; Paek, E.; Hu, W.; Mitlin, D., Sulfur-Grafted Hollow Carbon Spheres for Potassium-Ion Battery Anodes. *Adv. Mater.* **2019,** *31* (30), 1900429.

422. Wang, W.; Jiang, B.; Qian, C.; Lv, F.; Feng, J.; Zhou, J.; Wang, K.; Yang, C.; Yang, Y.; Guo, S., Pistachio-Shuck-Like $MoSe_2$/C Core/Shell Nanostructures for High-Performance Potassium-Ion Storage. *Adv. Mater.* **2018,** *30* (30), 1801812.

423. Bin, D.-S.; Lin, X.-J.; Sun, Y.-G.; Xu, Y.-S.; Zhang, K.; Cao, A.-M.; Wan, L.-J., Engineering Hollow Carbon Architecture for High-Performance K-Ion Battery Anode. *J. Am. Chem. Soc.* **2018,** *140* (23), 7127-7134.

424. Bin, D.-S.; Chi, Z.-X.; Li, Y.; Zhang, K.; Yang, X.; Sun, Y.-G.; Piao, J.-Y.; Cao, A.-M.; Wan, L.-J., Controlling the Compositional Chemistry in Single Nanoparticles for Functional Hollow Carbon Nanospheres. *J. Am. Chem. Soc.* **2017,** *139* (38), 13492-13498.

425. Hu, X.; Liu, Y.; Chen, J.; Yi, L.; Zhan, H.; Wen, Z., Fast Redox Kinetics in Bi-Heteroatom Doped 3D Porous Carbon Nanosheets for High-Performance Hybrid Potassium-Ion Battery Capacitors. *Adv. Energy Mater.* **2019,** *9* (42), 1901533.

426. Li, D.; Ren, X.; Ai, Q.; Sun, Q.; Zhu, L.; Liu, Y.; Liang, Z.; Peng, R.; Si, P.; Lou, J.; Feng, J.; Ci, L., Facile Fabrication of Nitrogen-Doped Porous Carbon as Superior Anode Material for Potassium-Ion Batteries. *Adv. Energy Mater.* **2018,** *8* (34), 1802386.

427. Chen, M.; Wang, W.; Liang, X.; Gong, S.; Liu, J.; Wang, Q.; Guo, S.; Yang, H., Sulfur/Oxygen Codoped Porous Hard Carbon Microspheres for High-Performance Potassium-Ion Batteries. *Adv. Energy Mater.* **2018,** *8* (19), 1800171.

428. Lu, J.; Wang, C.; Yu, H.; Gong, S.; Xia, G.; Jiang, P.; Xu, P.; Yang, K.; Chen, Q., Oxygen/Fluorine Dual-Doped Porous Carbon Nanopolyhedra Enabled Ultrafast and Highly Stable Potassium Storage. *Adv. Funct. Mater.* **2019,** *29* (49), 1906126.

429. Gong, J.; Zhao, G.; Feng, J.; An, Y.; Li, T.; Zhang, L.; Li, B.; Qian, Z., Controllable Phosphorylation Strategy for Free-Standing Phosphorus/Nitrogen Cofunctionalized Porous Carbon Monoliths as High-Performance Potassium Ion Battery Anodes. *ACS Nano* **2020,** *14* (10), 14057-14069.

430. Qian, Y.; Jiang, S.; Li, Y.; Yi, Z.; Zhou, J.; Li, T.; Han, Y.; Wang, Y.; Tian, J.; Lin, N.; Qian, Y., In Situ Revealing the Electroactivity of P-O and P-C Bonds in Hard Carbon for High-Capacity and Long-Life Li/K-Ion Batteries. *Adv. Energy Mater.* **2019,** *9* (34), 1901676.

431. Wang, H.; Zhai, D.; Kang, F., Solid electrolyte interphase (SEI) in potassium ion batteries. *Energy Environ. Sci.* **2020,** *13*, 4583-4608.

432. Zhang, R.; Huang, J.; Deng, W.; Bao, J.; Pan, Y.; Huang, S.; Sun, C.-F., Safe, Low-Cost, Fast-Kinetics and Low-Strain Inorganic-Open-Framework Anode for Potassium-Ion Batteries. *Angew. Chem. Int. Ed.* **2019,** *58* (46), 16474-16479.

433. Zhang, Z.; Li, M.; Gao, Y.; Wei, Z.; Zhang, M.; Wang, C.; Zeng, Y.; Zou, B.; Chen, G.; Du, F., Fast Potassium Storage in Hierarchical $Ca_{0.5}Ti_2(PO_4)_3$@C Microspheres Enabling High-Performance Potassium-Ion Capacitors. *Adv. Funct. Mater.* **2018,** *28* (36), 1802684.

434. Deng, L.; Yang, Z.; Tan, L.; Zeng, L.; Zhu, Y.; Guo, L., Investigation of the Prussian Blue Analog $Co_3[Co(CN)_6]_2$ as an Anode Material for Nonaqueous Potassium-Ion Batteries. *Adv. Mater.* **2018,** *30* (31), 1802510.

435. Zeng, C.; Xie, F.; Yang, X.; Jaroniec, M.; Zhang, L.; Qiao, S.-Z., Ultrathin Titanate Nanosheets/Graphene Films Derived from Confined Transformation for Excellent Na/K Ion Storage. *Angew. Chem. Int. Ed.* **2018,** *57* (28), 8540-8544.

436. Chen, J.; Yang, B.; Hou, H.; Li, H.; Liu, L.; Zhang, L.; Yan, X., Disordered, Large Interlayer Spacing, and Oxygen-Rich Carbon Nanosheets for Potassium Ion Hybrid Capacitor. *Adv. Energy Mater.* **2019,** *9* (19), 1803894.

437. Zhou, X.; Chen, L.; Zhang, W.; Wang, J.; Liu, Z.; Zeng, S.; Xu, R.; Wu, Y.; Ye, S.; Feng, Y.; Cheng, X.; Peng, Z.; Li, X.; Yu, Y., Three-Dimensional Ordered Macroporous Metal–Organic Framework Single Crystal-Derived Nitrogen-Doped Hierarchical Porous Carbon for High-Performance Potassium-Ion Batteries. *Nano Lett.* **2019,** *19* (8), 4965-4973.

438. Chang, X.; Zhou, X.; Ou, X.; Lee, C.-S.; Zhou, J.; Tang, Y., Ultrahigh Nitrogen Doping of Carbon Nanosheets for High Capacity and Long Cycling Potassium Ion Storage. *Adv. Energy Mater.* **2019,** *9* (47), 1902672.

439. Qiu, D.; Guan, J.; Li, M.; Kang, C.; Wei, J.; Li, Y.; Xie, Z.; Wang, F.; Yang, R., Kinetics Enhanced Nitrogen-Doped Hierarchical Porous Hollow Carbon Spheres Boosting Advanced Potassium-Ion Hybrid Capacitors. *Adv. Funct. Mater.* **2019,** *29* (32), 1903496.

440. Liu, Y.; Lu, Y.-X.; Xu, Y.-S.; Meng, Q.-S.; Gao, J.-C.; Sun, Y.-G.; Hu, Y.-S.; Chang, B.-B.; Liu, C.-T.; Cao, A.-M., Pitch-Derived Soft Carbon as Stable Anode Material for Potassium Ion Batteries. *Adv. Mater.* **2020,** *32* (17), 2000505.

441. Qian, Y.; Jiang, S.; Li, Y.; Yi, Z.; Zhou, J.; Tian, J.; Lin, N.; Qian, Y., Water-Induced Growth of a Highly Oriented Mesoporous Graphitic Carbon Nanospring for Fast Potassium-Ion Adsorption/Intercalation Storage. *Angew. Chem. Int. Ed.* **2019,** *58* (50), 18108-18115.

442. Wang, W.; Zhou, J.; Wang, Z.; Zhao, L.; Li, P.; Yang, Y.; Yang, C.; Huang, H.; Guo, S., Short-Range Order in Mesoporous Carbon Boosts Potassium-Ion Battery Performance. *Adv. Energy Mater.* **2018,** *8* (5), 1701648.

443. Hu, X.; Zhong, G.; Li, J.; Liu, Y.; Yuan, J.; Chen, J.; Zhan, H.; Wen, Z., Hierarchical porous carbon nanofibers for compatible anode and cathode of potassium-ion hybrid capacitor. *Energy Environ. Sci.* **2020,** *13* (8), 2431-2440.

444. Liu, X.; Elia, G. A.; Qin, B.; Zhang, H.; Ruschhaupt, P.; Fang, S.; Varzi, A.; Passerini, S., High-Power Na-Ion and K-Ion Hybrid Capacitors Exploiting Cointercalation in Graphite Negative Electrodes. *ACS Energy Lett.* **2019,** *4* (11), 2675-2682.

445. Dong, S.; Shen, L.; Li, H.; Pang, G.; Dou, H.; Zhang, X., Flexible Sodium-Ion Pseudocapacitors Based on 3D $Na_2Ti_3O_7$ Nanosheet Arrays/Carbon Textiles Anodes. *Adv. Funct. Mater.* **2016,** *26* (21), 3703-3710.

446. Kim, H.; Park, K.-Y.; Cho, M.-Y.; Kim, M.-H.; Hong, J.; Jung, S.-K.; Roh, K. C.; Kang, K., High-Performance Hybrid Supercapacitor Based on Graphene-Wrapped $Li_4Ti_5O_{12}$ and Activated Carbon. *ChemElectroChem* **2014,** *1* (1), 125-130.